Attosecond time-resolved experiments - towards biomolecules

im Fachbereich Physik der Freien Universität Berlin eingereichte

Dissertation

zur Erlangung des Grades

Dr. rer. nat.

Christian Neidel

Berlin 2017

Erstgutachter: Prof. Dr. Marc J. J. Vrakking (Betreuer)
Zweitgutachter: Prof. Dr. Thomas Schultz

Tag der Disputation: 2017-06-30

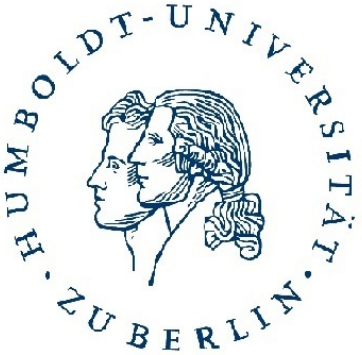

Die vorgestellten Arbeiten wurden durchgeführt am *Max-Born-Institut* für Nichtlineare Optik und Kurzzeitspektroskopie in Berlin-Adlershof, der *Humboldt Universität zu Berlin* in Berlin-Adlershof und dem *FOM Institut AMOLF* in Amsterdam.

Eidesstattliche Erklärung

(gemäß §7, Ziffer (4) der Promotionsordnung vom 02.09.2013 des Fachbereichs Physik an der Freien Universität Berlin)

Die vorliegende Dissertationsschrift wurde von mir selbstständig angefertigt. Alle Hilfen und Hilfsmittel, die beim Erstellen der Arbeit verwendet wurden, habe ich an den entsprechenden Stellen angegeben. Alle Textstellen, die wörtlich oder dem Sinn nach auf Publikationen oder Werken anderer Autoren beruhen, sind als solche kenntlich gemacht.

Die Arbeit hat bisher weder in der gegenwärtigen noch in einer anderen Fassung dem Fachbereich Physik der Freien Universität Berlin oder einer anderen Universitätsfakultät vorgelegen.

Ort, Datum	Unterschrift

To

Elisabeth †

Contents

Introduction

Ancient Greek philosophers discussed the *atomos* as the smallest building block of matter. Today, the word *atom* refers to the smallest chemical unit that consists of a positively charged nucleus surrounded by a negatively charged cloud of electrons.[1] Atoms can combine to form larger units, e.g., molecules and crystals. These units in turn are the preponderant constituents of matter in its gaseous, liquid or solid state.

Attempts to isolate and observe the smallest units of matter have therefore been a human endeavor for millennia. Apart from satisfying the natural human curiosity, scientific explorations and discoveries offer palpable benefits to mankind in general. To name a few examples, Fleming's discovery of penicillin [2] led to a revolution in medicine, Maxwell's theory of electrodynamics [3] is the foundation for modern society and Ostwald's experiments on catalysis [4] helped to make chemical synthesis more efficient and to lower industrial pollution.

Investigating the characteristics of molecules as well as atomic and molecular interactions by exploitation of electromagnetic radiation is a common tool used by physicists and chemists around the world to contribute to scientific progress. In 1905, Einstein explained the photo-electric effect by assuming that electro-magnetic radiation of frequency ν can be described in a particle-like manner [5], i.e., consisting of indivisible quanta with an energy of $E = h \cdot \nu$, where h is Planck's constant[2]. Matter can be ionized by absorbing a photon, i.e., a quantum of light is absorbed and an electron is emitted. Therefore, the photon energy needs to be larger than the ionization potential (work function). This effect

[1] In contrast to electrons, the nucleus is not indivisible. It is composed of positively charged protons and electrically neutral particles (neutrons), which by themselves consist of so-called quarks [1].

[2] Planck's constant denotes the quantum of action, which is the smallest change in energy possible within a given time window.

lies at the heart of the experiments presented here.

In addition to the linear (single-photon) interaction of light and matter, also non-linear interaction is a subject of this work. In 1931, Göppert-Mayer described two-photon processes for the first time [6]. She claimed that it should be possible for matter to become ionized by absorbing two photons at the same time, even if the energy of a single photon alone would not be sufficient to overcome the ionization potential. For a long time, these predictions could not be verified experimentally. The probability of simultaneous absorption of two photons is much lower than the probability for single-photon absorption. To observe the predicted multi-photon processes, many photons must be available in a very small volume within a very short time window. Nowadays, the observation of such multi-photon processes can be easily achieved by pulsed laser light sources, which in turn are also based on non-linear (multi-photon) processes and closely related to the field of non-linear optics.

The working principle of the laser[3] is provided by the effect of stimulated emission and was postulated by Einstein in 1916 [7]. In 1960, Maiman demonstrated the first working laser [8]. In 1961, Franken et al. irradiated a non-linear crystal with a laser and discovered that it emits the second harmonic of the incident light [9]. Thereafter, Kaiser and Garett observed the simultaneous excitation of a crystal by two photons [10]. Another non-linear response of matter to incident laser light was found by Maker et al. in 1964 [11]. They discovered that the refractive index of liquids changes as a function of laser intensity. Today, it is known that this effect is caused by a term of the refractive index that varies quadratically with the applied electric field (linear with intensity). The so-called *Kerr effect* is widely used in modern solid state lasers [12]. By applying a technique called *Kerr-lens mode locking*[4], it became feasible to build high-repetition rate laser sources that produce strong ultrashort light pulses. These pulses can be as short as vibrational periods of molecular bonds, i.e., on the order of tens of femtoseconds ($1\,\mathrm{fs} = 1 \cdot 10^{-15}\,\mathrm{s}$). Among others, amplified Kerr-lens mode-locked solid state lasers[5] paved the way towards *femtochemistry*

[3]Laser: Light Amplification by Stimulated Emission of Radiation.

[4]The Kerr lens arises through the spatial intensity distribution of the Gaussian-shaped beam in a laser cavity. Due to the intensity variation, the non-linear refractive index is modulated accordingly leading to self-focusing because the indices of refraction are different for the intense inner part of the beam and its less intense outer part.

[5]This is the most common type of laser used to investigate ultrashort dynamics in molecules.

[13, 14], i.e., the investigation of atomic motion in molecules using femtosecond lasers.

The physical description of photo-initiated electronic excitation and ionization of molecules and the subsequent nuclear motion are based on the *Born-Oppenheimer approximation* [15] and the related *Franck-Condon principle* [16]. The quantum nature of molecular energetics is described by wavefunctions that can be determined through the Schrödinger equation [17, 18]. Within the Born-Oppenheimer framework, the electron-nuclear wavefunction can be factorized into two parts. The separation leads to an electronic wavefunction, depending parametrically on the nuclear coordinates, and a nuclear wavefunction. The physical reasoning behind the Born-Oppenheimer approximation is based on the difference in mass between the heavy atomic nuclei and the electrons, which are three to five orders of magnitude lighter than the nuclei. Born and Oppenheimer assumed that the electronic charge distribution in the molecule adapts instantaneously to the positions of the nuclei, i.e., it changes adiabatically. Therefore, the electronic energy for different positions of the nuclei, as calculated by the Schrödinger equation within the Born-Oppenheimer approximation, forms a potential energy surface[6] (PES). The Franck-Condon principle is an application of the Born-Oppenheimer approximation for a sudden change of the electronic state (photo-excitation or -ionization). It is assumed that the nuclear coordinates can be regarded as frozen during a quantum transition from one electronic state to another. The population of excited states depends on the initial state such that the overlap of the nuclear wavefunctions of the initial and final state is maximized.

As a pioneer in the field of femtochemistry, Zewail was awarded the Nobel price in 1999 [19]. Exploiting ultrashort laser pulses, he used an optical pump-probe scheme to study molecular dynamics in real time. The same concept is still used in modern laser experiments and works as follows: Two laser pulses exhibiting a variable time delay are focused onto a molecular target. The first laser pulse excites or ionizes the molecules, which subsequently propagate on excited potential energy surfaces. After a well-controlled amount of time, a second laser pulse probes the new state. This experiment is repeated for a series of time delays between the two pulses. The result is a stroboscopic movie of the excited molecule. The available time resolution is only limited by the duration of the laser pulses.

The femtosecond pump-probe scheme was used to study excited state dynamics and

[6] For a molecule, a manifold of potential energy surfaces exists as there are many possible electronic configurations.

chemical reactions [20, 21] as well as for steering reactions in the framework of coherent control [22, 23]. In 1991, Baumert et al. studied multi-photon ionization of sodium dimers [24]. The pump-probe delay controlled the branching ratio between the molecular parent ion Na_2^+ and the fragment Na^+. These types of experiments were analyzed within the framework of the Born-Oppenheimer approximation ignoring the possible coupling of electronic and nuclear degrees of freedom. Indeed, the duration of conventional femtosecond laser pulses is too long to control or observe non-adiabatic electronic motion in real time. Investigating molecular dynamics on timescales down to the attosecond regime ($1\,\mathrm{as} = 1 \cdot 10^{-3}\,\mathrm{fs}$) might enable the experimentalist to track and control electron dynamics and their interplay with nuclear dynamics.

Electron dynamics are initiated by preparing an electronic wavepacket consisting of a superposition of stationary electronic states. The beat period of the resulting electronic oscillation is given by $\Delta E \Delta T = 2\pi\hbar$. The spacing between electronic states ranges from eV to meV for highly exited states. Therefore, the electronic timescale is on the order of as to fs. E.g., $\Delta T = 827\,\mathrm{as}$ when the states involved are spaced by $\Delta E = 5\,\mathrm{eV}$ and $\Delta T = 827\,\mathrm{fs}$ when the spacing is $\Delta E = 5\,\mathrm{meV}$. The aforementioned Born-Oppenheimer approximation is only valid when the electronic timescale is much smaller than that of the nuclear motion. Hence, the approximation becomes inappropriate when 1) the electronic motion is much slower than the nuclear motion or 2) the electronic and nuclear timescales are similar. The first scenario is known as the *inverse Born-Oppenheimer* regime (IBO) and occurs in Rydberg systems. In this case, the nuclei can adapt to the position of the slow-moving Rydberg electrons and these electrons move in the averaged potential of the nuclei [25]. In the second case, the energy spacing of the electronic potential surfaces becomes very small and the surfaces approach a so-called conical intersection (avoided-crossing of potential energy curves in one dimensional systems). As a result, the molecular system can undergo non-adiabatic transitions from one electronic state to a neighboring state [26, 27]. Electron dynamics that are much faster than any nuclear dynamics are investigated within the framework of the *post-Born-Oppenheimer* regime [28]. The charge distribution in molecules after sudden excitation can exhibit rich dynamics before the nuclear motion sets in (*charge migration*). These post-Born-Oppenheimer dynamics can last for several femtoseconds, approaching the timescale of nuclear motion [28]. Due to the onset of nuclear dynamics, the coherent electronic motion decoheres, resulting in charge localization (*charge transfer*).

The non-adiabatic potential caused by charge migration processes might significantly influence the nuclear motion until the electron distribution relaxes. Up to this point, the concept of electrons adapting instantaneously to the nuclei fails. Hence, controlling electron dynamics on the attosecond timescale might provide a control parameter to steer chemical reactions, e.g., the dissociation of a diatomic molecule.

The investigation of ultrafast processes in molecules beyond the Born-Oppenheimer regime opens two new and highly interesting routes for physics and chemistry. On a fundamental scale, it allows to follow electronic motion and coupled electron-nuclear dynamics in real time. On the other hand, the insights might be exploited to achieve control over photo-induced chemical reactivity beyond the femtochemistry approach mentioned above. In the field of mass spectrometry, e.g., it would be desirable to control bond cleavages site-specifically to allow for unambiguous composition elucidation.

The experimental observation of electronic rearrangements in molecular systems and its possible influence on subsequent nuclear dynamics has been performed for more than 20 years. In 1995, Weinkauf et al. observed site-specific dissociation following charge transfer in biomolecules [29, 30]. Polypeptides carrying an aromatic amino acid at their C-terminal were activated by resonant multi-photon ionization (REMPI) of the aromatic compound. The hole charge migrated to the opposite site (N-terminal) of the peptide, as observed by monitoring the fragmentation pattern after the molecules were irradiated by a second laser pulse. In 1998, Remacle et al. studied these experiments theoretically and introduced a model to describe *charge-directed reactivity* [31]. A positive charge created in a peptide propagated rapidly through the molecule and initiated dissociation at its final location, indicating that reactivity can follow charge migration and subsequent charge transfer. In 1999, Cederbaum et al. showed theoretically that correlated electron dynamics could occur in molecular systems before any nuclear dynamics can set in [32] (post-Born-Oppenheimer regime). In 2003 Breidbach et al. claimed that electron correlation is an essential ingredient for hole migration to take place [33]. Three main mechanisms in the process of charge migration after sudden ionization were deduced. 1) The hole can migrate from one end of the molecule to the other as discussed above. 2) It can oscillate back and forth within the molecule, or 3) the hole charge density delocalizes over the whole molecule, depending on the states involved in the initial ionization process.

In the following years, the process of ultrafast charge migration was studied theoretically

for a large number of model systems. In 2005, Kuleff et al. investigated charge migration in the amino acid glycine [34]. A hole created after sudden ionization becomes localized within the molecule after 3 fs or it becomes distributed over the molecule within 8 fs, depending on the molecular orbital in which the hole was created. In the same year, Hennig et al. calculated that the hole charge created by ionization of a certain orbital of N-methyl acetamide migrated almost completely from one side of the molecule to the other within about 4 fs [35]. Also in 2005, Breidbach showed computationally that correlated electron dynamics can occur within only 50 as [36]. The speed of charge migration, even through large molecules like polypeptides, can be explained by the correlation of the electronic distribution. Charges do not necessarily have to propagate along the bonds in extended molecules, but can vanish at one side and reappear on the opposite side if the relevant electronic states are delocalized to a sufficient extend. Kuleff et al. reported on charge migration in a ring-structure molecule in 2010. The calculations showed that the hole *jumps* over the ring [37] rather than migrating along the bonds. In 2014, Perveaux et al. theoretically investigated whether the charge oscillation in neutral O_3 between the two bonds can be followed experimentally [38]. The authors concluded that it is feasible to follow these dynamics with attosecond laser pulses but the experimental energy resolution might be an issue. In 2016, Popova-Gorelova et al. predicted a charge oscillation period of about 10 fs for indole after sudden ionization and theoretically showed that these electron dynamics can be observed with time- and angle resolved photo-electron spectroscopy [39].

The interplay of fast charge migration and somewhat slower nuclear rearrangements in larger molecules was studied for fewer cases. In 2005, Lehr et al. conducted femtosecond pump-probe experiments on the molecule PENNA, which served as a model peptide [40, 41]. The investigated charge transfer took place on a timescale of 80 fs and probably involved electronic as well as nuclear motion. A theoretical study of the dynamics after sudden ionization in glycine also focused on the interplay between the electron distribution and the nuclear rearrangement. In 2007, Kuleff and Cederbaum investigated charge migration in glycine for three different conformers [42] and found that, for slightly different positions of the nuclei, charge dynamics after sudden ionization differ dramatically. Another amino acid was the subject of ultrafast pump-probe measurements in 2012 by Belshaw et al. [43]. A 1.5 fs extreme ultraviolet (XUV) pump pulse ionized phenylalanine site-specifically at the phenyl group. Thereafter, the charge hole migrated to the amine site within

30 fs. The migration was probed by a 6 fs long pulse in the visible spectral range, which preferentially created another charge at the amine site, leading to dicationic immonium ions[7]. In accordance with theory, it was proposed that the charge distribution after the first ionization event begins to oscillate on a timescale faster than 5 fs. Due to the coupled electronic-nuclear motion, this coherent oscillation decoheres, leading to a charge localization at the amine site. In 2015, Vacher et al. pointed out that the electron dynamics after sudden ionization may decohere too fast to be probed experimentally due to the widths of the nuclear wavepacket [44]. In the same year, Despré et al. demonstrated theoretically that charge oscillations induced by sudden ionization in benzene last for about 10 fs and therefore survives the nuclear motion-induced dephasing [45].

Using small molecules, the charge distribution during dissociative ionization was not only observed but also controlled on the attosecond timescale. In first experiments, homonuclear diatomic molecules (H_2 and D_2) were dissociated by single ionization. The negative charge localization was determined by laboratory frame experiments, measuring the direction of ejection for the positively charged fragment. The nucleus carrying the remaining electron could be controlled in different ways [46–48]. In 2006, Kling et al. reported the control of electron localization during dissociation of the deuterium molecular cation D_2^+ [46]. A carrier envelope phase (CEP, Section 1.1) stable 5 fs near-infrared (NIR) laser pulse created a coherent superposition of the two lowest electronic states in the cation, of which the upper one is repulsive. The superposition resulted in charge oscillations between the two nuclei. As the internuclear distance increased, the electron was trapped at one or the other nucleus, depending on the CEP. In 2010, isolated attosecond pulses (IAP, Section 1.1) and 6 fs short NIR laser pulses were used by Sansone et al. to control electron localization in dissociative photo-ionization of molecular hydrogen and molecular deuterium [47]. After ionization by the attosecond pulse, the remaining electron was localized on one of the nuclei. The localization was achieved by a NIR field-induced coupling of the two lowest electronic states in the cation when the IAP pulse preceded the NIR pulse. At pulse overlap, localization was achieved by two interfering ionization pathways. While the auto-ionizing Q_1 state was populated by an XUV photon from the IAP, the repulsive σ_u state was populated by an XUV and an additional NIR photon. After the decay of

[7] The term *dicationic immonium ion* denotes the doubly charged parent amino acid molecule that experienced a loss of the carboxyl group COOH. Immonium ions are generally denoted as $^+NH_2{=}CH{-}R$, where R is a rest compound.

the Q_1 state to the bound σ_g state, both pathways interfere upon dissociation as the asymptotic energies of the σ_u and the σ_g states are fairly close. In both cases, the pulse delay between the IAP and the NIR pulse controlled the side[8] of localization within the molecule. In another pump-probe experiment, reported in 2011 by Kelkensberg et al., the branching ratios between electronic states upon dissociative photo-ionization could be controlled using attosecond pulse trains[9] (APTs, Section 1.1) and an accompanying 30 fs NIR laser pulse [49, 50]. The APT ionized molecular hydrogen preferentially to the two lowest lying electronic states of the cation, while the field of the NIR laser induced transitions within and between the corresponding ionization continua. This resulted in interfering two-photon dissociation pathways.

Attosecond time resolved experiments on complex (bio-) molecules are sparse [51]. Nevertheless, in 2014, Calegari et al. measured charge migration in the amino acid phenylalanine [52], an experiment very similar to that of Belshaw [43] described above, but with higher temporal resolution. A charge migration process was initiated in the cation by an ionizing attosecond XUV pulse and probed by further ionizing the parent cation with a 4 fs short NIR pulse. The authors found an oscillation in the yield of the doubly charged immonium fragment with respect to the pump-probe delay and concluded that the charge oscillates from one site of the parent cation to the opposite with a period of 4.3 fs prior to fragmentation. Attosecond dynamics in multi-electron systems were also investigated by analyzing high-order harmonic spectra (see Section 1.1), a technique called *High Harmonic Spectroscopy* (HHS). First experiments were conducted with smaller molecules, e.g., N_2, Br_2 and CO_2 [53–56]. In 2015, Kraus et al. impulsively aligned iodoacytelene and measured high-order harmonic spectra from the aligned cation. The authors used the measured amplitudes and phases of the spectra and reconstructed the charge migration in the cation induced by strong-field ionization [57]. Further attosecond experiments on multi-electron systems and accompanying theoretical studies are desirable to gain a better understanding of the fundamental processes occurring in molecules on the timescale of electronic motion.

It is worth noting that all measurements of attosecond dynamics in molecules were so

[8] with respect to the laser polarization

[9] Attosecond pulse trains are generated by high-order harmonic generation by focusing an infrared laser pulse in a gaseous medium (Section 1.1). The resulting XUV radiation consists of odd harmonics of the driving laser field. In the time domain, the individual bursts of the attosecond pulse train are spaced by half the laser period, which is 1.3 fs for an 800 nm laser field.

far conducted in cations[10]. In 2014, Mignolet et al. showed theoretically that the dipole moment in neutral LiH can be varied by a NIR electric field such that the direction of ionization due to an accompanying attosecond XUV pulse train is tailored [60]. Another theoretical study from Muskatel et al. showed that sudden electronic excitation in neutral N_2 and subsequent purely electronic dynamics in the neutral can affect the dissociation behavior [61]. Nevertheless, tracking electron dynamics in neutral molecules on the attosecond timescale is still a widely unexplored task that requires further development of experimental, as well as, theoretical techniques. Last but not least, experimental techniques remain to be established to study larger systems, such as peptides, which are extensively discussed in theory but sparsely investigated in time-resolved experiments.

In conclusion, the work presented here is motivated by two branches of research: femtochemistry and the investigations of electron dynamics. In femtochemistry, molecular reactions are observed in real time or can be steered by manipulating the nuclear motion [14, 19]. Chemical reactions, e.g., dissociation can also be induced via charge transfer processes resulting from charge migration [42, 62], leading to charge-directed reactivity [29, 30]. Consequently the question arises, whether it is possible to steer chemical reactions through the concerted manipulation of electrons on their natural time scale. Studies of this kind may pave the way towards a new field of research, *attochemistry* [63, 64].

In the framework of this thesis, three major experiments were performed. Pump-probe measurements on small molecules (N_2, CO_2 and C_2H_4) were conducted with attosecond time resolution (Part I) and showed that (a) the electron distribution in neutral molecules could be altered and observed on a sub-femtosecond timescale (Chapter 3) and (b) the coupling of electronic and nuclear degrees of freedom on the attosecond to femtosecond timescale is relevant to molecular dissociation initiated by sudden photo-induced ionization (Chapter 4). To survey the possibilities for ultrafast dynamical studies and their exploitation in site-specific fragmentation of larger molecules, a high-resolution mass spectrometer was coupled to a femtosecond laser system and the feasibility of ultrashort laser pulse-induced dissociation for peptide sequencing was investigated (Chapter 6). These experiments pave the way towards charge migration, charge transfer and optimal control studies in biologically relevant molecules.

[10]For atoms, ultrafast electron dynamics were also studied in the neutral [58, 59]

Part I

Attosecond molecular experiments

Chapter 1

Fundamentals of attosecond XUV science

To witness chemical reactions, intra-molecular rearrangements and charge redistribution (Figure 1.1) in real time is a long-standing scientific goal as motivated in the preceding introduction. Fast electronic and nuclear dynamics can only be investigated with tools delivering extraordinary time resolution, i.e., pump-probe techniques with ultrashort laser pulses [65, 66]. Here, it is worthwhile to consider the fastest relevant timescale, namely that of electronic motion in atoms and molecules.

Bohr's model describes the classical period of an electron in its revolution around the nucleus [67–69]. Bohr assumed electrons in atoms to be trapped in quantized orbits. Therefore they have a quantized angular momentum $L = n\hbar$, where $\hbar$ is Planck's constant divided by 2π and n is the principal quantum number. Classically, the electron's angular momentum is defined as $L = m_e v r$ with m_e being the electron's mass, v its velocity and r the radius of the electron orbit. Combining the two equations for the angular momentum reveals an expression for the electron velocity

$$v = \frac{n\hbar}{m_e r} = \frac{s}{T}, \tag{1.1}$$

where $s = 2\pi r$ is the circumference of the electron's orbit and T denotes the orbital period. Setting $r = a_{\mathrm{Bohr}} = 0.5\,\text{Å}$ (Bohr radius) and $n = 1$ for the first orbit yields $T = 136\,\mathrm{as}$

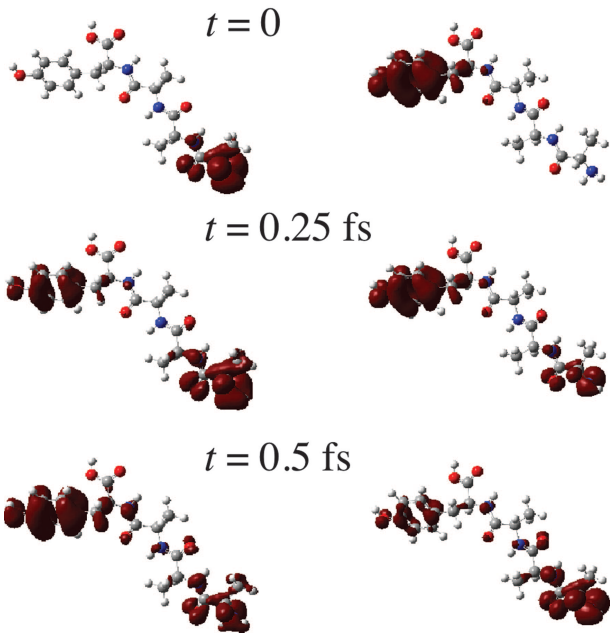

Figure 1.1: Calculated ultrafast hole migration dynamics after sudden ionization of the peptide YAAA (Y - tyrosine, A - alanine). The spheres denote: gray - carbon, white - hydrogen, red - oxygen, blue - nitrogen. The dark red contributions depict the hole density for the highest occupied molecular orbital (HOMO, left) and the second highest (HOMO-1, right). The charge migration process from one side of the tetrapeptide to the opposite was calculated to take place within 500 as. This figure is reproduced from [62].

(1 as = $1{\cdot}10^{-18}$ s). Quantum mechanical measurements do not allow for the direct observation of this ground state orbital motion, but do allow to observe charge oscillations that result from the coherent superposition of electronic states. An example is the charge oscillation in the molecular hydrogen cation H_2^+, resulting from a coherent superposition of its two lowest-lying electronic states. The energetic difference of these states is roughly 10 eV, which corresponds to a beat period of about 415 as. In order to witness this motion, i.e., to investigate photo-induced molecular dynamics on electronic timescales [62, 70], laser pulses with pulse durations on the order of a few hundred attoseconds have to be utilized.

A common way to create such pulses is to exploit the mechanism of high-order harmonic generation (HHG) [71], which is studied in detail since the late eighties of the last century. In 1987, Rhodes and McPherson et al. reported the first high-order harmonic spectrum from rare gases [72, 73]. Laser pulses of 350 fs duration, a central wavelength of 248 nm and a pulse energy of 20 mJ focused into a neon gas target produced harmonics up to the 17^{th} harmonic (HH17, 14.6 nm). Nowadays, a common approach for HHG is to use an infrared (IR), near-infrared (NIR) or mid-infrared (MIR) laser with high average power, focused into a gaseous medium in a gas cell or a hollow core fiber. This typically leads to the generation of radiation in the extreme ultraviolet (XUV), soft x-ray, or even in the x-ray region of the electromagnetic spectrum [64, 74]. In order to further enhance the XUV

photon flux [75] and to further tailor the XUV spectra, different colors can be combined to one synthetic driving field [76]. In any case, the broad spectra of the generated XUV pulses support very short pulses in the attosecond regime.

In the experiments at hand, a near-infrared (NIR) laser with a central wavelength of $\lambda_{\mathrm{NIR}} = 800\,\mathrm{nm}$ (photon energy $E_{\mathrm{NIR}} = 1.55\,\mathrm{eV}$) is focused to reach intensities of about $10^{14}\,\mathrm{W/cm^2}$ and leads to harmonics with photon energies of up to $E_{\mathrm{HH}} \approx 54\,\mathrm{eV}$, which corresponds to the 35^{th} harmonic. XUV photons allow to investigate weaker bound valence and stronger bound inner shell electrons, as well as hole migration processes within molecules [42] upon single-photon excitation. Ensuring single-photon events in the experiment significantly reduces the complexity of the analysis compared to experiments where multi-photon processes occur.

In the following chapter, the process of high-order harmonic generation, as well as the generation of attosecond pulse trains and isolated attosecond pulses, will be explained in detail. The chapter is completed by a short introduction to some techniques to measure and characterize attosecond radiation.

1.1 High-order harmonic generation

The interaction of atoms and molecules with an intense focused laser field results in numerous phenomena. Moderately strong fields lead to multi-photon ionization (MPI) and, if more photons are absorbed than necessary to ionize the system, above-threshold ionization (ATI) occurs (Figure 1.2 (a)). Even stronger fields lead to a significant deformation of the electronic potential energy surfaces and tunnel ionization becomes likely (Figure 1.2 (b)), accompanied by ATI. In this case, the ATI structure would be formed by the interference of electron wavepackets generated at different instants within the laser field. If the laser field is strong enough, the potential can be disturbed such that the ionization barrier is energetically even below the highest occupied state and the electron can be considered unbound (Figure 1.2 (c)).

The transition between the MPI and tunneling regimes was first described by Keldysh

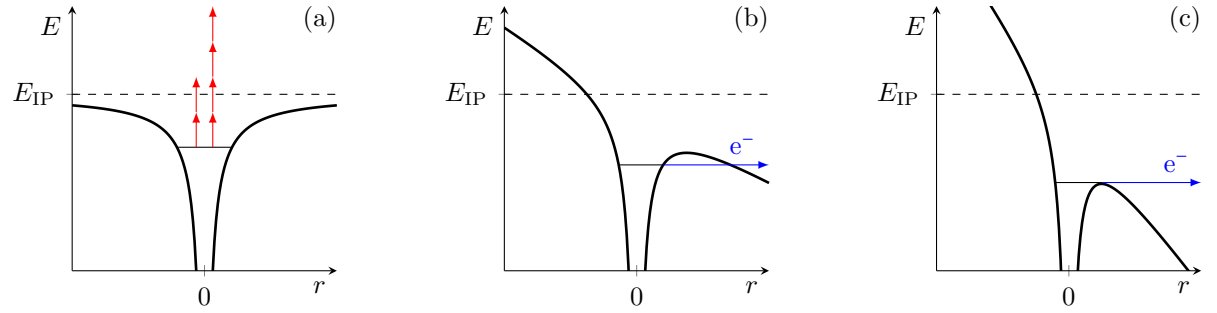

Figure 1.2: Snapshot of the Coulomb potential near the atomic core (nuclear position at $r = 0$) at the moment of ionization by a strong laser field. The laser intensity increases from left to right. (a) Multi-photon ionization (MPI), $\gamma > 1$. The atom absorbs a number of laser photons, where the sum of the photon energies is sufficient to ionize the system. Above-threshold ionization (ATI) occurs when more photons are absorbed than necessary for the electron to escape the Coulomb potential. (b) Tunnel ionization, $\gamma < 1$. The potential barrier is slightly suppressed by the laser electric field and the electron can tunnel out of the bound potential possibly resulting in ATI. (c) Barrier-suppression, $\gamma \ll 1$. The barrier is strongly suppressed by the laser field, such that the electron can be considered unbound leaving the vicinity of the Coulomb field.

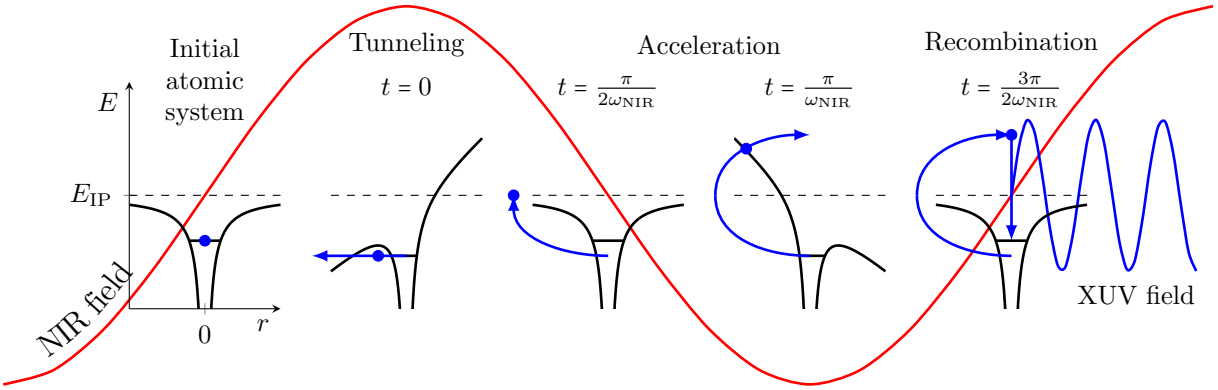

Figure 1.3: Visualization of the classical three-step model of high-order harmonic generation. Step 1 (Tunneling): The initial Coulomb potential (black solid line) of an atom is disturbed by a strong laser field (red solid line) and an electron (blue dot) can tunnel through the potential well. Step 2 (Acceleration): The electron is accelerated by the laser electric field. Step 3 (Recombination): If the electron returns back to the ion, it can recombine by emitting XUV radiation (blue sinusoidal curve). The photon energy corresponds to the energy the electron accumulated during the acceleration process and E_{IP}.

[77]. The Keldysh parameter

$$\gamma = \sqrt{\frac{E_{\mathrm{IP}}}{2U_{\mathrm{p}}}} \tag{1.2}$$

was introduced to indicate which ionization mechanism dominates. The Keldysh parameter depends on the ionization potential E_{IP} and the ponderomotive potential U_{p}. The latter is defined as the time average of a free electron's kinetic energy due to its quiver motion under the influence of the laser field. It is given by

$$U_{\mathrm{p}} = \frac{e^2 I_{\mathrm{NIR}}}{2m_{\mathrm{e}}\epsilon_0 c\omega_{\mathrm{NIR}}^2}, \tag{1.3}$$

were e is the elementary charge, m_{e} the electron mass, ϵ_0 the vacuum permittivity, c the speed of light and I_{NIR} and ω_{NIR} the intensity and central angular frequency of the driving laser.

Combining Equations (1.2) and (1.3) leads to an interpretation of the Keldysh parameter as a tunneling time in units of $1/\omega_{\mathrm{NIR}}$. In this sense, γ evaluates whether the electron can tunnel out of the potential before the laser field reverses sign.

In moderately strong laser fields and in the limit of high frequencies, $\gamma > 1$, the system under investigation can be described in the perturbative multi-photon picture. In the low-frequency limit and for strong laser fields, $\gamma < 1$, the ionization process is non-perturbative and therefore the tunnel regime dominates. This regime is normally exploited in high-order harmonic generation. A semiclassical explanation of HHG has been introduced by Corkum in 1993 [78], while a quantum mechanical approach was presented by Lewenstein et al. one year later [79].

The classical model of high-order harmonic generation describes the process in three steps (see Figure 1.3). In the first step, the potential of an atomic or molecular system is disturbed by the strong electric field of a focused laser, leading to tunnel ionization ($\gamma < 1$). In the second step the freed electrons are accelerated by the laser electric field away from the remaining ion. When the electric field reverses sign, the electrons are accelerated back towards the ion to recombine, resulting in the emission of XUV photons in the third step.

1.1.1 The spectrum

High-order harmonic spectra contain a strong low energy contribution, a plateau and a cutoff region (Figure 1.4). The cutoff energy E_{cutoff} depends on the ionization energy E_{IP} of the generation gas and the ponderomotive potential U_{p} created by the laser field. It can be approximated by [78]

$$E_{\text{cutoff}} = E_{\text{IP}} + 3.17U_{\text{p}}. \tag{1.4}$$

From equation 1.3 it can be seen that

$$U_{\text{p}} \approx \lambda_{\text{NIR}}^2 I_{\text{NIR}} \tag{1.5}$$

and the cutoff of the HHG spectrum can be experimentally varied by tailoring the laser intensity I_{NIR} or the driving laser wavelength λ_{NIR}.

The symmetry of the generation process results in a spectrum that consists of odd harmonics as depicted in Figure 1.4. The ion and the electron can be regarded as a driven Hertz' dipole. If the driving field $\boldsymbol{E} = \boldsymbol{E_0} \cos \omega_{\text{NIR}} t$ becomes very strong, the dipole oscillation reacts anharmonically and the optical Kerr effect [80] has to be taken into account, i.e., the induced polarization can be written as

$$\boldsymbol{p} = \epsilon_0 \left(\chi_1 \boldsymbol{E} + \chi_2 \boldsymbol{EE} + \chi_3 \boldsymbol{EEE} + ... \right), \tag{1.6}$$

where χ_j is the jth order susceptibility [81]. It follows that a strong optical field can cause the induced dipoles of the atoms or molecules in a medium to oscillate at higher harmonic

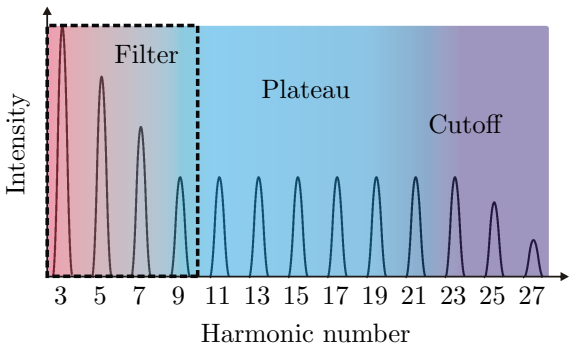

Figure 1.4: Diagram of a high-order harmonic spectrum. The spectrum contains only odd multiples of the driving laser frequency. It consists of three different parts: a rapidly decreasing perturbative regime (low energy harmonics), a non-perturbative plateau region and a cutoff region (harmonics exhibiting the highest energy).

frequencies, leading to a new optical wave with frequencies of $q\omega_{\mathrm{NIR}}$, where q denotes the harmonic order. For even harmonics (q is even) the emitted waves of frequency $q\omega_{\mathrm{NIR}}$ interfere destructively, while odd harmonics interfere constructively. Strictly speaking, the Taylor expansion used in Equation (1.6) only holds true in the perturbative regime, while high-order harmonic generation is a non-perturbative process.

Parity conservation in gaseous media gives another argument for the odd-harmonic structure [82–84]. In high-order harmonic generation, the initial and final states of the atomic or molecular system under consideration are equal and therefore no parity change is encountered. On the other hand, the parity change associated with the absorption of n photons and consecutive emission of a single harmonic photon is -1^{n+1}. Therefore, n can only be an odd integer in order to conserve the parity of the system and the harmonic energy must be an odd multiple of the initial photon energy.

By breaking the driving laser field symmetry, e.g., by superimposing the NIR field with its second harmonic, the production of even harmonics is possible, as well [85]. In this case, the electric field of the two half-cycles in the fundamental are no longer symmetric with respect to each other. As a result, odd and even harmonics show constructive interference.

1.1.2 Harmonic phase-locking

The temporal structure of high-order harmonic emission was theoretically investigated, e.g., by Antoine et al. [86] and a very important joint experimental and theoretical study was later conducted by Mairesse et al. [87]. They found that harmonic radiation is produced by two distinct electron trajectories. Based on the time the electrons spend in the continuum after ionization, these trajectories are called *long* or *short*. The contributions exhibit opposite chirp[1] with respect to each other. In addition, electron trajectories with return times in between the long and short trajectories produce XUV photons with the highest energies (cutoff harmonics).

The three types of electron trajectories in the HHG process (long trajectories, short trajectories, cutoff trajectories) are depicted in Figure 1.5. Electrons from the long trajectories are emitted earlier during the laser cycle and recombine later than the electrons

[1]The term *chirp* refers to the temporal variation of the instantaneous frequency of the signal.

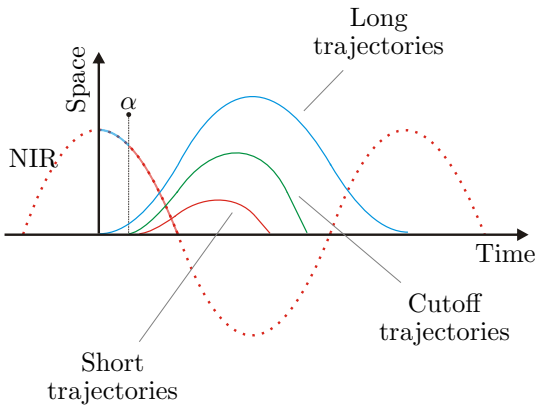

Figure 1.5: Illustration of the long and short trajectories during the high-order harmonic generation process. The NIR field (dotted red line) drives electrons on long (blue) and short (red) trajectories. The electrons on the long trajectories are born earlier in the NIR cycle and return later to the ion than the electrons on the short trajectories. Electrons on the steepest ($\max\left\{\frac{\partial x}{\partial t}\right\}$) trajectories (green, born at $\alpha = 17\,°$) generate the cutoff harmonics. As can be seen, the chirps of the harmonics from the two different trajectories have opposite sign.

from the short trajectories. As a consequence, the maximum distance of the involved electrons from the parent ion is larger for the long trajectories than it is for the short trajectories. Taking into account that the velocity of the electrons returning to the ion is proportional to the slope of the trajectories at the zero crossing, it is obvious that the recombination of electrons from the green trajectories (emitted at $\alpha = 17\,°$ after the cycle maximum) result in the highest energy XUV photons.

It was shown in [87] that the high-order harmonics exhibit a particular phase relation. The calculations predicted that the return times of the electrons vary nearly linear with the harmonic order, i.e., the spectral phase of the harmonics is quadratic. A deviation from this behavior was found for the cutoff trajectories, where the return times are almost constant. Consequently, the cutoff harmonics exhibit a linear spectral phase.

The calculations also predicted that the XUV radiation is emitted within a time window that corresponds to about a quarter of the driving laser field cycle if the long trajectories can be rejected. Together with the fact that the three-step sequence of high-order harmonic generation is repeated every half cycle of the driving field, the temporal structure of the high-order harmonic spectrum (its Fourier transform) forms a train of ultrashort sub-femtosecond light bursts.

1.1.3 Phase matching

The conversion efficiency of high-order harmonic generation is on the order of 10^{-6}. Constant et al. reported the conversion of $6 \cdot 10^{15}$ NIR photons (1.5 mJ, 800 nm) into $8 \cdot 10^{9}$ photons of the 15^{th} harmonic [88]. In the present experiments, $\geq 10^{7}$ harmonic photons per laser pulse can be obtained [89]. The probability for the gas under investigation to absorb these harmonic photons (photo-absorption probability[2]) is estimated to be on the order of 10^{-4}. I.e., 10^{3} absorption events per laser shot during the experiments can be achieved if the high-order harmonic generation process is optimized.

To maximize the conversion efficiency, the interaction region of the driving laser with the generation gas needs to be maximized without loosing phase matching conditions, described in the following paragraphs. For this purpose, a ≈ 1 mm thick cylindrical gas cell with a maximum pressure of several tens of mbar is employed in the present experiments.

The harmonic radiation only interferes constructively over the whole laser-gas interaction region if the fundamental and the harmonics stay in phase (Figure 1.6). The underlying phase-matching depends on a variety of parameters [90–93]. These parameters have to be balanced such that the phase mismatch Δk between the qth harmonic and the driving laser (NIR) vanishes, i.e.,

$$\Delta k_q = k_q - q k_{\text{NIR}} = 0 \tag{1.7}$$

holds true. Possible phase mismatches of the harmonics and the fundamental originate from macroscopic, microscopic and geometrical phase effects

$$\Delta k_q = k_q - q k_{\text{NIR}} = \Delta k_{q,\text{geo}} + \Delta k_{q,\text{mac}} + \Delta k_{q,\text{mic}} \tag{1.8}$$

and the individual terms will be discussed in the following paragraphs.

The phase mismatch depend on the intensity variation of the driving laser across the focus. Assuming a Gaussian laser pulse propagating along z with a Rayleigh length $b = {\rho^2\pi}/{\lambda_{\text{NIR}}}$, where the focal beam waist is typically on the order of $\rho = 50\,\mu$m, the intensity variation

[2]The particle density in the experiments is estimated to be $10^{14}\,\text{cm}^{-3}$. The laser-molecule interaction region is about 2 mm in length. The photo-absorption cross section is typically on the order of $10^{-17}\,\text{cm}^2$.

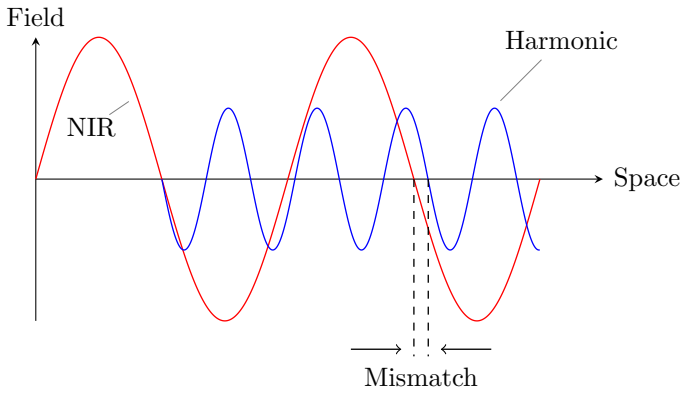

Figure 1.6: Illustration of phase mismatch. The field of the driving laser is shown as a red line while the qth harmonic is drawn in blue. A small phase mismatch of the NIR field and the emitted harmonic is depicted. Harmonics can only add up coherently if the driving field stays in phase with the harmonic fields over the whole laser-gas interaction region.

on axis reads [94]

$$I_{\mathrm{NIR}}(z) = I_{\mathrm{max}} \cdot \frac{1}{1 + \left(\frac{z}{b}\right)^2}, \tag{1.9}$$

where I_{max} is the laser peak intensity in the focus at $z = 0$.

The geometrical phase mismatch arises from the Gouy phase $\phi_{\mathrm{G}} = \arctan z/b$ [95], which defines the phase accumulated by a focused laser beam in addition to the phase accumulated by a plane wave of the same frequency [96]. This additional phase results in an irregular spacing of the wavefront close to the focus [97] and shifts the electrical field with respect to its envelope by π upon propagation through the focal spot. Ruffin et al. and Lindner et al. observed this behavior experimentally using laser pulses with only a few field cycles [98, 99]. The Gouy phase of the focused NIR field in high-order harmonic generation varies much more rapidly along z as compared to the Gouy phase of the harmonic radiation because the Rayleigh length of the harmonics is much larger than that of the fundamental[3] [100]. Thus, the geometrical phase mismatch depends predominantly on the Gouy phase shift acquired by the NIR radiation:

$$\Delta k_{q,\mathrm{geo}} = -q\partial_z \phi_{\mathrm{G}}. \tag{1.10}$$

The macroscopic phase mismatch $\Delta k_{q,\mathrm{mac}} = \Delta k_{q,\mathrm{n}} + \Delta k_{q,\mathrm{pl}}$ originates from neutral gas dispersion ($\Delta k_{q,\mathrm{n}}$) and plasma dispersion ($\Delta k_{q,\mathrm{pl}}$) [101]. Both depend on the pressure in

[3] The ratio of divergence of the harmonic and the fundamental beam is typically about $1:5$.

the generation region and on the fraction of ionized molecules and therefore also on the intensity of the fundamental field. In the multi-photon picture[4], the rate of ionization, $W \propto I_{\mathrm{NIR}}^{l}$, scales with the lth power of the laser intensity if the order of the process is l [102]. Ionization of, e.g., argon with an ionization potential of $E_{\mathrm{IP}} = 15.8\,\mathrm{eV}$ by an 800 nm laser is an 11^{th} order process. In this case, the fraction of ionized atoms is given by $\eta(z) = 1 - \exp\left(-I_{\mathrm{NIR}}^{l}(z)/I_{\mathrm{sat}}^{l}\right)$ for the on-axis contribution, where I_{sat} is the saturation intensity [103]. This parameter depends on E_{IP} and is estimated to be about $I_{\mathrm{sat}} = 5 \cdot 10^{14}\,\mathrm{W/cm^2}$ for argon [104]. Thus, the phase mismatch due to neutral gas dispersion can be calculated by [101]

$$\Delta k_{q,\mathrm{n}} = q\frac{2\pi}{\lambda_{\mathrm{NIR}}} P_{\mathrm{n}} \delta_{\mathrm{n}} \left(1 - \eta\right), \tag{1.11}$$

where P_{n} is the pressure in the generation cell normalized to ambient pressure (i.e., fractional pressure). The difference δ_{n} of the index of refraction n between the harmonics and the fundamental is $\delta n = -4 \cdot 10^{-4}$ at ambient pressure (considering Argon and the 21^{st} harmonic) and scales with P_{n} [105]. The second term of the macroscopic phase mismatch due to plasma dispersion is [101]

$$\Delta k_{q,\mathrm{pl}} = \frac{q^2 - 1}{q} \eta P_{\mathrm{n}} r_{\mathrm{e}} \lambda_{\mathrm{NIR}} N_{\mathrm{atom}}, \tag{1.12}$$

where $r_{\mathrm{e}} = e^2/4\pi\epsilon_0 m_{\mathrm{e}} c^2$ is the classical electron radius and N_{atom} denotes the atomic number density at ambient pressure. I.e., the phase mismatches due to both, the neutral gas dispersion and the plasma dispersion, scale linear with the pressure in the HHG cell.

The third effect, the microscopic phase mismatch, originates from the intrinsic phase the electron accumulates during the time it spends under the influence of the laser field. The accumulated phase mismatch reads [106]

$$\Delta k_{q,\mathrm{mic}} = -\tau_q \partial_z U_{\mathrm{p}}(z) = -\tau_q \cdot \frac{e^2 I_{\mathrm{max}} \lambda_{\mathrm{NIR}}^2}{8\pi^2 m_{\mathrm{e}} \epsilon_0 c^3} \cdot \partial_z \left[\frac{1}{1 + \left(\frac{z}{b}\right)^2}\right], \tag{1.13}$$

neglecting a potential intensity dependence of the return time of the electron, τ_q. The

[4]Under normal HHG conditions the process takes place in the transition region to tunnel ionization. Nevertheless, the MPI picture is chosen here for simplicity and to show the principles.

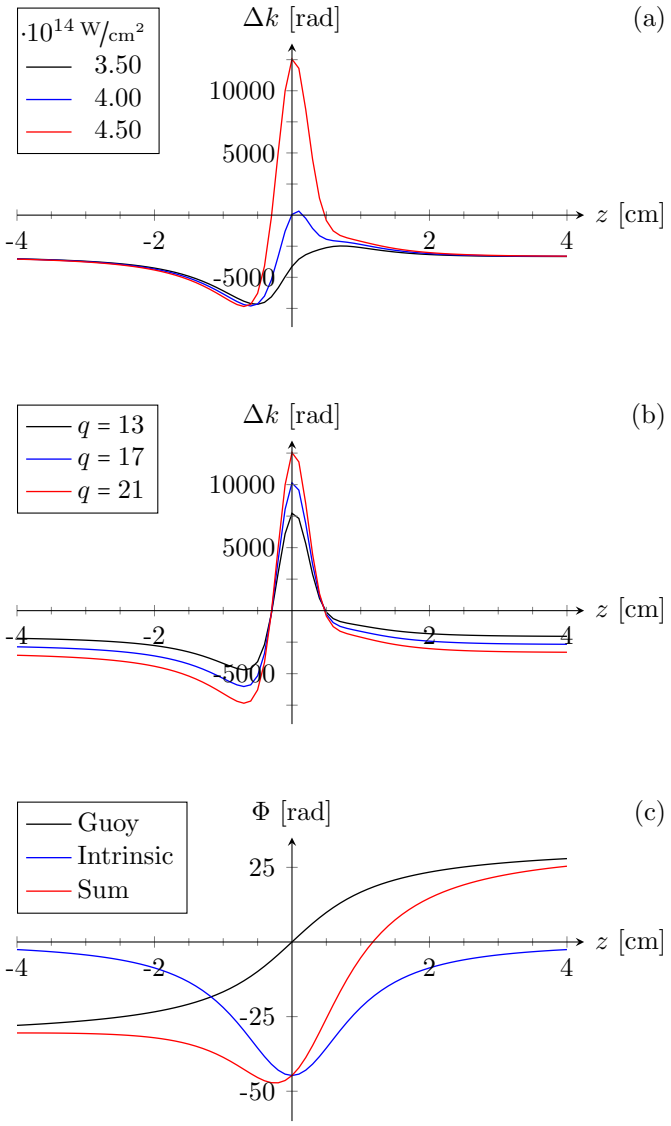

Figure 1.7: Phase mismatch Δk due to the Gouy phase, the intrinsic phase, the plasma dispersion, and the neutral gas dispersion across the focus ($z = 0$) of the driving field. Δk is calculated by Equation (1.8) for (a) different intensities ($q = 21$) and for (b) different harmonics ($I_{\max} = 4.5 \cdot 10^{14}\,\mathrm{W/cm^2}$). The two zero crossings in (a) and (b) are attributed to phase matching of the short (positive z, behind the focus) and long (negative z, in front of the focus) trajectories (see Figure 1.5). (c) Gouy phase, intrinsic phase, and their sum ($q = 21$, $I_{\max} = 4.5 \cdot 10^{14}\,\mathrm{W/cm^2}$). The plots illustrate: (1) By varying the laser field intensity, the phase matching position can be shifted. (2) Phase matching occurs for all harmonics at the same position. (3) Without plasma dispersion and without neutral gas dispersion, the phase matching position would be further away from the laser field focus.

return time might be approximated as a linear function of q in the plateau region [87]. Thus, $\tau_q = aq + b$ where the parameters a and b are chosen such that the behavior obtained in [87] is reproduced. I.e., the time between the emission of consecutive harmonics (consecutive return times) in argon at laser intensities above $1.5 \cdot 10^{14}\,\mathrm{W/cm^2}$ is about 90 as and this train of bursts is centered at about 1.5 fs with respect to the ionization time in an 800 nm laser field.

Figure 1.7(a) and (b) shows the total phase mismatch across the focus (Equation 1.8) for different peak intensities $I_{\max}$ and different harmonic orders q, respectively. For typical

experimental conditions and the aforementioned approximations, two points of phase matching can be found on the optical axis: one in front of the focus and the other one behind the focus.

In the experiment at hand, the cell is located about 10 mm behind the focus to achieve the best harmonic output on axis. Already in 1996, Salieres et al. found that by accurately adjusting the cell position with respect to the laser focus, it is possible to find two positions where the harmonic conversion efficiency is maximized [107]. By neglecting the macroscopic effects, Balcou et al. explained this observation by a balancing of the intrinsic and the Gouy phase [106]. In this case, the maximum in front of the focus is only present off-axis (long electron trajectories) while the maximum behind the focus is located on-axis (short electron trajectories) [86]. The microscopic phase mismatch can compensate for the mismatch evolving from the Gouy phase due to its intensity dependence across the focus, which is depicted in Figure 1.7(c), where only the Gouy and the intrinsic phase and their sum is plotted. It can be seen that when neglecting the macroscopic effects, the phase matching position would be further away from the laser focus.

Although not treated here, a side remark might be given about the phase matching along the laser pulse envelope: Due to the laser pulse intensity slope and the intensity dependence of the macroscopic and microscopic phase mismatch, phase matching along the pulse envelope is non-trivial. Experimentally the intra-pulse phase matching can be achieved among other things by varying the chirp of the driving field [108], [109] and [110].

1.2 Attosecond pulse trains

High-order harmonic generation is fundamental to the generation of attosecond pulses. Five years after the first high-order harmonics generated in gaseous media were reported [73], Farkas et al. suggested HHG as a possible source of attosecond pulses provided that the high-order harmonics are phase-locked [111]. In 2001, Paul et al. published the first measurement demonstrating the experimental production of an attosecond pulse train [112].

An example of an attosecond pulse structure together with the generating laser electric field is depicted in Figure 1.8. Due to the HHG generation process, the individual XUV

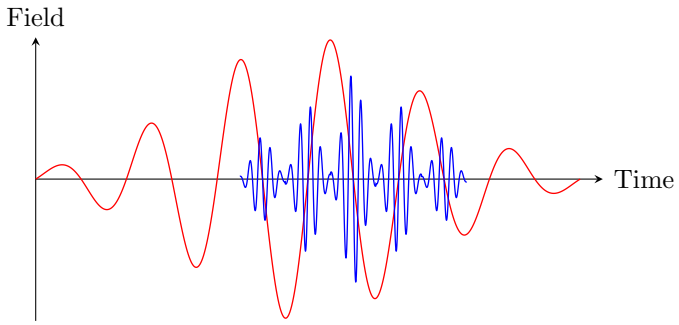

Figure 1.8: Cartoon of an attosecond pulse train (blue) and a NIR electric field (red) in the time domain. In high-order harmonic generation, a femtosecond NIR driving laser pulse generates an attosecond pulse train (XUV), such that the individual XUV bursts are synchronized to the zero-crossings of the NIR electric field.

bursts are synchronized to the zero-crossings of the NIR electric field and the bursts within the APT can be as long as half an optical cycle of the driving field. In order to further shorten the bursts, experimental measures have to be taken, which will be described in the following paragraph.

1.2.1 Burst compression

As shown above, attosecond pulse trains can be generated by means of high-order harmonic generation. The APT in the time domain consists of a number of bursts separated by the half-cycle period of the driving laser, i.e., 1.33 fs for a NIR laser field with a central wavelength of 800 nm. The spectrum of the APT is composed of a series of odd harmonics (see Figure 1.9 (a)). Harmonics are generated from long and short electron trajectories with opposite chirp, as depicted in Figure 1.5. The so-called *atto-chirp* stems from the intrinsic phase accumulated during high-order harmonic generation and is the reason for relatively long burst durations on the order of 1 fs of the harmonic beam. In addition, the XUV beam is divergent due to the spatial distribution of photons generated by electrons from the long trajectories[5].

To obtain high-quality attosecond pulse trains with spectrally sharp harmonics and the shortest possible XUV bursts, the APT must be further optimized. After the generation process, the APT propagates through a thin aluminum foil, which filters the fundamental

[5]The XUV beam generated by the short trajectories is also divergent due to the divergence of the generating NIR beam but less divergent than the XUV beam generated by the electrons from the long trajectories.

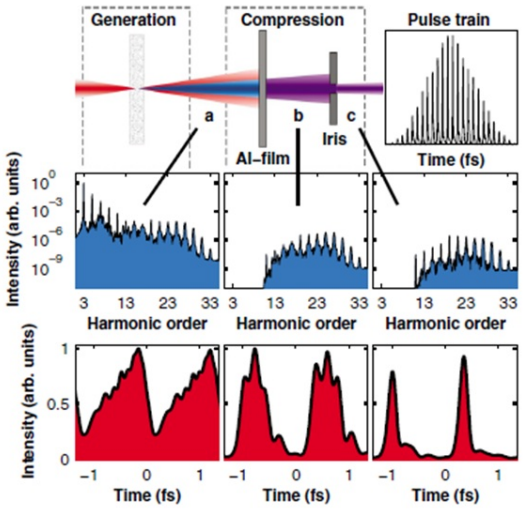

Figure 1.9: Scheme of temporal burst compression. Higher-order harmonics are generated by focusing a strong NIR pulse into a rare gas. An aluminum foil cuts off the lower harmonics from the spectrum. It also compresses the XUV pulses because the dispersion of the XUV light is such that it partially compensates the intrinsic atto-chirp. An iris discriminates the XUV light produced from the long trajectories. This approach results in temporally compressed attosecond bursts. The image is reproduced from [113].

wavelength and the lower harmonics below the 11^{th} order (see Figure 1.9 (b)). In addition, the aluminum filter also compensates the intrinsic atto-chirp [114], because the dispersion for XUV light in aluminum is such that the higher energy photons are stronger delayed than the lower energy photons. This means that the aluminum foil acts as a compressor for the harmonics generated by the short trajectories. Harmonics resulting from the long trajectories are suppressed by an aperture behind the aluminum filter exploiting the fact that they have a larger divergence. By the aforementioned procedure, the bursts are compressed from approximately 1 fs to approximately 300 as. The duration of the overall attosecond pulse train is about half of the *full width at half maximum* (FWHM) of the femtosecond driving laser pulse (in the present case about 15 fs).

1.3 Isolated attosecond pulses

A future prospect in attosecond science is to carry out pump-probe experiments with isolated attosecond pulses (IAPs) to investigate pure electron dynamics in atoms and molecules. The first IAP with a pulse duration of about 650 as was generated by Hentschel et al. in 2001 [115]. Not only does the temporal structure differ from the previously discussed attosecond pulse trains, but also the spectrum. The temporal and spectral structure of the light pulses are connected via a Fourier transformation. While a train of pulses in the time domain transforms into a series of peaks in the spectral domain

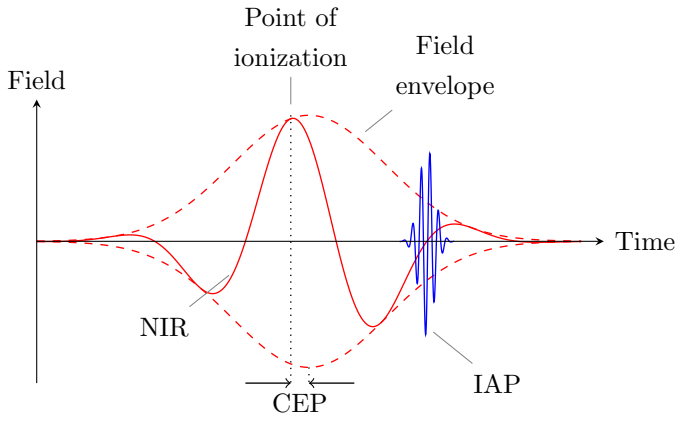

Figure 1.10: Generation of an IAP from a few-cycle NIR pulse. The intensity to ionize atoms is only large enough once within the pulse resulting in the generation of a single XUV burst. To ensure the single ionization event the CEP has to be optimized and stabilized.

(Section 1.1.1), the Fourier transformation of a single attosecond burst yields a continuous spectrum[6].

Isolated attosecond pulses can be obtained by filtering the spectrum of an APT. Using only the highest frequencies (cutoff region with linear spectral phase) from the generated harmonic spectrum guarantees that the XUV light stems merely from the highest intensities of the NIR driving laser and is therefore limited in pulse duration. In this sense it is favorable to use very short few-cycle driving pulses. As a consequence, ionization and recombination in the HHG process might only occur only once within the NIR laser pulse (Figure 1.10).

In order to obtain few-cycle NIR pulses, the output from amplified Ti:Sa lasers are spectrally broadened by self-phase modulation in hollow-core fibers, filled with an inert gas at several hundreds of mbar [116]. An alternative approach is to use filamentation to broaden the spectrum significantly [117]. A comparison of both methods is presented by Gallmann et al. [118]. Both methods generate supercontinuum spectra, which support optical or NIR pulses shorter than 5 fs. Compression of the broadened pulses is achieved by chirped mirrors [119, 120]. The resulting pulses contain only a few optical cycles. Thus, the *carrier envelope phase* (CEP) becomes relevant. The CEP is defined as the phase offset of the electric field oscillations with respect to the pulse envelope, which is depicted in Figure 1.10. To reproducibly generate IAPs from few-cycle pulses, the CEP must be both stabilized and controlled [66].

[6]These broad and continuous spectra, makes these pulses especially well suited for attosecond transient absorption experiments.

The highest energy photons are produced by the most intense part of the driving field. Thus, using a few-cycle pulse with a suitable CE phase, the cutoff part of the harmonic spectrum should be emitted only once per NIR pulse and should deliver a continuous spectrum. A single attosecond pulse can then be obtained by spectrally filtering the XUV light such that only the cutoff photons are contained in the XUV burst. Baltuska et al. used this approach and showed that the XUV spectrum can be changed from a spectrum of distinct harmonics to a continuum spectrum by varying the CEP [121]. By spectrally filtering the XUV spectrum and using only 1.5 cycle 720 nm pulses, Goulielmakis et al. generated 80 as pulses in 2008 [122].

If the duration of a CEP stabilized pulse exceeds the number of field cycles sufficient to produce IAPs, several gating techniques can be utilized to ensure a single XUV burst per NIR pulse [123]. In the process of high-order harmonic generation ionization and recollision plays an important role (Chapter 1.1). Therefore, the employed gating techniques manipulate either the ionization process [124] or the recollision process [125].

Ionization gating exploits the phase-matching conditions during high-order harmonic generation [126]. The generation medium is completely ionized before the pulse maximum and as a consequence the plasma dispersion cannot be compensated by the neutral gas dispersion in the trailing edge of the pulse. Therefore, efficient high-order harmonic generation only occurs in the leading edge of the driving pulse and the generation of isolated attosecond pulses is possible if the intensity increase in the leading edge is steep enough. The CEP in this case is a parameter to vary the energy maximum of the XUV spectrum.

Polarization gating alters the electron recollision probability in the process of high-order harmonic generation. Using elliptically polarized laser pulses Budil et al. observed a suppression of high-order harmonic generation already in 1993 [127]. Sansone et al. exploited the effect and used the polarization gating technique to generate IAPs of 130 as duration [128]. The driving laser pulse is devided in two collinear propagating circular polarized pulses separated by a few femtoseconds. A time-varying polarization of the combined field is such that the electrons can only recombine to generate XUV radiation at the maximum of the field, where the field polarization is linear. Thus, efficient harmonic generation can only occur in a very short time window around the center of the driving pulse.

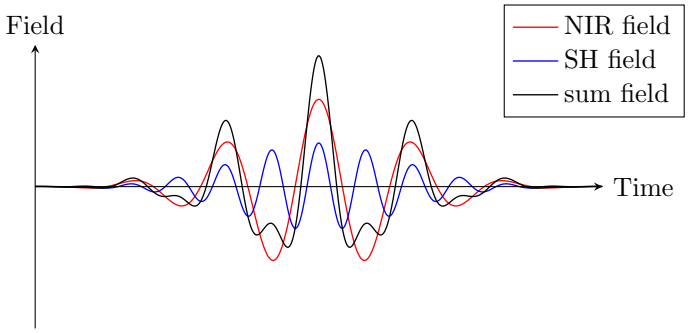

Figure 1.11: Field synthesis in the process of optical gating. A near-infrared field (NIR) is collinearly overlapped with its second harmonic (SH). The synthesized field (sum) shows an enhanced field maximum and suppressed secondary minima. Thus, only one XUV burst can be generated per field cycle in high-order harmonic generation.

Optical gating suppresses harmonic generation except for the highest intensity field cycle of the driving laser pulse by tailoring the light electric field as depicted in Figure 1.11. A superposition of the fundamental field with its second harmonic and control of their relative phase can produce an electric field that is only intense enough to produce sufficient harmonic radiation once within the pulse even if the pulse does not contain only a single optical cycle.

The world record in generating the shortest attosecond pulses was achieved in 2012 by Zhao et al. [129]. The authors used polarization gating together with optical gating, a technique called double optical gating (DOG) [130, 131]. DOG allows to create a very narrow time window for harmonic generation even with slightly longer pulses than needed for polarization gating only. In this scheme, in addition to a time-dependent polarization gate, a weak second harmonic field co-propagates with the harmonic driving laser. Thus, the electric field symmetry of the NIR pulse is broken [85], as depicted in Figure 1.11 for linear polarized fields. Therefore, the delay between the two opposite circularly polarized pulses in the polarization gating scheme is less sensitive, which makes the technique experimentally easier to handle. In addition, the delay can be reduced in the DOG scheme, allowing for slightly higher intensities and therefore higher XUV photon output.

Besides *temporal gating* techniques also *spatial gating* might be feasible to generate isolated attosecond pulses [132]. In 2012, Vincenti and Quéré proposed to exploit the *attosecond lighthouse effect* to accomplish IAP production [133]. The experimental demonstration followed one year later [134]. A wavefront tilt with respect to the pulse front of the high-order harmonic driving field translates to a spatial chirp in the focus resulting in a wavefront rotation in time. As a result, harmonic radiation generated in consecutive optical

cycles will exhibit slightly different axes of propagation. Thus, employing an orifice to discriminate all but one path allows to select an isolated attosecond pulse from high-order harmonic radiation generated by few-cycle pulses in the first place.

In the MBI laboratories it was recently possible to generate IAPs and to carry out IAP pump-NIR probe studies on multi-electron systems [135]. The laser system is the one described in Chapter 2. The 1 kHz output with 3 mJ, 20 fs pulses is utilized. The CEP of the oscillator and the amplifier is stabilized to a standard deviation of 200 mrad over a time period of over an hour. In order to achieve a stable laser operation necessary for the generation of IAPs, several issues of the laser systems are addressed: The Mazzler, compensating the gain narrowing, is shut off as the device prohibits CEP stabilization for an unknown reason. In addition, to minimize thermal instabilities the compressor gratings are actively water cooled and the cooling system for the pump lasers is changed for a water/water thermal exchanger. The output beam of the laser system is then focused to an intensity of about $5 \cdot 10^{14}\,\mathrm{W/cm^2}$ into a 1 m long hollow core fiber with an inner diameter of about 300 μm, filled with neon at a pressure of 2 bar. The beam pointing of the laser is actively stabilized to achieve a stable coupling efficiency. After the fiber, the pulse energy is 1.5 mJ with a self-phase modulated spectrum supporting theoretical pulse durations below 3 fs. The beam is subsequently compressed with a chirped mirror compressor consisting of 10 mirrors supporting a phase compensation of 40 $\mathrm{fs^2}$ each. Experimentally, a pulse duration of 5 fs was demonstrated. Applying polarization gating, high-order harmonics are generated in argon and spectrally filtered with aluminum foil. With pulse durations between 6 fs and 7 fs, IAPs of about 200 as can be generated.

1.4 Characterization of attosecond XUV light pulses

In the present work, femtosecond NIR pulses and XUV attosecond pulse trains were employed to investigate electron and nuclear dynamics in molecules. In order to present reasonable interpretations of the molecular pump-probe experiments, the utilized pulses must be characterized. Unfortunately, it is not possible to transfer the pulse duration measurements available for UV or NIR frequencies into the XUV range due to a lack of suitable optics. Mirrors for the XUV spectral region exhibit only small reflectivity and

non-linear crystals are not available, because XUV light is easily absorbed by matter.

In this section, different approaches to measure the pulse duration of short XUV pulses will be presented. In the first part, a two-color femtosecond NIR-APT XUV scheme is explained, which can be used to reconstruct the temporal structure of the bursts within the APT. The second part gives a brief introduction to the characterization of isolated attosecond pulses.

1.4.1 Reconstruction of attosecond beating by interference of two-photon transitions (RABITT)

Attosecond pulse trains (APTs) can be generated by means of high-order harmonic generation. The electric field of the generated XUV light as a function of time $E(t)$ can be expressed as a sum of harmonic waves

$$E(t) = \sum_q a_q \cos(q w_{\mathrm{NIR}} t + \phi_q), \tag{1.14}$$

where q is an odd integer and ω_{NIR} is the angular frequency of the fundamental field and therefore $q\omega_{\mathrm{NIR}}$ is the angular frequency of the qth harmonic. The amplitudes a_q of the individual frequencies and their respective phases ϕ_q have to be determined to characterize the harmonic field.

In order to determine the harmonic amplitudes a_q, a flat-field XUV spectrometer [136] can be applied. Alternatively, the harmonic amplitudes can also be determined by measuring the photo-electron spectrum (PES) of a rare gas ionized by the harmonic radiation taking into account the photo-ionization cross section in the XUV spectral region of interest.

The harmonic phases ϕ_q are then the missing parameters to determine the temporal structure of the harmonic radiation by Equation 1.14. Provided that the APT under investigation is uncompressed, the spectral phase of the harmonics is expected to be quadratic [87].

In 2001 Paul et al. proved for the first time that an APT was generated experimentally [112]. A technique known today as *reconstruction of attosecond beating by interference of two-photon transitions* (RABITT) [139] was utilized: The energy-resolved photo-electron

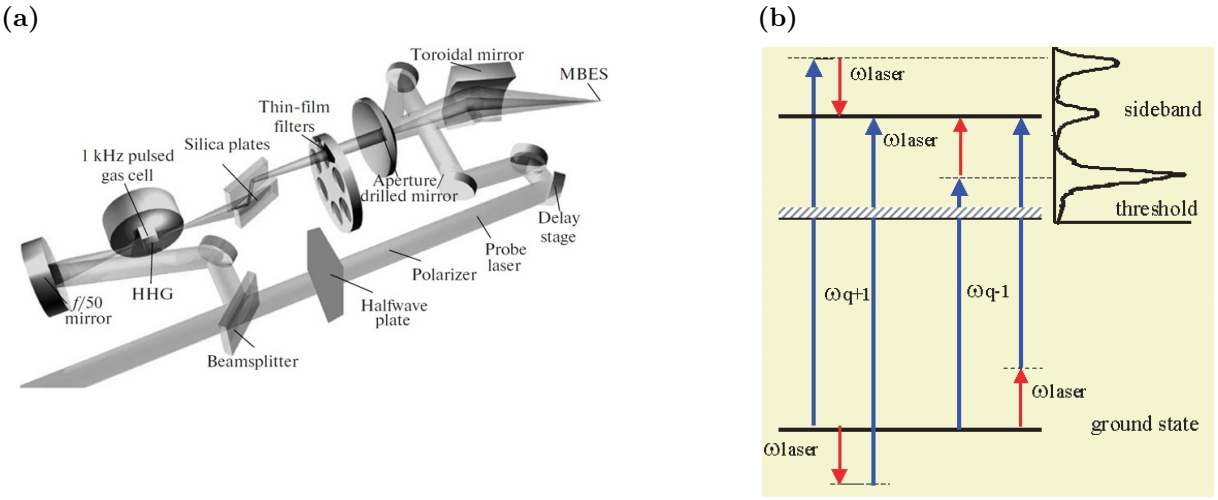

Figure 1.12: Scheme of a RABITT experiment. (a) RABITT experimental setup. The incoming beam is split into a pump beam responsible for generating harmonics and a probe beam. The pump beam is focused into a gas cell and spectrally filtered by a thin aluminum foil. The probe beam passes a delay stage and is recombined with the harmonics on a cored mirror. Both beams are focused into the interaction region of an electron spectrometer. Figure taken from [137]. (b) Energies of electrons generated in the RABITT process. Electrons can be generated by single-photon absorption of a harmonic photon with energy $E_q = \hbar\omega_{\text{laser}}$, where q is the odd harmonic number and ω_{laser} is the driving laser angular frequency, or the electrons absorb or emit an additional NIR laser photon leading to sidebands in the PES. The sideband intensities oscillate as a function of pump-probe delay, where the oscillations originate from an interference between electrons from two different pathways ($E_q + E_{\text{NIR}}$ and $E_{q+2} - E_{\text{NIR}}$). Figure taken from [112].

spectrum of a rare gas ionized by an APT in the presence of a NIR field was measured as a function of XUV-NIR time delay (Figure 1.12 (a)). The APT pump and the NIR probe fields must be phase-locked. To this end, a NIR laser pulse is split into two separate pulses by a beam splitter. One part of the pulse generates the APT while the other (NIR probe pulse) is collinearly overlapped with the APT downstream. The APT is swept temporally over the NIR probe pulse, sampling its electric field. In this quasi pump-probe measurement, photo-electron spectra change as the instantaneous NIR electric field changes due to the modulated probability to induce continuum transitions. In addition to the photo-electron energies stemming from ionization by odd harmonics, sidebands occur at electron energies corresponding to even harmonics (Figure 1.12 (b)). These electrons are formed by absorption or emission of one NIR photon in addition to the absorption of an

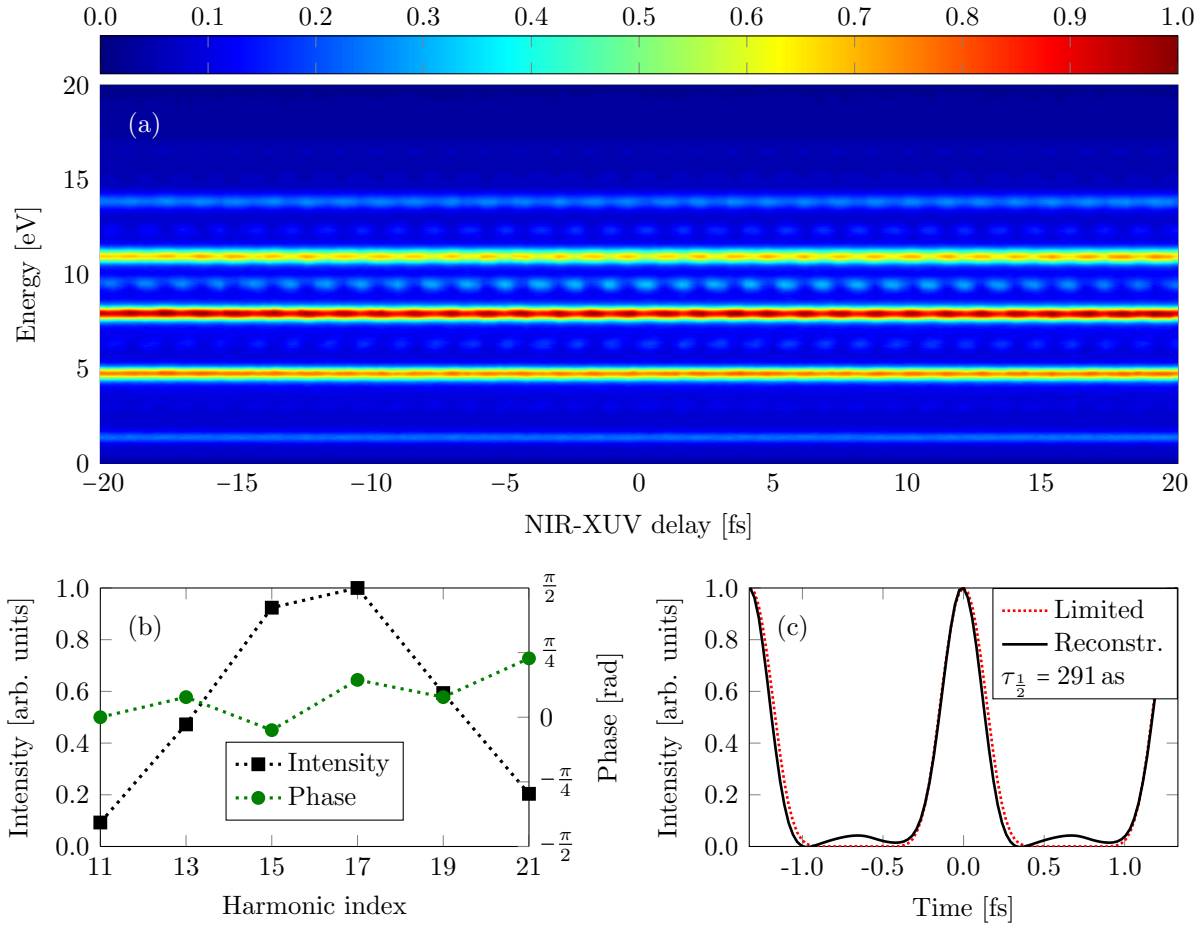

Figure 1.13: RABITT measurement and burst reconstruction. The high-order harmonics were generated in xenon. (a) RABITT data recorded with a velocity map imaging spectrometer (VMIS, see Chapter 2) The signal stems from electrons created by ionization of argon. (b) Intensity distribution of the harmonics obtained from (a) by integrating along the time axis and correcting for the total photo-ionization cross section [138]. The phases were obtained by fitting the oscillations of the sidebands to a sine function and setting the phase of the 11^{th} harmonic arbitrarily to zero. (c) Reconstructed average burst and Fourier limit. The FWHM of the burst is $\tau_{\frac{1}{2}} = 291\,\text{as}$.

XUV photon. Therefore, each sideband exhibits contributions from two different two-color pathways involving adjacent harmonics. The two pathways interfere leading to oscillations of the sideband signal as a function of the APT-NIR delay at twice the NIR field frequency.

Neglecting a small atomic phase contribution allows to write the sideband signal $S_{q+1}(t)$

as a function of the relative pulse delay t as

$$S_{q+1}(t) = S_0 \cdot \cos\left(2\omega_{\mathrm{NIR}} t + \Delta\phi_{q|q+2}\right), \tag{1.15}$$

where S_0 is the maximum signal of the sideband and $\Delta\phi_{q|q+2}$ is the phase difference of the two contributing harmonics [112, 137]. Thus, the sideband oscillations directly reveal the relative magnitude of the harmonic phases ϕ_q. Therefore, it is possible to reconstruct the temporal structure of the APT by applying Equation (1.15) and using the result in conjunction with Equation (1.14).

Figure 1.13 (a) shows a typical RABITT measurement carried out in the attosecond laboratory at the MBI. Xenon was used for the process of high-order harmonic generation, while argon was used as the target gas in the electron spectrometer. The oscillatory period is 1.3 fs, which is half the period of the 800 nm fundamental laser. The calibration of the energy axis is straightforward, due to the knowledge of the ionization potential of the target gas ($E_{\mathrm{IP,Ar}} = 15.8\,\mathrm{eV}$) and the energetic separation of signals generated by adjacent harmonics, which is $\Delta E = 2\hbar\omega_{\mathrm{NIR}}$.

Phases and relative intensities shown in Figure 1.13 (b) are deduced from the measurement plotted in Figure 1.13 (a). Using these data as the input of Equation (1.14), the average temporal shape of the bursts in the attosecond pulse train is obtained and depicted in Figure 1.13 (c). This fairly simple technique is used in attosecond laboratories around the world as a fast and robust check of the quality of APTs.

The RABITT technique only allows to determine the average shape of the individual pulses in the APT. Non-averaged information could be obtained by a technique, developed by Kim et al. in 2010 [140]. The principle is similar to RABITT, but instead of measuring the RABITT signal over a short delay time (6 – 10 fs), the scan runs over the complete NIR pulse (20 – 40 fs). This information is used as the input for the method of complete reconstruction of attosecond bursts (CRAB). Kim et al. were able to obtain information about the individual bursts in an attosecond pulse train. Nevertheless, for the experiments presented in the present thesis, it is sufficient to know the average temporal structure of the individual pulses within the attosecond pulse train by characterizing them with the RABITT technique.

1.4.2 Streaking

As discussed above, optical gating techniques lead to isolated attosecond pulses. As RABITT can only be used to determine the pulse duration of the bursts within an APT, the question arises how to determine the exact pulse duration of IAPs. Therefore, new techniques have been developed to characterize isolated attosecond XUV pulses. A mature method is attosecond streaking, briefly introduced here.

Attosecond streaking was proposed in 2002 by Itatani et al. as a way to measure isolated attosecond pulses [141]. Here, the IAP co-propagates with a few-cycle NIR pulse, which is often the pulse that generated the XUV pulse. Both beams are focused into a rare gas and can be mutually time delayed. The XUV pulse ionizes the gas and the resulting photo-electrons show a spectral structure that corresponds to the spectral structure of the XUV pulse but with kinetic energies shifted by the ionization potential of the gaseous medium. The photo-electron spectrum (PES) is recorded as a function of the XUV-NIR delay. Depending on this delay, the photo-electrons undergo a momentum shift due to the vector potential $A_\omega = -\int E_\omega \mathrm{d}t$ arising from the NIR electric field E_ω. As a consequence, the center of energy of the PES bands is shifted and the kinetic energy distribution width is altered. This effect is called streaking. If the XUV burst is chirped, the PES can experience an additional broadening due to A_ω. The strength of this additional broadening varies with the sign of A_ω and therefore with the XUV-NIR time delay [66]. Comparing the streaked and the non-streaked PES renders possible to retrieve the IAP duration [115].

A streaking measurement where the electric fields can be arbitrarily complex is *frequency-resolved optical gating for complete reconstruction of attosecond bursts* (FROG-CRAB) [142]. The measurement is basically the same as for the attosecond streak camera method but the dressing pulse does not have to be the HHG driving pulse. The dressing pulse is used as a temporal phase gate to record the PES. Applying the so-called *principal component generalized projects algorithm* (PCGPA) [143] to the measured trace, yields information on the spectral width of the XUV pulse, its chirp and the electric field of the dressing laser. In 2006, Sansone et al. used FROG-CRAB to reconstruct a 130 as XUV pulse generated by polarization gating of a 5 fs driving pulse [128].

Chapter 2

The attosecond experimental setup

A growing number of laboratories around the world utilize attosecond and XUV technology to investigate atomic and molecular processes [64, 144, 145]. All these experimental setups are sophisticated and highly developed in terms of light pulse parameters (duration, energy), stability, reliability and automation [146]. Time-resolved measurements with attosecond precision require outstanding stability of all mechanical and optical elements. In the experiment described here, laser pulses have to propagate about 10 m from the laser amplifier to the experimental interaction region. It is necessary to record and evaluate the pointing and power stability of the laser beam and to account for it in the data analysis. The most important issue for the quality of attosecond experiments is the determination and stabilization of the temporal delay between the two laser pulses in the pump-probe measurements. In the experimental section below, both the laser and the delay stability will be discussed in greater detail. First, a short introduction of the setup will be presented, starting with an outline of the laser amplifier and the optical paths through the experiment, followed by a description of the vacuum chambers and the spectrometers.

2.1 The laser system

The attosecond beamline utilizes a newly developed Ti:Sa laser system (Amplitude Technology), based on chirped pulse amplification (CPA). The Amplification stages are

pumped by four Nd:YLF pump lasers, delivering a combined power of about 230 W. A schematic of the laser system is given in Figure 2.1. The subsequent description follows the red arrows, which denote the path of the seed beam through the amplifier.

The seed beam is generated by a Rainbow™ oscillator (FEMTOLASERS), operating at 76 MHz. It exhibits a spectral width from the visible to the near-infrared (NIR) region of 300 nm leading to pulse durations of less than 7 fs in terms of full width at half maximum (FWHM). To amplify these short pulses, they are temporally stretched in a grating stretcher and pre-amplified in a regenerative amplifier operated at a repetition rate of 10 kHz. The beam is boosted to about 4.4 W in a multipass amplification stage downstream before the pulse is split into two individual beams. Up to this point, the system is pumped by about 30 % of the output of an Etna™ pump laser (THALES). The remaining 70 % of the Etna™ laser are used to pump the last amplification stage in the 10 kHz arm before the beam is compressed. The specified output power of this arm is 20 W.

The second arm of the laser operates at 1 kHz and is pumped by three Evolution™ pump lasers (COHERENT). After the common booster stage, a Pockels cell couples out a small portion of about 50 mW of the pre-amplified beam into the 1 kHz booster stage, where it is amplified to 9 W. A last amplification stage, equipped with a cryogenically cooled laser crystal, increases the laser beam power to 27 W prior to recompression. The resulting output power is 20 W due to losses on the gratings of the compressor.

To achieve the specified final pulse duration of ≤ 20 fs (FWHM) at 20 W of output power[1], the pulse shaping capabilities of two *acousto-optic modulators* (AOMs) [147, 148] are exploited. To attain an optimal amplified pulse spectrum in the regenerative amplifier, a first feedback loop controls an *acousto-optic programmable gain control filter* [149] (Mazzler™, FASTLITE) for amplitude shaping to minimize the effect of gain narrowing of the spectrum. A second feedback loop optimizes the spectral phase of the output beam by means of an *acousto-optic programmable dispersive filter* (AOPDF) [150] (Dazzler™, FASTLITE), which modifies the spectral phase of the seed beam prior to amplification. The AOM settings are monitored by a technique called *spectral phase interferometry for direct electric field reconstruction* (SPIDER) [151] to ensure shortest pulse durations.

[1]The work was conducted, when the laser system was still in the development stage. Therefore, a pulse duration of about 30 fs at an output power of about 15 W was provided for the experiments described in this thesis.

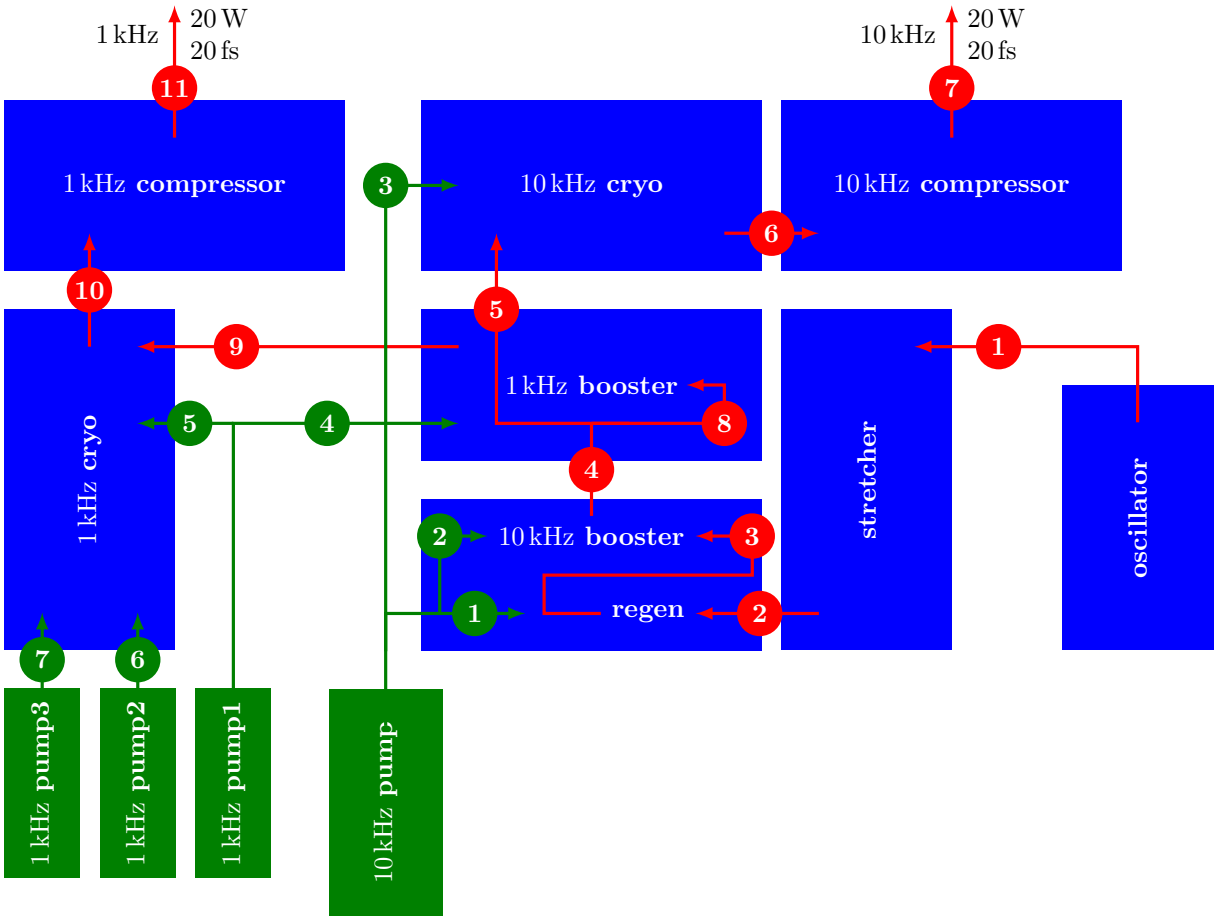

Figure 2.1: Overview of the laser system. The setup generates two beams with an average power of 20 W each. The beams operate at repetition rates of 10 kHz and 1 kHz, respectively. The system consists of a fs-oscillator, a stretcher stage, a regenerative amplifier, two booster stages and two separate cryogenic cooled amplification and compressor stages. The amplifier is pumped by four pump lasers with a combined power of about 230 W. *(Detailed power specifications for the pump lasers are (green) 1:* 12.7 W, *2:* 16 W, *3:* 100 W, *4:* 15 W, *5, 6 and 7:* 30 W *each. Power specifications for the amplified beams are (red) 1:* 0.18 W *(seed), 2: unknown, 3: unknown, 4:* 4.4 W, *5:* 3.3 W, *6:* 26 W, *7:* 20 W, *8:* 0.05 W, *9:* 3 W, *10:* 27 W, *11:* 20 W*)*

In the experiments described in this thesis, 20 % of the power of the 1 kHz arm are used, i.e., a pulse energy of about 3 – 4 mJ. This is sufficient to pump the high-order harmonic generation process and, in addition, to have a second beam with intensities up to 10^{14} W/cm^2 for pump-probe experiments.

2.2 The beamline

The experimental setup for HHG and the spectrometers were built at the AMOLF institute in Amsterdam. Later, the machine was moved to the MBI laboratories in Berlin. The basic setup was presented in several publications [50, 152]. A schematic overview of the experiment is shown in Figure 2.2.

The beam diameter of the amplified laser beam is reduced by 1/3 (to about 18 mm) by means of a mirror telescope, prior to entering a Mach-Zehnder type interferometer. A beam splitter (BS), located on a micrometer delay stage (step size $\Delta\tau = 6.67$ fs), splits the incoming laser beam into two arms. 60 % of the laser pulse are reflected from the beam splitter to form the high-order harmonic generation arm of the interferometer.

The beam is steered into the HHG vacuum chamber via a focusing mirror (FM1) with a focal length of 500 mm. The intensity is sufficient to generate high-order harmonics (Section 1.1) in a small gas cell that is filled with a rare gas. Generated XUV light is separated from the remaining NIR light and low-order harmonics (<H11) by a thin (300 nm) aluminum filter. The foil also compresses the generated attosecond XUV bursts, because the dispersion of harmonics in aluminum is such that it compensates for the intrinsic atto-chirp (Section 1.1). The result is an attosecond pulse train (APT) that lasts for about 20 fs. The duration of the individual bursts within the APT is about 300 as to 450 as FWHM, depending on the high-order harmonic generation gas. The burst duration was measured by the RABITT technique (Section 1.4.1). After the filter, the APT has to pass a 1.5 mm aperture, which is the center hole of the so-called recombination mirror (RCM). The aperture also removes XUV photons resulting from long trajectories in the HHG process, because their divergence is larger than the divergence of the XUV stemming from the short trajectories.

The second arm of the interferometer carries 40 % of the incoming beam, which is transmitted through the initial beam splitter. This beam is reflected into the recombination chamber (RC) via a focusing mirror (FM2) ($f = 500$ mm) to match the divergence of the beam in the HHG arm. This focusing mirror is mounted on a piezo-driven delay stage (PS). The piezo stage controls the path length difference of the two interferometer arms with nanometer precision and therefore the delay of the two pulses with attosecond accuracy.

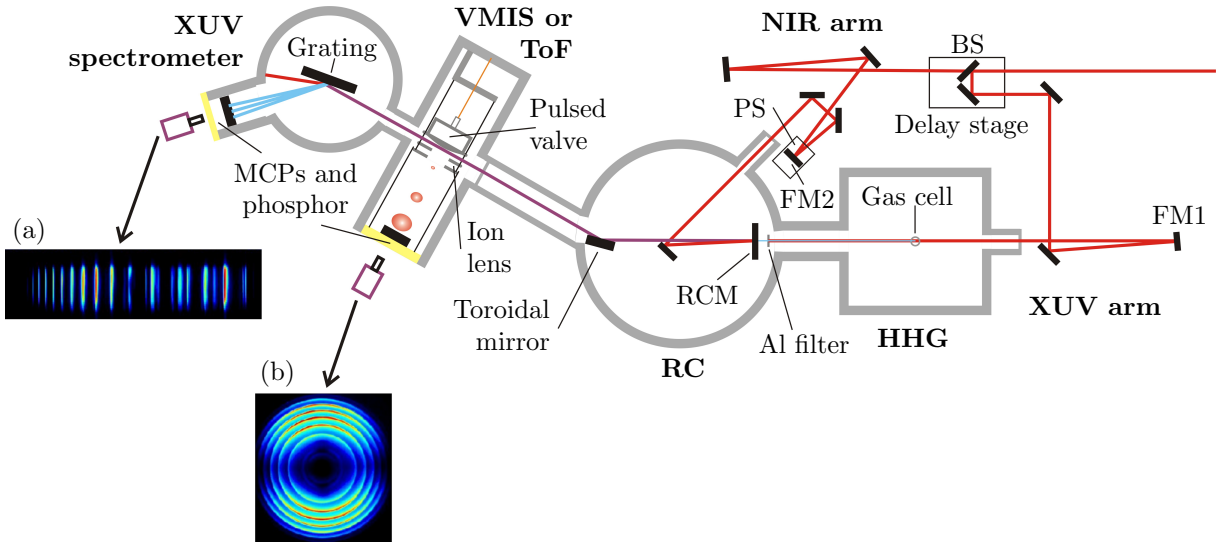

Figure 2.2: Experimental scheme. The laser beam from the commercial Ti:Sa system is split into two parts by a beam splitter (BS) to form a Mach-Zehnder type interferometer. The reflected, more intense portion of the beam is focused (FM1) into a gas cell (located inside the HHG vacuum chamber) containing a rare gas to generate high-order harmonics. The weaker part is focused (FM2) into the recombination chamber (RC) to match the divergence of the first beam and propagates towards the front surface of the recombination mirror (RCM). This mirror possesses a center hole through which the XUV beam generated via HHG is transmitted from the backside. Both beams now propagate collinearly and are focused into the interaction region of a velocity map imaging spectrometer (VMIS) by a toroidal mirror. The VMIS is capable of measuring ions or electrons angle- and energy-resolved (b). The high-order harmonic spectrum can be monitored in real time by an XUV spectrometer downstream (a). The relative delay of the XUV and NIR beams used in the pump-probe experiments can be controlled with attosecond precision by means of a piezo-driven delay stage (PS).

Inside the recombination chamber, the NIR beam is reflected off the surface of the RCM to collinearly recombine it with the XUV beam. Both beams are focused into the interaction region of the spectrometer by a toroidal mirror, located at the exit of the recombination chamber.

A grazing incidence toroidal mirror [153, 154] is used as focusing element, because no mirror materials or dielectric coatings reflect the broad XUV spectrum efficiently under normal incidence. Toroidally shaped mirrors do not create the strong astigmatism that would occur upon using spherically shaped surfaces in a grazing incidence geometry. The two different radii, a small radius of curvature r in the sagittal plane and a large radius

of curvature R in the meridional plane, allow to compensate for the astigmatism. The experimental setup works in $1:1$ imaging mode ($2f$-$2f$ geometry). The distance of the toroidal mirror from the HHG focus is about 800 mm, as is the distance from the toroidal mirror to the experiment, i.e., the focal length of the toroidal has to be $f = 400\,\text{mm}$. Due to experimental constraints (e.g., the spot size on the surface of the toroidal mirror), the incidence angle of the beams on the toroidal is fixed to $\theta = 15\,^\circ$. It follows by the toroidal formula,

$$\frac{2}{R\cos\alpha} = \frac{1}{f} = \frac{2\cos\alpha}{r}, \tag{2.1}$$

that the two radii of the toroidal are $R = 3090\,\text{mm}$ and $r = 206.84\,\text{mm}$, taking into account that $\alpha = 90\,^\circ - \theta$. The spatial quality of the focused beam is very sensitive to any misalignment of the toroidal mirror with respect to the incoming laser beam. Therefore, accurate daily alignment is ensured by utilizing two irises. The first is installed right in front of the HHG chamber and the second is the hole in the recombination mirror itself. If the direction of the incoming beam is fixed and reproducibly adjusted on a daily basis, only the requirement for a precise alignment of the toroidal coordinates remains. The proper alignment of the toroidal is made feasible by mounting it on a five axes adjustable stage. These axes are adjusted such that the astigmatism of the focused beam is minimized.

After the toroidal mirror, the accurately focused NIR and XUV beams irradiate the molecules under investigation in the interaction region of a velocity map imaging spectrometer (VMIS) [155]. Photo-electrons or photo-ions created in the active region of the spectrometer are electrostatically accelerated and focused by means of an electrostatic lens system onto a two-dimensional detector consisting of microchannel plates and a phosphor screen. Depending on the ratio between the repeller plate voltage (acceleration) and the extractor voltage (focusing), the spatial coordinates of charged particles along the laser propagation axis (spatial imaging) or the momentum distribution of charged particles in the laser focus (velocity map imaging) are mapped onto the two dimensional detector plane (see Figure 2.3). The VMIS assembly used in the attosecond laboratory at the MBI makes use of a special design [156]. The molecular beam is directly injected through a small capillary (diameter $\approx 50\,\mu\text{m}$), incorporated into the repeller plate of the VMIS. This allows for up to three orders of magnitude higher gas densities in the experiment compared to setups where a molecular beam is injected into the interaction region of the VMIS

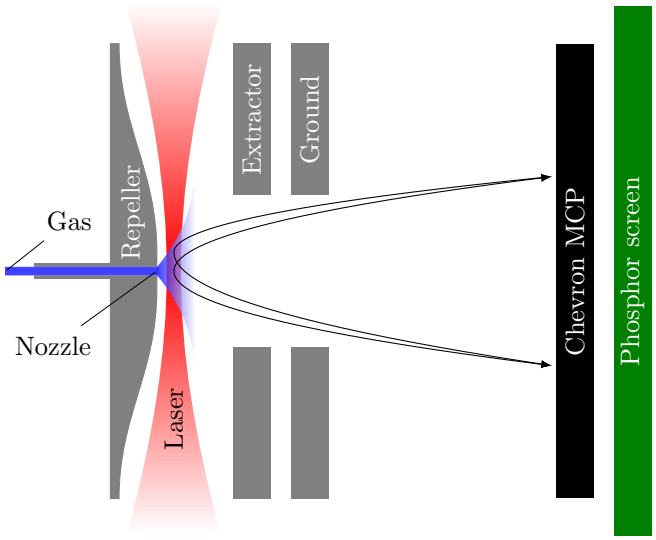

Figure 2.3: Velocity map imaging spectrometer (VMIS) with the gas injection system integrated in the repeller plate. A laser beam (red) ionizes atoms or molecules (blue) close to the nozzle, which results in charged particles accelerated towards the MCP/ phosphor screen detector. In VMI mode, particles originating from a finite interaction region but with equal initial momentum are focused by the extractor and ground electrodes to the same position on the detector plane. The black trajectories stem from particles ionized at two different positions along the laser focus with equal absolute velocity but opposite direction.

through a skimmer. The signal-to-noise ratio in the experiments is higher accordingly [89]. The spatial imaging mode of the VMIS is used during alignment, but the spectrometer is operated in velocity map imaging mode for data acquisition. In VMI mode, a gating voltage is applied to the front of a microchannel plate of the detector to make sure that only one species (i.e., a specific mass/charge ratio) is seen by the detector assembly. The three dimensional momentum distribution projected onto the two dimensional detector is reconstructed from the recorded images by means of an iterative Abel inversion [157]. The reconstruction yields angular- and energy-resolved information about the products formed upon photo-ionization of atoms and molecules.

Behind the VMIS chamber, a flat-field XUV spectrometer is installed [136]. After interacting with the molecules in the VMIS, the XUV photons are dispersively reflected and focused by a grating with variable line spacing (Hitachi, 600 $^{\text{Grooves}}/_{\text{mm}}$, radius of curvature 5.649 m) onto another MCP-phosphor screen stack. The resulting spectrum is recorded with a camera. This gives the ability to monitor the high-order harmonics spectrum during the measurement and, therefore, to track the conditions of the HHG process in real time.

2.3 Attosecond stability

The setup described above is used to measure electron dynamics in molecules on an attosecond timescale. The pump-probe geometry must therefore attain a stability that results in a temporal jitter between the beams with a root mean square (RMS) value of less than 100 as to fully exploit the time resolution given by the duration of the attosecond bursts. Unfortunately, there are several sources of instability.

Mechanical vibrations introduced by vacuum pumps, power supplies and chiller units in the lab have to be minimized. Therefore, the optics inside the vacuum chambers are mounted on vibrationally decoupled breadboards. The breadboards are directly attached to the optical table without contact to the walls of the chambers. This construction has the disadvantage that the optical height is higher than desirable. To still guarantee a satisfactory mechanical rigidity, the optic holders are not directly mounted on the optical table but on an elevated second breadboard on top of the optical table.

Instabilities can also be caused by airflow which can disturb the laser beam, e.g., by changing the refractive index of air due to density fluctuations. This leads to differences of the optical path length in the two arms of the interferometer.

In addition, the laser itself shows fluctuations in the output power, depicted in Figure 2.4 (a), in beam pointing and pulse duration. Occasionally, these fluctuations can become large and exhibit distinct frequencies, which can be seen as modulations of various laser parameters resulting in signal artifacts. If the pointing stability is poor, the spatial overlap of the pump and the probe beam and the overlap with the molecular beam in the interaction region of the VMIS is not guaranteed. Assuming a path length in the interferometer of about 2 m and a pointing stability of 10 μrad, the spatial drift of the beams with respect to each other would be on the order of 20 μm. Taken into account that the focal spot size is only about 100 μm, it becomes apparent that a drift of the beam would lead to unwanted signal variations. Another source of signal fluctuations can be a breathing of the laser spot size, as shown in Figure 2.4 (c). These spot size fluctuations can be as large as 20 %, i.e., 20 μm. The instabilities are probably caused by the pump lasers and directly affect the high-order harmonic signal.

Several active and passive control mechanisms were implemented to handle all the afore-

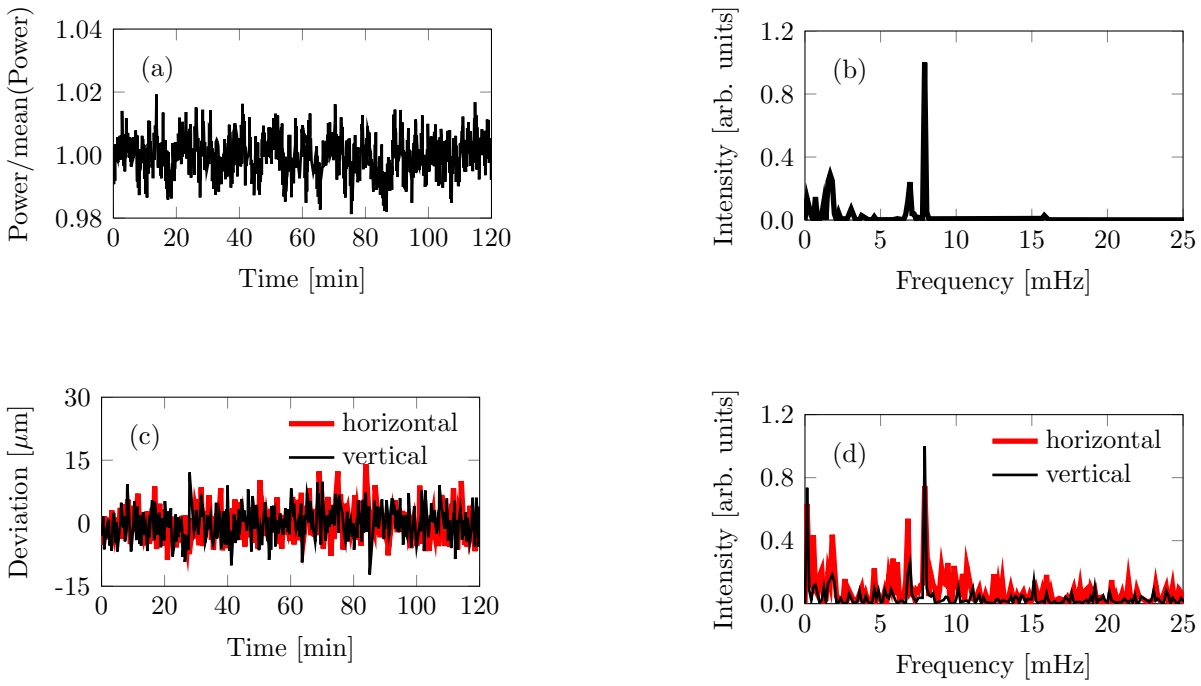

Figure 2.4: Stability of the laser amplifier output. (a) Power measurement after the compressor and (b) its Fast Fourier Transform (FFT). (c) Measurement of the deviation of the spot size from its mean value and (d) its FFT. The measurement was carried out 3 m from the amplifier output. The beam was focused with $f = 800$ mm. The Fourier analysis reveals a clear modulation with a period of 2.1 min (7.9 mHz) in both signals.

mentioned issues. First of all, the relative optical path lengths in the interferometer were actively stabilized. A second narrow band laser, called stabilization laser, propagates parallel to the main laser in the interferometer. Before the stabilization laser beams can reach the toroidal mirror, they are coupled out of the recombination chamber by a pick-up mirror. The separate beams of the secondary laser are non-collinearly overlapped in the horizontal direction. This leads to an interference pattern consisting of equally spaced stripes that can be recorded by a camera. Applying a Fast Fourier Transformation (FFT), information on the relative change of the optical path length of the two interferometer arms is obtained. The information is sent back to the piezo-driven delay stage, located in the NIR-only arm of the interferometer, which adjusts its position accordingly. If the mechanical stability of the floor of the laser lab is good enough and if the PID parameters

(see, e.g., [158] and references therein) controlling the piezo stage are chosen correctly, the temporal jitter of the two arms in the interferometer can be as small as 10 as RMS. On the other hand, a frequency drift of the stabilization laser can not be taken into account by the stabilization software, which may result in a faulty stabilization. In a pump-probe experiment, the APT is delayed with attosecond precision with respect to the NIR pulse, leading to an observable that depends on the exact delay of the APT with respect to the NIR electric field. The investigated observable could show, e.g., a high yield when the bursts of the APT are synchronized with the extrema of the electric field of the NIR and a low yield when the bursts are synchronized with the zero-crossings. If the stabilization laser frequency drifted during the measurement, the software would stabilize the optical path length difference on incorrect values. This would lead to a signal oscillation that is longer or shorter than the actual period of the NIR electric field, depending on the time direction of the scan.

The aforementioned issues are serious if the stabilization laser is a non-frequency stabilized helium-neon (HeNe) laser, as it was the case in the past. HeNe lasers can show significant frequency drifts due to thermal effects (cooling or heating of the cavity), leading to a change of the longitudinal mode spectrum. Another source of frequency instability can arise from the fact that non-frequency stabilized HeNe lasers always support at least three longitudinal modes. This is due to their gain profile, which can lead to mode jumps during operation. To overcome problems resulting from frequency instabilities of the stabilization laser, a temperature stabilized distributed feedback (DFB) diode laser system was incorporated into the setup. DFB lasers provide a very narrow line width of about 10 MHz and only a single longitudinal mode is supported in the short cavity. Therefore, mode jumps are excluded. Both lasers were tested and compared in a Michelson interferometer. To minimize mechanical influences during the stability measurement, the footprint of the interferometer was designed to be as small as possible. In addition, the interferometer was boxed to avoid disturbances stemming from air fluctuations. To get a good comparison of the HeNe and DFB frequency stability, a flip-mirror was installed, which allowed to change between the different lasers without influencing any other optical element. Therefore, consecutive scans with the two lasers could be carried out in quick succession. The individual beams in the interferometer generated an interference pattern on a camera. The pattern was analyzed by the stabilization program, assuming the central

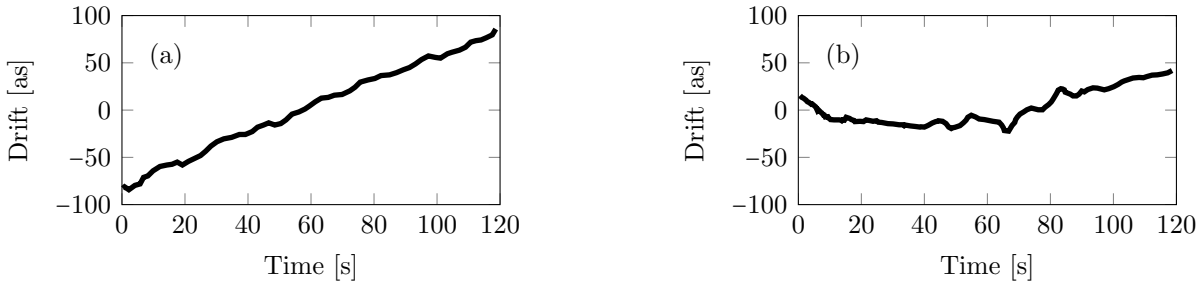

Figure 2.5: Comparison of the worst case stability of (a) the HeNe laser vs. (b) the DFB laser for 2 min. Both lasers are not frequency stabilized. The measurement was carried out in a boxed Michelson interferometer with a small footprint, so that the main delay drift can be attributed to a frequency drift of the lasers itself.

wavelength to be stable. The software calculated an optical path length difference of the interferometer arms when the interference pattern sweeps over the camera sensor. Measurements showed that the HeNe drifts are on the order of 100 $^{\text{as}}/_{\text{min}}$, while the drifts of the DFB were less than 40 $^{\text{as}}/_{\text{min}}$. In addition, the DFB wavelength of 761 nm is much closer to the central wavelength of the measurement laser (800 nm) than that of the HeNe (632.8 nm). Hence, the DFB beam is better reflected from the dielectric mirrors in the setup. This leads to an improved contrast of the linear interference fringes produced by the DFB on the camera and, therefore, to a higher quality of the stability measurement compared to the HeNe measurements. The contrast could be further improved due to the power tuning ability of DFB lasers.

The phase ϕ that is recorded and stabilized by the software depends on the offset Δx of the path length difference of the two interferometer arms and the wavelength λ of the stabilization laser such that $\phi = {}^{(\delta x+\Delta x)}/_{\lambda} \cdot 2\pi$, where δx is the path difference that corresponds to the attosecond delay during pump-probe measurements. Thus, the phase difference $\Delta\phi$ caused by a drift of the stabilization laser wavelength from λ_1 to λ_2 is given by

$$\Delta\phi = (\delta x + \Delta x) \cdot \frac{\Delta\lambda}{\lambda_1\lambda_2} \cdot 2\pi, \tag{2.2}$$

where $\Delta\lambda = |\lambda_1 - \lambda_2|$. From Equation 2.2 it can be seen that the phase is most insensitive to

wavelength drifts of the stabilization laser when the offset Δx of the path length difference of the two interferometer arms is small or even zero. As a consequence, the path length difference between the two arms of the interferometer was kept as small as possible. Due to technical limitations the best that could be achieved was $\Delta x \approx 1.5\,\mathrm{cm}$.

One might be interested in the stability in terms of a wavelength drift during the time period of a typical pump-probe measurement presented in the current work. Such a measurement takes about 12 min and the interferometer path difference for the stabilization laser is about 1.5 cm, as mentioned before. Taking into account the speed of light of $3 \cdot 10^8\,\mathrm{m/s}$, it follows that the virtual change of the optical path length within 12 min is about 144 nm and 360 nm for the DFB and HeNe, respectively. The DFB wavelength fits 19711 times and the HeNe wavelength 23704 times into the given path difference of 1.5 cm. Thus, the central wavelength of the DFB and HeNe might drift up to 7 pm and 15 pm within 12 min, respectively. Therefore, the DFB laser is a significant improvement over the HeNe laser. Additionally, the DFB laser is easy to operate, very robust and small, while being still inexpensive compared to frequency stabilized HeNe lasers. Nevertheless, it is still desirable to use a system with about one order of magnitude better wavelength stability ($50\,\mathrm{fm/min}$) to achieve measurements with small time drifts of only a few tens of attoseconds.

In conclusion, it is apparent that both stabilization lasers drift, but the DFB is about twice as stable as the HeNe. If a slight frequency discrepancy is detected in the pump-probe experiments, it can most likely be attributed to the wavelength drift of the stabilization laser. The setup could be further improved by decreasing the offset Δx of the path length difference between the two arms of the interferometer. Another option is to implement a measurement of the absolute frequency of the stabilization laser, e.g., with a Fabry-Perot interferometer. The recorded wavelength can be sent back to the stabilization software which uses this information in the stabilization process, avoiding wrong positions of the piezo delay stage due to instabilities of the stabilization laser.

Besides the optical path length changes that are stabilized actively, there are also other instabilities that can lead to incorrect measurements of the time signal in an attosecond pump-probe experiment. As seen in Figure 2.4, the laser output is not perfectly stable. This is, in principle, no problem, unless the laser output shows a stable oscillation instead of a random fluctuation. It could happen that the signal oscillation caused by the laser output shows up in the measurement or is even the dominant contribution. This is a

situation encountered during the current work. For example, the time it takes to record one measurement point is 15 s. If nine points per period of an oscillatory signal are recorded, a full cycle of the signal is recorded withing 2.3 min. This is indistinguishable from the period of the 2.1 min oscillation shown in Figure 2.4 caused by the laser. There is always a danger that the oscillatory behavior of an observed signal actually originates from measurement artifacts. In order to avoid this, the measurement program was reprogrammed such that it is synchronized with the XUV spectrometer and a power meter that measures the relative output power of the laser system directly after the compressor. The experimentalist is thereby able to record the fluctuations in both the NIR power and the number of XUV photons. In the analysis later on, one can easily see whether the measured oscillations stem from changes in the photon flux or whether they can be assigned to an actual two-color pump-probe signal.

It is clear that a lot of effort is required to reliably measure attosecond time-resolved dynamics in molecules. Under consideration of the aforementioned stability concerns, it is possible to observe dynamics in smaller molecules on the timescale of electronic motion.

Chapter 3

Charge oscillations in neutral molecules - the attosecond Stark effect

The following chapter is based on the publication "Probing Time-Dependent Molecular Dipoles on the Attosecond Time Scale" by Neidel et al. [159].

3.1 Introduction

The emergence of new attosecond laser techniques permits addressing fundamental questions regarding the interaction between light and matter by providing access to electronic properties in real time [66]. One way to observe electron dynamics on these extremely short timescales in molecules, is to use an interferometric method described in Chapter 2. An attosecond pulse train (APT) is collinearly overlapped with a near-infrared (NIR) pulse. Due to the nature of APT generation, the pulse train is phase locked to the NIR electric field. This enables the experimentalist to observe dynamics on a sub-NIR field cycle timescale, an advantage not accessible with conventional femtosecond pump-probe spectroscopy. The technique was previously employed to probe attosecond single electron dynamics in cations [47, 48]. Kelkensberg et al. reported an APT-NIR phase sensitivity

on the fragment yield in dissociative photo-ionization of molecular hydrogen [49]. Oscillations in the yield of high-kinetic energy fragments were assigned to a NIR field-induced coupling of ionization continua, which results in quantum interferences of indistinguishable ionization pathways.

So far, the observed attosecond timescale effects in molecules were all explained in terms of dynamics in ionic systems. These first experimental results have been complemented by theoretical work describing several scenarios for inducing and observing attosecond electron dynamics in neutral molecules [160, 161]. Burnus et al. have shown how the electron density in molecules can be transiently modulated on the attosecond timescale by moderately strong laser fields, leading to electronic excitation [162]. An experimental approach that would allow observing attosecond electron dynamics in neutral molecules remains to be developed.

It is well known that the absorption of a photon requires both energy and momentum conservation. Consequently, short-wavelength radiation is absorbed in the vicinity of atomic nuclei [163], explaining why in X-ray photo-absorption inner-shell excitation is favored over valence excitation. Therefore, it may be anticipated that attosecond XUV/X-ray pulses should be suitable for probing time-dependent electron localization in molecules, and that the short wavelength/high photon energy of the attosecond pulses provides a highly local time-dependent probe of the electron density near the atomic centers in the molecule.

Classically, the initial step of laser excitation corresponds to the acceleration of an electron by the periodic light electric field, which creates a time-dependent dipole. The induced dipole may only last during the interaction when the electron density responds to the electric force exerted by the dressing field, or persists if the interaction led to the formation of a coherent superposition of electronic states. The corresponding changes in the charge density may produce sub-cycle time-dependent modifications of physical molecular properties, such as variations in the photo-ionization yield.

In the present case, the time-dependent dipole during the interaction of a molecule with a light field is considered. This process can also be described in terms of the occurrence of Stark shifts in the molecular photo-absorption spectrum. Indeed, attosecond probing of NIR-induced molecular electron dynamics may be regarded as an ultrafast

variant of molecular Stark spectroscopy, which is a well-established tool for extracting information on structure and chemical bonds in molecules, where the sensitivity of a given transition to a static (or oscillatory) external electrical perturbation is measured. Molecular Stark spectroscopy thereby provides direct information on the polarizability tensor of the molecular sample. The possible advantage employing intense laser fields in Stark spectroscopy (enabling extensive control over the field strength, oscillation period, etc.) was already pointed out by Bublitz and Boxer in 1997 [164].

In this chapter results are presented, which illustrate for the first time - with attosecond time resolution - the effect of a moderately strong NIR laser field on the photo-ionization efficiency of a series of small to midsize molecules (N_2, CO_2 and C_2H_4). In the experiments, a moderately strong NIR femtosecond pump pulse interacts with molecules and induces a time-dependent polarization that is probed by photo-ionization through an XUV attosecond pulse train. As a result, the parent molecular ion yield oscillates as a function of the pump-probe time delay. The origin of the oscillatory signal is interpreted in terms of a time-dependent screening induced by the polarization of the molecules, which alters the photo-ionization probability. The findings are supported by many-body, real-time, real-space, time-dependent density functional theory (TDDFT [165, 166]) calculations and demonstrate the possibility to observe charge migration in a large variety of neutral molecular systems.

3.2 Theoretical modeling

The theoretical work presented in this paragraph was conducted by our collaborators in the group of Dr. Franck Lépine (Lyon University).

The real-time, real-space formulation of TDDFT including the Octopus [167] and the Teleman [168] packages is used to perform the calculations. Details will be presented elsewhere [169]. TDDFT is particularly suited for investigating ultrafast electronic dynamics in complex molecules since it allows a dynamical mean-field representation of the complex interaction between a laser field and a many-body system [170]. As a consequence, it can be used for studying both the linear and non-linear response in two-color femtosecond NIR-attosecond XUV pump-probe experiments.

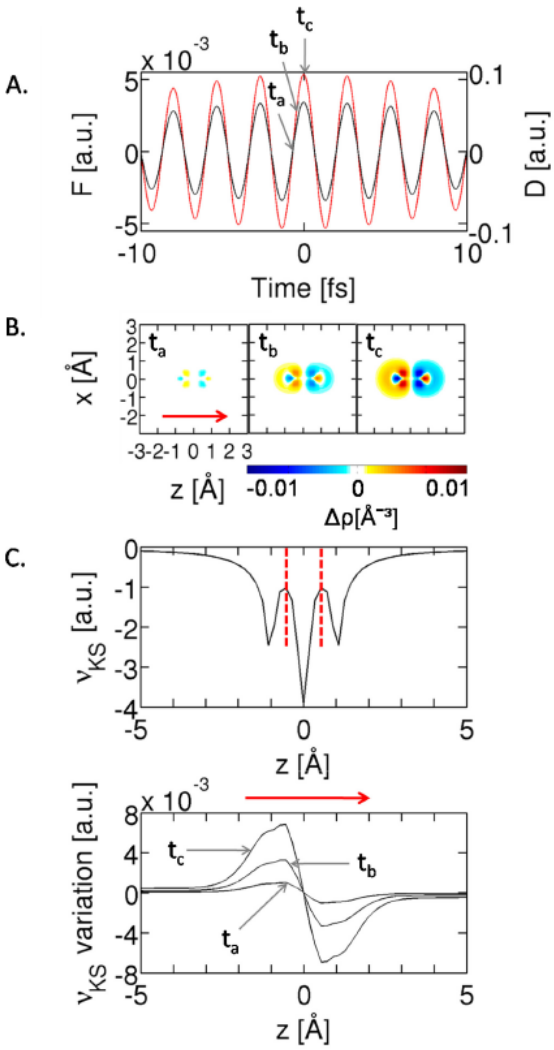

Figure 3.1: A.: Calculated molecular dipole D (black curve) induced by a NIR femtosecond laser field F (red curve), for the case of an aligned N_2 molecule interacting with a 30 fs, 800 nm, 10^{12} W/cm² laser pulse. The NIR field induces an adiabatic time-dependent dipole that corresponds to a displacement of the charge density distribution around the fixed nuclei. B.: Field-induced electronic density changes at three different time delays (field strengths) (see A.). Times chosen are $t_a = t_0 + 75$ as, $t_b = t_0 + 334$ as and $t_c = t_0 + 667$ as, where t_0 corresponds to the time of a zero-crossing of the laser electric field. The color scale indicates an increase (red) or decrease (blue) of the electron density around the nuclei. The red arrow indicates the direction of the light electric field. C.: Kohn-Sham potential V_{KS} for an aligned N_2 molecule (upper panel in C.), where the position of the nuclei are shown with red dashed lines. Variation of V_{KS} when an electric field is present (lower panel in C.). The Kohn-Sham potential acts as a screening field when the polarized molecule interacts with an ionizing XUV laser pulse (see also Figure 3.2).

To illustrate how the electronic density in a neutral molecule is driven on an attosecond timescale by the electric field of an incident NIR laser, calculations were performed for an N_2 molecule interacting with a linearly polarized 800 nm laser field. The laser intensity was set to 10^{12} W/cm² to avoid noticeable ionization. The molecular axis of the N_2 molecule is aligned along the light electric field. Figure 3.1 A. shows the computed time-dependent dipole of the molecule (black curve), which follows adiabatically the time-dependent light electric field (red curve). At the chosen wavelength and laser intensity, the electrons are simply driven by the instantaneous light electric field without significant population transfer to electronically excited states. Therefore, after the laser field has ended, the molecule remains in the ground state. Classically, the time-dependent variation of the

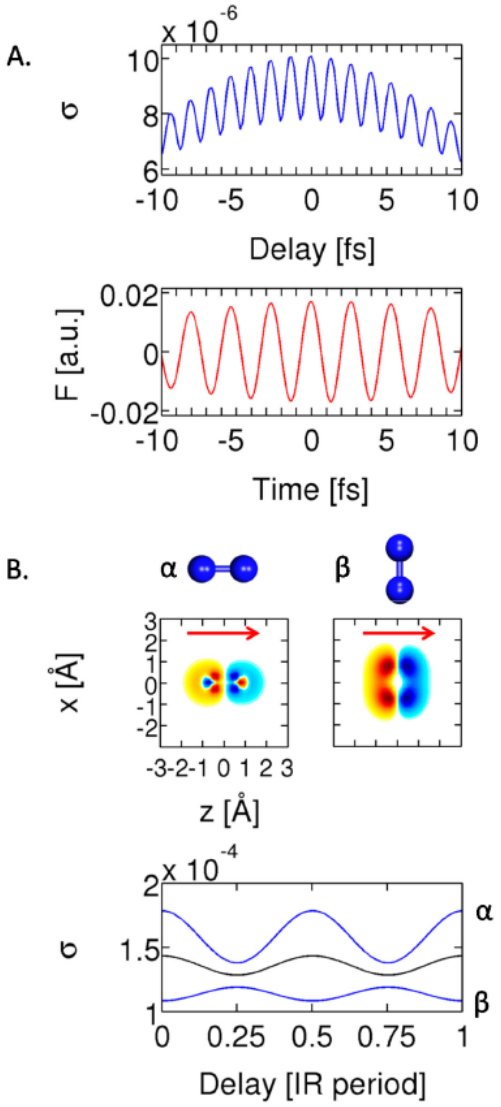

Figure 3.2: A.: Ionization probability σ plotted as a function of the NIR-XUV pump-probe delay (upper panel). For a delay dt in the delay scan, the XUV is overlapped in time with an instantaneous NIR electric field F that can be read off at time $t = dt$ in the lower panel. The maximum ionization is observed when the APT is synchronized with the extrema of the NIR electric field. The calculation was performed in 2D in order to decrease the computational time. B.: The electron density is shown for the case when the molecules are aligned along (left) or perpendicular (right) to the laser polarization axis (upper panel). Variation of the ionization probability σ for the two different cases of the molecular alignment (lower panel). Importantly, although showing a pronounced dependence on the alignment, the field-induced oscillation persists in the case of alignment-averaged calculations (black curve).

dipole reflects an oscillatory motion of the electrons along the molecular axis, and is accompanied by time-dependent changes in the localization of the electrons around the nuclei. This is illustrated in Figure 3.2 B., which shows the variation of the electron density (i.e., the difference between the electronic density with and without the laser field), at three different times (indicated in the upper panel of Figure 3.1 A.), corresponding to three different laser field strengths. The electron density variation is largest at the maximum of the laser electric field, where the charge distribution is displaced on both sides of the molecule as well as between the nuclei. This leads to an asymmetric charge distribution, which generates the molecular dipole plotted in Figure 3.1 A.

The time-dependent change of the electron localization around the nuclei induces changes in the interaction between the molecule and an attosecond XUV pulse ionizing the molecule. In the ionization process, the transition of one electron into the ionization continuum is determined by the XUV field and by the average potential that describes the interaction of the electron with all other electrons and ions within the molecule. In terms of mean field theory, this additional potential corresponds to the Kohn-Sham potential [171]. The Kohn-Sham potential, calculated for N_2 along the molecular axis, is plotted in Figure 3.1 C., together with its variation under the influence of the NIR electric field. When the XUV light interacts with the polarized molecule, its effect on the individual electrons within the molecule is screened by the Kohn-Sham potential, leading to either an increase or decrease of the ionization efficiency.

Figure 3.2 plots the ionization probability of an N_2 molecule which is fixed-in-space. The molecule is polarized by a femtosecond NIR pump pulse (central wavelength: 800 nm, pulse duration: 30 fs, intensity: 10^{12} W/cm^2). In addition, an XUV attosecond pulse train (duration of individual bursts: 300 as, intensity: 10^9 W/cm^2, one XUV burst per NIR half-cycle, photon energy centered at 35 eV) ionized the molecule. For a given NIR-XUV delay, the ionization yield is calculated as the total electronic charge that is transferred into the continuum after 120 fs of time propagation. The calculation is repeated for different NIR-XUV pump-probe delays leading to the upper curve presented in Figure 3.2 A. The lower panel in Figure 3.2 A. shows the NIR electric field for better comparison of the timings. The ionization yield is maximized when the APT is synchronized to the extrema of the NIR electric field. The opposite holds when the APT is synchronized with the zero crossings of the laser electric field. Consequently, the total ionization yield oscillates as a function of the NIR-XUV delay with a period that is half the period of the NIR electric field. As discussed above, this oscillation is due to the influence of screening of the XUV light electric field by the NIR-induced polarization of the molecule, and as such is a manifestation of the time-dependent localization of the electrons within the molecule. The effect observed in the calculation can be as large as 20 % and strongly depends on the NIR intensity.

Variations of the ionization yield were previously observed in attosecond pump-probe experiments on helium atoms [172]. In these experiments, the bandwidth of the XUV light (with a 10 eV wide spectrum centered around 25 eV) was partially below the field-free

ionization threshold of helium (24.58 eV), allowing the efficient population of excited states below the ionization threshold, which could subsequently be ionized by the NIR pulse. Conversely, in the case presented here, both in the experiment and in the theory shown in Figure 3.2, a situation is considered where the XUV photon energy is tuned well above the ionization threshold of the molecule (which is typically below 16 eV), and where the NIR-XUV delay-dependent ionization yield reflects NIR field-induced electron dynamics in the neutral molecule. The variation of the ionization yield can be considered as a variation of the opacity of the molecule, similar to the time-dependent changes in the absorbance of fused silica due to NIR field-induced polarization that were recently reported [173].

In gas phase experiments, laser pulses usually interact with randomly aligned molecules. Figure 3.2 B. shows the effect of molecular alignment. The amplitude of the NIR-XUV delay-dependent oscillations is noticeably decreased when the NIR and XUV pulses are polarized perpendicularly to the molecular axis (blue curve). Moreover, in this case, the yield oscillations are out of phase with the oscillations that occur for molecules aligned along the laser polarization, so that the maximum of ionization occurs when the NIR electric field is zero. Importantly, the yield oscillations remain observable in alignment-averaged calculations (black curve in Figure 3.2 B.), albeit with a reduced amplitude.

3.3 Experimental results

To experimentally verify the possibility to observe the effects predicted above, an experimental arrangement containing a two-color NIR+XUV Mach-Zehnder-type interferometer and a mass spectrometric detection system was used. A detailed description of the experimental apparatus is presented in Chapter 2. Particularities are briefly presented here.

High-order harmonics were generated in xenon or argon by focusing 2 mJ of the NIR femtosecond laser into a gas cell. The cutoff of the XUV spectra were around harmonic 21 (xenon) and 31 (argon) which in the latter case corresponds to an energy of 48 eV. The NIR pump pulse energy was 1 mJ and tuned to result in an intensity of $10^{13}\,{}^{\mathrm{W}}/_{\mathrm{cm}^2}$ at the molecular target. A VMI was used in gated Time-of-Flight mode to detect photo-ions. To illustrate the generality of the observations, ion yield measurements were conducted for N_2,

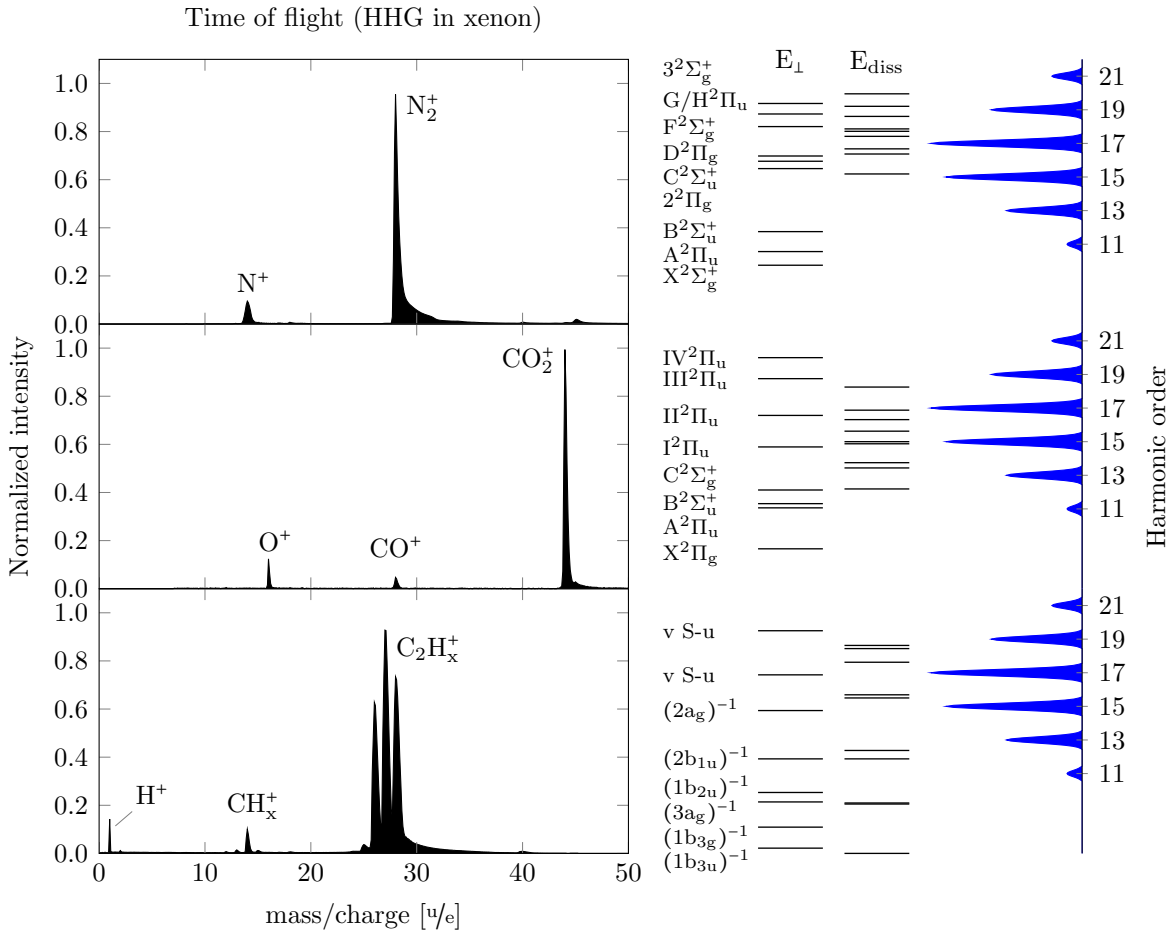

Figure 3.3: Time-of-flight fragment spectra for N_2, CO_2 and C_2H_4 ionized by high-order harmonic radiation generated in xenon. The plots are normalized to their maximum signal. The middle panel shows the energies and terms of the lowest cationic states (see [174], [175] and [176] for N_2, CO_2 and C_2H_4, respectively). The vertical ionization energy is denoted as $E_\perp$ and the dissociation energy is abbreviated as E_{diss}. The right hand side of the figure shows a stylized high-order harmonic spectrum, where the amplitudes are taken from a typical RABITT measurement (Section 1.4.1).

CO_2 and C_2H_4. The measurements consisted of recording the cationic species produced by XUV-induced ionization as a function of the delay between the femtosecond NIR pump pulse and the APT XUV probe pulse, which were phase-locked. The XUV pulse train was characterized by means of the RABITT technique (Section 1.4.1).

Figure 3.3 plots the time-of-flight spectra recorded with the VMIS for the three molecular species (N_2, CO_2 and C_2H_4) after interaction with the APT (generated in xenon) without

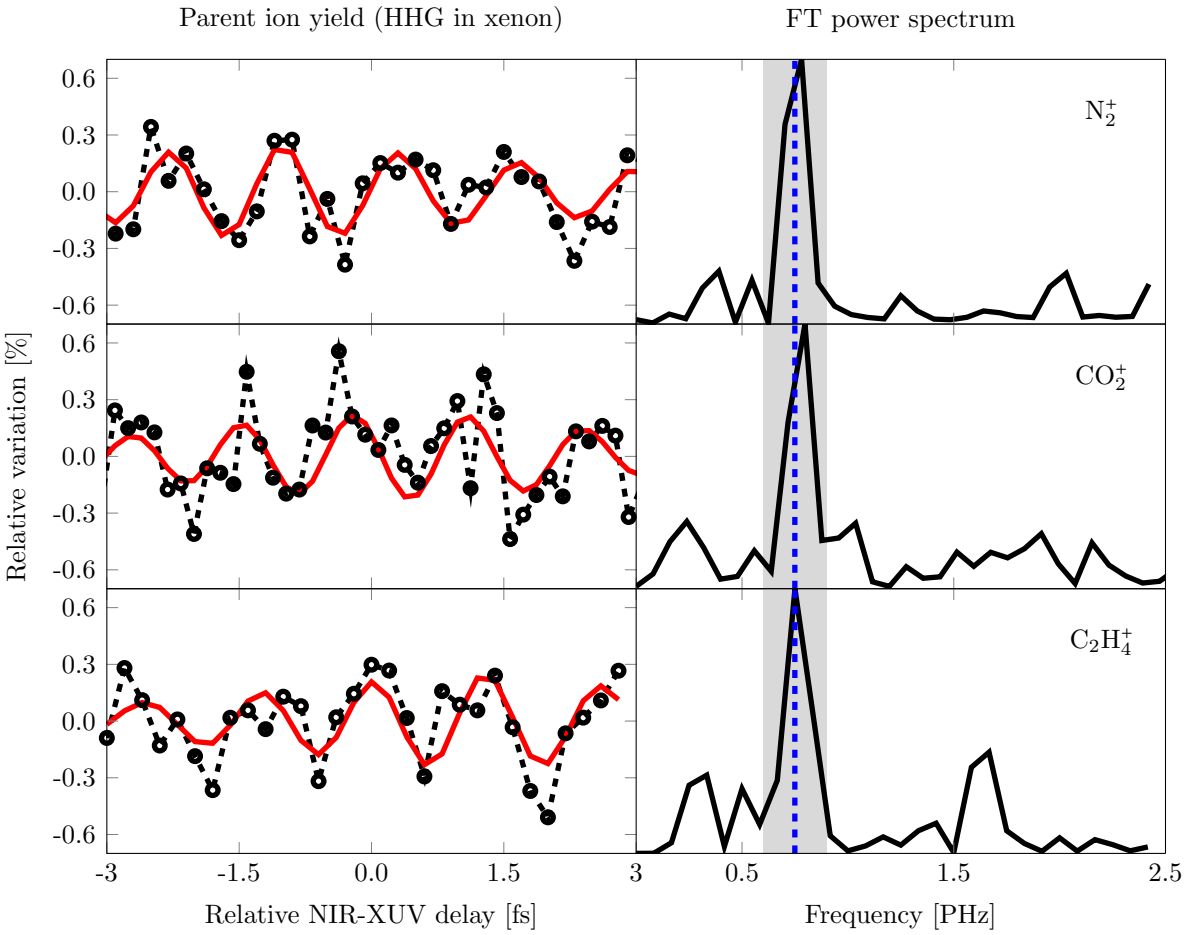

Figure 3.4: Experimentally measured ion yields for N_2^+, CO_2^+ and $C_2H_4^+$ using attosecond pulse trains generated in xenon. The relative variation of the signal is shown as a function of NIR pump-XUV probe delay (dashed black lines) in the left panels. The FT power spectra (solid black lines) are plotted in the right panels. The shaded gray area is used in an inverse Fourier transformation, of which the results are plotted as the solid red curves in the left panels. Note that the phases of the different oscillations cannot be compared because the time offset was chosen arbitrarily for each measurement. The yields oscillate with a periodicity corresponding to half the period of the NIR field, which is indicated by the dashed blue line in the FT power spectra.

the dressing NIR field. In N_2 the ionization leads mainly to the formation of an intense parent ion peak where the molecular ion is formed in one of its three first ionic states, namely the $X^2\Sigma_g^+$, $A^2\Pi_u$ and $B^2\Sigma_u^+$ states. The XUV photon energies used in this experiment also enables accessing the pre-dissociative $C^2\Sigma_u^+$ state and the dissociative $F^2\Sigma_g^+$ state, which leads to the observed N^+ peak in the mass spectra (see also Chapter 4). In CO_2,

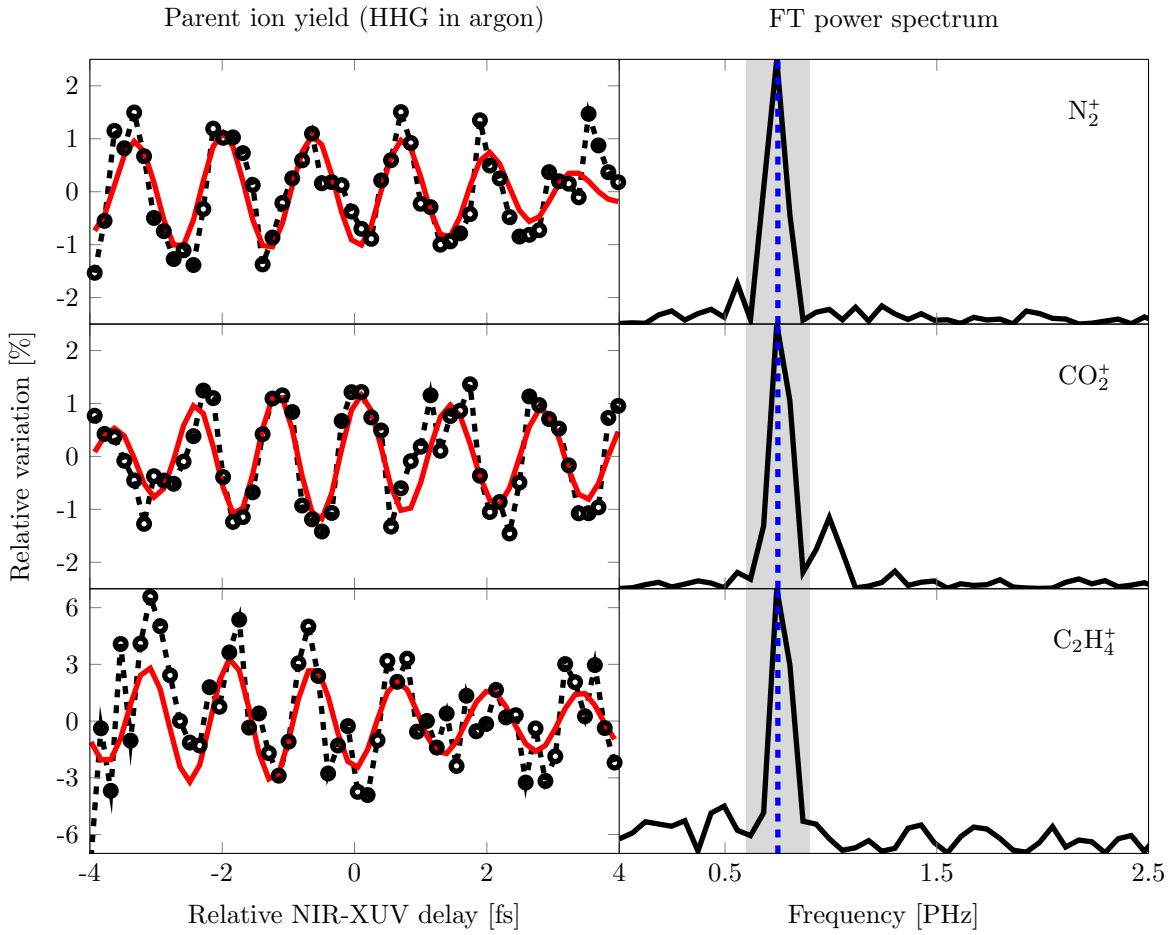

Figure 3.5: Experimentally measured ion yields for N_2^+, CO_2^+ and $C_2H_4^+$ using attosecond pulse trains generated in argon. The relative variation of the signal is shown as a function of NIR pump-XUV probe delay (dashed black lines) in the left panels. The FT power spectra (solid black lines) are plotted in the right panels. The shaded gray area is used in an inverse Fourier transformation, of which the results are plotted as the solid red curves in the left panels. Note that the phases of the different oscillations cannot be compared because the time offset was chosen arbitrarily for each measurement. The yields oscillate with a periodicity corresponding to half the period of the NIR field, which is indicated by the dashed blue line in the FT power spectra.

three charged fragments are observed, as well as a main contribution from the CO_2^+ parent ion. The first four ionic states $X^2\Pi_g$, $A^2\Pi_u$, $B^2\Sigma_u^+$ and $C^2\Sigma_g^+$ are involved in the observed ionization process. Dissociation may arise by pre-dissociation of the vibrationally excited C-state, which lies well above the dissociation limits at 19.1 eV ($CO_2^+ \rightarrow O^+ + CO$) and at 19.5 eV ($CO_2^+ \rightarrow CO^+ + O$). More extensive fragmentation is observed for C_2H_4. This

molecule has the lowest ionization potential (E_{IP} = 10.5 eV) of the three molecules tested and many states can be involved in the ionization/dissociation process. Synchrotron experiments have shown the possible contribution of up to six stable ionic states to the parent ion peak [177]. Fragments arise from ionization to higher ionic channels, such as the $C^2\Sigma_u^+$ and $F^2\Sigma_g^+$ states. The highest photon energy available in our experiment can lead to excitation of additional states. However, as the photo-excitation cross section decreases with the photon energy, their contribution can be considered negligible.

In Figures 3.4 (APT generated in xenon) and Figures 3.5 (APT generated in argon) the variation of the singly charged parent ion yields versus pump-probe delay is shown. The right columns show the Fourier transform power spectra of the oscillations, which exhibit a dominant frequency of 0.75 PHz, indicating a period equal to half the period of the electric field oscillation of the NIR laser. In the case of N_2 a modulation of about 1 – 2 % is observed in the yield of the cation indicating that the NIR field polarizes the neutral molecule. As observed in the TDDFT calculations (Figure 3.2) the APT is a sensitive probe to the redistribution of the electronic density. The fact that the experimentally observed oscillation is smaller than the calculated one is likely due to the fact that the experiment involves averaging over the laser focal volume and the molecular alignment, and is furthermore influenced by nuclear degrees of freedom, which were not included in the TDDFT calculation.

Similar experiments were performed on other molecules and oscillations with various amplitudes are shown for CO_2^+ (about 2.5 %) and $C_2H_4^+$ (about 6 %) in the case of APT generation in argon (Figure 3.5) and somewhat smaller modulation depths when the APT is generated in xenon (Figure 3.4). The dependence of the modulation depth on the chosen molecule indicates the influence of the molecular polarizability tensor. In the case of randomly oriented molecules, the average scalar polarizability is considered. Thus, the amplitudes of the oscillations increase with the total polarizability of the target molecule: N_2: 1.71 Å^3, CO_2: 2.507 Å^3, C_2H_4: 4.18 Å^3).

3.4 Discussion

TDDFT calculations were performed on CO_2 and C_2H_4 following the same protocol as described in the case of N_2 (see Section 3.2). In Figure 3.6, the amplitude of the time-dependent variation of the ionization yield resulting from two-color (NIR and XUV) excitation is plotted for N_2, CO_2 and C_2H_4 as a function of their calculated polarizability tensor components along the molecular axis. As in Figure 3.2 A., molecules aligned along the laser field axis are considered. The monotonically increasing behavior observed illustrates the fact that a higher polarizability leads to a stronger variation of the ionization yield because the electron distribution is localized within the neutral molecule more efficiently, thereby creating a larger screening potential. Please note that the polarizability along the molecular axis is higher for CO_2 than for C_2H_4. If the average polarizability is considered, the order is reversed.

The oscillations measured in the experiment at hand exhibit a maximum oscillation depth in the few percentage range and a period equal to half the period of the NIR field. The amplitudes of the oscillations are smaller than the amplitudes calculated with TDDFT although the NIR intensity in the experiment is roughly two times higher. This could be expected because the molecules in the experiment are not aligned along the laser polarization and the signal measurement involves focal volume averaging.

Comparison of the Figures 3.4 and 3.5 reveals that the modulation of the ionization yield is four times higher if the NIR field-induced charge redistribution was probed by an APT generated in argon gas (cutoff energy $E_{\mathrm{cutoff}} \approx 51\,\mathrm{eV}$) compared to ionization by an APT generated in xenon ($E_{\mathrm{cutoff}} \approx 33\,\mathrm{eV}$). To verify that the modulation depth is a function of photon energy, additional systematic measurements have to be conducted. The TDDFT calculations could not confirm the experimental observation of the dependence of the ionization yield on the photon energy, so far. The reason is that the numerical noise increases with increasing photon energies because the ionization cross-sections (and therefore the signal) decreases for higher photon energies. Nevertheless, a possible explanation for the photon energy dependence of the modulation depth of the ionization cross-section might be given in terms of conservation of momentum and energy. The ionization cross-section increases with decreasing distance between the electron and the atomic cores if the photon energy is sufficient. Additionally, as can be seen in Figure 3.1 C.

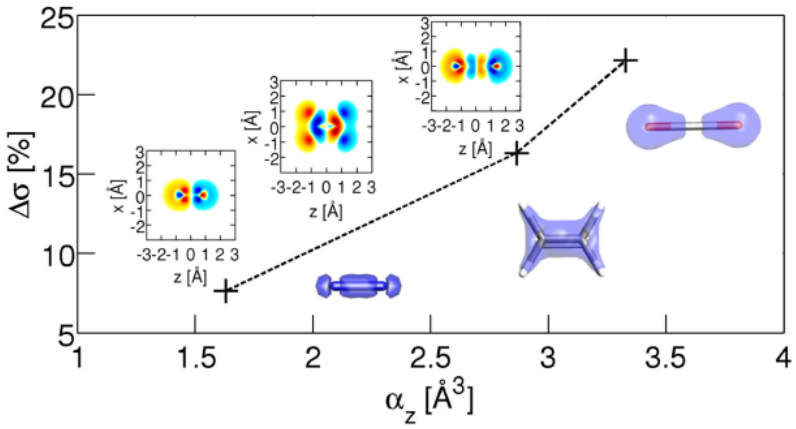

Figure 3.6: TDDFT calculations of the modulation depth of the XUV-induced ionization yield $\Delta\sigma$ of aligned molecules (N_2, CO_2, C_2H_4), as a function of the polarizability tensor components along the molecular axis α_z. The NIR-induced charge displacement increases with the polarizability of the molecule, enhancing the screening effect that leads to the ionization yield variations. The induced change in the electron density at the maximum of the NIR electric field is shown above the data points, while the ground state chemical bonding structure is shown to the right.

the potential variation is the highest close to the nuclei. Therefore, the sensitivity of the XUV radiation on the NIR-induced molecular polarization would increase with increasing XUV photon energy. Indeed, the TDDFT calculations revealed that the mean distance between the positive and negative charges in the molecule undergoes an oscillation that follows the NIR field oscillations. On the other hand, the variation of the mean distance between the electron cloud and the atomic centers is rather small and might not be large enough to explain the observed modulation of the ionization cross-section and therefore also not the measured photon energy dependence of the modulation depth of the ionization cross-section.

In addition to the parent ionization yield also the photo-fragment yield oscillates if the XUV ionization process is accompanied by an infrared field [49, 50]. It could be argued that the parent ion yield fluctuates because the fragment ion is produced more or less efficiently depending on the relative phase between the pump and probe pulses. This would imply that the oscillation of the parent ion yield is out of phase with respect to the fragment ion yield. In fact, consecutive measurements were performed on N_2, which allows for a comparison of the relative phases of N_2^+ and N^+ yields (Figure 3.7). It turned out that both the parent ion yield and the fragment ion yield are oscillating in phase.

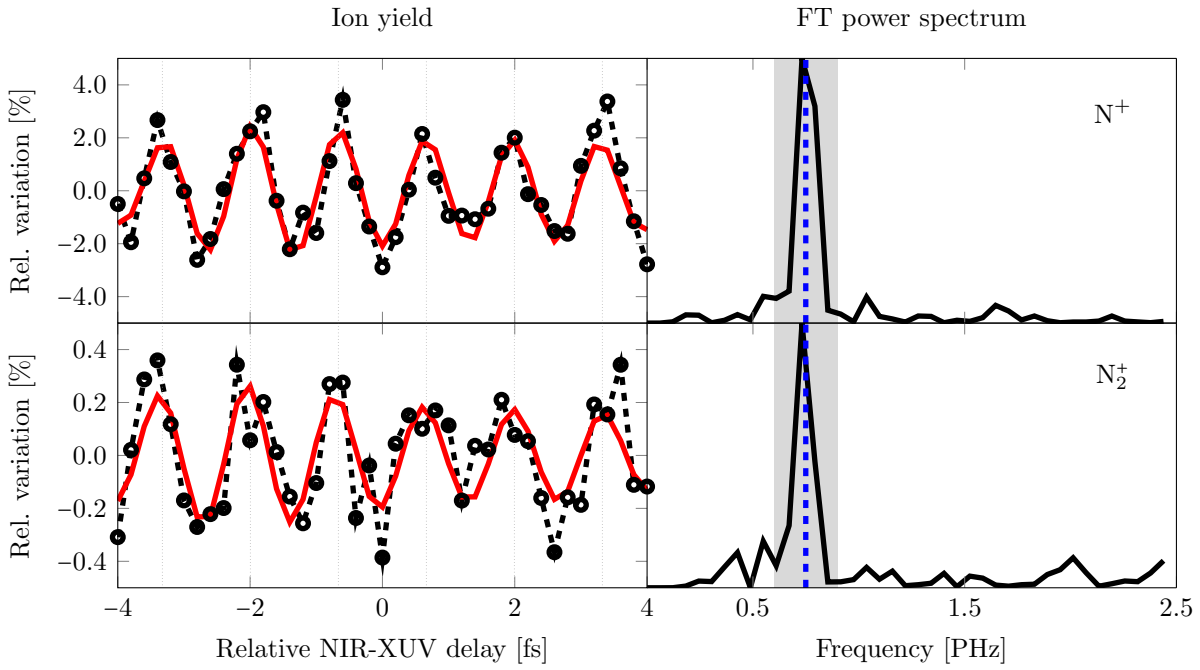

Figure 3.7: N^+ and N_2^+ photo-ion yields of the APT ionization process of the NIR field-dressed N_2 molecule. The black dashed curve represents the sum of consecutively recorded scans. The right panel shows the FT power spectra of the measurements. The blue line indicates the frequency corresponding to half the NIR cycle. The shaded gray area contains the part of the FT power spectrum that is inverse Fourier transformed to obtain the red solid line in the left panel. The oscillations in both data sets show exactly the same phase, i.e., the fragment ion yield, the parent ion yield as well as the total yield is oscillating with twice the driving laser frequency.

Therefore, the modulation of the parent ion yield cannot be caused by a modulation of the fragment ion yield. This is further supported by a measurement recording the signal oscillation stemming from the overall $C_2H_x^+$ progression. A modulation depth of 0.6 % and a relative abundance of the fragment signal (H^+ and CH_x^+) of 3 % with respect to the $C_2H_x^+$ signal was observed (in the case of xenon as the HHG gas). If the fragment signal caused the parent ion signal modulation, the modulation depth of the fragment yields would have been at least as large as 20 % assuming that the $C_2H_x^+$ signals oscillate exactly out of phase and the CH_x^+ signal in phase with respect to the H^+ signal. Modulations as high as 20 % of the fragment ion yields in these types of experiments were never observed in the attosecond laboratories of the MBI and, to the best of my knowledge, were not reported in the literature. The parent ion oscillation that was observed in the present experiment

is therefore not caused by the effect of an oscillatory production of ionic fragments in dissociative photo-ionization experiments.

The aforementioned considerations support the interpretation that the NIR field modulates the probability distribution of the electrons in neutral molecules which can be probed by an XUV APT. The experiment at hand can be regarded as the first example of molecular attosecond Stark spectroscopy. Given that the observed NIR electric field-induced changes in the XUV ionization yield depend on detailed properties of the orbitals involved in the ionization (symmetry, ionization cross-section and polarizability), experiments such as the ones discussed here could be used to completely characterize the polarizability tensors of the states involved, especially when they are carried out with aligned molecules. This goal, as well as the application of the method to more complex systems, will be pursued in the near future.

3.5 Conclusion

It was demonstrated that NIR-driven time-dependent dipoles in neutral molecules can be observed by means of variations of the ionization efficiency by an attosecond XUV pulse train. The effect is understood in terms of a screening of the XUV field by the NIR-induced polarization. The amplitude of the attosecond oscillations is determined by the polarizability tensor of the electronic states involved in the absorption of the XUV light and therefore represents a first implementation of molecular Stark spectroscopy on the attosecond timescale. In future, this approach could not only be used to measure time-dependent molecular polarizability tensors in more complex molecules, but might also allow monitoring of electronic screening and attosecond electronic motion during chemical reactions. Finally, the capability to modulate molecular opacity could find applications in investigations of XUV-induced damage of bio-molecules.

Chapter 4

Photo-dissociation of N_2 influenced on the attosecond timescale

4.1 Introduction

Influencing molecular dynamics on the electronic timescale may provide additional control over the outcome of chemical reactions as compared to established femtochemistry [13]. Kling et al. controlled the direction of ejection of charged fragments in the laboratory frame upon photo-dissociation of molecular deuterium by manipulating the remaining electron in the ion with CEP stable lasers [46]. Belshaw et al. observed ultrafast electron dynamics and their interplay with nuclear dynamics in the ion of the amino acid phenylalanine [43]. Probing the dissociation of molecules with attosecond precision may lead to new insights into the coupled electron-nuclear rearrangements resulting in bond breakage and bond formation.

In the current work, the dissociative photo-ionization of nitrogen molecules is investigated with attosecond time resolution. Nitrogen molecules were exposed to the sequence of an APT and a co-propagating NIR pulse. The N^+ kinetic energy release (KER) spectrum is recorded as a function of pump-probe delay by means of velocity map imaging [155, 156, 178]. Time-dependent oscillations were observed in the vibrational substructures in the KER spectrum, which exhibit complex phase relations as a function of the N^+ kinetic

energy. In conjunction with theory it was found that the origin of this behavior can be attributed to a coupling between attosecond electron dynamics and femtosecond nuclear motion. As a result, the attosecond pump-probe delay controlled the branching ratios in the kinetic energy distribution of the N^+ fragments upon dissociative photo-ionization of molecular nitrogen.

4.2 Experimental

The experimental setup is described in detail in Chapter 2. However, specificities are briefly presented here. The XUV spectrum, resulting from high-order harmonic generation in xenon, spanned an energy range of 15.5 eV centered around 25 eV (harmonics 11 to 21). The duration of the bursts within the attosecond pulse train was determined to be about 300 as (FWHM) using the RABITT technique . The reconstruction is presented in Section 1.4.1.

Temporal and spatial overlap of the XUV APT pump and the femtosecond NIR probe beam was carefully checked by ionization of argon with XUV pulses and streaking of the resulting photo-electrons by the NIR field. In this manner, time zero ($t_0 = 0$ fs) could be determined with an accuracy of ±2 fs. Negative time delays correspond to situations where the NIR pulse precedes the XUV pulse.

N_2^+ potential energy surfaces in the relevant energy range have been reported (see, e.g., [174, 179–182]) and will be presented in the following with respect to the N_2 $X^1\Sigma_g^+$ ground state. The current work focuses on the dynamics of two-color XUV+NIR ionization from the ground state of N_2 ($X^1\Sigma_g^+$) and subsequent dissociation. Relevant potential energy curves and the dissociation limits L_1, L_2, and L_3 of the N_2^+ cation are depicted in Figure 4.1. Low-energy N^+ KER fragments (0.00 – 1.50 eV) resulting from XUV ionization of N_2 mainly stem from the $C^2\Sigma_u^+$- and the $F^2\Sigma_g^+$-state of the molecular cation [174], after dissociation into the L_1 and L_3 continuum, respectively. The L_2 continuum is not reached because a spin-flip would be required.

The N_2^+ cationic states $C^2\Sigma_u^+$ and $B^2\Sigma_u^+$ exhibit the same symmetry resulting in non-adiabatic coupling. Thus, part of the C-state population predissociates via the B-state into the L_1 continuum at 24.29 eV [180]. The spectrum of the resulting N^+ fragments map

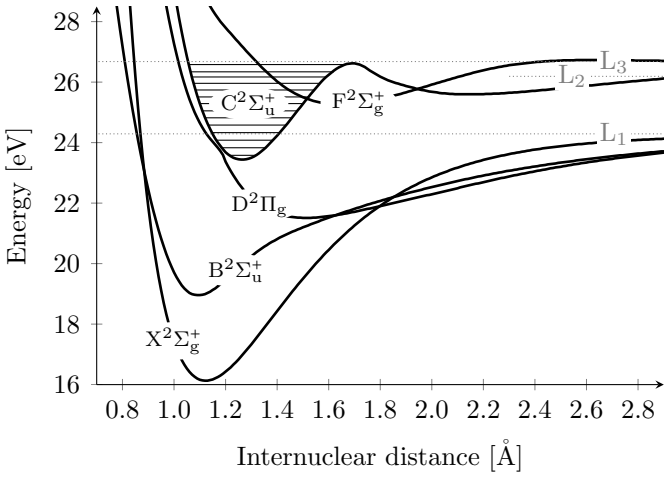

Figure 4.1: Diagram of the N_2^+ potential energy curves in the relevant energy region and the first three dissociation limits L_1, L_2, and L_3. The zero of the energy scale corresponds to the energy of neutral N_2.

the vibrational progression of the C-state up to 1.00 eV (Figure 4.2). The L_1 continuum is energetically just below the vibrational state $\nu = 3$ of the C-state and can be directly excited by photons of the 17$^{\text{th}}$ harmonic ($hf_{\text{HH17}} = 26.35\,\text{eV}$, where f is the harmonic frequency). The molecules can also be dissociated by absorbing a photon of the 15$^{\text{th}}$ harmonic ($hf_{\text{HH15}} = 23.25\,\text{eV}$) and an additional NIR photon ($hf_{\text{NIR}} = 1.55\,\text{eV}$). The lifetimes τ of the predissociative vibrational states of the N_2^+ C-state are $\tau(\nu = 3) \approx 8\,\text{ns}$ and $\tau(\nu \geq 4) \leq 5\,\text{ns}$ [183, 184], much longer than the laser pulse duration. Consequently, most of the expected N_2^+ decomposition occurs after the XUV-NIR pump-probe pulse sequence.

Absorbing a photon of harmonic 19 ($hf_{\text{HH19}} = 29.45\,\text{eV}$) or harmonic 17 and an additional NIR photon leads to population of the F-state and direct dissociation into the L_3 continuum at 26.68 eV [180]. Fragments generated by this process contribute to the broad signal around 1.00 eV in the KER spectrum. This was validated by recording the N^+ KER spectrum when N_2 was ionized by high-order harmonics exhibiting higher cutoff energies [179]. A larger contribution around 1.00 eV was observed due to the increased probability to populate the N_2^+ F-state.

In conclusion, irradiating N_2 molecules using photons with energies below the L_1 continuum results in bound population in the ionic C-state ($\nu < 3$) and lower-lying electronic states. Photon energies in between the L_1 and L_3 dissociation energies lead to predissociation of the C-state population ($3 \leq \nu < 14$) to L_1 via the B-state. If the photon energy is sufficient to reach the L_3 continuum, direct dissociation via the ionic F-state can be observed.

4.3 Results

XUV ionization of molecular nitrogen results in bound population in the ionic Σ_u^+ C-state and several vibrational states are excited within the Franck-Condon region. N_2^+ predissociates via the B-state into the L_1 continuum. The KER spectrum of N^+ fragments after XUV ionization maps the vibrational progression of the $C^2\Sigma_u^+$ state and is plotted in Figure 4.2. In addition, the KER spectrum obtained after XUV ionization in the presence of a non-resonant NIR field is plotted (cycle averaged). Both signals are normalized for better comparison. However, it should be noted that the two-color signals are twice as strong as the one-color signals. The broad contribution around $0.70 - 1.00\,\mathrm{eV}$ shows a stronger enhancement than the signal below $0.70\,\mathrm{eV}$ and the signal above $1.00\,\mathrm{eV}$ but the additional NIR radiation does not influence the structure of the N^+ KER spectrum significantly.

If the KER spectrum is recorded as a function of pump-probe delay between the XUV APT and the NIR femtosecond laser pulse, a clear variation on the femtosecond timescale and distinct attosecond oscillations in the individual energy bands can be observed. A corresponding measurement is shown in Figure 4.3. The data set is angle-averaged and the basis for the following analysis. Within the two dimensional intensity plot, white dashed horizontal lines mark 25 meV wide integration bounds used to determine the time-dependent yield variations of the different energy bands plotted in Figure 4.4. The yield of the bands between $0.38\,\mathrm{eV}$ and $0.83\,\mathrm{eV}$, as well as the overall signal, could be well described by a second-order polynomial function. On the other hand, the yield of the two bands around $0.14\,\mathrm{eV}$ and $0.26\,\mathrm{eV}$ substantially differs from this behavior. Therefore, the time-dependent signals in Figure 4.4 were fitted to a 5^{th} order polynomial to retrieve the time of maximum yield for each energy band individually. The N^+ overall yield reaches its maximum $6 - 8\,\mathrm{fs}$ after the two pulses reach maximum overlap at $t_0 = 0\,\mathrm{fs}$. The individual energy bands behave in a more complicated manner and exhibit strong shifts in their maximum yield with respect to t_0 (Figure 4.4). The lowest band peaks around the maximum pulse overlap ($t_{\max}(0.14\,\mathrm{eV}) = -0.7\,\mathrm{fs}$) while all other bands are shifted to positive delays. This effect is most distinct for the energy band around $0.38\,\mathrm{eV}$, which peaks at $13.7\,\mathrm{fs}$. The temporal shifts of the maximum yield might indicate contributions from sequential pathways during excitation, ionization and dissociation. Another indicator

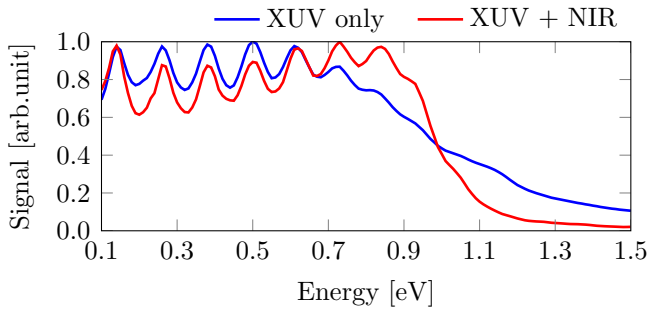

Figure 4.2: Typical N^+ KER spectra when N_2 is ionized by XUV radiation (blue) and when the XUV is accompanied by a moderately strong NIR laser field (red, cycle averaged). The data sets are normalized to their maximum. The relative signal strength (XUV only : XUV+NIR) is 1 : 2. The yield of the N^+ KER fragments exhibits strongest NIR field-induced enhancement for the energy range of 0.70 – 1.00 eV.

for the significance of sequential processes is the pronounced attosecond yield oscillation from the lowest band ($E = 0.14\,\mathrm{eV}$) around 25 fs, well after t_0.

In Figure 4.5 the currently discussed measurement is analyzed in more detail. To compare parallel and perpendicular contributions (with respect to the laser polarization axis), the inverted VMI data within ±25 ° segments parallel (middle column) and perpendicular (right column) to the laser polarization axis is plotted. The lowest row plots the yield, while the central and upper row illustrates the result of a sliding window Fourier analysis showing the modulation depth of the oscillatory part of the signal and its phase, respectively. A detailed description of these plots is presented in the following.

The analysis of the fast oscillating contribution started with an auto-correlation of the signal shown in Figure 4.3, which revealed a modulation frequency of $f_0 = 0.769\,\mathrm{PHz}$ (1.3 fs). This frequency corresponds to twice the frequency of the NIR laser field oscillations. Oscillations at this frequency were analyzed for the angle-averaged signal, the parallel, and the perpendicular contributions separately. In order to retrieve the modulation depth and phases as a function of delay, the polynomial fit in Figure 4.4 was subtracted for each energy, leaving only the rapid oscillating contribution. A sliding temporal window of ≈ 8 fs ($6 \cdot 1.3\,\mathrm{fs}$) was chosen for the Fourier transformation (FT), i.e., at each energy a Fourier transform was calculated for each delay step with a time window width of ≈ ±4 fs. The FT signal was further analyzed for each delay step and energy, by comparing the FT amplitude (modulation depth) A at f_0 to the amplitude average $\bar{A}$ of all other frequencies. The Fourier signal (modulation depth and phase) was taken into account if a pre-defined signal-to-noise condition was met, i.e., $\bar{A}/A(f_0) < 0.1$. I.e., only modulations, of which the

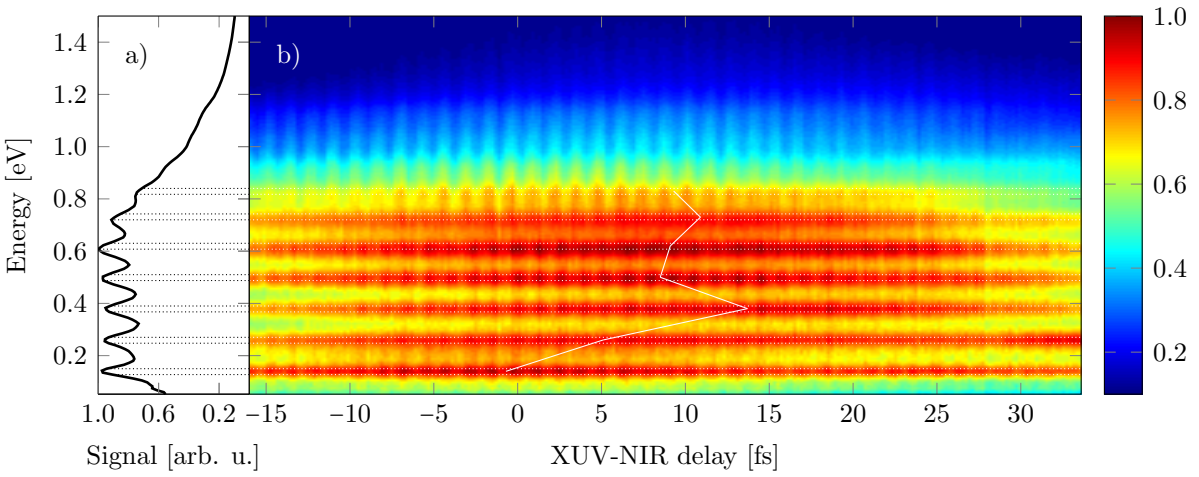

Figure 4.3: Vibrationally-resolved N^+ KER spectrum after dissociative ionization of N_2. Panel a) shows the time-integrated signal of the delay scan plotted in panel b). The vibrational bands exhibit different evolutions as a function of XUV-NIR pump-probe delay on a femtosecond timescale. In addition, the signal clearly shows an attosecond modulation. Time zero was determined by streaking of photo-electrons resulting from XUV ionization of argon. The white solid line indicates the maximum signal of the various energy bands. The black dotted lines in a) and white dashed lines in b) indicate the integration limits ($\Delta E = 25\,\mathrm{meV}$) for the plots in Figure 4.4.

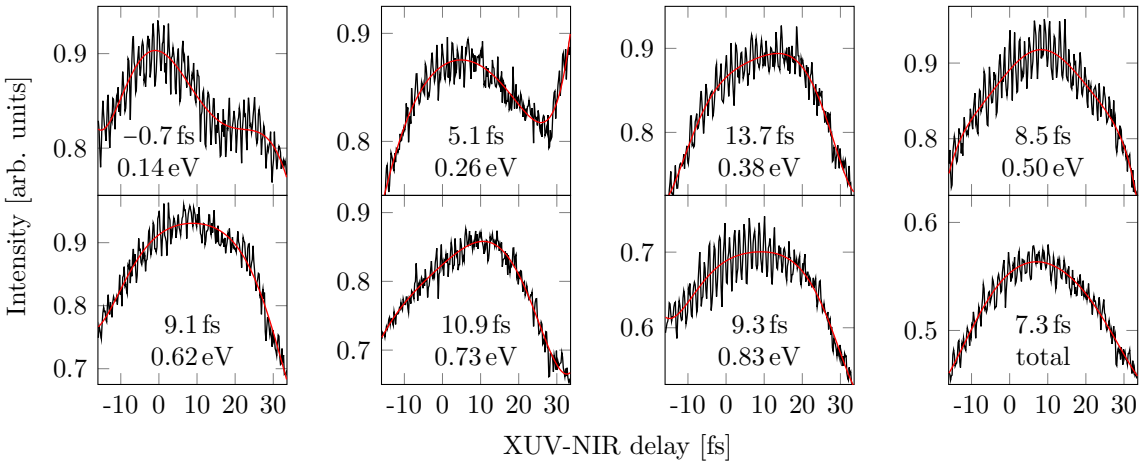

Figure 4.4: XUV-NIR delay dependence of the individual contributions in the N^+ KER spectrum marked in Figure 4.3. The intensity is normalized such that the value of the largest signal in Figure 4.3 is equal to one. The measured data is plotted as solid black curves, while the red line denotes a 5^{th} order polynomial fit. The textual insets show the central energy of the bands as well as their fitted temporal maximum. The width of the integration window is $\Delta E = 25\,\mathrm{meV}$ as in Figure 4.3.

modulation depth is at least as strong as 10 % of the maximum modulation, are taken into account to suppress measurement noise. A numerical issue arises due to the limited time window. The experimental frequency f_0 might be distributed over neighboring points of the frequency grid and its amplitude $A(f_0)$ was therefore interpolated. The phase was calculated as the weighted average of the phases of the contributing frequency components. An alternative approach is to use zero-padding, which gives slightly smoother phases.

The lower row in Figure 4.5 illustrates that the femtosecond dynamics are different for parallel and perpendicular contributions of the signal. While the perpendicular signal peaks around the maximum pulse overlap, the parallel contributions mainly stem from sequential transitions and peak at positive delays ($\tau \approx 25$ fs, XUV before NIR). The band at 0.26 eV seems to peak even after[1] 33 fs, while the lowest band at 0.14 eV exhibits its maximum slightly before the maximum pulse overlap at $\tau \approx -5$ fs.

The overall signal is modulated by about 5 % and the modulation depth in Figure 4.5 (middle panel, left) clearly shows three distinct regions that exhibit an oscillation in the signal, which is stronger than the overall signal modulation. The energy region just below 1.00 eV is strongly modulated, while the band at 0.14 eV shows a somewhat weaker oscillation depth. The third region around 0.50 eV exhibits three modulated bands in the angle-averaged signal, which correspond to the vibrational bands at 0.38 eV, 0.50 eV and 0.61 eV. At maximum pulse overlap, the modulation depth is up to 10 % at 0.83 eV and 6 % at 0.50 eV. These modulations are even stronger if plotted separately for the parallel and perpendicular signals, as can be seen in the middle panel of Figure 4.5.

Analyzing the modulation depth for the perpendicular and parallel contributions separately reveals that the oscillation at 0.14 eV and the oscillation just below 1.00 eV mainly stem from a perpendicular transition. The lowest energy band shows a clear attosecond oscillation in the perpendicular contribution even well after the maximum pulse overlap ($\tau \approx 25$ fs). A parallel character is predominantly found for the oscillations at 0.38 eV, 0.50 eV, 0.61 eV and 0.73 eV. In contrast to all other signals, the modulation depth of the band at 0.50 eV in the parallel signal does not peak at maximum overlap of the two laser pulses but at $\tau \approx 15$ fs.

[1] Data above 33 fs is not available so far due to the outstanding experimental conditions required for attosecond scans with a duration of about ≈ 100 fs. These investigations will be the subject of future work.

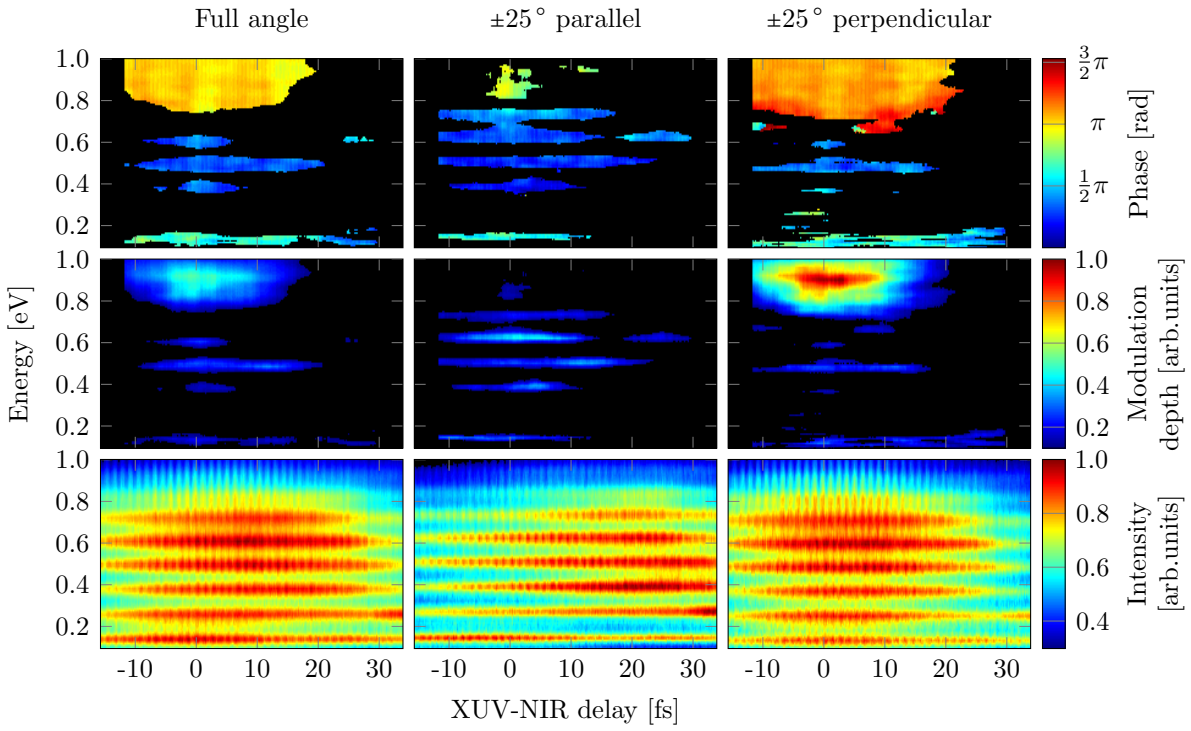

Figure 4.5: Full angle-integrated N^+ XUV-NIR pump-probe signal in comparison to the parallel and perpendicular contributions (lower row), the modulation depths (central row) and phases (upper row) at a frequency of $f_0 = 0.769\,\mathrm{PHz}$ (1.3 fs). Black areas denote regions were the amplitude of the modulation is below the signal-to-noise ratio.

A very interesting feature of the data is revealed by the phase plot in Figure 4.5 (upper panel). The oscillations in the three regions of the angle-integrated data show clear phase jumps with respect to each other. The phase difference between the oscillations at 0.50 eV and 0.90 eV is about $^2/_3\,\pi$, while the phase difference between the oscillations at 0.50 eV and 0.14 eV is about $^1/_3\,\pi$.

Although not discussed further in the theoretical description in Section 4.4, it should be noted here that the oscillation in the band at 0.61 eV reappears at $\tau \approx 25\,\mathrm{fs}$ and exhibits a positive phase shift compared to the phase of the oscillation at the same energy at maximum pulse overlap. By contrast, the oscillation at 0.14 eV and $\tau \approx 25\,\mathrm{fs}$ (perpendicular contribution) shows a negative phase shift with respect to the same oscillation at t_0. This might be a hint to a complex interplay of nuclear and electron dynamics.

For a better comparison the KER spectrum and relative modulation depths are plotted for

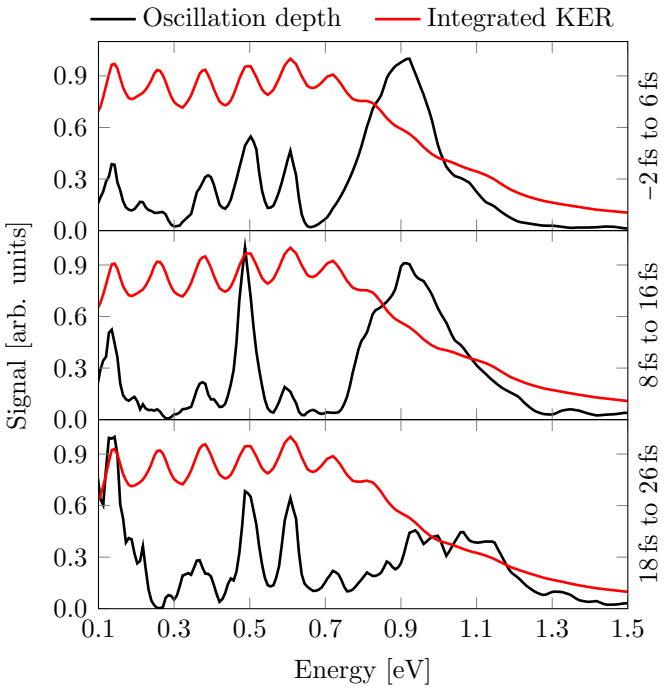

Figure 4.6: Normalized KER spectra (red) and relative oscillation depths (black) as a function of energy for three different time windows within the scan range. The modulation strengths of different regions in the KER spectrum depend on the pump-probe delay, while the spectrum itself undergoes only minor changes.

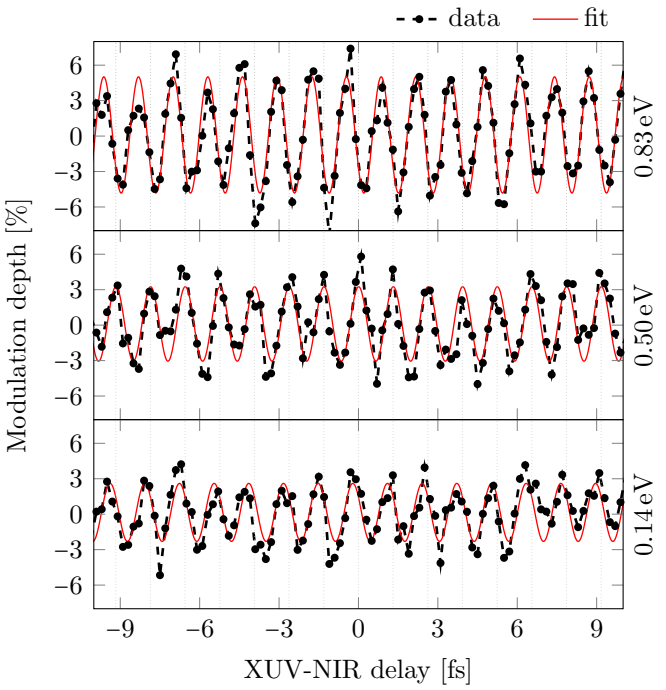

Figure 4.7: Signal oscillations (black) as a function of the XUV-NIR pump-probe delay of three selected regions in the N^+ KER spectrum and sinusoidal fits (red). To guide the eye, the vertical gray dashed lines indicate the 1.3 fs half-cycle period of the NIR field. The yield oscillations are phase shifted with respect to each other and exhibit two prominent phase jumps of about 127° (0.83 eV) and 60° (0.14 eV) each with respect to the oscillation at 0.50 eV.

three different delays (Figure 4.6). A time window of 8 fs was centered at 2 fs, 12 fs and 22 fs. To obtain the KER spectrum, the selected data sets were integrated over the time window. The KER spectra within the selected intervals do not show significant differences. The modulation depths, on the other hand, differ substantially. It turns out that oscillations of the energies around 0.14 eV, 0.50 eV and 0.93 eV exhibit strong modulation at all three instances for the full angle integrated data, but their relative strengths vary. The yield of the lowest energy fragments shows the strongest modulation when the XUV pulse precedes the NIR pulse. In contrast, the modulation for the high-energy region dominates at maximum temporal overlap of the two pulses. The modulation of the mid-energy band exhibits the largest depth just after maximum overlap. Here, the modulation at high-kinetic energies is already significant.

As already seen in Figure 4.5 (upper panel) the phases of the oscillations of the bands are strongly shifted with respect to each other. To illustrate this effect in more detail, Figure 4.7 depicts the oscillations of three bands with the strongest modulation depth around t_0. In order to retrieve the relative phases the data sets were subject to a sinusoidal fit with constant amplitude (red curves in Figure 4.7). The phase of the oscillation of the central band at 0.50 eV was set to be zero. The higher energy band exhibits a phase shift of 127 ° ($\approx 2/3\,\pi$), while the oscillation of the low energy band at 0.14 eV shows a phase shift of 60 ° ($\approx 1/3\,\pi$).

In conclusion, the measurement of the kinetic energy spectrum shows a large background stemming from predissociation of the N_2^+ C-state ($\nu \geq 3$) to the dissociation limit L_1 and direct dissociation of the F-state to the dissociation limit L_3 (Figure 4.8). On top of this signal, an oscillatory behavior could be observed as a function of APT XUV pump-femtosecond NIR probe delay. The oscillation period equals half the period of the NIR field. Large phase shifts of these oscillations as a function of energy could be observed as well as varying relative modulation depths as a function of delay.

In order to shine light on the femtosecond dynamics and the attosecond oscillations, a series of calculations have been performed taking several direct and sequential two-photon pathways into account. The calculations will model the dissociative ionization of N_2 ionized by an attosecond XUV pulse train accompanied by a moderately strong NIR field.

4.4 Theoretical description

The calculations presented in this section were developed and carried out in the group of Prof. Misha Ivanov (Max-Born-Institut, Berlin and Imperial College, London) by Lukas Medišauskas in close collaboration with the author. Potential energy surfaces and dipole coupling strengths were calculated by Dr. Serguei Patchkovskii (National Research Council, Ottawa) and Dr. Alex Harvey (Max-Born-Institut, Berlin). The Results were published in 2015 [185].

Oscillations as observed in the measurement originate from interferences of indistinguishable quantum pathways. Let $a\mathrm{e}^{-\mathrm{i}\phi_a(t)}$ and $b\mathrm{e}^{-\mathrm{i}\phi_b(t)}$ be the time-dependent and complex probability amplitudes for a quantum system to evolve from an initial state $|i\rangle$ to a final state $|f\rangle$ via two different possible paths A and B. Here a molecular two-color photoionization experiment with an XUV and an accompanying NIR laser pulse is considered. Let pathway A involve the absorption of a harmonic photon (harmonic number $n+1$, where n is an even integer) and emission of a NIR photon. Pathway B shall involve the absorption of another harmonic photon (harmonic number $n-1$) and an additional absorption of a NIR photon. Both pathways might involve dynamics in the molecular ion, where an additional molecular phase ϕ_a^{mol} and ϕ_b^{mol} is acquired, respectively. Thus, the resulting phases of the pathways are $\phi_a(t) = (n+1)\omega t - \omega(t+\delta t) + \phi_a^{\mathrm{mol}} + \phi_a^{\mathrm{e}^-}$ and $\phi_b(t) = (n-1)\omega t + \omega(t+\delta t) + \phi_b^{\mathrm{mol}} + \phi_b^{\mathrm{e}^-}$, where $\phi_a^{\mathrm{e}^-}$ and $\phi_b^{\mathrm{e}^-}$ are the phases of the departing electron acquired during ionization and δt is the delay between the harmonics and the NIR field oscillations with frequency ω. The probability to detect the system in the final state is then given by

$$\langle f|f\rangle \approx \left|a\mathrm{e}^{-\mathrm{i}\phi_a(t)}|i\rangle + b\mathrm{e}^{-\mathrm{i}\phi_b(t)}|i\rangle\right|^2. \tag{4.1}$$

Equation (4.1) can be expanded to

$$\begin{aligned}\langle f|f\rangle &\approx a^2 + b^2 + ab\mathrm{e}^{-\mathrm{i}(\phi_a(t)-\phi_b(t))} + ab\mathrm{e}^{-\mathrm{i}(\phi_b(t)-\phi_a(t))} \\ &= a^2 + b^2 + 2ab\cos\left(\Delta\phi_{ba}\right),\end{aligned} \tag{4.2}$$

where $\Delta\phi_{ba} = \phi_b(t) - \phi_a(t) = 2\omega\delta t + \Delta\phi_{ba}^{\mathrm{mol}} + \Delta\phi_{ba}^{\mathrm{e}^-}$. Thus, the interference of the quantum pathways A and B creates an oscillation of the final state probability as a function of time

delay δt with twice the frequency of the NIR electric field. In addition, the phase of this interference with respect to the NIR field encodes the ionization phase and the molecular phase of the states involved.

In the case at hand, N_2 molecules are ionized to N_2^+ by XUV photons accompanied by a NIR laser field. The ion dissociates to N and N^+ fragments, and the KER spectrum of the N^+ fragments is recorded. The spectrum resembles the $C^2\Sigma_u^+$ vibrational distribution of N_2^+ and the N^+ fragments therefore stem from the L_1 dissociation limit (Figure 4.1). Hence, the common initial state of the interfering pathways is the ground state of the N_2 molecule and the final state is comprised of the kinetic energy of the N^+ fragments and their internal quantum state determined by the N_2^+ dissociation limit. The final state also involves the energy and angular momentum of the continuum electron, which are not measured here. In order to result in interferences the energy and angular momentum of the continuum electron, the internal final state as well as the kinetic energy of the fragments resulting from different pathways must be equal.

In Figure 4.5 it can be seen that the oscillations between 0.3 eV and 0.7 eV are strongest for the parallel part in the KER spectrum and the oscillations below 0.2 eV mainly stem from the perpendicular contribution in the KER spectrum. In addition, the oscillations in the higher energy region are strongest near the XUV-NIR pulse overlap, while the oscillations in the low-energy region are most pronounced at positive delays (Figure 4.6). Therefore, the higher kinetic energy fragments seem to be produced by direct two-photon transitions, while the pathways leading to low kinetic energy fragments incorporate a sequential process.

Possible interfering ionization and dissociation pathways leading to the aforementioned oscillations in the KER spectrum are depicted in Figure 4.8. The left panel shows the parallel contribution with pathways ② and ④, while the perpendicular contribution with pathways ① and ③ is drawn in the right panel.

The parallel contribution (Figure 4.8, left panel) may originate from two interfering XUV±NIR two-photon ionization pathways from the N_2 ground state $X^1\Sigma_g^+$ to the N_2^+ $C^2\Sigma_u^+$ state, namely HH17 ionization to the N_2^+ $X^2\Sigma_g^+$ state and subsequent absorption of a NIR photon (pathway ②) and HH19 ionization to the N_2^+ $F^2\Sigma_g^+$ state and subsequent emission of a NIR photon (pathway ④). Both pathways lead to predissociation of the

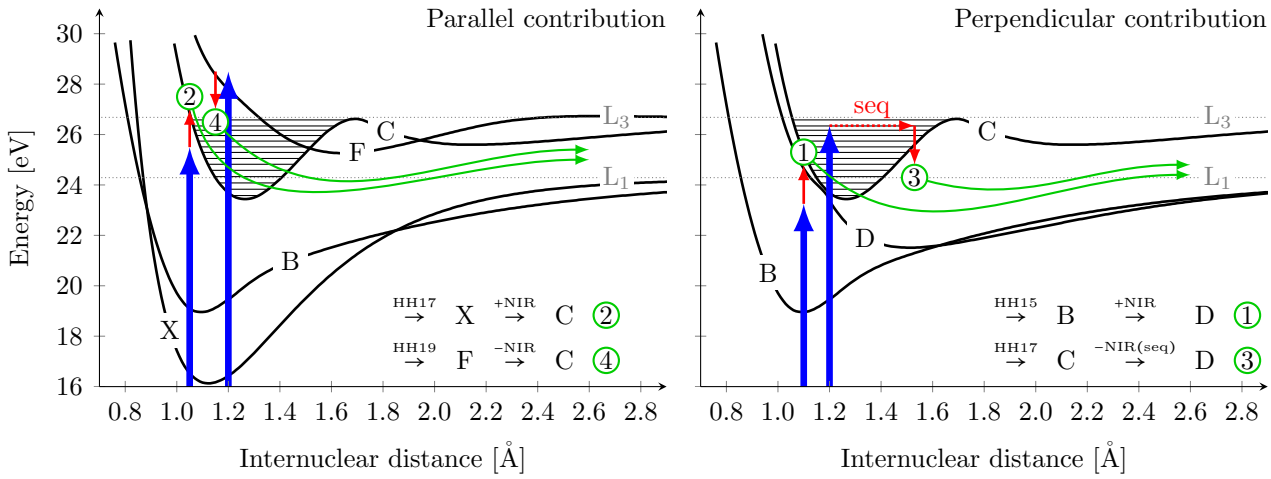

Figure 4.8: Selected N_2^+ potential energy surfaces and dissociation pathways resulting in interferences leading to the observed time-dependent yield variation of N^+ fragments in the recorded KER spectra. Left panel: The parallel contribution stems from direct two-photon ionization (HH17+NIR and HH19-NIR) of the N_2 $X^1\Sigma_g^+$ ground state to the N_2^+ $C^2\Sigma_u^+$ state. The resulting wavepackets (green) propagate to the dissociation limit L_1 and result in interfering N^+ KER fragments around 0.5 eV. Right panel: The perpendicular contribution results from a direct two photon ionization (HH15+NIR) of the N_2 $X^1\Sigma_g^+$ ground state to the N_2^+ $D^2\Pi_g$ state and a one-photon ionization (HH17) of the N_2 $X^1\Sigma_g^+$ ground state to the N_2^+ $C^2\Sigma_u^+$ and a sequential transition by emission of a NIR photon also to the N_2^+ $D^2\Pi_g$ state. The resulting wavepackets (green) propagate to the dissociation limit L_1 and result in interfering N^+ KER fragments below 0.2 eV.

N_2^+ $C^2\Sigma_u^+$ state to the dissociation limit L_1, where they interfere and oscillations in the $C^2\Sigma_u^+$ vibrational structure are measurable in the KER spectra around 0.5 eV. The process described here, is known from molecular RABITT experiments [49].

The perpendicular contribution (Figure 4.8, left panel) may stem from interfering direct and sequential two-photon processes. In the direct case, N_2 is ionized from the $X^1\Sigma_g^+$ ground state to the N_2^+ $D^2\Pi_g$ state via HH15 ionization to the N_2^+ $B^2\Sigma_u^+$ state and subsequent absorption of a NIR photon (pathway ①). In the sequential case, HH17 ionization to the N_2^+ $C^2\Sigma_u^+$ state occurs. The launched vibrational wavepackets now propagate on the PES and can be promoted after a certain time to the N_2^+ $D^2\Pi_g$ state by emission of a NIR photon (pathway ③). Both pathways lead to dissociation via L_1 and result in interfering N^+ KER fragments below 0.2 eV.

In order to verify that the proposed pathways could be responsible for the interferences,

numerical calculations were performed by solving the time-dependent 1D Schrödinger equation. Several vibrational wavepackets were propagated along the potential energy surfaces (PES) of N_2^+. In the calculations only the ionization and dissociation pathways for wavepackets emerging from two-photon transitions were taken into account. Higher-order processes are less probable and will not lead to $2\omega_{NIR}$ oscillations. Pathways resulting from XUV-only dissociation are not considered, since the final states of the electron and the ion from different pathways need to be identical in order to result in an interference.

The PES and dipole couplings between the states were obtained from CAS (complete active space[2]) calculations using *GAMESS* [188, 189] and the *Molpro* quantum chemistry packages [190, 191]. Wavepacket propagations were performed using the split-operator FFT method [192]. Couplings between potential energy surfaces induced by the NIR field were explicitly included, such that the propagation was carried out on laser-coupled potential energy surfaces. The ionization by the attosecond XUV pulse train was accounted for by starting the propagation from Franck-Condon wavepackets in ionic states. Direct two-photon transitions were simulated by promoting the initial wavepacket on an intermediate (virtual, X and B) state populated by absorption of the first (harmonic) photon. This way, the sudden switch-on of the field, once the calculation has started, effectively simulates the transition and captures the correct phase acquired from the NIR field. As each burst in an attosecond pulse train creates vibrational wavepackets, these wavepackets were added up coherently for each final photo-electron energy to obtain the correct signal. The final signal was obtained by integrating over all the photo-electron energies.

The pulse parameters were chosen similar to the ones applied in the experiment. The NIR pulse was centered at 780 nm, its pulse duration was 30 fs and the intensity was $10^{13}\,\mathrm{W/cm^2}$. The spectral width of the APT was about 13 eV centered around harmonic 15. An envelope function was used to limit the APT duration to 15 fs FWHM.

The simulations reveal that the four two-photon pathways, depicted in Figure 4.8, are of comparable strength and can interfere. The result of the calculation is shown in Figure 4.9. The upper panel shows the KER when the different pathways are summed incoherently, while the lower panel presents the outcome of the simulation when the pathways add

[2]More precisely: A CASSCF-MRCISD procedure (**C**omplete **A**ctive **S**pace **S**elf-**C**onsistent **F**ield **M**ulti-**R**eference **C**onfiguration **I**nteraction method including **S**ingle and **D**ouble excitations) [186] with an aug-ccp-VTZ Gaussian basis [187] was used.

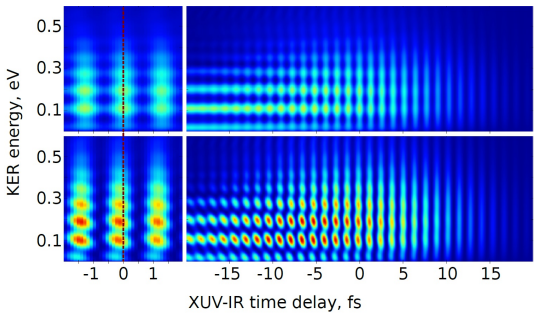

Figure 4.9: Simulated N^+ KER spectrum after dissociative ionization of N_2 by an APT accompanied by a femtosecond NIR field. The oscillations originate from an interference of a direct and a sequential two-photon dissociation pathway. The upper panel shows the incoherent sum, while the lower panel shows the coherent sum of the two pathways. Large phase differences of the oscillation are only visible in the coherent case. Note that the definition of the time arrow is reverse to that used in the experimental section.

up coherently. In this case, the phase of the oscillations in the delay scan as a function of energy is non-trivial and differs strongly from the incoherent case, were the phase is kinetic energy-independent. The calculations show that a coherent sum of direct and sequential transitions leads to large phase differences as observed in the experimentally obtained KER spectrum. This supports the notion that the experimental KER spectra depend on the phase of the photo-electron, acquired during ionization and the phase of the vibrational wavepacket accumulated during propagation to the dissociation limit.

The interpretation is also supported by two other aspects: (1) The calculations show that a coherent sum of the considered pathways leads to slightly shifted maxima of the energies in the KER spectrum [185]. Indeed, the experimental data show that the maximum modulation does not exactly coincide with the maxima of the KER spectrum (Figure 4.6). (2) The maximum modulation is not centered around maximum pulse overlap but is shifted to positive time delays. This effect is clearly visible in the simulated spectrum (Figure 4.9) as well as in the measured modulation amplitude (Figure 4.5).

4.5 Summary and conclusion

XUV APT pump-femtosecond NIR probe experiments on the dissociative ionization of N_2 resulted in a mixture of femtosecond and attosecond dynamics observed in the KER spectrum of N^+ fragments. The femtosecond dynamics give rise to an involvement

of sequential pathways accompanied by direct two-photon transitions. On top of the background signal, which can partially be explained by predissociation of the N_2^+ C-state population, oscillations of the N^+ fragment yield were observed in the KER spectrum as a function of pump-probe delay. The individual oscillations of the energies associated with the vibrational distribution of the N_2^+ C-state exhibited large phase shifts as a function of energy, which cannot be explained by RABITT-like processes. The computational analysis showed that these oscillations could be partially explained by an interference of a direct and a sequential photo-dissociation pathway. In this case, the initial electronic phase acquired during ionization can significantly influence the outcome of the molecular decomposition. Therefore, the results can be interpreted as an implementation of attosecond control to a chemical dissociation reaction in a molecular multi-electron system.

Part II

Short pulse laser fragmentation of biomolecules

Chapter 5

Sequence elucidation of peptides

Mass spectrometry is not only used in the field of proteomics [193, 194], but also for chemical, biological and environmental sciences. The technique is exploited to identify and characterize drugs [195], doping substances in sports [196, 197], and other biologically relevant molecules, including peptides and pollutants [193].

Physical methods for ionization and fragmentation (*activation*) lie at the heart of mass spectrometric analysis. Novel activation methods may extend the reach of mass spectrometry in particular in the field of proteomics [198]. The work described here explores intense femtosecond near-infrared laser light pulses as a possible activation tool. High power lasers were first coupled to FT MS instruments in 1984 by Bowers et al. [199]. Since then, a variety of experiments investigating biological samples based on photo-induced fragmentation were reported [200, 201]. So far, no experiments were conducted using near-infrared femtosecond lasers in combination with high mass-resolving and high-accuracy analyzers, e.g., *Fourier transform mass spectrometers* (FT MS).

Intense and ultrashort pulse laser sources may be a well-suited activation tool as the radiation easily ionizes molecules (charging capability) [202]. Such an activation may be highly non-linear and non-adiabatic, depositing a large amount of energy in the molecules. Furthermore, the short pulse duration may favor localized reactions that occur before electron-nuclear energy redistribution processes. Resulting fragmentation and ionization processes can create multiply-charged fragments, which may facilitate structure elucidation

of large peptides and proteins. Whether *femtosecond laser-induced dissociation* (fs-LID) creates a sufficient number of protein fragments to allow primary structure elucidation of peptides [203] is an open question that will be addressed in this work.

Excitation and ionization of peptides by femtosecond laser radiation also raises interesting questions about physical processes in large molecules. Is the non-resonant interaction process localized or does the laser interact with the whole molecule? Is the laser-molecule interaction of adiabatic (ergodic fragmentation) or non-adiabatic (non-ergodic fragmentation) nature? In which intensity regime (MPI, Tunneling, Over-the-barrier) do the processes occur? Is the fragmentation/ionization process of sequential nature, i.e., is a single laser pulse sufficient to induce the observed processes? How does the coupling of electronic and nuclear degrees of freedom influence the fragmentation?

Optically-induced charge transfer processes in small peptides cause site-specific charge-driven cleavages [29, 30]. These processes play an important role in biological reactions but also in the degradation of biological matter. Characterization of charge-driven reaction pathways is therefore of fundamental interest to chemistry and biology. Combining ultrashort laser pulse sources with FT MS instruments is a prerequisite to extend charge transfer investigations to large species. The work presented here may therefore also be considered as a step towards such studies and towards related time-resolved measurements. The experimental setup developed during the course of this thesis would also allow pulse shaping experiments on peptides and proteins to establish a pulse shape database for site-specific fragmentation. Experiments of this kind were already started for amino acids [204, 205].

Some experimental issues have to be addressed before the scientific questions mentioned above can be resolved. Is it possible to couple intense femtosecond laser sources with available FT MS instruments without major reconstructions? Can fs-LID produce enough signal, i.e., is the cross-section for photo-chemical processes large enough? For applications in biology it is also important to maximize the information content of fs-LID fragmentation spectra: What parameters can be used in an fs-LID proteomic experiment to tailor the fragmentation character?

All these questions will be addressed in Part II of this thesis. A summary of the answers found and a detailed discussion is presented in Section 6.3.

5.1 Fourier transform ion cyclotron resonance mass spectrometers

For primary structure elucidation of proteins and peptides, it is essential to assign the fragments generated by activation with high confidence. Therefore, the mass spectrometer must provide outstanding mass resolution and mass accuracy. Fourier transform mass spectrometer (FT MS) instruments are widely employed in modern mass spectrometric studies [206]. The most common FT MS is the Fourier transform ion cyclotron resonance (FT-ICR) mass spectrometer [207]. As in all Penning traps, charged particles can be stored (trapped) for a long time, which allows for highly accurate measurements. The physical principle of ICR spectrometers was already described in 1932 by Lawrence et al. [208]. They derived the frequency for the motion of a charged particle in a magnetic field with a field strength B, the so-called angular cyclotron frequency

$$\omega_c = \frac{zB}{m}, \tag{5.1}$$

which is inversely proportional to the mass/charge ratio (m/z) of the charged particle. Therefore, ICR instruments allow to measure masses of charged particles in a known charge state by measuring the cyclotron frequency. Spinning ions in a magnetic field induce oscillating image currents in detector plates. The frequency of the image current can be precisely measured and delivers mass information with unrivaled accuracy.

After Lawrence's early experiments, the technique evolved rapidly. The *omegatron* used radio frequencies to resonantly extend the particle orbits, such that the ions hit a charge collector device [209]. The signal-to-noise level could be improved by modulating experimental parameters, resulting in a modulation of the signal with a known frequency (pulsed operation) [210]. The Fourier-transform type ICR spectrometer was introduced by Marshall and coworkers [211]. They presented the FT-ICR technique in combination with a frequency-sweep excitation scheme. The excitation frequency is consecutively resonant with the cyclotron frequencies of a broad band of ions of various m/z values. Therefore, the different species in the ICR cell are consecutively excited into larger cyclotron orbits. This allows the detection of a broad band mass range [212] in a single excitation step. In 1983, Allemann et al. used a superconducting magnet as the magnetic field source. A field

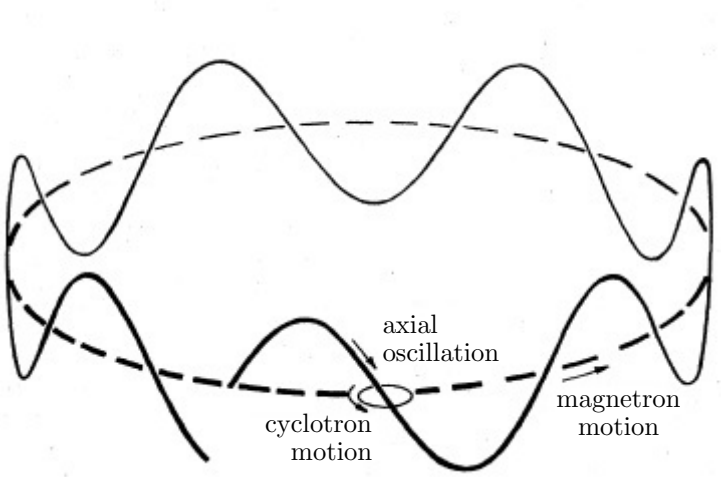

Figure 5.1: Illustration of the three different types of motion in a Penning trap. The axial motion is an oscillation along the laser propagation axis (x-direction) and the magnetic field lines. The bi-circular cyclotron and magnetron motion is located in a plane perpendicular to the magnetic field lines. Figure adapted from [213].

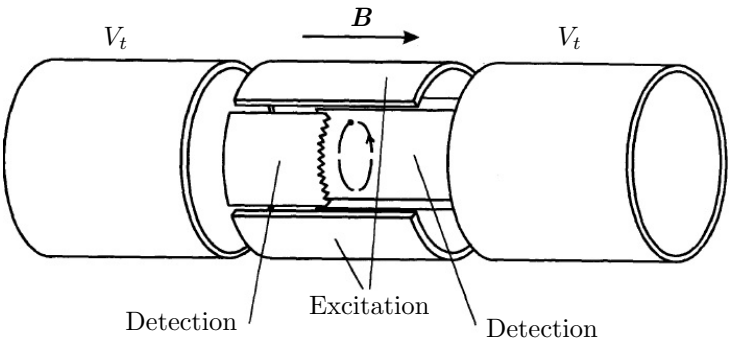

Figure 5.2: Illustration of the ICR cell geometry used in the experiments at hand. The indicated circular motion within the cell corresponds to the magnetron orbit. Note that the B field is rotated 90° with respect to the B field in Figure 5.1. Figure adapted from [214].

strength of up to 4.7 T allowed measurements with the highest mass resolution ($m/\Delta m > 10^5$ at $m/z = 866\,\mathrm{u/e}$) obtained at this time.

Once trapped, the molecules translate back and forth in the cell in a region of constant magnetic field $\boldsymbol{B} = (B, 0, 0)$ on the central spectrometer axis (x-direction). In addition to the trapping oscillation, the ions also perform a fast cyclotron (Equation 5.1) and a slower magnetron bi-circular motion due to the Lorentz force that they encounter in the $\boldsymbol{B}$-Field [213]. This three-fold motion is depicted in Figure 5.1.

The cyclotron motion of charged particles, with angular frequency ω_c, is solely due to the magnetic field, as can be seen from Equation 5.1. The magnetron motion is caused by the fact that magnetic and electric fields are used to store charges in three dimensions. The trapping electric field is such that the particles oscillate harmonically back and forth between the trapping electrodes, i.e., the potential ϕ along the x-direction

is quadratic in x. From Maxwell's equations in vacuum (see, e.g., [81]), it is known that $\nabla \boldsymbol{E}(x,y,z) = -\nabla(\nabla\phi(x,y,z)) = 0$. In order to fulfill $\nabla^2\phi(x,y,z) = 0$ for a harmonic potential in the x-direction, the electric field has to contain a radial component E_r, with $r = \sqrt{y^2 + z^2}$. This component leads to the so-called $\boldsymbol{E} \times \boldsymbol{B}$ drift, which shows up as the magnetron motion in Figure 5.1. Solving the classical equation of motion [213] reveals two eigenfrequencies of the system

$$\omega_{\pm} = {}^1\!/_2 \left[\omega_c \pm \sqrt{\omega_c^2 - 2\omega_t^2} \right], \tag{5.2}$$

where

$$\omega_t = \sqrt{{}^{q\alpha}\!/_m} \tag{5.3}$$

denotes the angular trapping frequency, with $\alpha = \text{const}$ describing the trapping parameters such as trapping voltage (V_t), the dimension of the trap, and its geometry. Many different cell geometries are available today [215]. The smaller frequency in Equation 5.2 is the magnetron frequency $\omega_- = \omega_m = {}^{\omega_t^2}\!/_{2\omega_+}$, while the larger frequency is the reduced cyclotron frequency $\omega_+ = \omega_c - \omega_m$. While the cyclotron frequency leads to a spinning motion around a magnetic field line, the magnetron frequency moves the ions around the cell center.

The superposition of the axial and the bi-circular motion leads to a cigar-shaped ion cloud during storage [216]. The exact dimensions and position of the ion cloud prior to excitation depends on various experimental parameters, e.g., injection time, injection angle, a possible axis offset or skew, and the initial ion kinetic energy. Barlow et al. determined the influence of these parameters [217] by using a non-commercial spectrometer. The authors found the axial extensions of the cloud prior to excitation to be about 10 % of the cell length and the ratio of this extension with respect to the cloud diameter to be about 25.

The activation of trapped ions creates a variety of fragments. The cyclotron radii of these fragments are subsequently excited to a few centimeters. During excitation, the cyclotron radius exceeds the magnetron radius and fragments of equal mass/charge-ratio are bunched in the yz-plane, while the ion cloud stays extended in the x-direction [218]. The extended cyclotron motion now induces an ac voltage in the detector plates. The recorded modulated signal is called *free induction decay* (FID) and its Fourier transform

is proportional to z/m (Equations 5.1, 5.2 and 5.3) and provides the mass measurement.

The advantage of FT-ICRs over other mass spectrometric devices, such as Wiley-McLaren type Time-of-Flight (ToF) spectrometers [219] or conventional Penning traps, is their high mass resolution and accuracy for a wide mass/charge range[1]. Frequency-based mass measurements (FT-ICR, Orbitrap) deliver the most accurate wide-range fragment mass determination available today. The mass accuracy $\frac{|m_{exp}-m|}{m}$ of frequency measurement-based spectrometers is nowadays on the order of 10^{-6} (ppm, parts-per-million). FT-ICRs also allow to resolve the isotopic progressions for a large range of mass peaks [195, 206]. The resolution $R = m/\Delta m$ can exceed 10^6. Fragments with masses[2] of about 10^4 u differing by only one proton or one neutron ($m = 1$ u) are distinguishable. Resolved isotope progressions allow to determine the charge states of the fragments in FT MS spectra: Assuming a charge state of $z = 10$, an isotope progression is expected with a difference in mass/charge ratio for adjacent isotopic peaks of

$$\frac{m_2}{z} - \frac{m_1}{z} = \frac{1\,\mathrm{u}}{z} \overset{\text{exp.}}{=} 0.10\,\mathrm{u/e}. \tag{5.4}$$

Resolving such an isotope progression therefore allows a mass assignment with high confidence.

5.2 Peptide structure and nomenclature

Peptides are composed of amino acids. Several hundred amino acids are known [221]. Only a minority of amino acids, called *proteinogenic* amino acids are found in proteins of organisms. Most organisms encode 20 proteinogenic amino acids in their DNA. These *canonical* amino acids are tabulated in Table 5.1.

Canonical amino acids are α-amino acids. They contain a carboxyl group, -COOH, an amino (or amine) group, -NH_2, and a specific side chain, R. The different structural parts of amino acids are indicated by colored rectangles in Figure 5.3. The bond between the carboxyl carbon and the carbon atom bearing the side chain (C_α) is called α-bond. The side

[1] Sophisticated versions of ToF analyzers can also reach a high mass-resolving power [220], with the advantage of detecting even large analytes (protein-protein complexes, DNA etc.)

[2] Atomic mass unit: $1u = 1.66 \cdot 10^{-27}$ kg.

Canonical amino acid	Composition (-H_2O)	Residue mass [u]	3-letter code	1-letter code	SC character	Rel. PA
Alanine	C_3H_5NO	71.03711	Ala	A		0.85
Arginine	$C_6H_{12}N_4O$	156.10111	Arg	R	Guanidyl	1.00
Asparagine	$C_4H_6N_2O_2$	114.04293	Asn	N	Amide	0.92
Aspartic acid	$C_4H_5NO_3$	115.02694	Asp	D		0.86
Cysteine	C_3H_5NOS	103.00919	Cys	C		0.86
Glutamic acid	$C_5H_7NO_3$	129.04259	Glu	E		0.93
Glutamine	$C_5H_8N_2O_2$	128.05858	Gln	Q	Amide	0.89
Glycine	C_2H_3NO	57.02146	Gly	G		0.84
Histidine	$C_6H_7N_3O$	137.05891	His	H	Aryl	0.95
Isoleucine	$C_6H_{11}NO$	113.08406	Ile	I		0.89
Leucine	$C_6H_{11}NO$	113.08406	Leu	L		0.87
Lysine	$C_6H_{12}N_2O$	128.09496	Lys	K		0.95
Methionine	C_5H_9NOS	131.04049	Met	M		0.89
Phenylalanine	C_9H_9NO	147.06841	Phe	F	Aryl	0.88
Proline	C_5H_7NO	97.05276	Pro	P		0.88
Serine	$C_3H_5NO_2$	87.03203	Ser	S		0.86
Threonine	$C_4H_7NO_2$	101.04768	Thr	T		0.88
Tryptophan	$C_{11}H_{10}N_2O$	186.07931	Trp	W	Aryl	0.88
Tyrosine	$C_9H_9NO_2$	163.06333	Tyr	Y	Aryl	0.88
Valine	C_5H_9NO	99.06841	Val	V		0.87

Table 5.1: Canonical amino acids and their molecular composition. The compositions and the mono-isotopic mass of the amino acids are tabulated assuming the loss of a water molecule. Amino acids containing photo-active side chains (SC) are labeled. The proton affinity (PA) values stem from the NIST webpage and are presented relative to that of Arginine (1051 $^{kJ}/_{mol}$). The 1-letter code will be used in the following sections.

chain determines the physical and chemical characteristics of the amino acid. Particularly interesting for this work is the photo-activity of the peptides, which is enhanced if the

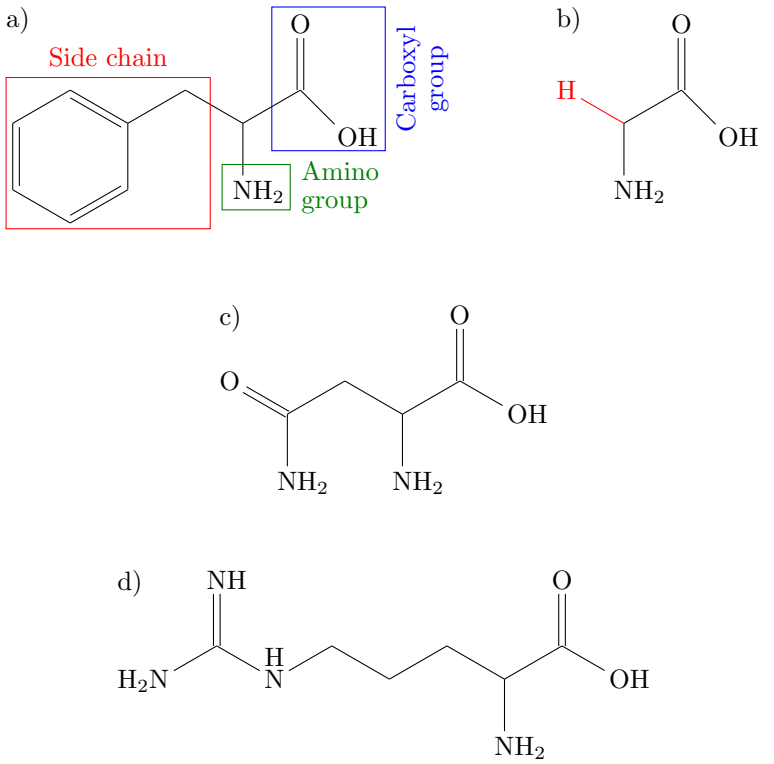

Figure 5.3: Chemical structure of four selected amino acids. Amino acids are composed of a carboxyl group (blue box), an amino group (green box) and a side chain (red box). The latter is determining the specific properties of the amino acid. a) Structure of phenylalanine, which contains an aryl group (aromatic chromophore) in the side chain. b) The smallest amino acid glycine, where the side chain is a single hydrogen atom. c) Asparagine containing an amide group (-$CONH_2$), and d) arginine with a guanidyl side chain (-$NHCNHNH_2$).

side chain bears an aryl group[3]. Phenylalanine (F, Figure 5.3 a)) contains an aryl group in its side chain and is one of four amino acids with photo-activity in the near-ultraviolet spectral region (the others are H, W, Y, see Table 5.1). Glycine is the smallest amino acid with a hydrogen atom forming the side chain (Figure 5.3 b)). Asparagine is one of two (N, Q) amino acids which contain an amide group (-$CONH_2$), as shown in Figure 5.3 c). Arginine contains a guanidyl group (-$NHCNHNH_2$) in its side chain (Figure 5.3 d)) and is easily protonated due to its large proton affinity. A similar behavior is found for lysine (K) [222]. As can be seen in Table 5.1, F, N, Q, and E also have large proton affinities but smaller than that of R and K. Among amino acids exhibiting the smallest proton affinities are D, S, and L.

Amino acids form peptides in a condensation reaction, i.e., by release of a water molecule[4] [223]. Peptide formation was observed for the first time in 1901 by Fischer et al. for the smallest peptide glycine-glycine [224]. Amino acids are covalently bound via peptide

[3] An aryl group is a chemical compound that contains an aromatic ring system.

[4] The tabulated amino acid masses already assume the loss of an H_2O molecule to simplify the calculation of peptide masses and their fragments.

bonds between adjacent amino acids. The amino acids thereby form a peptide backbone H_2N-CHR-CO-NH-CHR-COOH with the NH_2 amino group at the so-called *N-terminus* (or *N-terminal*) and the COOH carboxyl group at the *C-terminus* (or *C-terminal*) as depicted in Figure 5.4.

The structure of peptides can be divided in sub-categories. The tertiary structure denotes the global shape of a peptide. Many adjacent amino acids often form well-ordered (folded) subunits, such as β-sheets and α-helices, which are called secondary structure. The primary structure denotes the composition (amino acid sequence) of the peptides. The elucidation of the primary structure is the subject of mass spectrometric proteomics.

5.2.1 Nomenclature of peptide fragments

Sequence ions

The functional group -CO-NH-, indicated by blue colored atoms in Figure 5.4, is called peptide link [227], while the red colored bond is called peptide bond. Cleavage of a single peptide bond results in b- and y- fragments. The peptide fragment containing the terminal amino group is called b-fragment, and the peptide fragment containing the terminal carboxyl group is called y-fragment. In many cases, only one of the two fragments carries a charge and the other cannot be detected by mass spectrometry. The names a, x and c, z are assigned to fragments resulting from a bond cleavage left or right of the peptide link (see Figure 5.4). The position of the cleavage is denoted with a numerical subscript, which indicates the number of amino acids in the fragment. E.g, the term c_2 indicates a two-amino acid N-terminal fragment after cleavage of an N-C bond, while x_1 denotes a one-amino acid C-terminal fragment formed after a breakage of a C-C bond of the peptide backbone (see Figure 5.4).

Beyond the description of peptide-chain cleavages, a nomenclature is required to describe the loss of additional atoms. An unified nomenclature was introduced in 1984 by Roepstorff and Fohlman [225] and extended four years later by Biemann [226]. Roepstorff proposed an upper case nomenclature (A-fragment, B-fragment, etc.), using numerical indices and dashes to indicate hydrogen loss or addition. Biemann used lower case letters to avoid confusion with the single character amino acid notation. In addition, he proposed to

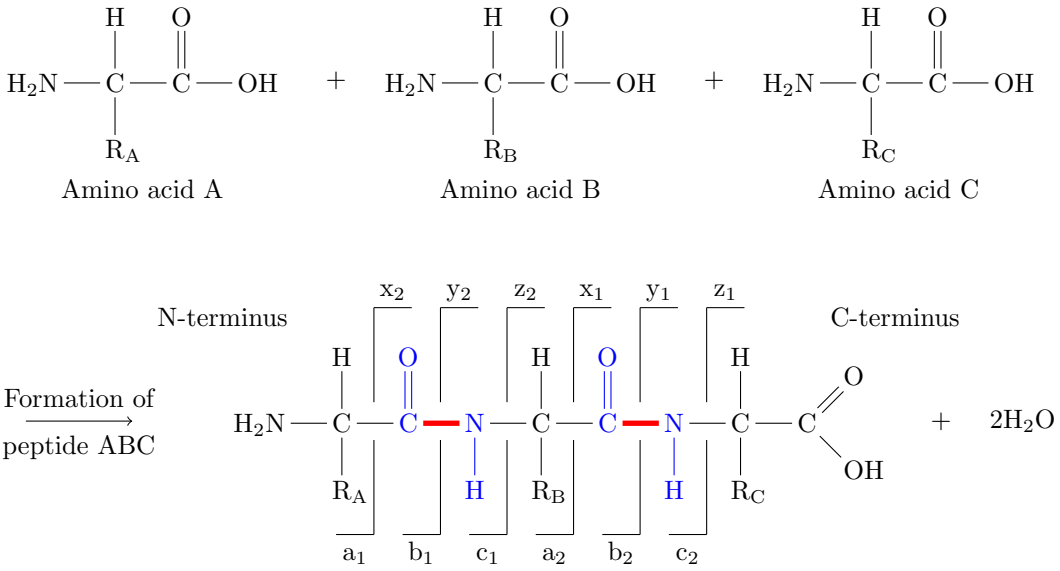

Figure 5.4: Formation of a peptide (bottom) from individual amino acids (top) and nomenclature for sequence ion cleavages [225][226]. The blue-colored atoms form the peptide link, of which the red-colored bond is the peptide bond. Cleavage of the peptide bond results in b-fragments (N-terminal fragments) and y-fragments (C-terminal fragments). Cleavage of the adjacent C-C or N-C bonds leads to a- and x- or c- and z-fragments. A number subscript denotes the position of the bond cleavage within the peptide backbone and the length of the resulting peptide fragment chain. In mass spectrometry, only charged fragments can be detected and the hooks point to the side where the charge is located.

Table 5.2: Composition of possible peptide fragments in the nomenclature of this work (see text). The term <1> denotes the peptide composition in terms of single-letter amino acid codes (see Table 5.1). The electron and the proton is labeled as e and p, respectively. The term $+/-s$ indicates addition/loss of species s.

a-fragment	b-fragment	c-fragment
+H+<1>-CO-e	+H+<1>-e	+H+<1>+NH-e
x-fragment	**y-fragment**	**z-fragment**
+CO+<1>+OH+p	+<1>+OH+p	-NH+<1>+OH+p

minimize the amount of dashes by labeling the most abundant type of a fragment without dashes. The y-fragments, as indicated in Figure 5.4, are often observed with an additional hydrogen atom and another proton at the N-terminal group (positively charged, allowing for cationic mass-detection). Y_1'' and y_1 is the Roepstorff and Biemann nomenclature for a corresponding single amino acid y-fragment. In this work, the lower-case nomenclature in combination with an explicit indication of the loss or addition of atoms or molecules during fragment formation is used, e.g., y_1 (±2H).

Table 5.2 summarizes the calculation of the mass of sequence ions. The term <1> denotes the amino acid composition of the fragment and is the sum of the amino acid masses presented in Table 5.1. As the amino acid masses are given assuming the loss of a water molecule, N-terminal fragments (a, b, c) are calculated by adding the mass of a hydrogen atom to the sum of amino acid masses (<1>). For C-terminal fragments (x, y, z), the mass of OH has to be added. b and y fragments result from a cleavage of the peptide link between two amino acids. a and x fragments result from a cleavage of the C-C backbone bond (α-cleavage) and the mass of CO is subtracted for the N-terminal fragment, while it is added for the C-terminal one. A cleavage of the N-C backbone bond results in c and z fragments. Here, the mass of NH has to be added to the N-terminal fragments and subtracted for the C-terminal fragment. In this work, positively charged fragments will be detected. Thus, the electron mass is subtracted for N-terminal fragments and the proton mass is added for C-terminal fragments. Fragments with a mass that is equal to a mass calculated by Table 5.1 are standard sequence ions. Any deviation, e.g., an additional hydrogen or a loss of a water molecule, will be indicated.

Commonly, most sequence fragments of protonated peptides are explained by the mobile proton model [228]. Peptides are normally charged prior to analysis by adding a proton. This proton might migrate along the peptide structure and statistically protonates atoms in the vicinity of the peptide link inducing fragmentation. This charge-directed process leads to a_1-, b_x- and y_x-fragments and subsequently from b_x to a_x- and b_{x-1}-fragments. The production of b- and y-fragments can be enhanced by the Proline and the Histidine effects, where the cleavage probability is enhanced close to these two amino acids. An overview of the fragmentation pathways of protonated peptides was presented by Paizs and Suhai [229].

Peptide backbone cleavages and therefore the production of sequence ions might also be

explained by an α-cleavage initiated by the creation of a radical site at the peptide link. This process is expected to be the dominant pathway when producing sequence ions in this work as the peptide link is strongly photo-active.

Other peptide fragments

Molecule-laser interactions in the intensity regime considered in this thesis often lead to multiple fragmentation and unusual bond cleavages. An additional nomenclature is required to denote fragments that contain neither the carboxyl nor the amino terminal group, i.e., the liberation of single amino acids (1AAS) or chains of amino acids (nAAS). Fragments can also undergo an additional cleavage in their side chain. If the charge is located on the side chain, the detected fragment is denoted as side chain cleavage (SC) ion. Some 1AAS, 2AAS and SC fragments for the small peptide MRFA are displayed and labeled in Figure 5.5.

Single amino acids (1AAS) are liberated mainly through α-cleavages[5] and occur as cations of type $[H_2N{=}C_\alpha H\text{-}SC]^+$ (1AAS immonium ions) and $[C_\alpha\text{-}SC]^+$ (α-type 1AAS ions). According to the nomenclature presented in Figure 5.5 a), an arginine (R) with and without the amino group will be denoted as R and R_α, respectively. A short notation depicts a 1AAS fragment with the backbone amino group (e.g., R) with a green box around the 1AAS sequence letter. A red box indicates the observation of a 1AAS fragment without the backbone amino group (e.g., R_α).

Figure 5.5 b) shows side chain cleavage fragments. These fragments are similar to 1AAS fragments but underwent an additional cleavage in the side chain of the amino acid. These fragment types are denoted with Greek letter sub- and superscripts, which indicate the positions of cleavages. α denotes the first carbon atom of the side chain, β the second, and so on. A superscript star (*) indicates fragments with an intact carbonyl group and serves to distinguish them from ions that underwent CO loss. SC fragments, e.g., can help to distinguish the amino acid leucin (L) from isoleucin (I), which have the same composition and nominal mass ($C_6H_{13}NO_2$). Due to the side chain sub-structures, the fragment I/L-(C_3H_7) is predominantly generated by a side chain cleavage occurring in leucin, while the fragment I/L-(C_2H_5) is due to the amino acid isoleucin.

[5]The cleavage of the α-bond between the C_α and the backbone carbonyl group.

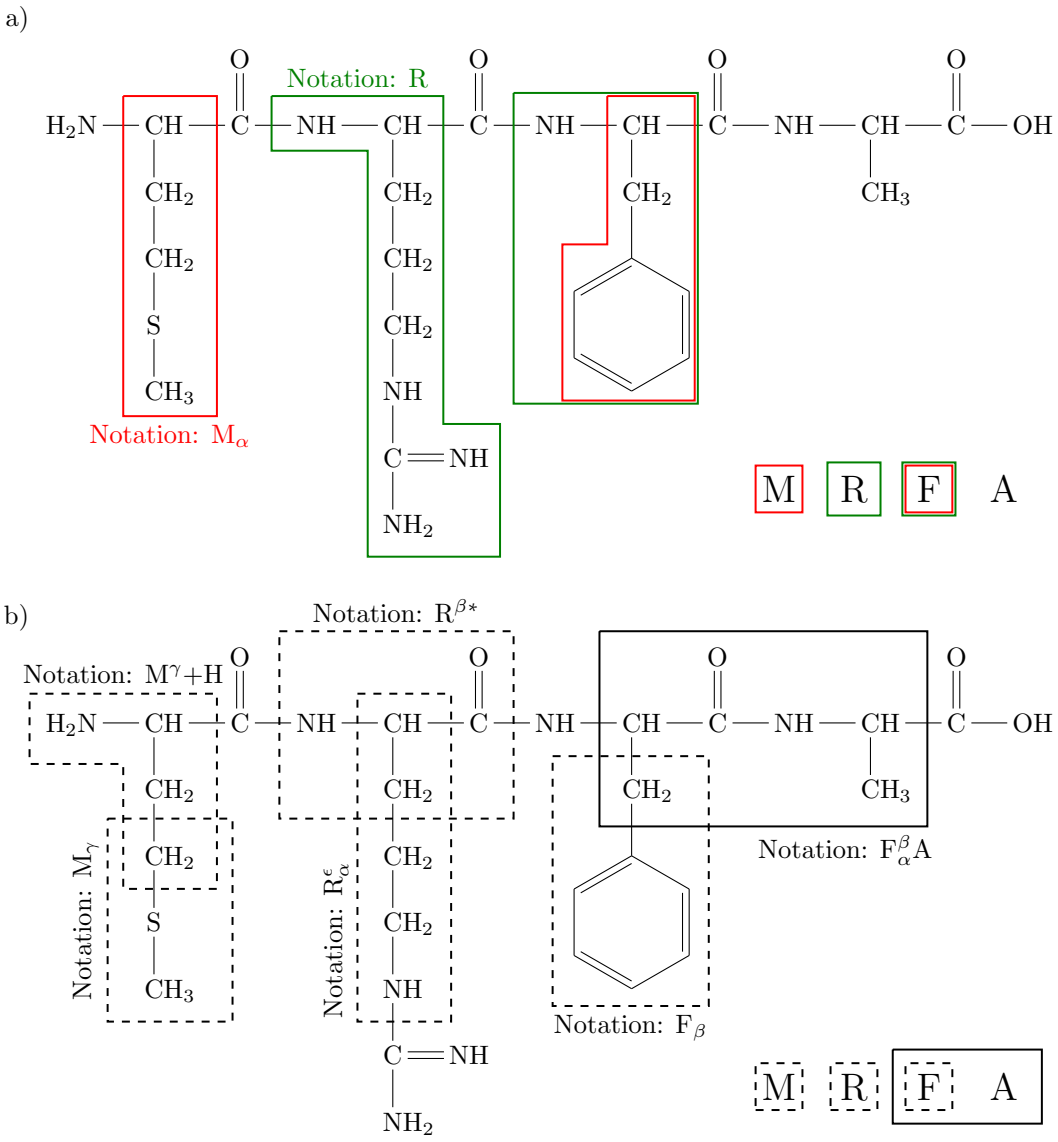

Figure 5.5: Extended nomenclature for fragments formed by multiple fragmentation and fragments detached from the backbone structure for the model peptide MRFA. a) Fragments resulting from amino acid stripping (AAS). Amino acid fragments containing the side chain and the -HN-CH- group are denoted by the single letter amino acid code (e.g., R, marked in green). The same fragments without the -NH- group are indicated with an α-subscript (e.g., M_α, marked in red). b) Fragments that underwent a cleavage in the side chain are denoted by a Greek letter sub- and/or superscript. The superscript denotes the position of the last side-chain atom in a fragment, counting from the backbone C_α (e.g., M^γ in the figure). The subscript denotes the position of the first side-chain atom. For both cases, a) and b), a superscript * (star) indicates that the fragment also contains the -(C=O)- group from the backbone structure. The insets on the right offer a color-coded short-hand notation of all indicated fragments.

Side chain fragments are commonly created by a so-called McLafferty rearrangement [230]. The process describes the cleavage of a neutral fragment from a parent radical cation, which hosts a double bond at the radical site. Here, the rearrangement might be initiated by the formation of a radical site at the amide link. Subsequently, a hydrogen atom from the C_γ of the side chain is transferred to the carbonyl oxygen leading to a neutral side chain compound. In order to be detectable in this work, the side chain must be charged. This charge can stem from an additional photo-activation in the side chain or from a mobile proton of the ionization process prior to MS analysis.

Internal fragments (nAAS), i.e., amino acid dimers and amino acid polymers, can also be cleaved from peptides as a unit. An example is shown in Figure 5.5 b): the internal fragment $F_\alpha^\beta A$ is of type 2AAS as it contains two C_α atoms from amino acid side chains.

To elucidate the composition and primary structure of peptides by mass spectrometry, a sufficient number of distinguishable fragments must be generated. The ideal activation method would produce all possible sequence fragments in a detectable charged state as well as a large number of 1AAS and SC fragments for sub-structure determination.

5.3 Common activation methods for mass spectrometric analysis

To elucidate molecular composition of large molecules, e.g., the sequence of proteins [198, 203], the parent molecule is activated and fragments into smaller subunits, which are mass analyzed. Common physical activation methods [231] are *electron capture dissociation* (ECD) [232], *collision-induced dissociation* (CID) [233], *black body infrared dissociation* (BIRD) [234] and *infra-red multi-photon dissociation* (IRMPD) [235, 236]. A common chemical method is Electron Transfer Dissociation (ETD) [237].

In mass spectrometry, the activation methods are divided into ergodic and non-ergodic methods. An activation process is called ergodic when the amount of energy introduced into the molecule is redistributed by *intra-molecular vibrational redistribution* (IVR) prior to fragmentation [238]. In this case, the fragmentation appears to be statistical and cleavages occur in the weakest bonds. Such a process creates a limited number of

fragments. Non-ergodic processes occur when the timescale of dissociation is faster than that for vibrational energy redistribution. Activation can then lead to the fracture of strong bonds. Therefore, non-ergodic activation can yield unusual fragments that often facilitate composition elucidation of molecules and specific sub-structures therein. Apart from ECD, all aforementioned methods are ergodic, i.e., dissociation occurs in the weakest bonds after the activation energy is redistributed within the molecule. Ergodic fragmentation patterns contain a limited number of fragments and offer insufficient information for composition elucidation of larger molecules.

IRMPD methods work in the ergodic regime and employ continuous wave (cw) or quasi-cw radiation. The simplest scheme is BIRD. Multiple photons of infra-red (IR) background radiation or IR radiation from a filament are absorbed by trapped molecules and cause dissociation. Other IRMPD methods use free electron lasers (FEL) [239] or CO_2 lasers in the mid-infrared range. The radiation heats the molecules and the energy is distributed over the molecule via IVR. The molecules absorb photons until the weakest bonds undergo dissociation. IRMPD activation dominantly leads to b- and y-fragments [231] and the fragmentation patterns are very similar to CID patterns [214].

CID is also ergodic and mainly creates b- and y-type sequence fragments. The dominant formation of b and y fragments from protonated precursors in ergodic activation is understood in terms of the proton mobility model [228]. The activation method mobilizes the proton and hetero atoms (nitrogen and oxygen) along the backbone get protonated statistically. The protonation weakens the peptide bonds and induces cleavages forming b and y fragments. If the proton is immobilized by strong basic side chains, Vicki et al. proposed a mechanism, where the carbonyl oxygen acquires a hydrogen atom from an adjacent side chain inducing the cleavage [228]. In most cases, y fragments dominantly occur protonated and with an additional hydrogen.

ECD is non-ergodic but still predominantly results in b and y fragments [232]. Type c and z fragments [240] and, to a smaller degree, type a and side chain fragments are also formed by ECD activation. ECD produces discharged protonated peptides, induces radical sites and results in a complex fragmentation pattern [241]. Besides sequence ions, the loss of side chains and amino acid residues was reported. ECD fragmentation is expected to proceed via a radical driven process, inducing multiple cleavages by single activation [241]. ECD does not produce immonium ions [242].

For mass spectrometric detection the fragments must be charged. None of the above-mentioned methods is capable of charging the investigated molecules to an appreciable degree. In the case of positively charged peptides, ECD and ETD activation even discharge the cations upon fragmentation. Therefore, many fragments remain uncharged and evade detection. This is a particular drawback when analytes from living cells are subjected to mass spectrometric investigation. In this case, the precursors are generated by soft ionization methods, e.g., Matrix-Assisted Laser Desorption and Ionization (MALDI) [243], resulting in a precursor charge state of 1+. This charge state is too low for activation by ETD or ECD. Higher charge states can be obtained via *electrospray ionization* (ESI[6]) [244] after the analyte is desalted.

Another challenging issue to be addressed in mass spectrometry is the presence of post-translational modifications (PTM[7]) in peptides and the elucidation of small sub-structures. CID efficiently dissociates labile bonds from post-translational marker molecules, which can make composition elucidation ambiguous. Non-ergodic ECD enables the location of post-translational sites [241].

5.4 Photo-chemical activation of peptides

In the ultraviolet and visible region of the electromagnetic spectrum, electronic excitation of peptides occurs from bonding π to anti-bonding π^* orbitals ($\pi\pi^*$ transitions) and from non-bonding n to π^* orbitals ($n\pi^*$ transitions). These transitions correspond to the lowest electronic transitions, i.e., the transitions from the highest occupied molecular orbital (HOMO) to the lowest unoccupied molecular orbital (LUMO). π orbitals are found in all peptides in the carbonyl groups -(C=O)- or in aryl groups of aromatic amino acids (Table 5.1). These two types of molecular sub-structures are often called chromophores. Non-bonding n orbitals are found in the lone pairs of oxygen and nitrogen atoms in the peptide backbone. Moreover, the nitrogen atom can donate its lone pair electrons to the carbon atom of the amide bond resulting in -(O-C)=NH- as the peptide link structure. In

[6]ESI is typically used to charge analytes prior to in-vacuum mass spectroscopic investigations.

[7]The process of *translation* denotes the synthesis of proteins in living cells. Many proteins are modified after translation, which alters their biochemical function. Such post-translational modification can be difficult to detect in mass spectrometry.

this configuration, the peptide link is polarized due to a positive character of the nitrogen site and a negative character of the oxygen site. The latter configuration and the one shown in Figure 5.4 form a resonance structure [245]. This resonance structure leads to an extended π system distributed along the O–C–N chain. The amino acids glutamine (Q) and asparagine (N) also bear an amide group in their side chains and therefore contain the same extended π system. Another extended π system is formed in the side chain of arginine (R). R contains a guanidyl group, which acts as a strong base. As the peptides investigated in this study are charged by protonation, arginine will be protonated and also forms a delocalized π system between the central carbon and all three adjacent nitrogen atoms.

Proteins exhibit a strong absorption band around 180 – 210 nm [246, 247], involving the $n\pi^*$ nitrogen/oxygen lone-pair excitation and the $\pi\pi^*$ transition of electrons in the resonance structure or the carbonyl double bond. These excitations are accessible by a four-photon process with 800 nm femtosecond pulses. An increased size of the delocalized π electron system results in a decrease of the energy gap between the HOMO and the LUMO. Aromatic systems, as found in tryptophane and phenylalanine, show maximum absorption between 250 nm and 350 nm [248, 249]. These aromatic amino acids can be efficiently excited by ultra-violet (UV) radiation or by a three-photon process with 800 nm radiation. Therefore, the peptide link and side chains containing chromophores are expected to be efficiently activated by UV radiation or by non-resonant multi-photon interaction with near-infrared (NIR) femtosecond laser pulses.

Nanosecond lasers at 193 nm and 266 nm were used for ultraviolet photo-dissociation (UVPD) experiments at relatively low intensities of about $10^9\,\mathrm{W/cm^2}$. If resonances are present, UVPD is very efficient and can completely dissociate small molecules. In 1984, Bowers et al. [199, 250] irradiated small oligopeptides by 193 nm nanosecond laser pulses and recorded broad-band UV absorption spectra. Aliphatic (non-aromatic and non-cyclic) peptides showed no absorption between 260 nm and 400 nm but a sharp increase in absorption below 250 nm. N-terminal a_x fragments were abundant when the dipeptide LA was irradiated by 193 nm nanosecond laser radiation. This indicated that the carbonyl in the peptide link can be resonantly excited, resulting in α-cleavages. From the 193 nm fragmentation pattern of the tripeptide LGF, Bowers et al. concluded that aryl groups (aromatic rings) can also be efficiently excited by UV radiation, resulting in z-type

fragments[8]. Weinkauf et al. resonantly ionized the aromatic ring located at the C-terminal of small peptides by nanosecond UV radiation (260 – 290 nm) and thereby created a hole in the electronic system [29, 30]. Depending on the peptide sequence, the authors observed the transfer of the hole charge from the aromatic site to the N-terminal. This was explained in terms of ionization energies of isolated amino acids. The charge could only migrate from the C-terminal to the amino group if the ionization potential of all intermediate amino acids was lower than that of the amino acid at the C-terminal. In this case, the positive charge (hole) could migrate easily over at least four consecutive amino acids via a through-bond mechanism. Using 266 nm nanosecond laser radiation, Gabryelski et al. saw efficient dissociation of oligopeptides containing amino acids with aromatic compounds [251]. They could observe a dominant amount of b-, c- and y-type fragments and even some *deep fragments*[9]. Investigating aliphatic and aromatic amino acids, Vorsa et al. demonstrated in 1999 that resonant femtosecond radiation of 195 nm and 260 nm dominantly leads to α-cleavages [252]. They concluded that the cleavage reaction is triggered by ionization of the aromatic compounds or the amino group.

5.4.1 Femtosecond laser-induced dissociation

The work described here uses non-resonant intense femtosecond laser pulses of up to $10^{15}\,\mathrm{W/cm^2}$ at 800 nm to activate protonated peptides. The ionization potential of peptide cations can be approximated by $E_{\mathrm{IP}}(z) = 9.8 + 1.1z$, as a function of the charge z of the peptide [253]. Assuming the peptide is abundant in charge state (CS) +1 and is ionized by photons with an energy of 1.55 eV (800 nm), ionization requires the absorption of seven to eight photons in the MPI regime. Although the peptide ionization energies were experimentally determined, the underlying processes were only discussed for smaller molecules [254]. The efficiency of intense femtosecond laser pulses to generate charged fragments and parent molecules in charge states larger than the initial charge state remains an open question that will be addressed in the experiments here.

An evaluation of the intensity regime is required to discuss the physical processes underlying

[8] UV excitation of aryl groups causes the neighboring peptide bond to break, at least when the aromatic amino acid is located at the C-terminal.

[9] In the literature, fragments originating from several consecutive fragmentation processes or very small fragments from larger compounds are called *deep fragments*.

fs-LID. In atomic physics, the Keldysh parameter $\gamma = {}^{\omega_0}/_{\omega}$ is a good indicator to distinguish between the multi-photon and the tunneling regime (Chapter 1.1). The Keldysh parameter compares the tunnel time (inverse of the frequency ω) to the laser optical period (inverse of the laser frequency ω_0). The potential in which the active electron moves is considered to be a δ-function (zero-range potential) or a Coulomb potential. Both assumptions yield reasonable values for the Keldysh parameter. As the size of the systems under investigation increases, short-range potentials might not be an appropriate approximation anymore [255, 256]. Levis and DeWitt developed a *structure-based model*, taking into account the spatial extent of the electron cloud in molecules [254]. The molecular electronic wavefunction is obtained by *ab initio* calculations. As a potential the authors chose the one-dimensional potential of the neutral that provides the largest distance between its classical outer turning points at the molecule's ionization potential (E_{IP}). This *optimal potential* is then superimposed with the laser electric field, revealing the tunneling barrier length Δx and therefore the tunneling frequency $\omega \propto {}^{\sqrt{E_{\mathrm{IP}}}}/_{\Delta x}$, which can be compared to ω_0. This adapted Keldysh parameter was compared to the Keldysh parameter obtained with a zero-range potential for different hydrocarbons [254]. Levis and DeWitt found that the tunnel regime was accessible with decreased laser intensity for increasing molecular size. While this adiabatic *molecular single active electron* (MSAE) approach can explain the lack of MPI features in the photo-electron spectra of extended molecules for rather low laser intensities, it fails to explain the experimentally observed wavelength dependence of the threshold intensity I_0 at which almost 100 % of the molecules become ionized. Lezius et al. developed a *non-adiabatic multi-electron* (NME) model, where I_0 is replaced by $I_0(\omega_0)$ [257, 258]. The model considers that delocalized electrons in the molecule are driven by the strong laser field, polarizing the molecule. Due to the delocalized nature of π electrons, the electronic response to the fast oscillating laser electric field is non-adiabatic. Additionally, the molecular electronic energy levels at frozen nuclear coordinates are strongly Stark shifted due to the varying electric field strength. In order to explain the rich fragmentation pattern of large molecules, Lezius et al. suggested stepwise multi-electron excitation in consecutive laser field cycles via non-adiabatic Landau-Zener transitions [259, 260]. In a more recent publication, Konar et al. suggested that polyatomic molecules under the influence of intense femtosecond laser fields fragment due to a two-step process [261]. First, the molecule becomes ionized by single electron ionization, where the photo-electron takes away most of the energy. Second, the ion is subsequently fragmented due to resonance

enhanced photon absorption from the same laser pulse.

The molecule can dissipate photo-induced energy via radiative and non-radiative processes possibly including a coupling of states with different multiplicity. Electronic de-excitation proceeds via the radiative processes of fluorescence (no change in multiplicity) and phosphorescence (change in multiplicity). Intersystem crossing (change in multiplicity) can also occur radiationless leaving the molecule in a vibrationally excited state. If the electronic de-excitation occurs radiationless without a change in multiplicity the process is called internal conversion. In large molecules with a high density of vibrational states the energy can also be redistributed to other vibrational modes in iso-energetic electronic states such that the energy is spread over the whole molecule (intramolecular vibrational redistribution). When the redistribution reaches a vibrational continuum the molecule dissociates which usually cleaves the weakest bonds. This process can only occur if the laser pulse durations are sufficiently long and vibrational modes can be effectively populated while IVR takes place. Therefore, IVR is not expected to play a dominant rule when fs-LID is used to activate the molecules.

The maximum laser intensity employed in this study is $\approx 10^{15}\,{}^{\mathrm{W}}/_{\mathrm{cm}^2}$ and well above the saturation intensities for large molecules [262]. Hence, the protonated precursors can be efficiently ionized, i.e., $[\mathrm{M+H}]^{+} \rightarrow [\mathrm{M+H}]^{2+} \rightarrow [\mathrm{M+H}]^{3+}$. When the molecule is highly charged it possibly dissociates by Coulomb explosion. Due to the high laser intensity ionization is possible at all sites of the molecules. If a dissociative energy curve is populated the molecule will directly dissociate close to the positive hole in the electronic structure leading to unspecific fragments, as the hole can be created anywhere in the molecule. On the other hand, the hole might also migrate to particular molecular sites inducing specific cleavages. Gil et al. calculated that a positive charge introduced by ionization of neutral gas-phase amino acids will relocate to the amine group or the aryl group for aliphatic and aromatic amino acids, respectively [263]. Such a process cannot be distinguished from specific and local ionization at the extended π systems in peptides, which would also induce cleavages in the backbone structure and in the side chain of aromatic compounds. In any case, energy dissipation may be accompanied by a loss of the neutral groups CO or CO_2 as these compounds are good leaving groups. Depending on the irradiation time, the fragments could also be further ionized and/or undergo secondary fragmentation when molecules interact with several laser pulses.

Lockyer et al. reported fs-laser fragmentation of valyl-valine at different wavelengths (266 nm, 400 nm and 800 nm) [264]. They observed a large number of deep fragments and found that aromatic amino acids are no prerequisite for efficient fragmentation (see also [265]). In the course of this thesis several highly relevant papers on the topic of fs-LID in mass spectrometry were published by the group of Dantus and Reid. In 2009, Kalcic et al. compared fs-LID and CID spectra of peptides containing eight to ten amino acids [266]. Although the dissociation efficiency for the parent ion was only about 10 %, fs-LID offered better peptide sequence coverage as compared to CID. In 2010, Smith et al. used fs-LID and a quadrupole ion trap to investigate the fragmentation behavior of phosphopeptides and identified the position of a post-translational modification (phosphomarker) [267]. This was not possible with conventional ergodic activation methods due to the labile character of the marker bond. They also found that fs-LID activation can generate all possible sequence ions (a, b, c, x, y, z). In another work of the same group, fs-LID was used to study the photolysis of medium-sized peptides [268]. Full sequence coverage was obtained for these peptides and dissociation efficiency (precursor depletion) reached 35 %. Smith et al. also showed that aromatic amino acids are not required for activation. In a recent study, Duffy et al. dissociated small polypeptides and single amino acids by 800 nm femtosecond laser radiation [269]. The dominant fragment ion was a side chain residue if the amino acid contained an aromatic compound, while for aliphatic amino acids the immonium ion (loss of the carboxyl group COOH) was dominant. Reitsma et al. dissociated protonated leucine enkephalin ($[YGGFL+H]^+$) with a 780 nm, 12 fs laser pulse and found that most of the fragments are immonium, side chain and small sequence ions formed in the MPI regime at intensities up to $10^{14}\,\mathrm{W/cm^2}$ [270].

Existing experiments using fs-LID on smaller polypeptides could not clearly establish the ergodicity of the activation process [266, 269, 271, 272]. Using low-intensity ($10^{9}\,\mathrm{W/cm^2}$) femtosecond radiation to dissociate β-carotene, Weinkauf et al. observed an ergodic fragmentation spectrum, while a non-ergodic fingerprint was detected when the polypeptide gramicidin D was photo-fragmented [30]. Grégoire et al. used 266 nm and 800 nm femtosecond radiation in a pump-probe scheme to photo-dissociate the protonated dipeptide WL. They concluded that some fragments are formed by ergodic processes, while others are due to a fast direct dissociation from electronic excited states. A typical sign for ergodic fragmentation is the loss of weakly-bound marker molecules, as observed in CID

experiments. In fs-LID spectra of peptides, marked with a weakly bound phosphate group, the fragmentation channel of marker loss was weak, indicating non-ergodic fragmentation [266]. The authors observed broadened time-of-flight peaks when they dissociated small peptides by 267 nm femtosecond radiation. This was attributed to delayed ergodic fragmentation. On the other hand, especially with 800 nm femtosecond radiation, a and z (and a smaller amount of y_1 and b_2) sequence fragments, as well as side chain fragments, were generated when the neutral tripeptide LLY was photo-dissociated. These results were attributed to radical-driven bond cleavages after ionization occurred at the oxygen atom (forming a radical cation, maybe accompanied by McLafferty rearrangement [230]). Konar et al. investigated the dissociation of smaller polyatomic molecules by femtosecond laser radiation and concluded that the fs-LID process is of ergodic nature [261].

The charging ability of fs-LID activation was already pointed out by Weinkauf et al. in 1994 [271] and precursor charging was observed in some fs-LID experiments [266–268]. Other fs-LID studies did not report on precursor charging or higher charged fragments [264, 269]. So far, charging of photo-fragments was not reported at all, maybe due to a lack of resolution of the employed mass analyzers.

The above-mentioned experiments indicate that fs-LID might be a valuable tool for proteomics, especially because femtosecond laser activation causes enhanced fragmentation of biomolecules as compared to nanosecond laser activation [273]. To establish the relevance of fs-LID in proteomics, this work used intense 800 nm, 40 fs laser pulses. The intensity used here reached about $10^{15}\,{}^{\mathrm{W}}/_{\mathrm{cm}^2}$, two orders of magnitude higher than in previous studies. The laser was coupled into a high-resolution, high-accuracy FT-ICR mass spectrometer for sequencing of large peptides. The properties of the mass analyzer allow for fragment assignment over a larger mass range with greater confidence as compared to published experiments.

Chapter 6

Femtosecond laser-induced dissociation and Fourier transform mass spectrometry

The work presented in this Chapter is based on a joint research project of the MBI and the laboratories of Prof. Linscheid at the Humboldt University in Berlin. The latter hosted the Fourier transform mass spectrometer. The experiments have been conducted and analyzed in close collaboration with Andreas Kühn. At the MBI the work was supervised by Prof. Hertel and Prof. Schultz.

6.1 Experimental

6.1.1 Laser system and beamline

A commercial Ti:Sa laser system, consisting of an oscillator (Tsunami, Spectra Physics) and an amplifier (Spitfire, Spectra Physics) was used for the experiments described here. The laser produced 40 fs pulses with up to 3 mJ pulses energy at a central wavelength of 800 nm. The repetition rate was 1 kHz.

A SPIDER [151] continuously monitored the pulse duration during the experiment. A

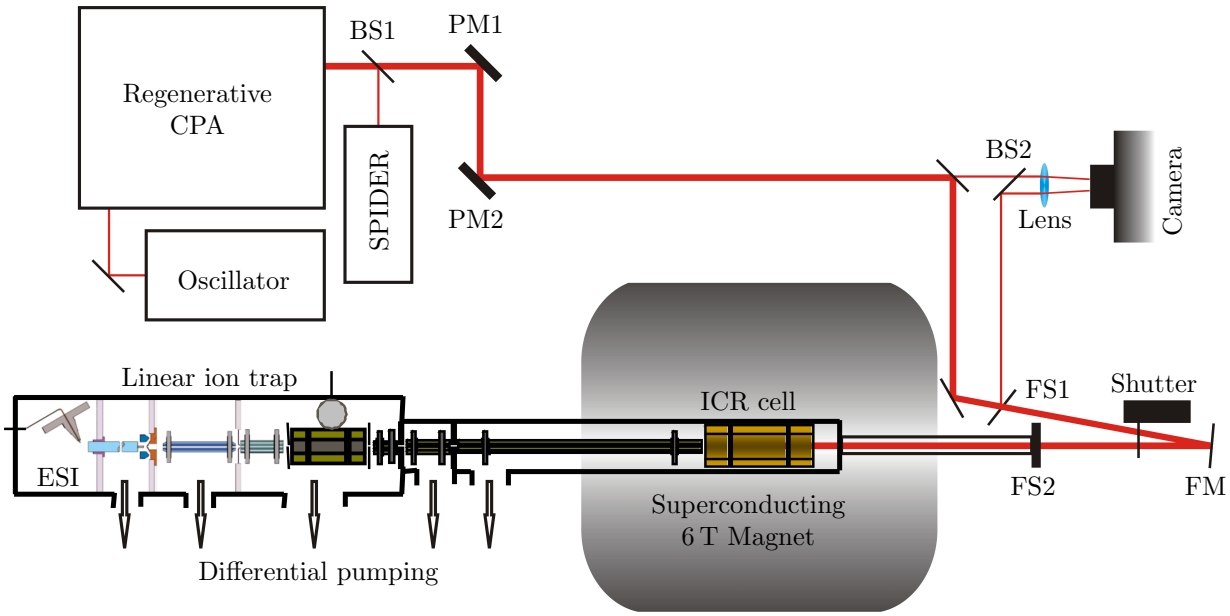

Figure 6.1: Scheme of the experimental setup. An amplified femtosecond laser is spatially stabilized and coupled to an FT-ICR mass spectrometer. A beamsplitter (BS1) couples a fraction of the laser radiation into a SPIDER for pulse duration analysis. A second beamsplitter (BS2) and a 300 μm thin quartz glass plate couple two additional diagnostic beams into a camera and allow spatial beam stabilization via two piezo-controlled mirror mounts (PM1, PM2). A focusing mirror (FM) reflects the beam through a 300 μm thin quartz glass window (FS2) into the ICR cell. A shutter controls the irradiation/ activation time. Molecules are charged and injected into the ICR cell via an ESI source. Ions are mass and charge selected in a quadrupol mass filter prior to the transfer into the ICR cell, which is pervaded by a 6 T magnetic field.

home-built beam stabilization system [274] (see Figure 6.1) actively stabilized the beam pointing to compensate for thermal drifts. To this end, diagnostic beams were picked up at two spots along the beam path. A leakage through a 45 ° dielectric coated high reflector provided the first diagnostic beam, while the second diagnostic beam for the feedback loop was reflected off a thin (300 μm) fused silica glass plate further downstream in the beam path. Both beams were recombined on a beam splitter and focused onto a camera. Software programmed in the course of this thesis stabilized the spot position on the camera by steering two piezo-driven mirror mounts. The system allowed a very accurate and stable laser positioning on a multi-hour timescale.

A spherical mirror ($r = -3$ m) focused the laser into the ICR cell. The fused silica entrance

window was 300 μm thin and was positioned as close as possible to the focusing optic to avoid non-linear effects within the window. Gaussian beam optics [275], the initial beam diameter[1] $d = 8\,\text{mm}$, and the focal length $f = 1.5\,\text{m}$ was used to estimate the focal beam diameter $d_0 = 2 \cdot \ln 2 \cdot \frac{f \cdot \lambda}{\pi \cdot d} = 66\,\mu\text{m}$. The maximum laser intensity I_0 in the focus is [275]

$$I_0 = 0.83 \cdot \frac{E}{\tau d_0^2} \quad , \tag{6.1}$$

where E is the pulse energy and τ is the pulse duration. Peak intensities of about $1 \cdot 10^{15}\,\text{W}/\text{cm}^2$ are reached in the ICR cell. The laser intensity varies by a factor of 2 along the propagation direction within the Rayleigh length of $l_R = \frac{\pi}{\lambda}\left(d_0/2\right)^2 = 4.3\,\text{mm}$. As it was technically impossible to evaluate the laser focal position with respect to the ion cloud stored in the ICR cell, the irradiation intensity can only be estimated to be in a range of $10^{13} - 10^{15}\,\text{W}/\text{cm}^2$. In any case the intensity should be sufficient to efficiently ionize the molecular species.

To irradiate molecular ions for controlled irradiation times a home-built laser shutter [276] was triggered by the FT-ICR software. Typical shutter opening times (i.e., activation times) range from 100 ms to 2 s.

6.1.2 FT-ICR mass spectrometer

Dilute molecular samples were provided by a syringe pump with a constant flow of $5\,\mu\text{L}/\text{min}$. Molecules were charged and injected into the vacuum system by an electrospray ionization source (ESI) [244]. A prototype of the hybrid mass spectrometer LTQ-FT from Thermo Finnigan was used. It provided two consecutive detector systems: A 2D linear ion trap (LTQ) and an FT-ICR mass spectrometer unit. The latter contains a cryogenically cooled 6 T superconducting magnet. The low mass resolution LTQ was used to collect and isolate molecular ions of a particular m/z range prior to ion transfer into the ICR cell. The purified sample was transferred into the high vacuum interaction and detection region (ICR cell) of the spectrometer by pulsed electric fields. Ions with $m/z = (50 - 2000)\,\text{u}/\text{e}$ could be detected in the ICR spectrometer.

[1] Full width at half maximum

To determine the eigenfrequencies of the ions (Equations 5.2 and 5.3), the geometrical cell parameter α has to be estimated. Assuming a typical trapping voltage of 10 V and taking into account the cell length of 100 mm and the open cylindrical design, the cell parameter is given by $\alpha = 7.736 \cdot 10^3\ {}^{\mathrm{V}}/_{\mathrm{m}^2}$ [277]. The trapping frequency of the lowest ${}^{m}/_{z} = 50\ {}^{\mathrm{u}}/_{\mathrm{e}}$ and highest ${}^{m}/_{z} = 2000\ {}^{\mathrm{u}}/_{\mathrm{e}}$ value is $\omega_t = 122$ kHz and $\omega_t = 19$ kHz, respectively.

Assuming a magnetic field strength within the cell of 6 T, the cyclotron frequency is $\omega_c = 11.578$ MHz and $\omega_c = 0.289$ MHz for the smallest and the highest m/z ratio, respectively. It follows that $\omega_+ = 11.577$ MHz and $\omega_- = 642$ Hz for ${}^{m}/_{z} = 50\ {}^{\mathrm{u}}/_{\mathrm{e}}$ and $\omega_+ = 0.288$ MHz and $\omega_- = 623$ Hz for ${}^{m}/_{z} = 2000\ {}^{\mathrm{u}}/_{\mathrm{e}}$. Thus, the magnetron frequency is comparable to the laser repetition rate, while the trapping frequency and the cyclotron frequency are much higher than the laser repetition rate (1 kHz). Synchronization of the ion cloud motion and the laser pulses is not considered.

As the present experiment employs a commercial spectrometer, the size of the ion cloud cannot be measured. Expected parameters are an ion cloud axial extension of about 1 cm with a diameter of 400 μm (Section 5.1). Before cyclotron excitation the cyclotron radius is small and the radial extent of the cloud is determined by the magnetron motion. Therefore, the initial magnetron radius can be estimated to be about $r_- = 200\,\mu$m. The kinetic energy stored in the magnetron motion is $E = \frac{1}{2} J \omega_-^2$ with the moment of inertia being $J = m r_-^2$. Assuming a particle with a mass of $m = 2000$ u and an angular magnetron frequency of $\omega_- = 623$ Hz the magnetron kinetic energy evaluates to $E = 0.2\,\mu$eV. This has to be compared to the kinetic energy release in Coulomb explosions which is on the order of eV and therefore much higher than the magnetron kinetic energy [278]. Hence, fragments created by Coulomb explosion might escape the radial trapping potential. With the available laser intensities it is expected that a substantial amount of photo-fragments will evade detection and the overall ion signal is expected to decrease with irradiation time.

The number of charges initially stored in the trap is on the order of $5 \cdot 10^5$ [279] and the ion number density is about $4 \cdot 10^{15}\ \mathrm{m}^{-3}$. As the laser intensity is well above the saturation intensity, each molecule inside the laser focus will be ionized. The laser beam diameter is about 17 % of the diameter of the ion cloud. The magnetron motion therefore determines the timescale of precursor depletion as the ion cloud has to pass by the laser several times. Full precursor depletion is expected after some seconds of laser activation.

Mass resolution and accuracy

To determine the mass resolution and mass accuracy of the mass spectrometer, the measured masses must be compared to known values. Masses of the relevant atoms are shown in Table 6.1.

Figure 6.2 shows a fragmentation spectrum of the protein lysozyme (m = 14305 u), activated by fs-LID. The blue-marked inset depicts an enlarged section (m/z = 1431.41 u/e) of the spectrum with the isotopic structure resolved. The isotopic heterogeneity is mostly due to ^{2}D (deuterium) and ^{13}C isotopes and the peaks are spaced by Δm = 1. The difference in mass/charge ratio for adjacent peaks is used to evaluate the charge state of the ion by Equation 5.4. In this case, a charge state z = +10 e is assigned and the exact mass of m = 14314 u can be determined for the detected species. A similar consideration of the parent ion signal near m/z = 1600 u/e reveals that the parent is nine-fold protonated ([M+9H]^{9}+, m = 14314 u). It can be concluded that the lysozyme parent ion was singly ionized in the activation process to form the daughter ion under consideration. A similar analysis of the peaks at $m/z \approx 1300$ u/z and $m/z \approx 1200$ u/z reveals that the activation can further ionize the parent ion ([M+9H]^{9}+) resulting in the eleven- and twelve-fold charged daughter ion.

The systematic analysis of isotope patterns is performed through computer-aided comparison of observed and simulated isotope progressions. All assigned species in the following sections account for possible isotope patterns. The isotopic mass of the most abundant isotope composition will be tabulated and discussed.

The resolution R of the spectrometer in this specific mass region is determined as follows: The full width at half maximum (FWHM) of the peak at m/z = 1431.41 u/e is 0.048 u/e. Two adjacent signals at 1431.41 u/e, separated by 0.048 u/e, can be distinguished. Therefore, the resolution of the mass spectrometer in this specific mass range is $R = \frac{m}{\Delta m} = {}^{1431.41\,\mathrm{u}}/_{0.048\,\mathrm{u}} =$

	H	^{12}C	^{14}N	^{16}O	^{31}P	^{32}S	e (electron)
mass [u]	1.007825	12.000000	14.003074	15.994915	30.973761	31.972071	$5.486 \cdot 10^{-4}$

Table 6.1: Masses of relevant atoms and the electron mass. Data from NIST webpage.

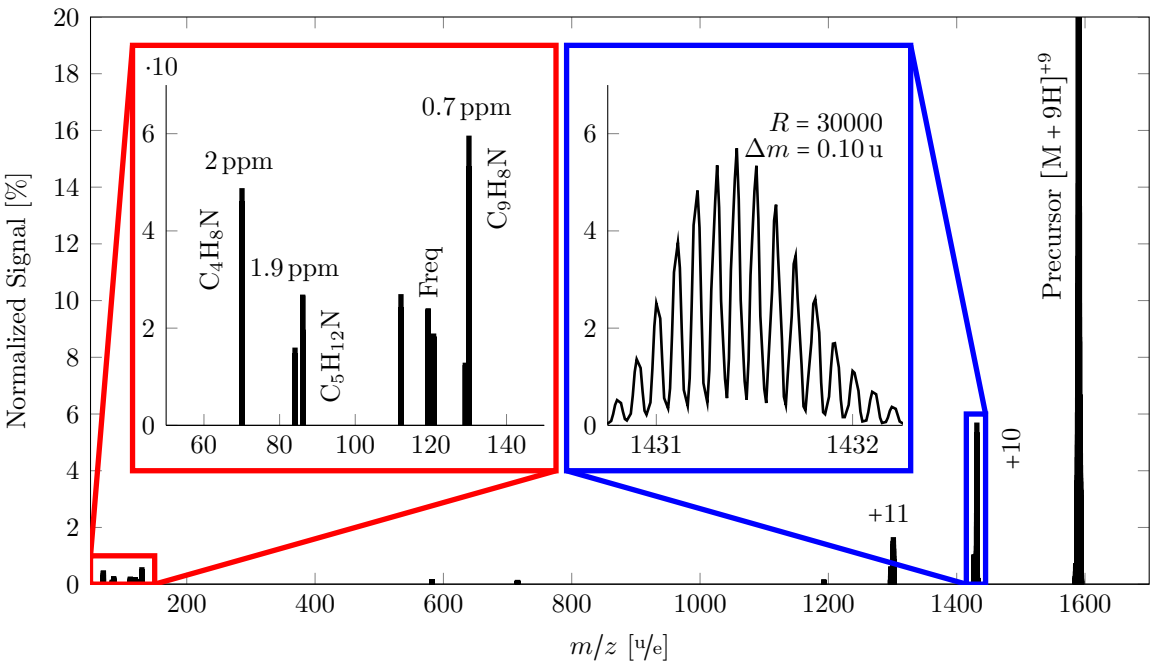

Figure 6.2: Fragmentation spectrum of lysozyme (m = 14305 u, nine-fold positively charged by protonation in the ESI process), activated by fs-LID. The left inset shows an enlarged section of the spectrum with the assignment and mass accuracy for selected fragments. The right inset shows the rich isotopic spectrum for photo-ionized Lysozyme (9-fold protonated, singly ionized).

30000. The resolution of the FT-ICR can be adjusted via software. The resolution is increased with increasing sampling time. Typical values of the resolution are between $R = 10{\cdot}10^3$ (survey scans) and $R = 10{\cdot}10^5$ (high-resolution scans) in the present experiments.

FT MS instruments provide an outstanding mass accuracy, which is specified in parts-per-million (ppm). For each mass signal, the accuracy denotes the difference between measured and calculated mass, normalized to the calculated mass. As depicted in the low mass region of Figure 6.2 (red inset), it is possible to assign mass/charge peaks to specific fragments with an accuracy on the order of 10^{-6}. For the mass signal at 86 u, the difference of the experimentally obtained mass m_{exp} = 86.09626 u and the calculated mass m_{calc} = 86.0964254 u (for $C_5H_{12}N$-e^-) is $|m_{exp} - m_{calc}| = 1.6 \cdot 10^{-4}$. Hence, the mass accuracy is $\frac{|m_{exp}-m_{calc}|}{m_{calc}}$ = 1.9 ppm in the selected mass range. Typical mass differences of different chemical species with identical nominal weight exceed 10 ppm. For example, to

distinguish N_2 (m_1 = 28.006148 u) from C_2H_4 (m_2 = 28.031300 u) at a nominal mass of m = 1000 u an accuracy of about $\left|\frac{m_1-m_2}{m}\right|$ = 25 ppm is required.

The red inset in Figure 6.2 also shows mass peaks in the low-mass region, annotated with "Freq". These peaks originate from electrical noise in the spectrometer. The "Freq" peak positions are known and do not affect the interpretation of the spectra.

The performance of the FT MS instrument in terms of resolution and accuracy allows to detect and assign mono-isotopic mass peaks. In addition, the isotope progression from natural (isotopically heterogeneous) samples can be compared to simulations to further increase the confidence in the peak assignment.

6.1.3 Molecular targets and data analysis

The combined femtosecond laser-Fourier transform mass spectrometer setup was used for peptide sequencing experiments. Different peptides with various charge states and the protein α-lactalbumin[2] were chosen as molecular targets, as summarized in Table 6.2.

All the molecules contain at least one aromatic amino acid (H, F, W, Y). The relatively large peptide Pep72 contains only one aromatic compound (F) in the center of its sequence. Histidine (H) and tryptophan (W) occur only in Pep73. The peptide 1P contains a phospho-marked serine, S[p] (a post-translational modification). 1P and Pep71 contain a phenylalanine at their N-terminus. In 1P no other aromatic compound occurs in the sequence.

A typical measurement consisted of a series of 50 consecutive MS scans. The scans were averaged and the centroids of the mass peaks were calculated by the Xcalibur software package (Thermo Fisher Scientific) prior to further data analysis. For all species, the ion target value in the LTQ was kept constant at $5 \cdot 10^5$. Measured fragment intensities were corrected for ion injection times and charge states of the detected signals to obtain corrected abundances, correlated to the actual number of ions. In the following, these numbers are referred to as *abundance*. The uncorrected signal of the FT mass analyzer is shown for FT spectra. Here, the signal will be normalized to the parent ion signal or to the maximum ion signal in the plotted range.

[2]This protein is abundant in milk and essential for digestion and is commonly studied [280, 281].

Sequence	Abbre-viation	Mono-isotopic mass [u]	Initial charge state (iCS)
MRFA	MRFA	524.264995	1+
FNDDFSR	Pep71	899.377334	1+ | 2+
VDEDQPFPAVPK	Pep72	1340.661219	1+ | 2+
LAAHPPSAFWR	Pep73	1251.651264	1+ | 2+ | 3+
FQS[p]EEQQQTEDELQDK	1P	2060.821174	2+
α-Lactalbumin (P00711)	aLact	14176.808756	9+

Table 6.2: Investigated molecules and corresponding abbreviations used in the current work. Lower case [p] denotes a post-translational modification (phosphorylation) of the preceding amino acid.

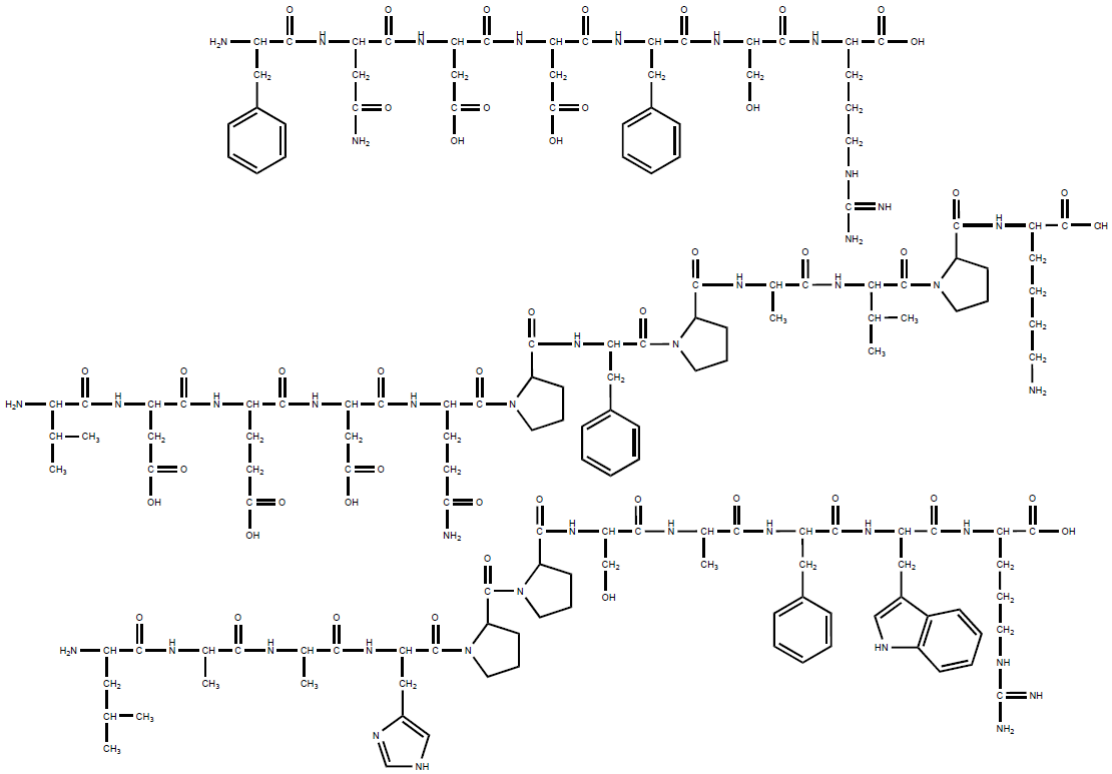

Figure 6.3: Structural formula of selected peptides from Table 6.2. Top to bottom: Pep71, Pep72, Pep73.

The peak assignment was supported by a home-built software. The programs suggested fragment compositions based on the known peptide sequence, accounting for the signal/noise (S/N) ratio and the accuracy of the assignment. Signals assigned here typically have S/N≥ 3 with an accuracy better than 10 ppm. The charge state assignment was performed by the FT MS instrument software and was manually confirmed by comparing the measured isotope progression to a calculated isotope progression.

A general survey of fragmentation patterns cannot be presented here, because the high density of mass peaks inhibits useful rendering. This is readily apparent, e.g., when considering the spectrum and the zoomed insets in Figure 6.2. Only for the two smallest peptides (MRFA (Figure 6.4) and FNDDFSR (Figure 6.12)), a survey spectrum is presented, showing the most abundant signals. For clarity, other fragmentation spectra are shown as snippets.

6.2 Experimental results

Fs-LID activation was investigated for a variety of peptides and the protein α-lactalbumin. In all cases, more than 50 % or, in some cases up to 98 % of the signal could be assigned to four major fragmentation channels, which will be referred to as *selected channels* in the following. These channels are important for peptide sequence elucidation and will be discussed in detail. The remaining signal results from small and unspecific fragments.

6.2.1 Fragmentation channels of MRFA

The fs-LID fragmentation of the small, singly charged model peptide MRFA (Figure 6.4) serves to illustrate the dominant fs-LID fragmentation channels. 40 ion signals with a signal/noise ratio larger than 3 could be identified. 25 of these signal peaks (63 %) were assigned with an accuracy better than 5 ppm. These signal peaks explain 88 % of the fragment signal. The signal assignment, the experimentally obtained mass, the fragment type, and its charge state are tabulated in Table 6.3. The assignment was used to annotate the fs-LID spectrum of MRFA as shown in Figure 6.4.

Peptide activation and subsequent dissociation by non-resonant femtosecond laser radiation

resulted in cleavages in the side chains of amino acids. SC fragments, e.g., M_γ or R^ϵ_α ions, were observed in the fs-LID spectra of MRFA. SC signals were especially large if the side chain contained a chromophore (R and F, see Table 6.3).

Fs-LID activation also lead to a stripping of single amino acids (1AAS). 1AAS fragments were detected for all amino acids in MRFA if the resulting m/z value was within the detectable mass range. 1AAS fragments dominantly occurred as immonium ions, i.e., amino acids that underwent a CO loss at the C-terminal with the charge located at the N-terminal. Therefore, the fs-LID spectrum showed signal peaks corresponding to M, R, and F. The immonium ion of alanine (A, m/z = 44.04948 u/e) was below the lower mass limit of the spectrometer and could not be observed.

A significant amount of fragments was assigned to amino acid dimers (2AAS), e.g., $M^\beta R^*$, $R_\alpha F$, and MR. The latter terminal fragment, which did not undergo a cleavage in its side chain, is a b_2 sequence ion. Note that short N-terminal sequence ions cannot be distinguished from 1AAS and 2AAS fragments. In the present case, the sequence of the peptides investigated is known and N-terminal fragments are denoted as such.

A large number of signal peaks was assigned to sequence ions (Seq), namely M (a_1, b_1), MR (a_2, b_2), FA (y_2), and RFA (y_3, z_3). b- and y-type fragments are most abundant.

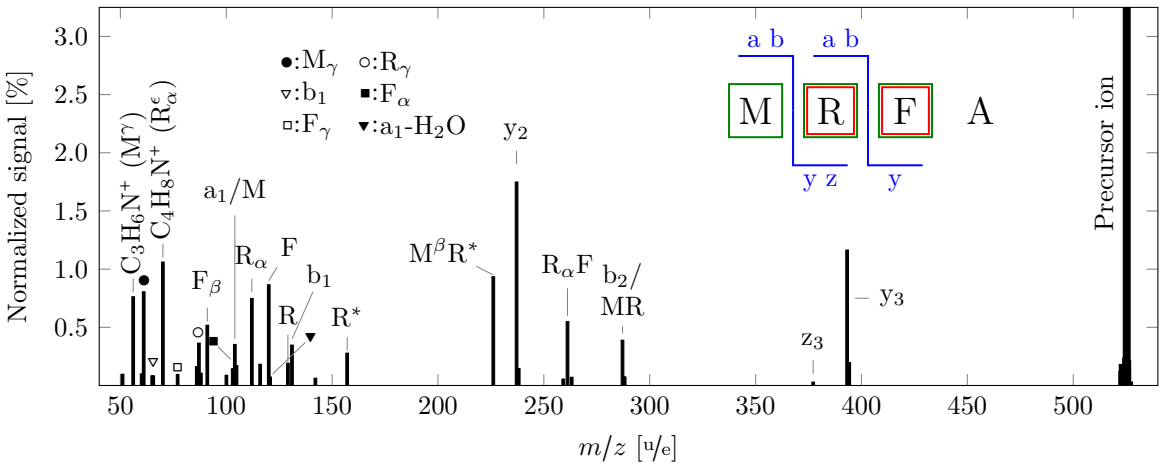

Figure 6.4: Annotated fs-LID fragmentation spectrum of MRFA (singly protonated), activated for 2 s with 2 mJ, 40 fs, 800 nm pulses. Sequence ions, 1AAS, 2AAS and SC fragments are labeled. The inset shows the short annotation of MRFA, marking the fragments observed. For clarity, 2AAS fragments are not indicated. Masses and abundance of the fragments can be found in Table 6.3.

m/z [u/e]	Fragment	CS	Abundance	m/z [u/e]	Fragment	CS	Abundance
All fragments			38660	**Amino acid dimers (2AAS)**			
				226.13113	$M^{\beta}R^{*}$	1+	2652
Side chain fragments (SC)				261.17221	$R_{\alpha}F$+H-e	1+	1557
56.04956	M^{γ}-H-e	1+	2165				
61.01066	M_{γ}-e	1+	2285	**Sequence ions (Seq)**			
70.06513	R^{ϵ}_{α}-e	1+	3011	65.51969	b_1-H/M*-e	2+	117
77.03858	F_{γ}-e	1+	269	104.05284	a_1/M+H-e	1+	1002
86.07128	R_{γ}-e	1+	461	120.56751	a_2-H_2O-H	2+	104
87.07856	R_{γ}+H-e	1+	1033	131.03993	b_1-2H/M*-H-e	1+	985
91.05368	F_{β}-e	1+	1469	237.12336	y_2+H	1+	4963
				238.13119	y_2+2H	1+	414
Single amino acid fragments (1AAS)				287.14104	b_2-H/MR*-e	1+	1104
103.05423	F_{α}-H-e	1+	408	288.14887	b_2/MR*+H-e	1+	208
112.08693	R_{α}-H-e	1+	2124	377.20575	z_3	1+	83
120.08078	F+H-e	1+	2457	393.22448	y_3+H	1+	3304
129.11348	R+H-e	1+	543	394.23230	y_3+2H	1+	558
157.10898	R*+H-e	1+	788				

Table 6.3: Fragment ion mass, assignment, charge state (CS), and abundance for fs-LID fragmentation of MRFA (singly protonated), activated for 2 s with 2 mJ, 40 fs, 800 nm pulses. The assignment was used for the annotation of Figure 6.4.

These fragments are particularly important for primary structure (amino acid sequence) elucidation of peptides and proteins. In conjunction with the 2AAS fragment $R_{\alpha}F$, the sequence ions yield complete sequence coverage for MRFA.

Charging of the precursor and its fragments

The b_1 and a_2 sequence fragments were also observed in charge state 2+, which is higher than the initial parent ion charge state of 1+ (Table 6.3). The isotope progression could be used to verify the charge state of the b_1 fragment. The a_2 fragment has a low abundance and lacks isotope peaks. Nevertheless, the accuracy of the assignment (2.3 ppm) allows a clear assignment.

Charging of the intact parent molecule (precursor) was not observed for MRFA. For larger peptides, the precursor charging (PC) channel could be identified. Pep73 in CS +1, activated by fs-LID, showed a signal from the doubly charged parent ion $[M+H]^{2+}$-CO_2 and the triply charged parent ion $[M+H]^{3+}$-CO_2. Upon activation of Pep73 in CS +2, the triply charged species $[M+2H]^{3+}$-CO_2 was observed. Activation of singly charged Pep71 and Pep72 also resulted in $[M+H]^{2+}$-CO_2 formation. In both cases, the triply charged species ($[M+2H]^{3+}$) could only be generated from the doubly protonated parent ion and does not show a loss of CO_2. For details on Pep73, see Section 6.2.3.

It should be noted that precursor charging occurs with different propensities for different peptides and is most prominent for Pep73 and the large peptide 1P. The PC channel contributes up to 23 % of fs-LID products for Pep73 and 1P, but less than 2 % for all other peptides when 3 mJ, 40 fs laser pulses are used for activation.

6.2.2 Experimental parameters

As presented in Section 6.1.1, the activation laser delivered 800 nm, 40 fs pulses with 3 mJ pulse energy and was operated at a repetition rate of 1 kHz. The laser peak intensity in the mass spectrometer was estimated from the laser parameters and focal conditions to be about $1 \cdot 10^{15}\,{}^{\mathrm{W}}/_{\mathrm{cm}^2}$.

Several experimental parameters were varied to obtain information about the fragmentation characteristics of proteins interacting with high-intensity ultrashort laser fields. The parameters include the size and initial precursor charge state (CS) of the protein targets, and laser parameters like pulse duration, pulse intensity and activation time.

In the following sections, a systematic study of how these parameters influence the fragmentation patterns is described. The analysis is presented for a subset of molecules, but agrees with the findings for all investigated species.

Laser intensity

The laser intensity $I \propto \frac{E}{\tau \cdot A}$ can be varied by changing the laser pulse duration τ, while maintaining constant pulse energy E or through tuning the pulse energy, while maintaining

	2 mJ	2.5 mJ	3 mJ
All fragments	3939	37656	35648
SC	0 (0)	500 (1)	428 (1)
1AAS	303 (1)	12847 (4)	13034 (4)
2AAS	0 (0)	1767 (4)	1117 (3)
Seq	459 (6)	13030 (32)	10452 (25)
PC(-CO_2)	1482	2301	3603
Selected channels	2244	30445	28634

Table 6.4: Abundance for Seq ions, 1AAS and 2AAS fragments, SC fragments, and PC(-CO_2) species. The values in brackets give the number of distinct fragments observed. The phosphopeptide 1P was irradiated with three different laser pulse energies for 2 s of activation time with a laser pulse duration of 40 fs.

constant pulse duration. First, the pulse energy was adjusted by using a short pulse attenuator consisting of a thin film polarizer and a waveplate. Later the laser pulse duration was varied by detuning of the grating compressor. Due to the non-resonant character of the activation processes, the resulting chirp is not expected to have a significant influence on the ionization or the fragmentation efficiency.

Variation of the pulse energy between 2 mJ and 3 mJ for an activation time of 2 s and a laser pulse duration of 40 fs altered the fragment abundance significantly as it is shown in Table 6.4 for the doubly charged peptide 1P. Almost an order of magnitude more fragments were observed when the laser pulse energy was increased from 2 mJ to 2.5 mJ. Only the PC channel is of comparable strength for the different pulse energies.

The PC channel was dominant for the lowest pulse energy of 2 mJ and created 38 % of all observed fragments. A smaller amount of sequence ions and a 1AAS fragment was observed (12 % and 8 %, respectively). 2AAS and SC fragments did not contribute to the fragment signal. About 57 % of the generated fragments resulted from the selected activation channels introduced in Section 6.2.1.

For higher pulse energies of 2.5 mJ and 3 mJ, Seq ions and 1AAS fragments were responsible

Table 6.5: Abundance for Seq ions, 1AAS and 2AAS fragments, SC fragments, and PC(-CO_2) species. The values in brackets give the number of distinct fragments observed. The phosphopeptide 1P was irradiated with two different laser pulse durations for 5 s of activation time with a laser pulse energy of 3 mJ.

	200 fs	40 fs
All fragments	40533	40469
SC	0 (0)	727 (1)
1AAS	9402 (4)	13988 (5)
2AAS	2018 (3)	2727 (3)
Seq	17248 (21)	13891 (14)
PC(-CO_2)	502	810
Selected channels	29169	32188

for 66 % and 69 % of the fragment signal. 2AAS fragments (5 % and 3 %), SC fragments (1 % for both energies), and PC ions (6 % and 10 %) formed a minor contribution. About 80 % of the generated fragments resulted from the selected channels.

Increasing the pulse energy from 2 mJ to 2.5 mJ and 3 mJ increased the number of PC ions by a factor of 1.5 and 2.4, respectively. The abundance of 1AAS fragments was enhanced by a factor of 43, as compared to low pulse energy. For Seq ions, the factor was about 25.

The 1AAS channel showed a comparable yield for both of the highest pulse energies (abundance of 12847 and 13034) and four distinct 1AAS fragments were identified. This number must be compared to the number of distinct amino acids in 1P. The peptide 1P consists of 12 amino acids, of which eight are distinguishable. I.e., 50 % of the amino acids can be identified with the current experimental parameters. 2.5 mJ pulses resulted in slightly more 2AAS fragments (abundance of 1767 and 1117), as compared to 3 mJ pulses. Also the number of distinct 2AAS fragments decreased from four to three. The same trend was observed for Seq ions (abundance of 13030 and 10452). The number of distinct Seq ions decreased from 32 to 25, when the pulse energy was increased from 2.5 mJ to 3 mJ. For both pulse energies only one SC fragment was observed, with a comparable but low abundance.

Table 6.5 shows results for peptide 1P, activated by non-resonant femtosecond laser pulses with pulse durations of 200 fs and 40 fs, respectively. To ensure sufficient signal intensities with the longer pulse duration, the activation time had to be set to 5 s and the pulse energy was kept at 3 mJ. Both pulse durations then generated a similar amount of fragments (abundance of about 40500) of which 72 % (200 fs pulses) and 80 % (40 fs pulses) contributed to the selected fragmentation channels.

A pulse duration of 200 fs resulted in 21 Seq ions with an abundance of 17248 and 4 1AAS fragments with an abundance of 9402. Three ions were assigned to 2AAS fragments (abundance of 2018) and ions stemming from the PC channel (abundance of 502). Fragments originating from side chain cleavages (SC) were not observed.

Shortening the pulse duration to 40 fs resulted in 14 different Seq ions with an overall abundance of 13891 and five 1AAS fragments with an abundance of 13988. The 2AAS and PC channels contributed 2727 and 810 ions to the signal. Also one side chain fragment (abundance of 727, F_β at $m = 91.05368$ u) was observed.

Activation time

The fragmentation patterns were studied for different activation times with 3 mJ pulse energy and 40 fs pulse duration. The applied activation times of 50 – 2000 ms correspond to activation by 50 to 2000 laser pulses. Precursor ion abundances are shown in Figure 6.5 as a function of fs-LID activation time. After 2 s of activation, the precursor ions were mostly depleted. The abundance of detected fragment ions reached up to 25 % of the initial precursor abundance.

In the case of Pep73, the number of detected fragments reached a maximum at 1 s, while Pep71 and Pep72 showed a monotonous fragment increase up to 2 s activation time. The abundance of fragment ions exceeded the number of precursor ions after activation times of 1000 ms for the largest peptide (Pep73). For Pep71 and Pep72 this happened after 1500 ms and 1250 ms, respectively. The protein aLact (Figure 6.5, right) in charge state 9+ was almost completely depleted after 1 s of activation and the abundance of fragments observed reached about 50 % of the initial precursor abundance. The fragment signal exceeded the precursor signal after 250 ms.

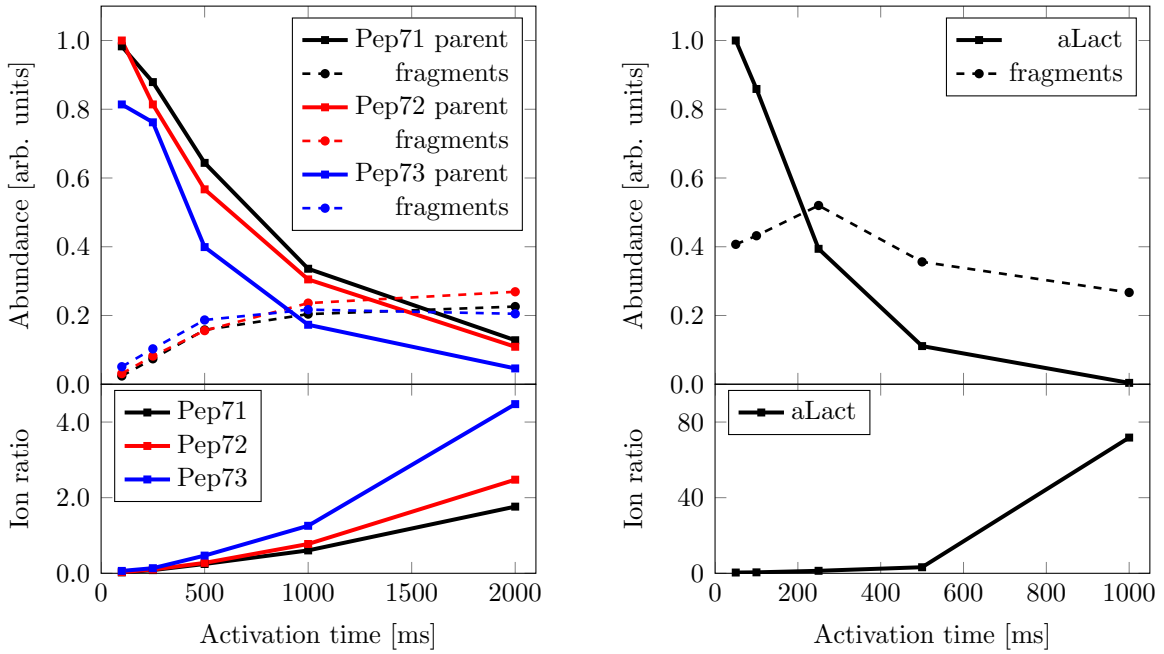

Figure 6.5: Relative number of precursor ions and fragments for several peptides (left) and aLact (right) as a function of activation time. The ion ratio denotes the fragment abundance with respect to the precursor abundance.

Figure 6.5 suggests that the efficiency to generate detectable fragments scales with the size of the precursor. Figure 6.5 also shows that the sum of precursor and fragment ions decreases significantly with increasing activation time.

For sequence elucidation, Seq ions and 1AAS/ 2AAS fragments are of particular value. It is therefore useful to consider the relative abundance of these fragments as a function of the activation time. Figure 6.6 compares the abundance of fragments in different types of activation channels. The plot considers the abundance of Seq ions, 1AAS and 2AAS fragments, fragments stemming from side chain cleavages (SC), and the PC channel. The sum of ions in these channels accounted for about 75 % (1000 ms activation time) and up to 98 % (500 ms activation time) of all fragments observed. Pep71, Pep72 and 1P exhibit a monotonous increase of fragment abundance with activation time, while Pep73 shows maximal fragment abundance at 1 s.

The contribution from Seq ions as compared to the overall fragment signal was about 45 %

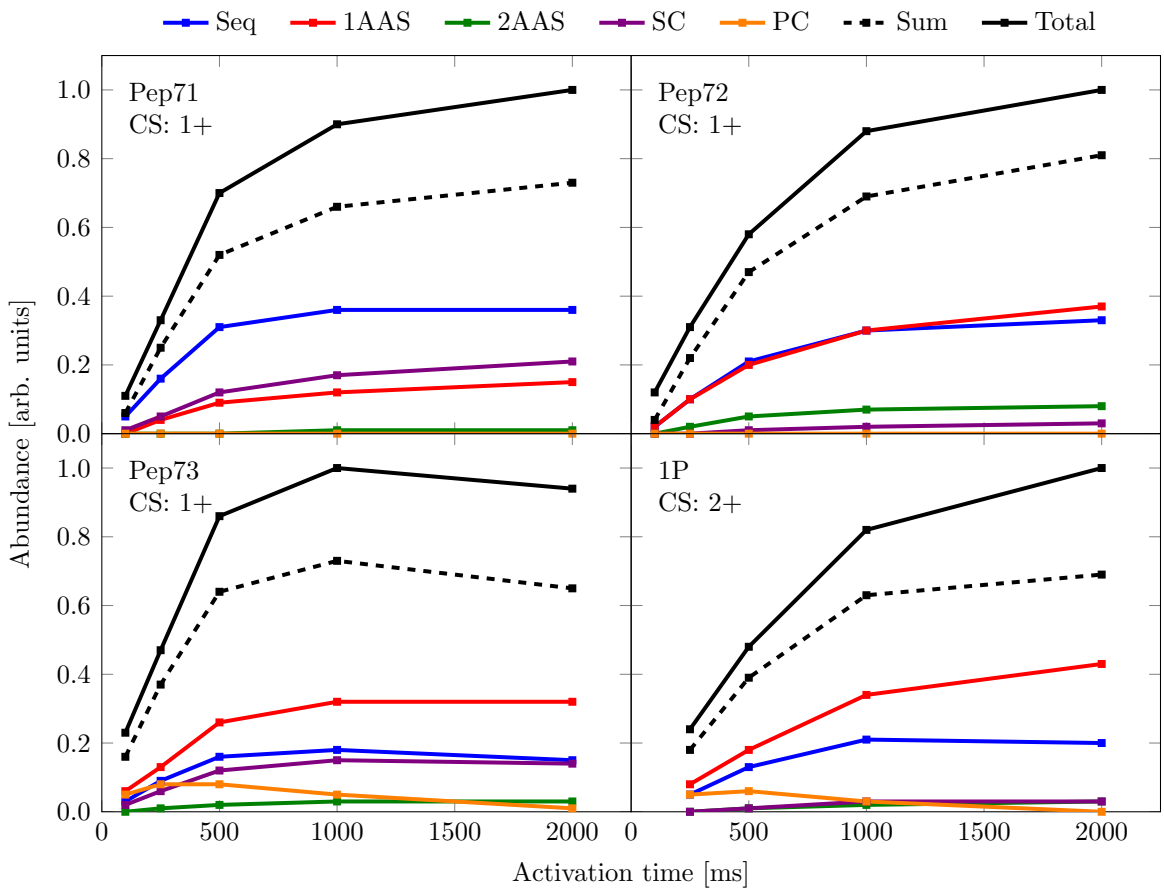

Figure 6.6: Abundance of Seq ions, 1AAS and 2AAS, SC fragments and PC species for selected peptides. The sum of these activation channels and the total number of fragments as a function of activation time is also indicated. CS denotes the initial precursor charge state.

(Pep71), 35 % (Pep72), 20 % (Pep73), and 25 % (1P) at activation times of 250 – 1000 ms. The contribution from 1AAS fragments was weaker for Pep71 (15 %), at a comparable level for Pep72 (35 %) and stronger for Pep73 (30 %) and 1P (40 %). The 1AAS channel increased with respect to the overall fragment signal as a function of peptide mass. 2AAS fragments were observed for all investigated peptides and showed the largest contribution for Pep72 (about 8 %). For the peptide Pep73 (containing W), precursor charging with accompanying loss of CO_2 gave a strong contribution of about 23 % at short activation times. Another prominent fragmentation channel for all peptides was side chains cleavage (SC). The relative contribution of SC fragments was 20 % for Pep71 and 15 % for Pep73.

Initial charge state

The initial charge state (CS) also affected the peptide fragmentation behavior. Figure 6.7 shows the number of precursor ions and fragment ions as a function of laser activation time for Pep73 in various charge states. The number of precursor ions in the ICR cell before activation was dependent on the selected charge state due to the transfer efficiency from the linear ion trap into the ICR cell. To meaningfully compare the precursor and fragment abundance for different charge states, the values in Figure 6.7 are normalized to the precursor abundance at the lowest irradiation time of 100 ms. This assumes that Fs-LID does not lead to extensive fragmentation within the first tens of milliseconds of activation for moderately large peptides.

The precursor depletion efficiency was slightly higher for higher initial CS. The maximum fragment abundance was reached at 1 s for all charge states. The doubly charged species (CS 2+) exhibited the lowest fragment abundance. Comparison of the fragment abundance to the precursor abundance (Figure 6.7, lower panel) indicates that the ratio of detectable fragments with respect to the precursor after activation increases with increasing CS. While the number of detectable fragments relative to the precursor abundance was equal for the lowest initial precursor charge states up to 1 s of fs-LID activation, it was always

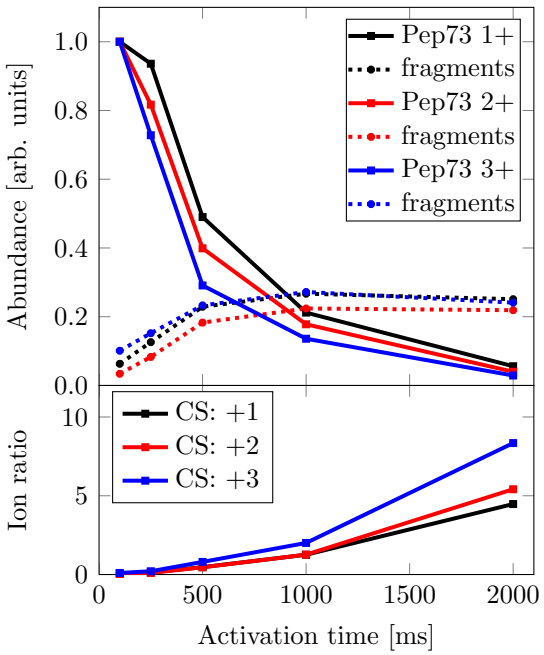

Figure 6.7: Fs-LID efficiency for three different initial charge states of the precursor (Pep73, upper panel) and the corresponding fragment/precursor ion ratio (lower panel). For better comparison, the values in the upper panel are normalized such that the precursor abundance at the lowest irradiation time of 100 ms equals one for all charge states.

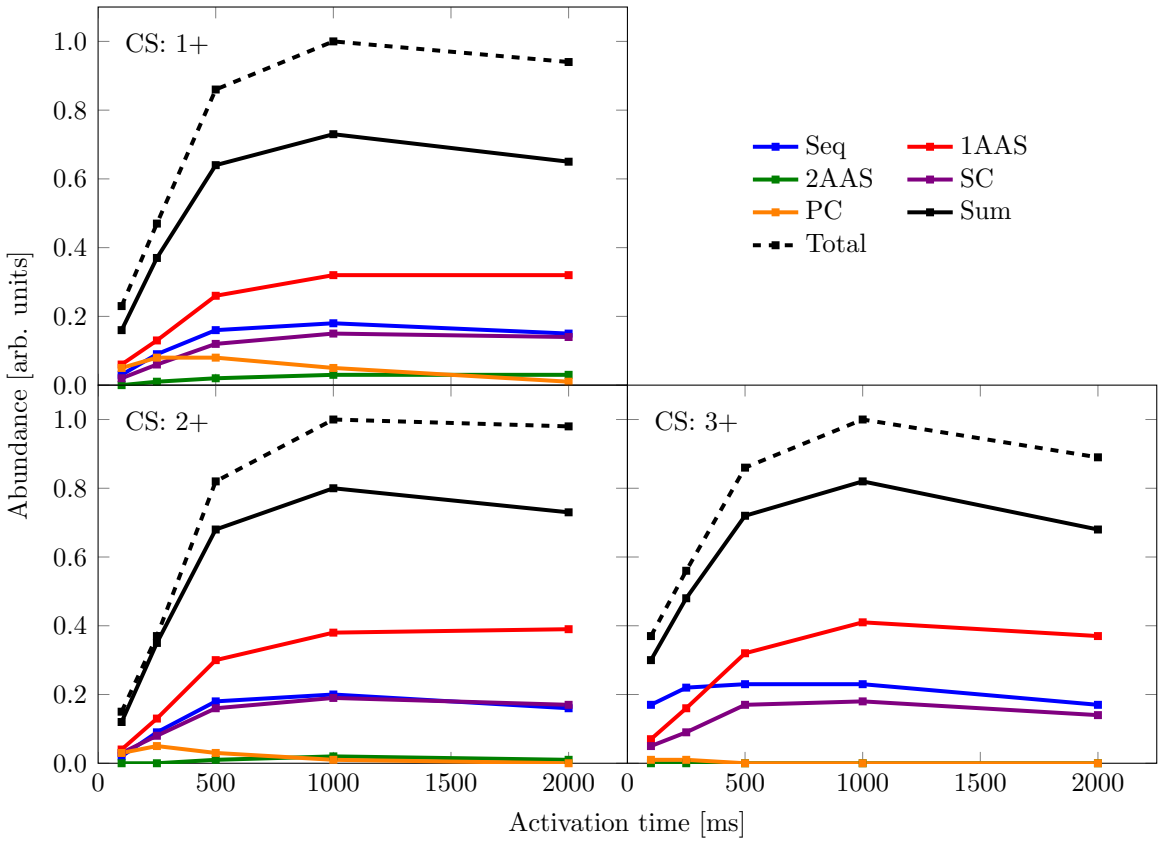

Figure 6.8: Abundance of selected channels for different iCS of the Pep73 precursor. Dashed black curves show the abundance of all detected fragments and are equal to the dashed curves in Figure 6.7.

higher for CS: 3+. At long irradiation times of 2 s, the fragment/precursor ratios were 1/2 : 2/3 : 1 for CS: 1+, 2+, and 3+, respectively.

Fragment abundances were also analyzed separately for Seq, 1AAS and 2AAS, SC and PC channels (Figure 6.8). For all precursor charge states and all activation times, the 1AAS fragment abundance was dominant and contributed almost 30 – 40 % to the total fragment signal. About 20 % of the fragments were Seq ions. In the case of precursors in CS 3+ and activation times of 100 – 250 ms the contribution of Seq ions exceeded that of 1AAS fragments. The probability to generate 2AAS fragments decreased with increasing initial charge state. The strongest contribution (3 %) of this species was reached at 1000 ms for charge state 1+. SC fragments showed a comparable contribution of about 15 % for all charge states. The relative abundance of the PC channel $[\mathrm{M}{+}n\mathrm{H}\text{-}\mathrm{CO}_2]^{(n+1)+}$ with

respect to the total abundance of fragments decreased with increasing charge state of the precursor ion and was prominent at small activation times of 100 – 250 ms. The PC channel contributed 23 % and 18 % for CS 1+, 19 % and 14 % for CS 2+, and 3 % and 2 % for CS3+.

6.2.3 Pathway reconstruction

The selected activation channels showed a similar evolution as a function of activation time at activation times larger than 500 ms (Figure 6.6, Figure 6.8), but the relative abundance of specific fragments, within these channels, exhibited a more complex temporal behavior (Figure 6.9) due to sequential fragmentation processes. One decomposition pathway of the phenylalanine compound in Pep72 was analyzed in detail (Figures 6.9, 6.10).

Pep72 contains a phenyalanin (F) in the center of its sequence. No other phenyl compound is present in the molecule. The abundance of the phenyl fragment, as well as the abundance of some decomposition-related fragments as a function of activation time is plotted in Figure 6.9. The chemical structure of these fragments and a possible fragmentation sequence is depicted in Figure 6.10. The strongest signal stems from the singly protonated precursor $[M+H]^+$. This signal is about 500 times higher in the first 500 ms than that of all fragments considered here. The precursor shows an exponential decay as a function of activation time. The PC channel leads to formation of the doubly charged species $[M+H]^{2+}$-CO_2. As the precursor depletes, the formation of the PC ion ceases and the $[M+H]^{2+}$-CO_2 abundance decreases due to further fragmentation.

The generation of the 1AAS fragment $[F+H]^+$, the corresponding amino acid fragment exhibiting SC loss ($[F_\beta]^+$), and the Seq ion y_7 is delayed and sets in before 250 ms. These three fragments can be generated directly from the protonated precursor $[M+H]^+$. As their formation is delayed, the dominant generation process probably involves two separate laser pulses. The first pulse further ionizes the precursor to form the doubly charged precursor $[M+H]^{2+}$-CO_2 and the second laser pulse fragments the PC ion to yield $[F+H]^+$, $[F_\beta]^+$, and y_7. These fragments might also be generated by other fragments (some long-lived intermediates) as the abundance of the singly and doubly charged precursor decreases stronger at longer activation times. The yield of $[F+H]^+$ and $[F_\beta]^+$ continues to increase after the decomposition of the $[M+H]^{2+}$-CO_2 species already set in (after 500 ms). The

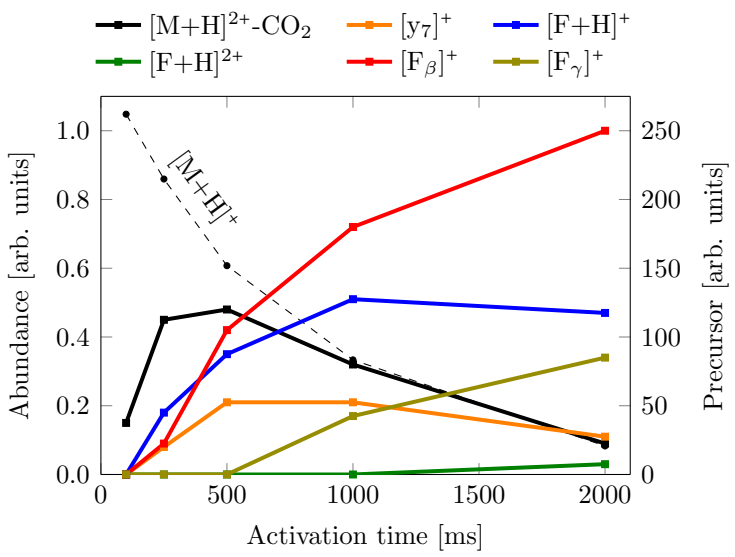

Figure 6.9: Abundance of selected fragments as a function of irradiation time (Pep72). The Figure depicts the scaled abundance of parent ions, as well as several AAS fragments, the doubly charged precursor and the singly charged Seq ion y_7.

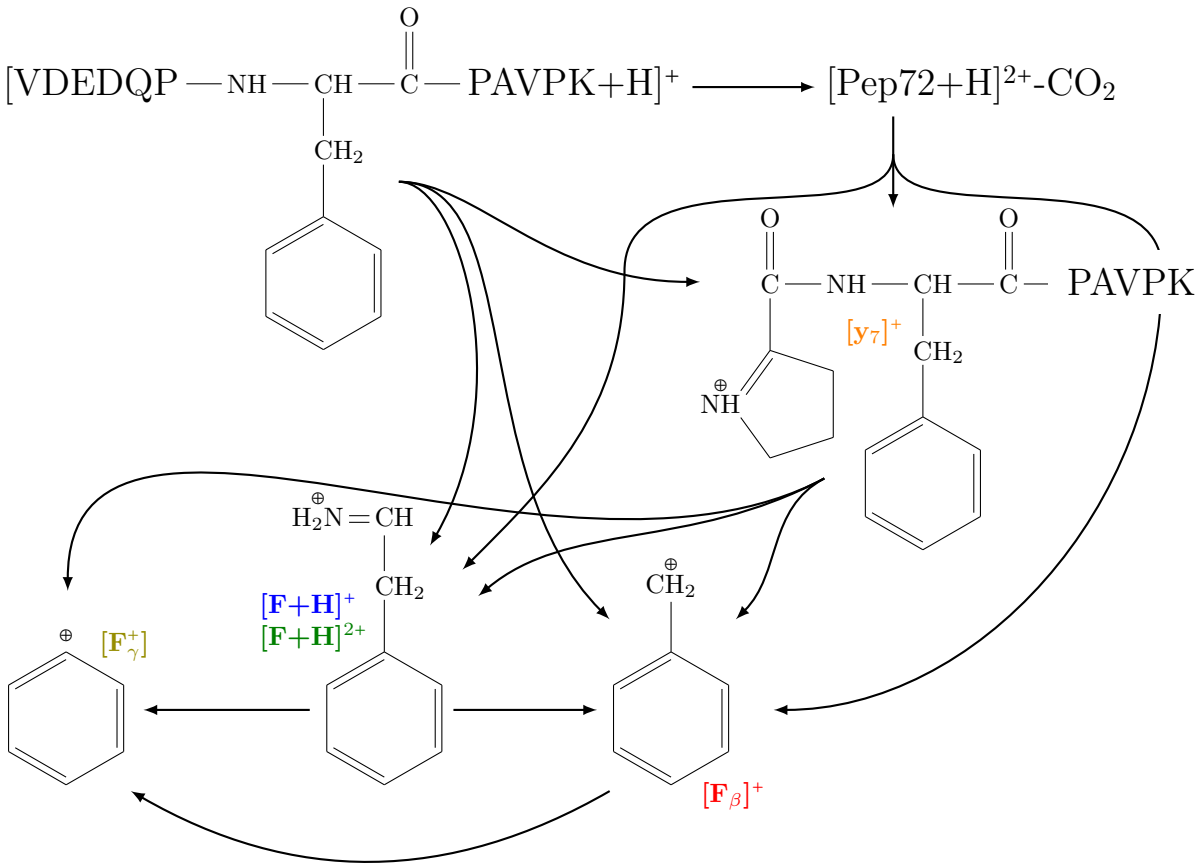

Figure 6.10: A decomposition pathway of Pep72 leading to phenyl fragment production. See Figure 6.9 for the dynamic measurement of the fragments.

abundance of the Seq cation y_7 follows mainly the decrease of its doubly charged precursors $[M+H]^{2+}$-CO_2, but the decrease is not as strong.

The generation of $[F_\gamma]^+$ only starts after 500 ms. Apparently, it is not directly generated from the precursor but through a secondary activation process. The fragments y_7 and $[F+H]^+$ must be abundant before the generation of $[F_\gamma]^+$ sets in. On the other hand, when the former two reach saturation the latter still increases. $[F\gamma]^+$ can also be generated from $[F_\beta]^+$, which exhibits increasing yield for all activation times and seems to be one of the most important precursors for $[F\gamma]^+$.

Another interesting fragment is the doubly charged phenylalanine $[F+H]^{2+}$. This fragment can only be seen at very long activation times of 2 s when the yields of the singly charged $[F+H]^+$, that of y_7 and that of the singly and doubly charged precursor $[M+H]^{2+}$-CO_2 decreased. Therefore, $[F+H]^{2+}$ cannot be directly produced from the precursors or y_7. This indicates that fs-LID, although with low probability, further charges the fragment $[F+H]^+$ after it was created.

6.2.4 Dominant fragments

Tables 6.6, 6.7 and 6.8 display the most abundant fragments for the peptides Pep71, Pep72 and Pep73 (see Table 6.2) after femtosecond laser-induced dissociation. Fragment signals originating from terminal amino acids, e.g., R_α and R_γ (C-terminal Pep71), K_α, K_β and K^* (C-terminal Pep72), V_α (N-terminal Pep72), L (N-terminal Pep73), were always strong. Fragments from amino acids which occur multiple times in the peptide sequence also show a strong contribution to the fragmentation spectra, e.g., D (Pep71), P and V_α (Pep72), and P (Pep73). Aromatic amino acids and amino acids bearing an extended π system (protonated guanidyl groups and amide groups) in their side chain also lead to strong fs-LID signals, e.g., the N_α and arginine (R) fragments from Pep71, the Q_α fragment from Pep72 and the H, W_β, H_β and F_γ fragments from Pep73.

As shown in Section 6.2.2, a minor part of the dominant fragments stemmed from Seq ions: y_2 (Pep71) and b_2, y_2, and $a_2(\text{-}H_2O)/y_5^{3+}$ (Pep72). Larger Seq ions probably fragmented into smaller compounds (1AAS and SC fragments) and were therefore not prominently observed.

Mass [u]	Fragment	Type	Abundance	Terminus	Quantity	Side chain/ character
120.08078	F+H-e	1AAS	18.5	N	2	•
91.05368	F_{β}-e	SC	5.5	N	2	•
70.06513	R^{ϵ}_{α}-e	SC	4.9	C		■
175.11895	y_1+H	Seq	4.4	C		■
103.05000	F_{α}-H-e	1AAS	2.9	N	2	•
70.02874	N_{α}-H-e	1AAS	2.5			□
112.08693	R_{α}-H-e	1AAS	2.5	C		■
87.07856	R_{γ}+H-e	SC	2.5	C		■
88.03931	D+H-e	1AAS	2.5		2	
262.15098	y_2+H	Seq	2.3			■

Table 6.6: The most prominent assignable fs-LID fragments for Pep71 (40 fs, 3 mJ activation). The abundance is presented as percentage of the total amount of fragments, averaged over three activation times (250 ms, 500 ms and 1000 ms). The symbols indicate: • (side chain aryl group), □ (side chain amide group) and ■ (side chain guanidyl group).

Mass [u]	Fragment	Type	Abundance	Terminus	Quantity	Side chain/ character
70.06513	P+H-e	1AAS	19.0		3	
72.08023	K_{β}-e	SC	12.6	C		
84.04439	Q_{α}-H-e	1AAS	3.7			□
215.10263	b_2	Seq	3.3			
244.16556	y_2+H	Seq	3.1			
84.08078	K_{α}-H-e	1AAS	2.8	C		
55.05423	V_{α}-H-e	1AAS	2.8	N	2	
169.09715	$a_2(\text{-}H_2O)/y_5^{3+}$	Seq	2.7			
226.15500	y_2(-OH)	Seq	2.1			
129.10224	K*+H-e	1AAS	1.8	C		

Table 6.7: The most prominent assignable fragments for fs-LID activation of Pep72. For parameters and definition of symbols see Table 6.6.

Mass [u]	Fragment	Type	Abundance	Terminus	Quantity	Side chain/ character
70.06513	P+H-e	1AAS	13.4		2	
110.07127	H+H-e	1AAS	9.4			•
130.06458	W_β-e	SC	4.4			•
86.09642	L+H-e/a_1	Seq	4.0	N		
87.07856	R_γ+H-e	SC	3.4	C		■
112.08693	R_α-H-e	1AAS	2.5	C		■
159.10023	z_1	Seq	1.9	C		■
81.04417	H_β-e	SC	1.7			•
77.03858	F_γ-e	SC	1.6			•
175.11895	y_1+H	Seq	1.6	C		■

Table 6.8: The most prominent assignable fragments for fs-LID activation of Pep73. For parameters and definition of symbols see Table 6.6. The PC channel is not included.

All 1AAS immonium ions (loss of carbonyl group) carried an extra hydrogen atom. The y-type Seq ions also contained an additional hydrogen. In contrast, α-type 1AAS fragments showed hydrogen loss. The SC fragments occurred without modification. An exception is R_γ, which is a strong base and bears an additional proton from the ESI process.

Amino acid fragments

The abundance of amino acid fragments varies strongly when peptides are activated by fs-LID. Table 6.9 presents the fragment abundances for all amino acids in Pep71, Pep72, and Pep73. If the amino acid occurred more than one time in the sequence, the corresponding signal was normalized according to the number of occurrence. The abundances shown represents the sum for spectra at five activation times (100 – 2000 ms). Each stated amino acid abundance is the sum of the signals from the immonium fragment, the α-type ion, and the side chain ion.

The two dominant amino acids signals for Pep71 stemmed from phenylalanine (F) and arginine (R). These amino acids have an extended electronic π system in their side chain:

Pep71		Pep72		Pep73	
Amino acid	Abundance	Amino acid	Abundance	Amino acid	Abundance
F	49626	V	30531	H	49215
R	45240	P	26164	R	30957
N	16691	Q	20877	P	28127
D	4562	K	13005	F	21359
S	3533	F	10047	W	18108
		E	5541	L	16392
		D	2661	S	1909

Table 6.9: Sum of amino acid fragments contribution (1AAS immonium + α-type 1AAS + SC) for Pep71, Pep72, and Pep73 activated by fs-LID (3 mJ laser pulse energy and 40 fs laser pulse duration). The contributions are summed over activation times of 100 – 2000 ms. The numbers were divided by the amino acid occurrences in the sequence.

The electrons are delocalized over several bonds. Asparagine (N), which bears an amide group in its side chain, also showed a large signal, although less strong than F and R. The abundance of aspartic acid (D) and serine (S) was weak.

Observations for Pep72 are quantitatively similar to those for Pep71. Amino acids with delocalized electronic systems in their side chain (glutamine (Q), lysine (K), and F) showed a large fs-LID signal, while the abundance of non-aromatic amino acids (glutamic acid (E), and D) was low. Exceptions were found for proline (P) and valine (V). The strong signal from valine may be explained by the fact that valine is the N-terminal amino acid and only a single bond has to be cleaved to create the valine fragment. Part of the apparent valine signal can also be generated from the K_β side chain fragment, as both compounds have the same mass ($m(C_4H_{10}N) = 72.08077\,\mathrm{u}$). As both compounds are isobaric, the fragment assignment is unclear. Enhanced cleavages at P sites is known to occur in other activation methods and is attributed to the large proton affinity of proline [228].

In Pep73, aromatic amino acids (histidine (H), tryptophane (W), and F) and R with a guanidyl group in its side chain dominated the amino acid signal. W has the largest delocalized electronic system but was less abundant than expected. P fragments were again very abundant, presumably due to the large proton affinity. Other amino acids (leucine (L) and S) gave less signals.

Early fragments

Fs-LID generated only a small amount of fragments within the first 100 ms of activation. Due to the small size of the laser focus and the larger size of the ion cloud in the spectrometer, it is expected that each molecule predominantly interacts with a single laser pulse. It might thus be helpful to analyze Seq ions created in the beginning of the activation process (Table 6.10) to elucidate cleavage mechanisms without the complication of sequential processes.

Table 6.10: Ion abundance generated within the first 100 ms of fs-LID activation (40 fs, 3 mJ, 100 ms) for Pep71, Pep72 and Pep73.

m/z [u/e]	Accuracy	Fragment	Type	Abundance
Pep71 (FNDDFSR)				
120.08072	0.4 ppm	a_1 /F+H-e	Seq/1AAS	3765
175.11909	0.8 ppm	y_1+H	Seq	591
70.06497	2.3 ppm	R^{ϵ}_{α}-e	SC	508
91.05411	1.2 ppm	F_{β}	SC	453
409.22119	4.4 ppm	y_3+H	Seq	280
262.11979	4.5 ppm	b_2	Seq	264
780.31029	9.0 ppm	x_6	Seq	240
262.15147	1.9 ppm	y_2+H	Seq	225
270.12059	3.4 ppm	x_2-H_2O-H	Seq	212
112.08689	0.3 ppm	R_{α}-H-e	1AAS	205
103.05414	1.0 ppm	F_{α}-H-e	1AAS	155
246.13322	3.9 ppm	z_2	Seq	133
245.12505	2.5 ppm	z_2-H	Seq	43
428.19973	6.3 ppm	$[M+H]^{2+}$ -CO_2	PC	11
524.24732	1.9 ppm	y_4+H	Seq	6

Table 6.10 continues on next page.

Table 6.10 continued from previous page.

m/z [u/e]	Accuracy	Fragment	Type	Abundance
Pep72 (VDEDQPFPAVPK)				
70.06497	2.2 ppm	P+H-e	1AAS	2150
72.08063	2.0 (2.1) ppm	a_1/ V+H-e/(K_β)	Seq/1AAS/SC	1557
244.16627	2.9 ppm	y_2+H	Seq	368
215.10306	2.0 ppm	b_2	Seq	265
169.09729	0.8 ppm	a_2-H_2O/y_5^{3+} -3H-2e	Seq	172
271.15313	1.8 ppm	x_2	Seq	165
226.15562	2.7 ppm	y_2-OH	Seq	136
648.84280	5.8 ppm	$[M+H]^{2+}$-CO_2	PC	101
243.15869	3.9 ppm	y_2	Seq	71
649.34578	4.3 ppm	$[M+H]^{2+}$-CO_2 (isotope)	PC	61
245.07737	2.3 ppm	DE+H-e	2AAS	47
511.32868	9.4 ppm	y_5+H	Seq	21
587.23824	12.8 ppm	b_5	Seq	12
Pep73 (LAAHPPSAFWR)				
70.06500	1.8 ppm	P+H-e	1AAS	3354
604.33914	8.4 ppm	$[M+H]^{2+}$-CO_2	PC	3143
110.07119	0.7 ppm	H(His)+H-e	1AAS	2520
604.84102	4.3 ppm	$[M+H]^{2+}$-CO_2 (isotope)	PC	2292
130.06507	0.5 ppm	W_β	SC	1434
87.07894	1.9 ppm	R_γ+H-e	SC	1076
86.09629	1.5 ppm	a_1/ L+H-e	Seq	1011
605.34295	0.4 ppm	$[M+H]^{2+}$ -CO_2 (isotope)	PC	761
159.10031	0.5 ppm	z_1	Seq	533
112.08684	0.7 ppm	R_α-H-e	1AAS	527

Table 6.10 continues on next page.

Table 6.10 continued from previous page.

m/z [u/e]	Accuracy	Fragment	Type	Abundance
1050.56728	14.6 ppm	a_{10}	Seq	415
175.11923	1.6 ppm	y_1+H	Seq	353
120.08066	0.8 ppm	F+H-e	1AAS	342
909.50606	13.1 ppm	c_9+2H-e	Seq	253
393.22643	5.0 ppm	b_4	Seq	241
1051.56922	8.2 ppm	a_{10} (isotope)	Seq	220
185.12866	1.1 ppm	b_2	Seq	216
158.11638	1.1 ppm	y_1-O/R*+2H-e	Seq/1AAS	215
159.09177	0.6 ppm	W+H-e	1AAS	182
562.28437	16.1 ppm	y_{10}^{2+}-O+2H	Seq	145
1121.59734	29.8 ppm	y_{10}-OH	Seq	56
562.78617	1.3 ppm	z_{10}^{2+}+2H	Seq	38
413.21814	30.0 ppm	z_7^{2+}-H_2O	Seq	33
576.30787	29.5 ppm	x_{10}^{2+}-O+2H	Seq	30
583.78222	3.8 ppm	x_{10}^{2+}+H	Seq	26
365.22957	0.0 ppm	a_4	Seq	21
860.44868	8.5 ppm	y_7+H	Seq	19
344.17517	10.0 ppm	z_2-H	Seq	15
910.50309	1.3 ppm	c_9+3H	Seq	15
517.27605	4.2 ppm	a_{10}^{2+}-O	Seq	13
578.31243	28.5 ppm	y_4	Seq	11
561.80353	25.0 ppm	y_{10}^{2+}-O+H	Seq	5

In Pep71 (FNDDFSR), phenylalanine (F+H) is the most abundant fragment. The ion can stem from the N-terminal F or from the center of the sequence. It was shown above that aromatic amino acids lead to enhanced fragmentation. Therefore, also F_α, F_β, R_α (+H), and R_α^ϵ show a strong contribution to the ion signal. The only additional N-terminal

Seq ion is b_2, while the C-terminal y-fragments are almost complete (y_1, y_2, y_3, y_4). All y-fragments were detected with an additional hydrogen atom as it is observed in CID. C-terminal x-fragments were generated next to the F (x_2 and x_6). Also the z_2 fragment results from a cleavage next to F but the z_6 fragment, which would be expected if the cleavage was induced by F, could not be observed. The PC channel is low in abundance for the small peptide Pep71.

The most abundant fragments for Pep72 (VDEDQPFPAVPK) is the proline immonium ion and the N-terminal a_1 fragments, which is isobaric with V and K_β and can therefore not be distinguished properly. The same holds for the a_2 (-H_2O) and the y_5^{3+} (-3H) fragments. The PC channel can be observed with an isotope peak and is stronger as compared to Pep71. N-terminal Seq ions are b_2 and b_5. C-Terminal fragments are y_2 and y_5. y_2 can be found unmodified, as y_2 (+H) and with a loss of OH. The latter cannot be used for sequence assignment if the sequence is unknown. The 2AAS fragment DE (or ED) is present in early fragmentation patterns but with low abundance. No particular activity could be detected for aromatic sites (F and Q). The overall sequence coverage is small within the first 100 ms of laser irradiation.

The largest fragment spectrum in early fragmentation spectra was found in Pep73 (LAAHPPSAFWR). The PC channel was very strong and was detected with two isotope peaks. Some large doubly charged fragments (a_{10}^{2+}, x_{10}^{2+}, y_{10}^{2+}, z_{10}^{2+}, and z_{10}^{2+}) were formed, as well as large singly charged Seq ions (a_{10}, y_7, and c_9). In addition, the N-terminal Seq ions a_1, b_2, a_4, and b_4 and the C-terminal y_1, z_1, z_2 (-H), and y_4 were observed. A major part of the signal stemmed from aromatic amino acid fragments, e.g., W (+H), W_β, His (+H), R_γ (+H), R_α (-H), and F (+H). The a_1 (L (+H)) fragment showed a strong contribution although no aromatic site is located at the N-terminal.

6.2.5 Amino acid stripping and peptide sequencing

Fs-LID is a promising activation method for sequence analysis of peptides. Unfortunately, sequence coverage for the protein aLact could not be achieved within the experimental parameter range explored in this work. On the other hand, identification of all 1AAS fragments of aLact was possible. The lower mass range, depicting the 1AAS mass region of the aLact fs-LID fragmentation spectrum, is shown in Figure 6.11. Glycine (G) and

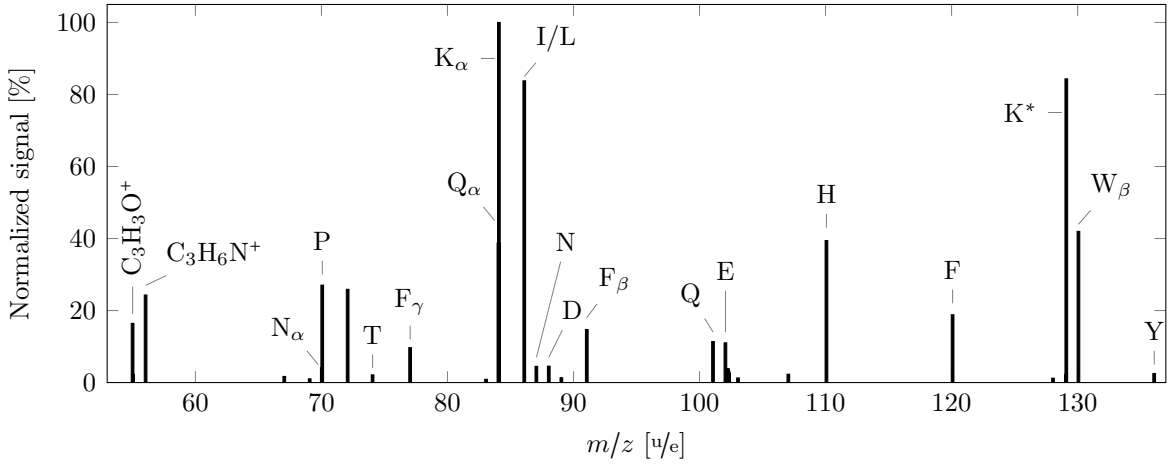

Figure 6.11: Fragmentation spectrum of aLact for the lower m/z range. The spectrum displayed is a composition of spectra recorded at different irradiation times.

alanine (A) are the only amino acids that have not been observed. The immonium ions of G and A have masses below the mass/charge limit of the spectrometer. The same effect was described for MRFA (Section 6.2.1). Cystein was not abundant in the fragmentation spectra as a 1AAS fragment, but could be identified through fragments lacking the SH_2 group. The identification of all amino acids in the peptides and protein is a valuable prerequisite for composition elucidation. Table 6.11 summarizes the 1AAS-fragments observed for different peptides and the protein aLact. A comparison with the peptide and protein sequences presented in Table 6.2 yields that all single amino acid fragments were generated for all species activated by fs-LID.

	K	I/L	H	Q	P	R	E	D	N	V	T	Y	F	M	W	S[p]	S	C	A	G
Pep71						●		●	●				●				●			
Pep72	●			●	●		●	●		●			●						■	
Pep73		●	●		●	●							●		●		●		■	
1P	●	●		●			●	●			●		●			●				
aLact	●	●	●	●	●	●	●	●	●	●	●	●	●	●	●		●	●	■	■

Table 6.11: 1AAS fragments found for the peptides under investigation. Except for cystein in aLact (red dot) and the smallest amino acids below the spectrometer mass limit (A and G, red squares), all amino acids in the peptides/ protein could be identified in the fs-LID fragmentation spectra (green dots).

Figure 6.12 shows the fs-LID fragmentation spectrum of Pep71. The most abundant signal stemmed from the immonium ion of phenylalanine. This amino acid occurs two times in the Pep71 sequence and one phenylalanine is located at the N-terminus. Here, only one cleavage is necessary to liberate the amino acid. Phenylalanine contains a chromophore and can be easily activated by non-resonant femtosecond laser light. Although less abundant, all other 1AAS fragments were observed as well (Table 6.12). 1AAS fragments occurred as immonium ions and F, N, and R were also generated as 1AAS fragments but lacking the amino group of the backbone structure (α-type 1AAS fragment).

For Pep72, Pep73, and 1P, most 1AAS fragments occurred as immonium ions, except for K and R, which were only observed lacking the amino group. The 1AAS fragments of F, N, Q, H, and E were observed as the immonium fragments as well as the α-type fragments. In all cases the immonium carried an additional hydrogen atom, while the α-type lacked a hydrogen.

The composition information from amino acid stripping (1AAS fragments) and information about the Seq ions can be used to fully determine the primary structure of unknown peptides. Fs-LID activation of Pep71 generated a large number of Seq ions. To enhance the number of detected Seq ions, it was useful to record spectra at different activation times. The c_4 Seq fragment (-OH) was observed doubly charged (m/z = 245.09005 $^{u}/_{e}$) and was only abundant at 250 ms and 500 ms. The singly charged x_3 fragment (m=435.19865 u) was observable at 2 s. The large z_6 fragment (m = 737.29748 u) was abundant between 250 ms and 500 ms, while the highly charged b_3^{3+}-H_2O (m = 120.71912 u) was only observed at 2 s. The most complete sequence series was achieved through Seq ions of type b and y. The number of x fragments was equal to the number of y fragments, but was less abundant. In addition, some a and z fragments could be identified. Sequence overlap was achieved for amino acids four (D) and five (F) and complete sequence coverage was achieved. A summary of some Seq ions including their mass accuracy is presented in Table 6.12.

For the twelve-amino acid peptide Pep72, the N-terminal fragments a (1, 2, 8, 10), b (1, 2, 3, 4, 5, 10), and c (1, 4, 7, 10), as well as the C-terminal fragments x (2, 4, 5, 8, 9, 11), y (1, 2, 3, 5, 7), and z (1, 2, 3, 4, 8) were observed. Sequence coverage could be achieved except for the PF order (amino acid six and seven). The 2AAS fragment QP did allow to identify the order of these amino acids in the center of the sequence. The corresponding mass peak was identified in the spectra recorded with activation times of 1 s and 2 s but

Fragment	m/z[u/e]	Accuracy	Fragment	m/z [u/e]	Accuracy
Seq ions			y_4+H	524.25009	7.2 ppm
a_1	120.08077	1.9 ppm	x_1-H	201.09905	0.9 ppm
a_3	349.15262	5.7 ppm	x_2-H	288.13096	2.5 ppm
a_5	611.24599	4.8 ppm			
b_1-2H	146.06047	1.6 ppm	**1AAS fragments**		
b_2	262.11945	3.2 ppm	F+H-e	120.08054	2.0 ppm
b_3	377.14741	4.9 ppm	F_α-H-e	103.05393	2.9 ppm
b_4	492.17660	8.3 ppm	N+H-e	87.05499	3.4 ppm
z_1	159.10023	0.3 ppm	N_α-H-e	70.02848	3.7 ppm
z_2	246.13226	3.4 ppm	D+H-e	88.03900	3.5 ppm
y_1+H	175.11895	0.0 ppm	S+H-e	60.04420	3.2 ppm
y_2+H	262.15163	2.5 ppm	R_α-H-e	112.08668	2.2 ppm
y_3+H	409.22345	6.0 ppm			

Table 6.12: Seq ions and 1AAS fragments of Pep71 created by fs-LID for an activation time of 500 ms. The protonated parent mass is $m\,([\mathrm{M}+\mathrm{H}]^+) = 900.38521$ u.

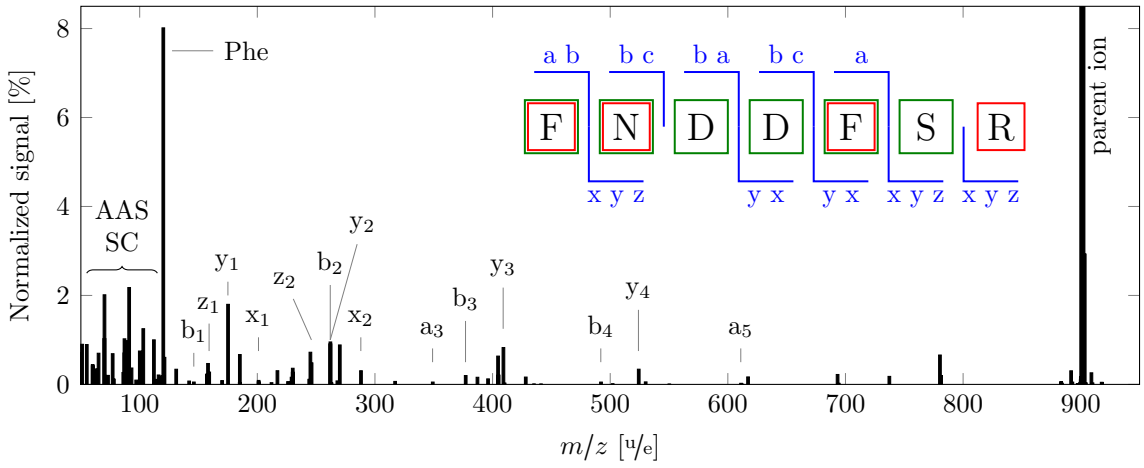

Figure 6.12: Fs-LID fragment spectrum of Pep71. The sample was laser activated for 500 ms. The short annotation presents all Seq ions and 1AAS fragments observed. Details about the most abundant Seq ions as well as fragments can be found in Table 6.12.

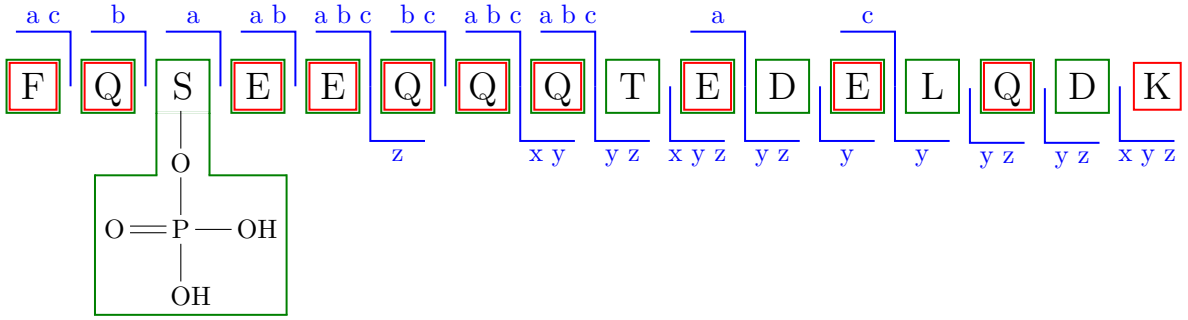

Figure 6.13: Indication of Seq ions and AAS fragments of 1P identified after fs-LID activation. Full sequence coverage was achieved and all possible single amino acids were found. The post-translational modification type and position within the peptide could be identified, as well.

the S/N was slightly below 3 (2.75).

Fs-LID of the eleven-amino acid peptide Pep73 created a smaller number of Seq ions. The N-terminal fragments were a (1, 2, 4, 8, 10), b (2, 4, 5), and c (1, 4, 9). The C-terminal fragments x (1, 10), y (1, 2, 4, 7, 10), and z (1, 2, 10) could be identified. The fragments y_2 and y_4 showed an OH loss and the C-terminal assignment was not straight-forward. In addition with the 2AAS fragments AA, AH, HP, and PP, the sequence could be assigned.

1P (m = 2060.8212 u) was studied to demonstrate the sequencing ability of fs-LID for a more complex peptide. This peptide is particularly interesting because it contains a phospho-serine (a common post-translational modification). As shown in Table 6.11, all 1AAS fragments were generated by fs-LID activation of the doubly charged precursor 1P. Most of the 1AAS fragments were abundant as immonium ions (green) and as α-type fragments (red) (Figure 6.13). Serine (S), threonine (T), leucine (L), and aspartic acid (D) could be observed as immonium ions while lysine (K) was merely abundant as the α-type 1AAS fragment. In addition, the phosphor marker was still attached to the serine after fragmentation, enabling the determination of the phosphorylation site. Full sequence coverage was achieved through a large number of Seq ions (Figure 6.13). The most complete Seq ions series resulted from nine y fragments. But also seven a, six b, six c, three x, and seven z fragments were observed. Sequence overlap was achieved for the central four amino acids. The number of Seq ions was sufficient to determine the sequence of 1P.

6.3 Discussion

Part two of this thesis investigated the feasibility of femtosecond laser activation in a high-resolution Fourier transform mass spectrometer and its utility for the structure elucidation of peptides and proteins. An 800 nm, mJ-level femtosecond Ti:Sa laser with a 1 kHz repetition rate was successfully coupled to an FT-ICR mass spectrometer. The laser allowed efficient molecular activation and thereby facilitated the structure analysis of small and large biomolecules. The ion cloud-laser overlap was sufficient to deplete the precursor ion signal (Section 6.1.2). Typically, 90 % of the precursor ions were fragmented after 2 s of activation time (Section 6.2.2). The complete activation achieved here greatly exceeded the 10 % activation reported in a previous fs-LID study [266]. This work has therefore established that fs-LID can serve as an efficient activation tool in peptide or protein mass spectrometry.

The activation mechanism of fs-LID is not yet established due to the small number of previous experimental studies. From an energetic point of view, it is clear that multiple infrared photons must be absorbed before covalent bonds are broken: The energy of a single 800 nm photon is approximately 1.6 eV and typical covalent bond strengths are in the range of several eV. Multiple photons can be absorbed within the short duration of a single laser pulse and additional photons may be absorbed from subsequent laser pulses if the molecule remains within the laser focus. Section 6.2.3 presents evidence for sequential fragmentation through the analysis of fragmentation dynamics on a time scale up to 2 s. E.g., the $[F_\gamma]^+$ fragment was not directly generated from the parent ion but predominantly from intermediate fragments such as $[F+H]^+$ or $[F_\beta]^+$. Such dynamic studies can be a useful tool for structure analysis and also to obtain mechanistic understanding of the fragmentation pathways. The data also indicated the presence of multiple parallel fragmentation pathways, which hampers the ability to interpret the decomposition pathways.

6.3.1 Experimental parameters

Typical acquisition times for the measurements presented here were 1 – 5 min with a mass resolution of 12500 to 50000, injection times of several hundred milliseconds, irradiation times of a few seconds, and averaging over 50 scans. The measurement times were therefore

in the typical range for MS experiments.

As the ion cloud is not necessarily pinned to the symmetry axis of the spectrometer, its overlap with the laser focus is not well defined. Thus, an important question to answer is how high the laser intensity in the experiment at hand really is. As the fragmentation patterns generated in this work are comparable to these of previous studies by Duffy et al. [269] with laser intensities of $10^{13} - 10^{14}\,\mathrm{W/cm^2}$, it can be concluded that the effective laser intensity in the current experiments is on the same order. This is significantly below the calculated in-focus intensity of $10^{15}\,\mathrm{W/cm^2}$. This may indicate that the laser focus and the ion cloud did not overlap completely and that most activation took place at substantially reduced maximum laser intensity. A comparison of the calculated Rayleigh length of 4 mm and the ion cloud elongation of several cm indicates that even for the best possible overlap, only a minority of ions interacts with the highest laser in-focus intensity.

In order to establish the current setup for mass spectrometric investigations of macromolecules, the measurement times must not exceed that of currently applied methods, while maintaining high-quality spectra. With increasing molecular mass, the fs-LID efficiency, as well as the ability to produce detectable fragments, increased. E.g., the fragmentation efficiency for Pep71 (m = 899 u) was smaller than for Pep72 (m = 1341 u) (Figure 6.5). The fragmentation efficiency also depended on the number of optically active amino acids, as exemplified in the fast decay of the Pep73 precursor (three aromatic amino acids) as compared the the Pep72 precursor (one aromatic amino acid). Therefore, the activation time can be shorter for larger molecules and for those containing more chromophores. For the protein aLact the maximum fragment number was already reached at 250 ms activation time (see aLact in Figure 6.5).

Enhanced information with tailored experimental parameters

Several experimental parameters can be varied to increase the information content of fs-LID spectra. In the following paragraphs the effects of the activation time, the initial charge state and the laser parameters are summarized.

The activation time controls the relative abundance of Seq fragments, 1AAS ions, SC and PC fragments (Section 6.2.2). Some low-abundant ions are only observable at specific

activation times. For example, the z_6 fragment of Pep71 was observed at 250 – 500 ms activation time, whereas the b_3^{3+}-H_2O fragment was abundant at 2 s. Therefore, the variation of the activation time can be utilized to find low-abundant species in the fragmentation patterns.

Using different initial charge states of the parent molecule did not change the relative abundance of the fragmentation pathways (1AAS, Seq, SC) when peptides were activated by fs-LID (Figure 6.8). Only the 2AAS channel and the efficiency of charge stabilization (PC) decreased with increasing initial charge state. On the other hand, the overall fragmentation efficiency for Pep73 was highest for the highest initial charge state (Section 6.2.2). It can be concluded that the utilization of precursor charge states larger than +1 can provide greater information for specific peptide compositions.

The laser pulse intensity, which can be varied by changing pulse duration or pulse energy, offers another parameter that allows to control the fragment abundances. Results summarized in Tables 6.4 and 6.5 show that longer activation times are required to create significant numbers of fragments for low pulse intensities. With an identical pulse duration of 40 fs and an identical activation time of 2 s, 2 mJ pulses created 10-fold less fragments as compared to 2.5 mJ pulses. On the other hand, spectra recorded with identical pulse energy of 3 mJ and the same activation time of 5 s showed that the fragment abundances were comparable for different pulse durations of 200 fs and 40 fs. At long activation times of 5 s and short pulse durations, the overall fragment abundance, as well as the Seq fragment abundance, increased but the number of distinct Seq ions decreased as compared to 2 s activation time.

In general, higher pulse energies and shorter pulse durations (higher intensities) decreased the required activation time for peptide sequencing and enhanced the abundance of structure-relevant fragments. Sufficient fs-LID activation times (40 fs pulse duration, 3 mJ pulse energy) were about 1 s for Pep73 (Figure 6.5). For other peptides, the fragment signal increased up to 2 s of activation time. These parameters represent the optimal values for fs-LID sequencing even though a systematic parameter variation slightly increased the available sequence information in special cases.

6.3.2 Composition elucidation and peptide sequencing

Liberation of 1AAS fragments

For composition analysis of peptides or proteins, the macromolecules must be fragmented down to the level of individual amino acids. Fs-LID leads to the liberation of all amino acids in the activated peptides (Tables 6.9 and 6.11). 1AAS fragments for all amino acids in large peptides occurred as immonium ions and often as α-type 1AAS fragments (Tables 6.6, 6.7, 6.8). The immonium ions always contained an additional hydrogen atom, while the α-type 1AAS fragments showed a loss of hydrogen. A possible explanation for this observation is presented later in (Section 6.3.3).

SC fragments are enhanced when an amino acid side chain with an extended electronic π system (not necessarily an aryl compound) is present. The combined information from 1AAS ions and SC fragments can be used to completely elucidate the amino acid composition of unknown peptides (Table 6.11).

Proteins are larger than peptides. Therefore, proteins have a more complex secondary structure and it may be difficult to liberate all 1AAS fragments due to non-covalent interactions after bond cleavage by laser activation. To address this issue, an example protein (aLact) was activated by fs-LID (Section 6.2.5). All 1AAS fragments with masses greater than the detection limit of the spectrometer ($m > 50\,\mathrm{u}$) could be detected. It can be concluded that all 1AAS fragments were liberated from the macro-molecule after fs-LID activation.

As the number of amino acids in proteins is larger than in peptides, there is a chance that all amino acids occur in the protein sequence. Consequently, there is no further information from experiments generating all 1AAS fragments from proteins. One open question would be whether the peak intensities of the fragmentation spectrum from these experiments can be used to determine the number of occurrences for the individual amino acids in proteins.

Unfortunately, as already known from the peptide experiments, the peak intensities of the 1AAS fragments largely depended on side chain characteristics. Therefore, the size of 1AAS ion and SC fragment signals could not be used to determine how often a particular

amino acid occurred in the protein sequence. This is probably due to different dissociation efficiencies for different side chains.

This finding is in line with previous work by Duffy et al., who showed that side chain cleavages dominated the fragmentation spectrum for aromatic amino acids, while the immonium ion was dominant for aliphatic amino acids [269]. We note that the work presented here is the first to report the 1AAS channels as the mass range of the spectrometers in published work was insufficient to detect these small fragments.

Sequence coverage

The sequence of peptides or proteins can be determined through the observation of multi-amino acid fragments. Many such fragments must be observed for complete sequence coverage, i.e., determination of the complete amino acid sequence. Although all 1AAS fragments were observed in fs-LID of aLact, protein sequence coverage could not be obtained (Section 6.2.5). An insufficient number of large fragments was observed.

Larger fragments, even if formed, may not separate from the precursor after activation: Due to their size, large fragments may stay bound through non-covalent interaction after covalent bonds have been cleaved. Such a non-covalent bonding mechanism was proposed to explain the lack of Seq ions in larger peptides activated by the non-ergodic process of ECD [282].

The initial hope was that extensive charging by photo-ionization might help to overcome the non-covalent forces, but the charging is either too weak or leads to the formation of small fragments. The fragments generated may also be too energetic to be trapped by the cell‘s electric field.

On the other hand, combining fs-LID with, e.g., CID in MS^n approaches would facilitate protein sequencing. In this case, the precursor ion is pre-fragmented in the ion trap prior to the FT-ICR cell and smaller sub-units can be subsequently activated by fs-LID [283, 284].

Peptide sequence coverage by fs-LID activation was demonstrated for MRFA, Pep71, Pep72, Pep73, and 1P (Section 6.2.5). Fs-LID generated a, b, c, and x, y, z Seq fragments. a, b, x, and y fragments gave the most complete sequence series (Figures 6.12 and 6.13).

The occurrence of a, b and y fragments is in line with MS^2 studies using low-energy collision methods [229].

The C-terminal y fragments always contained an additional hydrogen atom besides the proton expected from the ESI process (Section 6.2.4). This is also observed when established activation processes, e.g., CID, are employed [233].

The enhancement of bond cleavages in the vicinity of proline is known as the proline effect [229] and could also be observed by applying fs-LID for Pep72 (occurrence b_5 and y_5) and Pep73 (occurrence b_4 and y_7). Larger Seq fragments, where the cleavage occurred close to the center of the sequence (without an adjacent proline), were less abundant. Thus, Seq ions were preferentially created close to the terminals. So far, there is no apparent explanation for this behavior. Other activation methods dominantly lead to larger fragments. Fs-LID can therefore be used as a complementary activation in sequencing experiments.

For fs-LID, peptides containing few aromatic amino acids (e.g., Pep72) showed better sequence coverage than peptides with many aromatic amino acids (e.g., Pep73) (Section 6.2.5). This effect probably originates in the strong fs-LID activity of aromatic side chains (H, F, W, Y, R) (Table 6.9). Similar observations were reported before, where sequence coverage was demonstrated for significantly smaller peptides [267, 268].

In biological systems, post-translational modifications create new covalent bonds within peptides and proteins. Common post-translational modifications are phosphorylation (most commonly at serine and threonine), glycosysation, or the formation of disulfide bonds between cysteines. Post-translational modifications can strongly affect the biological properties of proteins or peptides [285]. The modifications are rather labile and are not easily detected [286, 287]. As shown in Section 6.2.5 for the peptide 1P, fs-LID allows to observe labile post-translational modifications. Activation of the large peptide 1P, which contains a single phospho-serine, led to the formation of the 1AAS fragment S[p], which could be detected in the fragmentation spectrum. Fs-LID can therefore identify at least one type of post-translational modifications. This is in contrast to established activation methods, e.g., CID, which preferentially cleaves post-translational modifications. Similar observations were recently reported by Smith et. al [267].

Fs-LID induces side chain cleavages and creates charged fragments that can be detected by mass spectrometric analysis. This capability can be used for substructure composition

elucidation, i.e., to distinguish isoleucine and leucine, whose 1AAS fragment mass is identical. This characteristic feature of fs-LID might also be helpful in the analysis of small molecules that contain mainly hydro-carbon chains, which are hard to break. In the course of this work, experiments on erucamides and caffeine confirmed this particular quality of fs-LID activation but the results are not within the scope of this thesis. The ability to induce extensive side-chain cleavages in peptides is also available through the established non-ergodic activation method of ECD [240, 241].

6.3.3 Physical processes

Based on the systematic identification of fragment types in Section 6.2 this section considers the physical fragmentation mechanisms of large peptides interacting with strong femtosecond laser fields.

Precursor charging

The charging capability of fs-LID [202] offers a solution to extend the limited sequence coverage standard fragmentation methods in MS proteomics. Here, activation normally coincides with decharging of the parent ion.

It is expected that fs-laser radiation efficiently induces charges in the peptide by multi-photon ionization or tunnel ionization (Section 5.4). These charges are predominantly formed in aromatic side chains (chromophores) or at other delocalized pi-systems, such as the peptide link or the guanidyl group. In this work precursor charging with significant yields for different peptides was observed and thereby some tentative insight into the precursor charging mechanisms could be gained.

Precursor charging by fs-LID was detected for Pep71, Pep72 and Pep73 (Figure 6.6). In all cases, the PC channel was accompanied by a loss of CO_2 (Section 6.2.4). The same observation was also made for the larger peptide 1P (Tables 6.4 and 6.5).

The PC channel was by far the largest in Pep73, which is the only peptide that includes tryptophan with the chromophoric side group of indole. In this case, W is adjacent to the C-terminal and the COOH group. Ionization of tryptophane probably leads to a

transfer of neutral hydrogen from the COOH group, leaving a radical at the C-terminus. Subsequently, the molecule can relax by loss of the CO_2 as a neutral leaving group. Also in Pep71 the easy-to-ionize guanidyl group is adjacent to the C-terminus and the same relaxation as in Pep73 can take place. The PC channel observed for Pep71 is weaker than in Pep73, which may reflect the lower ionization probability of the guanidyl group[3] as compared to the indole group[4] in Pep73.

In Pep72 the only aromatic side chain (F) is located in the center of the molecule and is separated by five amino acids from the C-terminal. Here, a hydrogen atom might be transferred to the backbone carbonyl group after photo-ionization of the peptide link. Alternatively, some folded protein structures might bring the aromatic side chain in close proximity with the carbonyl group, thereby facilitating a hydrogen transfer channel with loss of CO_2.

In summary, we can postulate that precursor charging is a common process upon fs-LID activation if suitable aromatic or delocalized chromophores are present. But the resulting multiply-charged peptide can only be observed in substantial amounts if it is stabilized by hydrogen transfer from a carboxylic acid group and loss of a neutral CO_2 group in proximate position. If this stabilization mechanism is absent, other fragmentation processes may deactivate the peptide under formation of significantly smaller fragments.

Multiply charged fragments

A number of multiply charged fragments were observed after fs-LID activation of singly charged parent ions. The Seq ion y_{10}^{+2} (-OH) formed from $Pep73^{+1}$ provides one example. Another is the 1AAS fragment $[F+H]^{2+}$ in Pep72 (Figure 6.9).

The number of multiply charged fragments was much smaller than expected based on the high laser pulse intensities. Furthermore, the number of ions observed (precursor + fragments) decreased as a function of activation time (Figure 6.5), and did not change significantly for increased laser pulse energies and intensities (Tables 6.4 and 6.5). To explain these observations, a significant loss of ions from the spectrometer is assumed. Two mechanisms for such a loss can be postulated: The m/z value of the fragments may

[3]Ionization energy of guanidine: 9.1 [eV].
[4]Ionization energy of indole: 7.8 [eV].

fall below the detector limit or their kinetic energy may be too high and the fragments may escape the ICR potential (Section 6.1.2). Both effects would be expected in the case of Coulomb explosion [202], which would lead to multiple energetic and potentially highly charged fragments.

Multiply charged fragments can be formed through three different pathways. The ESI-charged parent ion might be further charged by one laser pulse and fragmented by a subsequent laser pulse, with one of the fragments carrying both charges. Or, a single laser pulse can further charge the precursor ion with enough excess energy to cause subsequent fragmentation, leading to fragments carrying multiple charges. This process is similar to that discussed for precursor charging in the previous paragraph, but would involve the breaking of peptide bonds. Alternatively, the precursor may be fragmented and a subsequent laser pulse might charge the fragment carrying the ESI charge.

The pathway reconstruction for Pep72 fragmentation (Section 6.2.3) contains evidence for the sequential fragmentation and ionization process. The doubly charged species $[F+H]^{2+}$ only appeared after accumulation of the corresponding singly charged species $[F+H]^{+}$ (Figures 6.9). The latter yield decreased after 1 s of activation time due to decomposition into the SC fragments F_β and F_γ and due to fragment charging. The dynamic behavior observed is a clear indication that the molecules interact with multiple laser pulses. At long irradiation times, many small Pep72 fragments are observed and their further charging or fragmentation might create species with $m/z < 50$, below the detector limit.

In summary, the presented data shows evidence for multi-photon photo-ionization and charging of precursor and fragment molecules. Strong field ionization and associated coulomb explosion processes might also occur, but the limited m/z range of this experiment precludes the direct observation of small and highly charged fragments formed therein.

The charging ability of fs-LID might help to generate large numbers of charged fragments and thereby overcome the limited sequence coverage of standard fragmentation methods in MS proteomics. However, fs-LID charging seems to be associated with significant fragmentation and loss of ions because their mass/charge ratio falls below the detection limit of the spectrometer utilized. The method, within the technological constraints of this work, therefore offers no simple tool to greatly extend the sequence coverage in MS proteomics in terms of its charging capability.

Internal fragments

An analysis of the most abundant fragments helped to obtain a better understanding of the fs-LID fragmentation process. The fragment data obtained upon variation of experimental parameters (Section 6.2.2) showed that internal fragments are more efficiently generated than terminal fragments and the larger 2AAS fragments are less abundant than the smaller 1AAS fragments even for small activation times. In addition, the 1AAS channel resulted in all possible amino acid fragments for all investigated peptides, independent of masses and number of aromatic side chains within the peptide.

To form an internal 1AAS fragment at least two peptide bonds must be broken. Therefore, two sequential activation events occur or a single activation event leads to multiple peptide cleavages. In order to find a mechanism describing the internal fragments detected here, three basic types of activation and cleavage might be considered. (1) Ergodic fragmentation: The laser introduces energy into the molecule, i.e., the electronic system becomes exited. The energy is subsequently redistributed by electronic to vibrational relaxation. This can lead to the population of dissociative vibrational states, directly forming fragments [238]. Or the ESI proton becomes mobile, transfers to the peptide bond and induces a charge-directed cleavage [229]. (2) Non-ergodic fragmentation: The electronic excitation upon fs-LID activation reaches a dissociative electronic state before energy redistribution takes place and the peptide is cleaved at the site of activation. (3) Non-ergodic, followed by ergodic fragmentation: After the generation of a primary fragment by mechanism (2), there might be enough excess energy left to generate a secondary fragment by mechanism (1). As the ion cloud-laser focus overlap is imperfect and activation processes with very different laser intensities in the focus and out of focus can be expected, it is likely that ergodic and non-ergodic processes occur simultaneously.

Although a large number of the weak peptide bonds are broken upon fs-LID, ergodic fragmentation does not seem to play an important role in the formation of 1AAS fragments: When irradiating 1P, the post-translational modification (PTM) stays fully intact even for the 1AAS fragment S[p] (Section 6.2.5). This is not plausible for ergodic fragmentation, because the weak PTM bond is expected to break preferentially. Therefore, a solely ergodic fragmentation mechanism (1) is considered unlikely. Mechanism (2) is often proposed for photo-chemical activation of the peptide bond (see, e.g., [288]). Here the non-ergodic

fragmentation by VUV laser light is triggered by the electronic excitation of the carbonyl group in the backbone. It is claimed that the fragmentation follows a Norrish type-1 reaction [289]. In this case, no extra charge is induced prior to fragmentation and only 1AAS fragments bearing the ESI proton would be visible in the fragmentation spectra. This is in contradiction to the facts that fs-laser radiation tends to charge molecules [202] and that all possible 1AAS fragments have been detected in the experiments at hand. It might therefore be concluded that the mechanism underlying the generation of 1AAS fragments by fs-LID is charge-directed and radical-driven. A possible mechanism is proposed in the following paragraphs. As the data is inconclusive and the laser intensity distribution along the molecular cloud is broad, the explanation stays speculative.

As discussed in Section 5.4, the peptide link exhibits an extended electronic π system due to its resonance structure and can be efficiently ionized by fs-laser radiation. The efficient formation of 1AAS ions might therefore be explained by assuming that multiple peptide links are activated simultaneously or sequentially. The latter is supported by the observation that molecules were activated more than once when the irradiation times were increased (Section 6.2.3). On the other hand, sequential activation should lead to a substantial amount of internal fragments consisting of more than one amino acid, which were not observed even for short activation times. In addition, sequential activation should lead to an increasing number of 1AAS ions with increasing activation time. This is contradicted by the experimental data (see Figures 6.6 and 6.8), which shows a fairly stable ratio of 1AAS to other fragment types. It is therefore necessary to consider a possible mechanism for simultaneous activation of at least two peptide bonds.

As shown in Section 6.2.5, the dominant type of 1AAS fragments are immonium ions in charge state +1. A possible fs-LID mechanism leading to 1AAS singly charged immonium ions upon activation of peptides is presented in Figure 6.14. The center part of a peptide is shown in the upper panel. The resonance structure of the peptide link is indicated by dashed double bonds. The oxygen and nitrogen lone pairs contributing to the double bonds are depicted as dots.

In a first non-ergodic step, a peptide bond is ionized, a positive charge is left at the carbonyl group and a radical forms at the adjacent nitrogen. The N-terminal fragment is still excited and relaxes by hole migration to the C_α, resulting in a CO leaving group. The hole might migrate further to the adjacent Nitrogen inducing a McLafferty rearrangement

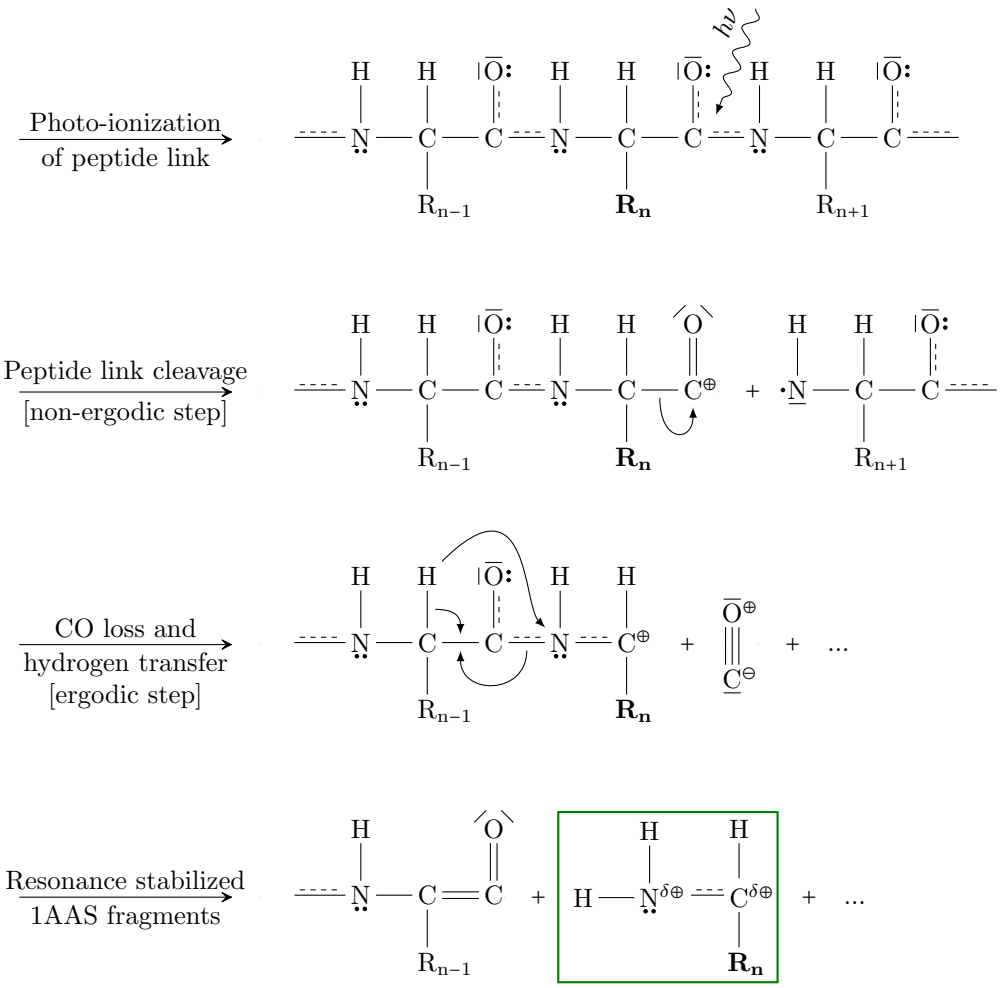

Figure 6.14: Proposed fs-LID activation mechanism to result in 1AAS immonium fragments (green box). The strong laser field creates a radical cation in the resonance structure of the peptide link resulting in a non-ergodic cleavage, followed by CO loss. A McLafferty rearrangement transfers an hydrogen atom and the resulting singly charged 1AAS immonium fragment is stabilized by forming a resonance structure.

leading to the second peptide bond cleavage.

The McLafferty hydrogen may originate from the C_α as shown in Figure 6.14 or may also stem from the C_γ of the side chain R_{n-1}, which would result in an additional SC cleavage.

This two-step mechanism of a non-ergodic cleavage and consecutive ergodic cleavage creates a singly charged immonium 1AAS fragment (green box) if the side chain was not

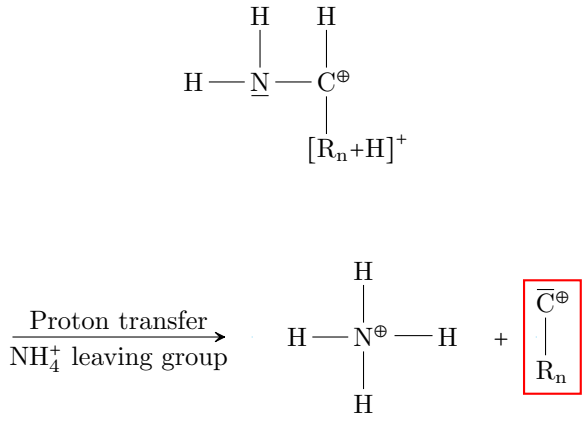

Figure 6.15: Proposed fs-LID activation mechanism to result in 1AAS α-type fragments (red box). If the side chain of the 1AAS fragment in Figure 6.14, lower panel, was protonated (ESI charge), the proton can be transferred to the amino group and the doubly charged fragment stabilizes by loss of ammonium (NH_4^+).

protonated. The immonium ion can stabilize by forming a resonance structure in the N-C bond, where the nitrogen lone pair partially contributes to the N=C double bond. The result is a delocalized positive charge between the nitrogen and the carbon atom.

1AAS fragments may also occur as singly charged α-type ions. Signal contributions of this type of 1AAS fragments are stronger for amino acids with higher proton affinity. Therefore, it is likely that the α-type fragments were generated when the ESI proton was located in the amino acid side chain. The 1AAS fragment of Figure 6.14 in the lowest panel is depicted in Figure 6.15 with an additional proton (ESI proton) attached to its side chain. This additional proton can transfer to the amino group forming NH_3^+, which is a bad leaving group. The small doubly charged compound can be stabilized by transferring another hydrogen atom from the C_α of the amino acid side chain to form ammonium (NH_4^+). Ammonium can be cleaved from the amino acid compound, forming the α-type 1AAS fragment (red box).

The strongly varying abundance for different 1AAS ions can be explained by non-adiabatic laser excitation of electronic π systems in the amino acid side chains (Section 6.2.4). Side chain fragments dominantly result from amino acids with delocalized electrons within in their side chain. As shown in Figure 6.6, Pep71 (F twice and R) and Pep73 (H, F, W and R) show a much stronger contribution from SC ions as compared to Pep72 (F) and 1P (F). It is likely that fs-laser radiation charges the chromophoric side chains with accompanying excitation of the electronic system. The induced hole charges may migrate along the carbon chain to the backbone inducing bond cleavages along the side chain and/or enhancing backbone cleavages resulting in 1AAS fragments as depicted in Figure

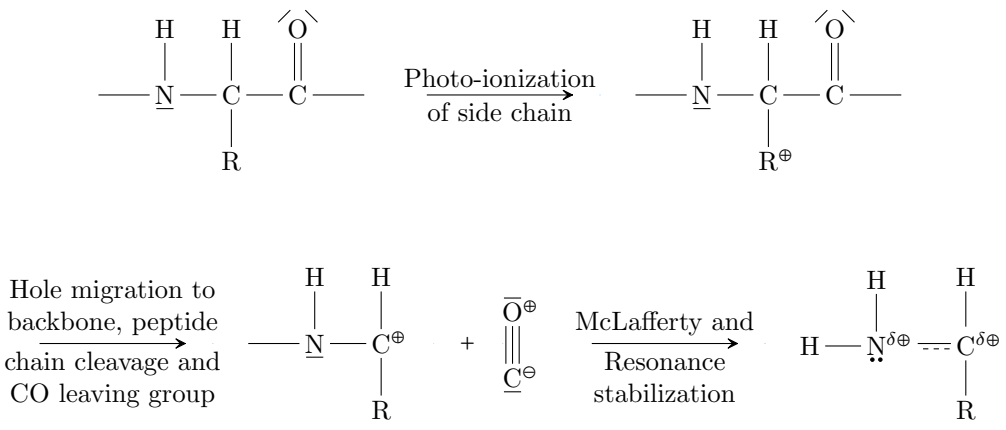

Figure 6.16: Activation of the amino acid side chain by fs-LID may contribute to the formation of 1AAS fragments explaining strongly varying signal contributions of 1AAS fragments for different amino acids.

6.16. Such charge migration in amino acids was previously reported in [43] and for small peptides in [263].

The proposal for a mechanism of fs-LID activation of peptides presented in Figures 6.14, 6.15 and 6.16 accounts for the following experimental findings: (a1) All possible 1AAS fragments were liberated. (b1) 1AAS fragments occur with varying abundances depending on their side chain characteristics. (c1) Amino acids with higher proton affinity tended to be formed as α-type fragments lacking an hydrogen atom. (d1) Amino acids with lower proton affinity tended to be formed as immonium fragments with an additional hydrogen atom. (e1) Larger Seg ions or 2AAS fragments were detected with low abundance compared to 1AAS fragments even for short irradiation times. (f1) Fs-LID activation seems to be non-ergodic, as PTM bonds did not break. On the other hand, the mechanism proposed cannot answer the following questions: (a2) Why was the PTM bond not broken in a subsequent ergodic step of the cleavage? (b2) Why did the overall ion signal decrease with longer irradiation times?

Follow-up experiments investigating small fragments generated by the fs-LID process, especially the ammonium (NH_4^+) molecule, would help to evaluate the mechanism proposed here. Further pump-probe investigations may also help to understand charge migration processes possibly involved in the generation of 1AAS fragments.

Ergodicity

An ongoing discussion in literature is about the ergodicity of the fs-LID process (Section 5.4.1). The current work might contribute to this discussion in some aspects.

The PC channel of the 1P fragmentation spectrum is the only prominent signal at 2 s when the laser pulse energy is 2 mJ (Table 6.4). Only a minor contribution stems from Seq ions and 1AAS fragments. This might indicate that the activation takes place in the MPI regime without major excitation of the electronic system.

On the other hand, at 2.5 mJ, all types of fragmentation channels exhibit strong activity. Therefore, a threshold intensity seems to be required to induce cleavages resulting in a variety of fragments. The threshold behavior and the stable fragment numbers when the pulse energy is further increased from 2.5 mJ to 3 mJ for fragments other than PC fragments, could indicate the transition from the MPI regime to tunnel or even Over-the-Barrier ionization. If the molecules are ionized, the energetic difference of excited electronic states becomes smaller, allowing for non-adiabatic polarization-induced Landau-Zener excitation (Section 5.4.1). This might explain why strong fragmentation signals are particularly abundant for aromatic amino acid compounds, where the above-barrier regime is accessed more easily.

Furthermore, amino acids that bear side chains with resonant structures (Section 6.2.4), amide groups and protonated guanidyl groups, lead to strong fragmentation. This supports the notion that intense non-resonant femtosecond radiation non-adiabatically activates peptides locally at extended π systems, which results in high excess energy, providing efficient subsequent fragmentation. This work therefore supplies strong evidence for non-ergodic fragmentation mechanisms.

In addition, the large number of different Seq ions (a, b, c, x, y, z), the 1AAS signal and the side chain cleavages also indicate that fs-LID is a non-ergodic process, similar to ECD. The results showed that the laser can interact with the molecules multiple times but the molecules cannot gather energy, as the fs-LID precursor decomposition efficiency is high. Instead, the molecules repeatedly fragment by interaction with consecutive laser pulses.

Moreover, it was shown that labile-bound marker molecules stay bound upon fs-LID and, in contrast to IRMPD, signals from internal fragments are small. Another indication of

non-ergodic fragmentation is the decrease of the total ion number, which could indicate highly kinetic fragments upon dissociation. This is not expected for IVR-based processes [236, 238].

6.4 Summary

A Fourier transform mass spectrometer setup was successfully coupled to a femtosecond laser system to allow peptide activation by fs-LID. Most fragments generated by fs-LID of peptides and proteins could be assigned to four major fragmentation channels: Precursor charging (PC), sequence ions (Seq), liberation of amino acids (1AAS) and side chain fragments (SC).

The sequencing ability of fs-LID was demonstrated for complex peptides and also for peptides with post-translational modifications. For multiple peptides, fs-LID generated all possible Seq fragments, 1AAS ions, and SC fragments, while keeping post-translational modifications intact. Fs-LID may therefore be considered as a valuable tool for peptide sequencing and offers an alternative to non-ergodic ECD. ECD can only be used in conjunction with ultra-high vacuum chambers and when strong magnetic fields are involved (FT-ICR), because the ECD electrons must be pinned by the magnetic field lines. Fs-LID does not depend on such constraints and can be used with all types of mass spectrometers. In addition, ECD discharges protonated peptides and thereby reduces the number of detectable charged fragments. In contrast, the current work shows that fs-LID can further charge the precursor and has the ability to create fragments in a charge state higher than that of the initial precursor. Unfortunately, fs-LID as implemented here seems to favor the formation of rather small fragments and the total number of observed ions is suppressed by the formation of fragments below the detection limit of the spectrometer.

Fs-LID also resulted in the liberation of all amino acids contained in the peptides or proteins investigated. These amino acid fragments occurred as singly charged cations. Photo-ionization seems to induce a substantial amount of charges. These charges may be homogeneously distributed along the peptide backbone, such that every amino acid compound can be liberated in charge state 1+. It may also be possible that the probability to photo-induce charges does not vary along the peptide backbone structure. In any case,

fs-LID can charge and liberate every single amino acid in a given peptide.

A drawback of fs-LID is the low abundance of fragments as compared to common activation methods. This issue might be addressed in future experiments by further exploring the available parameter range. Within the parameter range considered here, the information content of the fragmentation patterns could be enhanced by varying the laser pulse duration, laser pulse energy and activation time. Especially the variation of the activation time helped to modify the fragmentation pattern and thereby enhanced the information content available for peptide sequencing. As the fragmentation pattern is different to that obtained from other activation methods, fs-LID might be a valuable complementary tool for the field of peptide sequencing and proteomics.

Beyond exploring the proposed application in proteomic mass spectrometry, this work also started to clarify the processes underlying fs-LID of proteins. In this work, a large amount of data was collected but the molecules investigated and their fragmentation spectra were too complex to find deterministic explanations of the underlying activation processes.

Further experiments should be conducted in conjunction with tailored peptide species. It might be interesting, e.g., to fragment the peptides investigated here, where the aryl compounds are substituted by aliphatic amino acids to provide further information on the role of the peptide link in the activation process. Peptides with low proton affinity at the C-terminus and high proton affinity at the N-terminus may help to better understand the charge transfer along the backbone when the peptide link was ionized by fs-laser radiation.

In addition, optical pump-probe experiments in the attosecond to femtosecond regime, as conducted in the first part of this thesis, might contribute to answer the question how the electronic excitation/ ionization resulting from side chain π systems evolves and supports SC as well as backbone cleavages. Such experiments would help to understand the activation processes in large molecules in greater detail.

Summary and Outlook

In the framework of this thesis, two projects explored the ionization and fragmentation processes of molecules at the attosecond and femtosecond timescale. Firstly, electron dynamics in neutral molecules (Section 3) and correlated electron-nuclear dynamics in dissociative ionization of molecular nitrogen (Section 4) were investigated with attosecond time resolution. Secondly, a short pulse laser source was coupled to a Fourier transform mass spectrometer with high mass resolution and mass accuracy to study the fragmentation of proteins induced by femtosecond laser pulses (Section 6). The latter explored the utility of ultrafast pump-probe techniques for the analysis of biological macromolecules and offers a novel protocol for mass spectroscopy-based proteomics.

Attosecond experiments on neutral molecules showed that the molecular charge distribution can be controlled and probed on the natural timescale of electronic motion. This work is therefore part of a growing body of experimental studies (e.g., [290]) that show the feasibility of attosecond time-resolved molecular investigations. Molecules under the influence of a moderately strong femtosecond near-infrared (NIR) laser field displayed characteristic temporal signal modulations when ionized by an XUV attosecond pulse train. A comparison to theoretical simulations revealed that the electron cloud adiabatically follows the NIR electric laser field. The strength of electronic displacement, and therefore the XUV ionization probability, depended on the polarizability of the molecular species. The experiment demonstrated, for the first time, that charge redistribution in neutral molecules can be observed by employing attosecond laser pulses. This is particularly important for the investigation of dynamics in highly excited neutral molecules, which in the future might be initiated by a single attosecond XUV pulse. Therefore, laser sources providing isolated attosecond pulses with a sufficient number of photons will allow to

study highly excited state dynamics in molecules by attosecond pump-attosecond probe experiments.

The coupling of electronic and molecular motion in dissociative ionization of molecular nitrogen was investigated for molecules ionized by the harmonic radiation of an attosecond pulse train, while the molecule was influenced by a moderately strong NIR field. The fragment kinetic energy spectrum showed complex oscillations as a function of pump-probe delay. The oscillations exhibited large phase shifts as a function of kinetic energy. In addition, the relative modulation depths of the oscillations varied as a function of pump-probe delay. Comparison with theory revealed that the signal oscillation is caused by interference of direct and sequential two-photon pathways. The experiment implies that the electronic phase initially created upon ionization might influence the outcome of chemical reactions. This is an important step beyond traditional photo-chemical control schemes that hitherto focused on nuclear dynamics only. The experiments also show that attosecond pump-probe studies, together with theory, allow to investigate coupled electron-nuclear dynamics with attosecond time resolution. Exciting results may be expected in this field in the near future.

To extend optical pump-probe schemes to larger (bio-)molecules, a Fourier transform mass spectrometer was coupled to a high-intensity femtosecond laser source. The feasibility of femtosecond laser-induced dissociation (fs-LID) as an analytical tool was studied by fragmentation of peptides and proteins. The femtosecond laser was used to activate the peptides and the analysis of the resulting fragmentation patterns allowed to evaluate the sequencing capabilities of the fs-LID experimental protocol. Precursor charging and a large number of molecule-specific fragments, e.g., sequence ions, single amino acids, and side chain fragments were identified. Complete sequence coverage was achieved for peptides containing four to 16 amino acids. Complete amino acid stripping was found even for the protein α-Lactalbumin with a molecular weight of $m = 14178\,\mathrm{u}$. A wide experimental parameter range (laser power, pulse duration, activation time) was investigated here and led to unique fragmentation patterns. In addition, the experimental parameters could be feedback-controlled for automated analysis in the future. Fs-LID may therefore offer a valuable new tool for MS-based peptide sequencing.

Control experiments based on pulse shaping could be extended to large biomolecules. Earlier studies were conducted for single protonated amino acids [291] and small model

peptides [204, 205]. The systematic investigation of tailored pulses and resulting fragmentation patterns of peptides and proteins could allow to establish a database of pulse shapes for bond selective scissions. Femtosecond laser-induced dissociation in general, and pump-probe or control schemes in particular, may offer a versatile tool for unambiguous protein sequencing, doping analysis and drug discovery in the future.

Rich fs-LID spectra and the straightforward identification of product ions, demonstrated here, indicate that optical pump-probe experiments are practical even for large molecules. In particular, Fourier transform mass spectrometers in combination with attosecond pulse sources (as explored in the first part of this work) could be used in future experiments to study charge migration and coupled electron-nuclear motion in large bio-molecules. First experiments on this topic with ultrashort pulses were reported for the amino acid phenylalanine [43, 52]. The advent of attosecond pulses and the exploitation of modern mass spectrometer instruments will allow future ultrafast pump-probe experiments with complex peptides and proteins. The enormous accuracy of Fourier transform mass analyzers and the outstanding temporal resolution available through attosecond pulses might allow to follow and control molecular dynamics in biological relevant systems on the natural timescale of electronic motion.

References

[1] M. Fink, J. Geiger, H. Kleinpoppen, K. P. Lieb, N. Risch, P. Schmüser, and H. Spitzer, *Teilchen*, W. Raith, Ed., ser. Bergmann, Schaefer - Lehrbuch der Experimentalphysik 3-11-0109778. Walter de Gruyter & Co., 1992, vol. 4.

[2] A. Fleming. (1945). Nobel lecture: penicillin, [Online]. Available: http://www.nobelprize.org/nobel_prizes/medicine/laureates/1945/fleming-lecture.html.

[3] J. C. Maxwell, "A dynamical theory of the electromagnetic field", *Philosophical Transactions of the Royal Society of London*, vol. 155, pp. 459–512, Jan. 1865. DOI: 10.1098/rstl.1865.0008. [Online]. Available: http://rstl.royalsocietypublishing.org/content/155/459.short.

[4] W. Ostwald. (1909). Nobel lecture: on catalysis.

[5] A. Einstein, "Über einen die Erzeugung und Verwandlung des Lichtes betreffenden heuristischen Gesichtspunkt", *Annalen der Physik*, vol. 322, no. 6, pp. 132–148, 1905, ISSN: 1521-3889. DOI: 10.1002/andp.19053220607. [Online]. Available: http://dx.doi.org/10.1002/andp.19053220607.

[6] M. Göppert-Mayer, "Über Elementarakte mit zwei Quantensprüngen", *Annalen der Physik*, vol. 401, no. 3, pp. 273–294, 1931, ISSN: 1521-3889. [Online]. Available: http://dx.doi.org/10.1002/andp.19314010303.

[7] A. Einstein, "Strahlungsemission und -Absorbtion nach der Quantentheorie", *Verhandlungen der Deutschen Physikalischen Gesellschaft*, vol. 18, pp. 318–323, 1916.

[8] T. H. Maiman, "Stimulated optical radiation in ruby", *Nature*, vol. 187, no. 4736, pp. 493–494, Aug. 1960. [Online]. Available: http://dx.doi.org/10.1038/187493a0.

[9] P. A. Franken, G. Weinreich, C. W. Peters, and A. E. Hill, "Generation of optical harmonics", *Physical Review Letters*, vol. 7, no. 4, pp. 118–&, 1961. DOI: 10.1103/PhysRevLett.7.118.

[10] W. Kaiser and C. G. B. Garrett, "2-photon excitation in CaF_2 - Eu_2^+", *Physical Review Letters*, vol. 7, no. 6, pp. 229–&, 1961. DOI: 10.1103/PhysRevLett.7.229.

[11] P. D. Maker, R. W. Terhune, and C. M. Savage, "Intensity-dependent changes in refractive index of liquids", *Physical Review Letters*, vol. 12, no. 18, pp. 507–&, 1964. DOI: 10.1103/PhysRevLett.12.507.

[12] D. E. Spence, P. N. Kean, and W. Sibbett, "60-fsec pulse generation from a self-mode-locked Ti-sapphire laser", *Optics Letters*, vol. 16, no. 1, pp. 42–44, Jan. 1991. DOI: 10.1364/OL.16.000042.

[13] A. H. Zewail, "Femtochemistry: atomic-scale dynamics of the chemical bond", *Journal of Physical Chemistry A*, vol. 104, no. 24, pp. 5660–5694, Jun. 2000. DOI: 10.1021/jp001460h.

[14] ——, "Femtochemistry. past, present, and future", *Pure and Applied Chemistry*, vol. 72, no. 12, pp. 2219–2231, Dec. 2000. DOI: 10.1351/pac200072122219.

[15] M. Born and R. Oppenheimer, "Quantum theory of molecules", *Annalen Der Physik*, vol. 84, no. 20, pp. 0457–0484, 1927.

[16] E. U. Condon, "Nuclear motions associated with electron transitions in diatomic molecules", *Physical Review*, vol. 32, no. 6, pp. 0858–0872, Dec. 1928. DOI: 10.1103/PhysRev.32.858.

[17] E. Schrödinger, "Quantisierung als Eigenwertproblem (Erste Mitteilung)", *Annalen der Physik*, vol. 384, no. 4, pp. 361–376, 1926, ISSN: 1521-3889. [Online]. Available: http://dx.doi.org/10.1002/andp.19263840404.

[18] ——, "Quantisierung als Eigenwertproblem (Zweite Mitteilung)", *Annalen der Physik*, vol. 384, no. 6, pp. 489–527, 1926, ISSN: 1521-3889. [Online]. Available: http://dx.doi.org/10.1002/andp.19263840602.

[19] A. Zewail. (1999). Nobel lecture: femtochemistry: atomic-scale dynamics of the chemical bond using ultrafast lasers, [Online]. Available: http://www.nobelprize.org/nobel_prizes/chemistry/laureates/1999/zewail-lecture.html.

[20] A. Mokhtari, P. Cong, J. L. Herek, and A. H. Zewail, "Direct femtosecond mapping of trajectories in a chemical-reaction", *Nature*, vol. 348, no. 6298, pp. 225–227, Nov. 1990. DOI: 10.1038/348225a0.

[21] L. R. Khundkar and A. H. Zewail, "Ultrafast molecular reaction dynamics in real-time - progress over a decade", *Annual Review of Physical Chemistry*, vol. 41, pp. 15–60, 1990. DOI: 10.1146/annurev.physchem.41.1.15.

[22] E. D. Potter, J. L. Herek, S. Pedersen, Q. Liu, and A. H. Zewail, "Femtosecond laser control of a chemical-reaction", *Nature*, vol. 355, no. 6355, pp. 66–68, Jan. 1992. DOI: 10.1038/355066a0.

[23] R. J. Gordon and S. A. Rice, "Active control of the dynamics of atoms and molecules", *Annual Review of Physical Chemistry*, vol. 48, pp. 601–641, 1997. DOI: 10.1146/annurev.physchem.48.1.601.

[24] T. Baumert, B. Buhler, M. Grosser, R. Thalweiser, V. Weiss, E. Wiedemann, and G. Gerber, "Femtosecond time-resolved wave packet motion in molecular multiphoton ionization and fragmentation", *Journal of Physical Chemistry*, vol. 95, no. 21, pp. 8103–8110, Oct. 1991. DOI: 10.1021/j100174a019.

[25] F. Remacle and R. D. Levine, "On the inverse Born-Oppenheimer separation for high Rydberg states of molecules", *International Journal of Quantum Chemistry*, vol. 67, no. 2, pp. 85–100, 1998, ISSN: 1097-461X. [Online]. Available: http://dx.doi.org/10.1002/(SICI)1097-461X(1998)67:2%3C85::AID-QUA3%3E3.0.CO;2-U.

[26] D. R. Yarkony, "Conical intersections - the new conventional wisdom", *The Journal of Physical Chemistry A*, vol. 105, no. 26, pp. 6277–6293, Jun. 2001, ISSN: 1089-5639. DOI: 10.1021/jp003731u. [Online]. Available: http://dx.doi.org/10.1021/jp003731u.

[27] B. J. Sussman, D. Townsend, M. Y. Ivanov, and A. Stolow, "Dynamic Stark control of photochemical processes", *Science*, vol. 314, no. 5797, pp. 278–281, Oct. 2006. DOI: 10.1126/science.1132289.

[28] B. H. Muskatel, F. Remacle, and R. D. Levine, "The post-Born-Oppenheimer regime: dynamics of electronic motion in molecules by attosecond few-cycle spectroscopy", *Physica Scripta*, vol. 80, no. 4, p. 048 101, Oct. 2009. DOI: 10.1088/0031-8949/80/04/048101.

[29] R. Weinkauf, P. Schanen, D. Yang, S. Sonkara, and E. W. Schlag, "Elementary processes in peptides - electron-mobility and dissociations in peptide cations in the gas-phase", *Journal of Physical Chemistry*, vol. 99, no. 28, pp. 11 255–11 265, Jul. 1995. DOI: 10.1021/j100028a029.

[30] R. Weinkauf, P. Schanen, A. Metsala, E. W. Schlag, M. Burgle, and H. Kessler, "Highly efficient charge transfer in peptide cations in the gas phase: threshold effects and mechanism", *Journal of Physical Chemistry*, vol. 100, no. 47, pp. 18 567–18 585, Nov. 1996. DOI: 10.1021/jp960926m.

[31] F. Remacle, R. D. Levine, and M. A. Ratner, "Charge directed reactivity: a simple electronic model, exhibiting site selectivity, for the dissociation of ions", *Chemical Physics Letters*, vol. 285, no. 1-2, pp. 25–33, Mar. 1998. DOI: 10.1016/S0009-2614(97)01314-6.

[32] L. S. Cederbaum and J. Zobeley, "Ultrafast charge migration by electron correlation", *Chemical Physics Letters*, vol. 307, no. 3-4, pp. 205–210, Jul. 1999. DOI: 10.1016/S0009-2614(99)00508-4.

[33] J. Breidbach and L. S. Cederbaum, "Migration of holes: formalism, mechanisms, and illustrative applications", *Journal of Chemical Physics*, vol. 118, no. 9, pp. 3983–3996, Mar. 2003. DOI: 10.1063/1.1540618.

[34] A. I. Kuleff, J. Breidbach, and L. S. Cederbaum, "Multielectron wave-packet propagation: general theory and application", *Journal of Chemical Physics*, vol. 123, no. 4, p. 044 111, Jul. 2005. DOI: 10.1063/1.1961341.

[35] H. Hennig, J. Breidbach, and L. S. Cederbaum, "Electron correlation as the driving force for charge transfer: charge migration following ionization in N-methyl acetamide", *Journal of Physical Chemistry A*, vol. 109, no. 3, pp. 409–414, Jan. 2005. DOI: 10.1021/jp046232s.

[36] J. Breidbach and L. S. Cederbaum, "Universal attosecond response to the removal of an electron", *Physical Review Letters*, vol. 94, no. 3, p. 033 901, Jan. 2005. DOI: 10.1103/PhysRevLett.94.033901.

[37] A. I. Kuleff, S. Lunnemann, and L. S. Cederbaum, "Ultrafast charge migration following valence ionization of 4-methylphenol: jumping over the aromatic ring", *Journal of Physical Chemistry A*, vol. 114, no. 33, pp. 8676–8679, Aug. 2010. DOI: 10.1021/jp101256n.

[38] A. Perveaux, D. Lauvergnat, F. Gatti, G. J. Halász, Á. Vibók, and B. Lasorne, "Monitoring the birth of an electronic wavepacket in a molecule with attosecond time-resolved photoelectron spectroscopy", *The Journal of Physical Chemistry A*, vol. 118, no. 38, pp. 8773–8778, 2014, PMID: 25167166. DOI: 10.1021/jp508218n. eprint: http://dx.doi.org/10.1021/jp508218n. [Online]. Available: http://dx.doi.org/10.1021/jp508218n.

[39] D. Popova-Gorelova, J. Küpper, and R. Santra, "Imaging electron dynamics with time- and angle-resolved photoelectron spectroscopy", *Phys. Rev. A*, vol. 94, p. 013 412, 1 Jul. 2016. DOI: 10.1103/PhysRevA.94.013412. [Online]. Available: http://link.aps.org/doi/10.1103/PhysRevA.94.013412.

[40] R. Weinkauf, L. Lehr, and A. Metsala, "Local ionization in 2-phenylethyl-N,N-dimethylamine: charge transfer and dissociation directly after ionization", *Journal of Physical Chemistry A*, vol. 107, no. 16, pp. 2787–2799, Apr. 2003. DOI: 10.1021/jp021092c.

[41] L. Lehr, T. Horneff, R. Weinkauf, and E. W. Schlag, "Femtosecond dynamics after ionization: 2-phenylethyl-N,N-dimethylamine as a model system for nonresonant downhill charge transfer in peptides", *Journal of Physical Chemistry A*, vol. 109, no. 36, pp. 8074–8080, Sep. 2005. DOI: 10.1021/jp0210935.

[42] A. I. Kuleff and L. S. Cederbaum, "Charge migration in different conformers of glycine: the role of nuclear geometry", *Chemical Physics*, vol. 338, no. 2-3, pp. 320–328, Sep. 2007. DOI: 10.1016/j.chemphys.2007.04.012.

[43] L. Belshaw, F. Calegari, M. J. Duffy, A. Trabattoni, L. Poletto, M. Nisoli, and J. B. Greenwood, "Observation of ultrafast charge migration in an amino acid", *The Journal of Physical Chemistry Letters*, vol. 3, no. 24, pp. 3751–3754, 2012. DOI: 10.

1021/jz3016028. eprint: http://pubs.acs.org/doi/pdf/10.1021/jz3016028. [Online]. Available: http://pubs.acs.org/doi/abs/10.1021/jz3016028.

[44] M. Vacher, L. Steinberg, A. J. Jenkins, M. J. Bearpark, and M. A. Robb, "Electron dynamics following photoionization: decoherence due to the nuclear-wave-packet width", *Phys. Rev. A*, vol. 92, p. 040 502, 4 Oct. 2015. DOI: 10.1103/PhysRevA.92.040502. [Online]. Available: http://link.aps.org/doi/10.1103/PhysRevA.92.040502.

[45] V. Despré, A. Marciniak, V. Loriot, M. C. E. Galbraith, A. Rouzée, M. J. J. Vrakking, F. Lépine, and A. I. Kuleff, "Attosecond hole migration in benzene molecules surviving nuclear motion", *The Journal of Physical Chemistry Letters*, vol. 6, no. 3, pp. 426–431, 2015, PMID: 26261959. DOI: 10.1021/jz502493j. eprint: http://dx.doi.org/10.1021/jz502493j. [Online]. Available: http://dx.doi.org/10.1021/jz502493j.

[46] M. F. Kling, C. Siedschlag, A. J. Verhoef, J. I. Khan, M. Schultze, T. Uphues, Y. Ni, M. Uiberacker, M. Drescher, F. Krausz, and M. J. J. Vrakking, "Control of electron localization in molecular dissociation", *Science*, vol. 312, no. 5771, pp. 246–248, Apr. 2006. DOI: 10.1126/science.1126259.

[47] G. Sansone, F. Kelkensberg, J. F. Pérez-Torres, F. Morales, M. F. Kling, W. Siu, O. Ghafur, P. Johnsson, M. Swoboda, E. Benedetti, F. Ferrari, F. Lépine, J. L. Sanz-Vicario, S. Zherebtsov, I. Znakovskaya, A. L'huillier, M. Y. Ivanov, M. Nisoli, F. Martín, and M. J. J. Vrakking, "Electron localization following attosecond molecular photoionization.", eng, *Nature*, vol. 465, no. 7299, pp. 763–766, Jun. 2010. DOI: 10.1038/nature09084. [Online]. Available: http://dx.doi.org/10.1038/nature09084.

[48] K. P. Singh, F. He, P. Ranitovic, W. Cao, S. De, D. Ray, S. Chen, U. Thumm, A. Becker, M. M. Murnane, H. C. Kapteyn, I. V. Litvinyuk, and C. L. Cocke, "Control of electron localization in deuterium molecular ions using an attosecond pulse train and a many-cycle infrared pulse.", eng, *Physical Review Letters*, vol. 104, no. 2, p. 023 001, Jan. 2010.

[49] F. Kelkensberg, W. Siu, J. F. Pérez-Torres, F. Morales, G. Gademann, A. Rouzée, P. Johnsson, M. Lucchini, F. Calegari, J. L. Sanz-Vicario, F. Martín, and M. J. J.

Vrakking, "Attosecond control in photoionization of hydrogen molecules.", eng, *Physical Review Letters*, vol. 107, no. 4, p. 043 002, Jul. 2011.

[50] W. Siu, F. Kelkensberg, G. Gademann, A. Rouzée, P. Johnsson, D. Dowek, M. Lucchini, F. Calegari, U. De Giovannini, A. Rubio, R. R. Lucchese, H. Kono, F. Lépine, and M. J. J. Vrakking, "Attosecond control of dissociative ionization of O_2 molecules", *Physical Review A*, vol. 84, p. 063 412, 6 Dec. 2011. DOI: 10.1103/PhysRevA.84.063412. [Online]. Available: http://link.aps.org/doi/10.1103/PhysRevA.84.063412.

[51] F. Calegari, A. Trabattoni, A. Palacios, D. Ayuso, M. C. Castrovilli, J. B. Greenwood, P. Decleva, F. Martín, and M. Nisoli, "Charge migration induced by attosecond pulses in bio-relevant molecules", *Journal of Physics B: Atomic, Molecular and Optical Physics*, vol. 49, no. 14, p. 142 001, 2016. [Online]. Available: http://stacks.iop.org/0953-4075/49/i=14/a=142001.

[52] F. Calegari, D. Ayuso, A. Trabattoni, L. Belshaw, S. De Camillis, S. Anumula, F. Frassetto, L. Poletto, A. Palacios, P. Decleva, J. B. Greenwood, F. Martín, and M. Nisoli, "Ultrafast electron dynamics in phenylalanine initiated by attosecond pulses", *Science*, vol. 346, no. 6207, pp. 336–339, 2014, ISSN: 0036-8075. DOI: 10.1126/science.1254061. eprint: http://science.sciencemag.org/content/346/6207/336.full.pdf. [Online]. Available: http://science.sciencemag.org/content/346/6207/336.

[53] O. Smirnova, Y. Mairesse, S. Patchkovskii, N. Dudovich, D. Villeneuve, P. Corkum, and M. Y. Ivanov, "High harmonic interferometry of multi-electron dynamics in molecules", *Nature*, vol. 460, no. 7258, pp. 972–977, Aug. 2009, ISSN: 0028-0836. [Online]. Available: http://dx.doi.org/10.1038/nature08253.

[54] S. Haessler, J. Caillat, W. Boutu, C. Giovanetti-Teixeira, T. Ruchon, T. Auguste, Z. Diveki, P. Breger, A. Maquet, B. Carre, R. Taieb, and P. Salieres, "Attosecond imaging of molecular electronic wavepackets", *Nature Physics*, vol. 6, no. 3, pp. 200–206, Mar. 2010, ISSN: 1745-2473. [Online]. Available: http://dx.doi.org/10.1038/nphys1511.

[55] H. J. Worner, J. B. Bertrand, D. V. Kartashov, P. B. Corkum, and D. M. Villeneuve, "Following a chemical reaction using high-harmonic interferometry", *Nature*, vol.

466, no. 7306, pp. 604–607, Jul. 2010, ISSN: 0028-0836. [Online]. Available: http://dx.doi.org/10.1038/nature09185.

[56] P. Salières, A. Maquet, S. Haessler, J. Caillat, and R. Taïeb, "Imaging orbitals with attosecond and ångström resolutions: toward attochemistry?", eng, *Reports on Progress in Physics*, vol. 75, no. 6, p. 062 401, Jun. 2012. DOI: 10.1088/0034-4885/75/6/062401. [Online]. Available: http://dx.doi.org/10.1088/0034-4885/75/6/062401.

[57] P. M. Kraus, B. Mignolet, D. Baykusheva, A. Rupenyan, L. Horný, E. F. Penka, G. Grassi, O. I. Tolstikhin, J. Schneider, F. Jensen, L. B. Madsen, A. D. Bandrauk, F. Remacle, and H. J. Wörner, "Measurement and laser control of attosecond charge migration in ionized iodoacetylene", *Science*, vol. 350, no. 6262, pp. 790–795, 2015, ISSN: 0036-8075. DOI: 10.1126/science.aab2160. eprint: http://science.sciencemag.org/content/350/6262/790.full.pdf. [Online]. Available: http://science.sciencemag.org/content/350/6262/790.

[58] C. Ott, A. Kaldun, L. Argenti, P. Raith, K. Meyer, M. Laux, Y. Zhang, A. Blaettermann, S. Hagstotz, T. Ding, R. Heck, J. Madronero, F. Martin, and T. Pfeifer, "Reconstruction and control of a time-dependent two-electron wave packet", *NATURE*, vol. 516, no. 7531, pp. 374+, 2014, ISSN: 0028-0836. DOI: {10.1038/nature14026}.

[59] A. Kaldun, A. Blättermann, V. Stooß, S. Donsa, H. Wei, R. Pazourek, S. Nagele, C. Ott, C. D. Lin, J. Burgdörfer, and T. Pfeifer, "Observing the ultrafast buildup of a fano resonance in the time domain", *Science*, vol. 354, no. 6313, pp. 738–741, 2016, ISSN: 0036-8075. DOI: 10.1126/science.aah6972. eprint: http://science.sciencemag.org/content/354/6313/738.full.pdf. [Online]. Available: http://science.sciencemag.org/content/354/6313/738.

[60] B. Mignolet, R. D. Levine, and F. Remacle, "Control of electronic dynamics visualized by angularly resolved photoelectron spectra: a dynamical simulation with an ir pump and xuv attosecond-pulse-train probe", *Phys. Rev. A*, vol. 89, p. 021 403, 2 Feb. 2014. DOI: 10.1103/PhysRevA.89.021403. [Online]. Available: http://link.aps.org/doi/10.1103/PhysRevA.89.021403.

[61] B. Muskatel, F. Remacle, and R. Levine, "Attophotochemistry. probing ultrafast electron dynamics by the induced nuclear motion: the prompt and delayed predissoci-

ation of {n2}", *Chemical Physics Letters*, vol. 601, pp. 45–48, 2014, ISSN: 0009-2614. DOI: http://dx.doi.org/10.1016/j.cplett.2014.03.031. [Online]. Available: http://www.sciencedirect.com/science/article/pii/S0009261414001821.

[62] F. Remacle and R. D. Levine, "An electronic time scale in chemistry", *Proceedings of the National Academy of Sciences of the United States of America*, vol. 103, no. 18, pp. 6793–6798, May 2006. DOI: 10.1073/pnas.0601855103.

[63] Y. Bhattacharjee, "Measuring the immeasurable", *Nature*, vol. 412, no. 6846, pp. 474–476, Aug. 2001, ISSN: 0028-0836. [Online]. Available: http://dx.doi.org/10.1038/35087741.

[64] F. Calegari, G. Sansone, S. Stagira, C. Vozzi, and M. Nisoli, "Advances in attosecond science", *Journal of Physics B: Atomic, Molecular and Optical Physics*, vol. 49, no. 6, p. 062 001, 2016. [Online]. Available: http://stacks.iop.org/0953-4075/49/i=6/a=062001.

[65] T. Pfeifer, M. J. Abel, P. M. Nagel, A. Jullien, Z.-H. Loh, M. J. Bell, D. M. Neumark, and S. R. Leone, "Time-resolved spectroscopy of attosecond quantum dynamics", *Chemical Physics Letters*, vol. 463, no. 1-3, pp. 11–24, 2008, ISSN: 0009-2614. DOI: http://dx.doi.org/10.1016/j.cplett.2008.08.059. [Online]. Available: http://www.sciencedirect.com/science/article/pii/S0009261408011512.

[66] F. Krausz and M. Ivanov, "Attosecond physics", *Reviews of Modern Physics*, vol. 81, pp. 163–234, 1 Feb. 2009. DOI: 10.1103/RevModPhys.81.163. [Online]. Available: http://link.aps.org/doi/10.1103/RevModPhys.81.163.

[67] N. Bohr, "On the constitution of atoms and molecules", *Philosophical Magazine*, vol. 26, no. 151, pp. 1–25, Jul. 1913. DOI: 10.1080/14786441308634955.

[68] ——, "On the constitution of atoms and molecules", *Philosophical Magazine*, vol. 26, no. 153, pp. 476–502, Sep. 1913. DOI: 10.1080/14786441308634993.

[69] ——, "On the constitution of atoms and molecules", *Philosophical Magazine*, vol. 26, no. 155, pp. 857–875, Nov. 1913. DOI: 10.1080/14786441308635031.

[70] A. I. Kuleff and L. S. Cederbaum, "Tracing ultrafast interatomic electronic decay processes in real time and space.", eng, *Physical Review Letters*, vol. 98, no. 8, p. 083 201, Feb. 2007.

[71] M. Kohler, T. Pfeifer, K. Hatsagortsyan, and C. Keitel, "Chapter 4 - frontiers of atomic high-harmonic generation", in *Advances in Atomic, Molecular, and Optical Physics*, E. A. Paul Berman and C. Lin, Eds., vol. Volume 61, Academic Press, 2012, pp. 159–208. [Online]. Available: http://www.sciencedirect.com/science/article/pii/B9780123964823000041.

[72] C. K. Rhodes, "Physical processes at high-field strengths", *Physica Scripta*, vol. T17, pp. 193–200, 1987. DOI: 10.1088/0031-8949/1987/T17/022.

[73] A. McPherson, G. Gibson, H. Jara, U. Johann, T. S. Luk, I. A. McIIntyre, K. Boyer, and C. K. Rhodes, "Studies of multiphoton production of vacuum ultraviolet-radiation in the rare-gases", *Journal of the Optical Society of America B-optical Physics*, vol. 4, no. 4, pp. 595–601, Apr. 1987. DOI: 10.1364/JOSAB.4.000595.

[74] T. Popmintchev, M. C. Chen, D. Popmintchev, P. Arpin, S. Brown, S. Alisauskas, G. Andriukaitis, T. Balciunas, O. D. Mucke, A. Pugzlys, A. Baltuska, B. Shim, S. E. Schrauth, A. Gaeta, C. Hernandez-Garcia, L. Plaja, A. Becker, A. Jaron-Becker, M. M. Murnane, and H. C. Kapteyn, "Bright coherent ultrahigh harmonics in the keV X-ray regime from mid-infrared femtosecond lasers", *Science*, vol. 336, no. 6086, pp. 1287–1291, Jun. 2012. DOI: 10.1126/science.1218497.

[75] S. Haessler, T. Bal čiunas, G. Fan, G. Andriukaitis, A. Pug žlys, A. Baltu ška, T. Witting, R. Squibb, A. Zaïr, J. W. G. Tisch, J. P. Marangos, and L. E. Chipperfield, "Optimization of quantum trajectories driven by strong-field waveforms", *Phys. Rev. X*, vol. 4, p. 021 028, 2 May 2014. DOI: 10.1103/PhysRevX.4.021028. [Online]. Available: http://link.aps.org/doi/10.1103/PhysRevX.4.021028.

[76] C. Manzoni, O. D. Muecke, G. Cirmi, S. Fang, J. Moses, S.-W. Huang, K.-H. Hong, G. Cerullo, and F. X. Kaertner, "Coherent pulse synthesis: towards sub-cycle optical waveforms", *LASER & PHOTONICS REVIEWS*, vol. 9, no. 2, 129–171, 2015, ISSN: 1863-8880. DOI: {10.1002/lpor.201400181}.

[77] L. V. Keldysh, "Ionization in field of a strong electromagnetic wave", *Soviet Physics Jetp-USSR*, vol. 20, no. 5, pp. 1307–&, 1965.

[78] P. B. Corkum, "Plasma perspective on strong-field multiphoton ionization", *Physical Review Letters*, vol. 71, no. 13, pp. 1994–1997, Sep. 1993. DOI: 10.1103/PhysRevLett.71.1994.

[79] M. Lewenstein, P. Balcou, M. Y. Ivanov, A. L'Huillier, and P. B. Corkum, "Theory of high-harmonic generation by low-frequency laser fields", *Physical Review A*, vol. 49, no. 3, pp. 2117–2132, Mar. 1994. DOI: 10.1103/PhysRevA.49.2117.

[80] A. D. Buckingham, "Birefringence resulting from the application of an intense beam of light to an isotropic medium", *Proceedings of the Physical Society of London Section B*, vol. 69, no. 3, pp. 344–349, 1956. DOI: 10.1088/0370-1301/69/3/309.

[81] D. Jackson J, *Klassische Elektrodynamik*, 3rd ed., K. Müller, Ed., 3-11-016502-3. Walter de Gruyter & Co., 2002.

[82] T. Kreibich, M. Lein, V. Engel, and E. K. U. Gross, "Even-harmonic generation due to beyond-Born-Oppenheimer dynamics", *Physical Review Letters*, vol. 87, p. 103 901, 10 Aug. 2001. DOI: 10.1103/PhysRevLett.87.103901. [Online]. Available: http://link.aps.org/doi/10.1103/PhysRevLett.87.103901.

[83] H. M. Nilsen, L. B. Madsen, and J. P. Hansen, "On selection rules for atoms in laser fields and high harmonic generation", *Journal of Physics B: Atomic, Molecular and Optical Physics*, vol. 35, no. 17, p. L403, 2002. [Online]. Available: http://stacks.iop.org/0953-4075/35/i=17/a=104.

[84] K. Yamanouchi, *Lectures on Ultrafast Intense Laser Science 1*, ser. Lectures on ultrafast intense laser science. Springer, 2010, ISBN: 9783540959441. [Online]. Available: http://books.google.de/books?id=%5C_gzqjeJE75oC.

[85] J. Mauritsson, P. Johnsson, E. Gustafsson, A. L'Huillier, K. J. Schafer, and M. B. Gaarde, "Attosecond pulse trains generated using two color laser fields", *Physical Review Letters*, vol. 97, no. 1, p. 013 001, Jul. 2006. DOI: 10.1103/PhysRevLett.97.013001.

[86] P. Antoine, A. L'Huillier, and M. Lewenstein, "Attosecond pulse trains using high-order harmonics", *Physical Review Letters*, vol. 77, no. 7, pp. 1234–1237, Aug. 1996. DOI: 10.1103/PhysRevLett.77.1234.

[87] Y. Mairesse, A. de Bohan, L. J. Frasinski, H. Merdji, L. C. Dinu, P. Monchicourt, P. Breger, M. Kovacev, R. Taieb, B. Carre, H. G. Muller, P. Agostini, and P. Salieres, "Attosecond synchronization of high-harmonic soft X-rays", *Science*, vol. 302, no. 5650, pp. 1540–1543, Nov. 2003. DOI: 10.1126/science.1090277.

[88] E. Constant, D. Garzella, P. Breger, E. Mevel, C. Dorrer, C. Le Blanc, F. Salin, and P. Agostini, "Optimizing high harmonic generation in absorbing gases: model and experiment", *Physical Review Letters*, vol. 82, no. 8, pp. 1668–1671, Feb. 1999. DOI: 10.1103/PhysRevLett.82.1668.

[89] W. K. Siu, "Probing molecular dynamics using novel light sources", PhD thesis, Radboud Universiteit Nijmegen, 2011.

[90] P. Antoine, D. B. Milosevic, A. L'Huillier, M. B. Gaarde, P. Salieres, and M. Lewenstein, "Generation of attosecond pulses in macroscopic media", *Physical Review A*, vol. 56, no. 6, pp. 4960–4969, Dec. 1997. DOI: 10.1103/PhysRevA.56.4960.

[91] D. G. Lee, H. J. Shin, Y. H. Cha, K. H. Hong, J. H. Kim, and C. H. Nam, "Selection of high-order harmonics from a single quantum path for the generation of an attosecond pulse train", *Physical Review A*, vol. 63, no. 2, p. 021 801, Feb. 2001. DOI: 10.1103/PhysRevA.63.021801.

[92] M. B. Gaarde, J. L. Tate, and K. J. Schafer, "Macroscopic aspects of attosecond pulse generation", *Journal of Physics B: Atomic, Molecular and Optical Physics*, vol. 41, no. 13, p. 132 001, Jul. 2008. DOI: 10.1088/0953-4075/41/13/132001.

[93] V. Tosa, K. T. Kim, and C. H. Nam, "Macroscopic generation of attosecond-pulse trains in strongly ionized media", *Physical Review A*, vol. 79, no. 4, p. 043 828, Apr. 2009. DOI: 10.1103/PhysRevA.79.043828.

[94] J. B. Ashcom, "The role of focusing in the interaction of femtosecond laser pulses with transparent materials", PhD thesis, Harvard University, Cambridge, Massachusetts, 2003.

[95] R. W. Boyd, "Intuitive explanation of the phase anomaly of focused light beams", *Journal of the Optical Society of America*, vol. 70, no. 7, pp. 877–880, Jul. 1980. [Online]. Available: http://www.opticsinfobase.org/abstract.cfm?URI=josa-70-7-877.

[96] X. Wang, W. Sun, Y. Cui, J. Ye, S. Feng, and Y. Zhang, "Complete presentation of the gouy phase shift with the THz digital holography", *Optics Express*, vol. 21, no. 2, pp. 2337–2346, Jan. 2013. [Online]. Available: http://www.opticsexpress.org/abstract.cfm?URI=oe-21-2-2337.

[97] M.-S. Kim, A. d. C. Assafrao, T. Scharf, C. Rockstuhl, S. F. Pereira, H. P. Urbach, and H. P. Herzig, "Longitudinal-differential phase distribution near the focus of a high numerical aperture lens: study of wavefront spacing and Gouy phase", *Journal of Modern Optics*, vol. 60, no. 3, pp. 197–201, Feb. 2013, ISSN: 0950-0340. DOI: 10.1080/09500340.2013.765053. [Online]. Available: http://dx.doi.org/10.1080/09500340.2013.765053.

[98] A. B. Ruffin, J. V. Rudd, J. F. Whitaker, S. Feng, and H. G. Winful, "Direct observation of the Gouy phase shift with single-cycle terahertz pulses", *Physical Review Letters*, vol. 83, no. 17, pp. 3410–3413, Oct. 1999. DOI: 10.1103/PhysRevLett.83.3410.

[99] F. Lindner, G. G. Paulus, H. Walther, A. Baltuska, E. Goulielmakis, M. Lezius, and F. Krausz, "Gouy phase shift for few-cycle laser pulses", *Physical Review Letters*, vol. 92, no. 11, p. 113 001, Mar. 2004. DOI: 10.1103/PhysRevLett.92.113001.

[100] P. Salieres, T. Ditmire, M. D. Perry, A. L'Huillier, and M. Lewenstein, "Angular distributions of high-order harmonics generated by a femtosecond laser", *Journal of Physics B: Atomic, Molecular and Optical Physics*, vol. 29, no. 20, pp. 4771–4786, Oct. 1996. DOI: 10.1088/0953-4075/29/20/027.

[101] A. L. Lytle, "Phase matching and coherence of high-order harmonic generation in hollow waveguides", PhD thesis, University of Colorado, 2008.

[102] J. Eberly, J. Javanainen, and K. Rzazewski, "Above-threshold ionization", *Physics Reports-review Section of Physics Letters*, vol. 204, no. 5, pp. 331–383, Jun. 1991, ISSN: 0370-1573. [Online]. Available: http://www.sciencedirect.com/science/article/pii/0370157391901315.

[103] I. Shchatsinin, T. Laarmann, G. Stibenz, G. Steinmeyer, A. Stalmashonak, N. Zhavoronkov, C. P. Schulz, and I. V. Hertel, "C_{60} in intense short pulse laser fields down to 9 fs: excitation on time scales below e-e and e-phonon coupling", *Journal of Chemical Physics*, vol. 125, no. 19, p. 194 320, Nov. 2006. DOI: 10.1063/1.2362817.

[104] S. Larochelle, A. Talebpour, and S. L. Chin, "Non-sequential multiple ionization of rare gas atoms in a Ti : Sapphire laser field", *Journal of Physics B: Atomic, Molecular and Optical Physics*, vol. 31, no. 6, pp. 1201–1214, Mar. 1998. DOI: 10.1088/0953-4075/31/6/008.

[105] E. T. F. Rogers, "Modelling of capillary high harmonic generation", PhD thesis, University of Southampton, Sep. 2008.

[106] P. Balcou, P. Salieres, A. L'Huillier, and M. Lewenstein, "Generalized phase-matching conditions for high harmonics: the role of field-gradient forces", *Physical Review A*, vol. 55, no. 4, pp. 3204–3210, Apr. 1997. DOI: 10.1103/PhysRevA.55.3204.

[107] P. Salieres, A. L'Huillier, and M. Lewenstein, "Coherence control of high-order harmonics", *Physical Review Letters*, vol. 74, no. 19, pp. 3776–3779, May 1995. DOI: 10.1103/PhysRevLett.74.3776.

[108] Z. Chang, A. Rundquist, H. Wang, I. Christov, H. C. Kapteyn, and M. M. Murnane, "Temporal phase control of soft-X-ray harmonic emission", *Physical Review A*, vol. 58, no. 1, R30–R33, Jul. 1998. DOI: 10.1103/PhysRevA.58.R30.

[109] D. G. Lee, J. H. Kim, K. H. Hong, and C. H. Nam, "Coherent control of high-order harmonics with chirped femtosecond laser pulses", *Physical Review Letters*, vol. 87, no. 24, p. 243 902, Dec. 2001. DOI: 10.1103/PhysRevLett.87.243902.

[110] J. J. Carrera and S. I. Chu, "Extension of high-order harmonic generation cutoff via coherent control of intense few-cycle chirped laser pulses", *Physical Review A*, vol. 75, no. 3, p. 033 807, Mar. 2007. DOI: 10.1103/PhysRevA.75.033807.

[111] G. Farkas and C. Toth, "Proposal for attosecond light-pulse generation using laser-induced multiple-harmonic conversion processes in rare-gases", *Physics Letters A*, vol. 168, no. 5-6, pp. 447–450, Sep. 1992. DOI: 10.1016/0375-9601(92)90534-S.

[112] P. M. Paul, E. S. Toma, P. Breger, G. Mullot, F. Auge, P. Balcou, H. G. Muller, and P. Agostini, "Observation of a train of attosecond pulses from high harmonic generation", *Science*, vol. 292, no. 5522, pp. 1689–1692, Jun. 2001. DOI: 10.1126/science.1059413.

[113] R. Lopez-Martens, K. Varju, P. Johnsson, J. Mauritsson, Y. Mairesse, P. Salieres, M. B. Gaarde, K. J. Schafer, A. Persson, S. Svanberg, C. G. Wahlstrom, and A. L'Huillier, "Amplitude and phase control of attosecond light pulses", *Physical Review Letters*, vol. 94, no. 3, p. 033 001, Jan. 2005. DOI: 10.1103/PhysRevLett.94.033001.

[114] J. Mauritsson, P. Johnsson, R. Lopez-Martens, K. Varju, W. Kornelis, J. Biegert, U. Keller, M. B. Gaarde, K. J. Schafer, and A. L'Huillier, "Measurement and control of the frequency chirp rate of high-order harmonic pulses", *Physical Review A*, vol. 70, no. 2, p. 021 801, Aug. 2004. DOI: 10.1103/PhysRevA.70.021801.

[115] M. Hentschel, R. Kienberger, C. Spielmann, G. A. Reider, N. Milosevic, T. Brabec, P. Corkum, U. Heinzmann, M. Drescher, and F. Krausz, "Attosecond metrology", *Nature*, vol. 414, no. 6863, pp. 509–513, Nov. 2001. DOI: 10.1038/35107000.

[116] S. De Silvestri, M. Nisoli, G. Sansone, S. Stagira, and O. Svelto, "Few-cycle pulses by external compression", *Few-cycle Laser Pulse Generation and Its Applications*, vol. 95, pp. 137–177, 2004.

[117] V. P. Kandidov, S. A. Shlenov, and O. G. Kosareva, "Filamentation of high-power femtosecond laser radiation", *Quantum Electronics*, vol. 39, no. 3, pp. 205–228, Mar. 2009. DOI: 10.1070/QE2009v039n03ABEH013916.

[118] L. Gallmann, T. Pfeifer, P. M. Nagel, M. J. Abel, D. M. Neumark, and S. R. Leone, "Comparison of the filamentation and the hollow-core fiber characteristics for pulse compression into the few-cycle regime", *Applied Physics B-lasers and Optics*, vol. 86, no. 4, pp. 561–566, Mar. 2007. DOI: 10.1007/s00340-006-2503-8.

[119] M. Giguere, B. E. Schmidt, A. D. Shiner, M. A. Houle, H. C. Bandulet, G. Tempea, D. M. Villeneuve, J. C. Kieffer, and F. Legare, "Pulse compression of submillijoule few-optical-cycle infrared laser pulses using chirped mirrors", *Optics Letters*, vol. 34, no. 12, pp. 1894–1896, Jun. 2009.

[120] X. W. Chen, X. F. Li, J. Liu, P. F. Wei, X. C. Ge, R. X. Li, and Z. Z. Xu, "Generation of 5 fs, 0.7 mJ pulses at 1 kHz through cascade filamentation", *Optics Letters*, vol. 32, no. 16, pp. 2402–2404, Aug. 2007. DOI: 10.1364/OL.32.002402.

[121] A. Baltuska, T. Udem, M. Uiberacker, M. Hentschel, E. Goulielmakis, C. Gohle, R. Holzwarth, V. S. Yakoviev, A. Scrinzi, T. W. Hansch, and F. Krausz, "Attosecond control of electronic processes by intense light fields", *Nature*, vol. 421, no. 6923, pp. 611–615, Feb. 2003. DOI: 10.1038/nature01414.

[122] E. Goulielmakis, M. Schultze, M. Hofstetter, V. S. Yakovlev, J. Gagnon, M. Uiberacker, A. L. Aquila, E. M. Gullikson, D. T. Attwood, R. Kienberger, F. Krausz, and U. Kleineberg, "Single-cycle nonlinear optics", *Science*, vol. 320, no. 5883, pp. 1614–1617, Jun. 2008. DOI: 10.1126/science.1157846. [Online]. Available: http://www.sciencemag.org/content/320/5883/1614.abstract.

[123] F. Calegari, M. Lucchini, M. Negro, C. Vozzi, L. Poletto, O. Svelto, S. D. Silvestri, G. Sansone, S. Stagira, and M. Nisoli, "Temporal gating methods for the generation of isolated attosecond pulses", *Journal of Physics B: Atomic, Molecular and Optical Physics*, vol. 45, no. 7, p. 074 002, 2012. [Online]. Available: http://stacks.iop.org/0953-4075/45/i=7/a=074002.

[124] T. Pfeifer, A. Jullien, M. J. Abel, P. M. Nagel, L. Gallmann, D. M. Neumark, and S. R. Leone, "Generating coherent broadbandcontinuum soft-X-ray radiation byattosecond ionization gating", *Optics Express*, vol. 15, no. 25, pp. 17 120–17 128, Dec. 2007. DOI: 10.1364/OE.15.017120. [Online]. Available: http://www.opticsexpress.org/abstract.cfm?URI=oe-15-25-17120.

[125] I. J. Sola, E. Mevel, L. Elouga, E. Constant, V. Strelkov, L. Poletto, P. Villoresi, E. Benedetti, J.-P. Caumes, S. Stagira, C. Vozzi, G. Sansone, and M. Nisoli, "Controlling attosecond electron dynamics by phase-stabilized polarization gating", *Nature Physics*, vol. 2, no. 5, pp. 319–322, May 2006, ISSN: 1745-2473. [Online]. Available: http://dx.doi.org/10.1038/nphys281.

[126] M. J. Abel, T. Pfeifer, P. M. Nagel, W. Boutu, M. J. Bell, C. P. Steiner, D. M. Neumark, and S. R. Leone, "Isolated attosecond pulses from ionization gating of high-harmonic emission", *Chemical Physics*, vol. 366, no. 1-3, pp. 9–14, Dec. 2009, ISSN: 0301-0104. [Online]. Available: http://www.sciencedirect.com/science/article/pii/S0301010409002857.

[127] K. S. Budil, P. Salieres, A. L'Huillier, T. Ditmire, and M. D. Perry, "Influence of ellipticity on harmonic-generation", *Physical Review A*, vol. 48, no. 5, R3437–R3440, Nov. 1993.

[128] G. Sansone, E. Benedetti, F. Calegari, C. Vozzi, L. Avaldi, R. Flammini, L. Poletto, P. Villoresi, C. Altucci, R. Velotta, S. Stagira, S. De Silvestri, and M. Nisoli,

"Isolated single-cycle attosecond pulses", *Science*, vol. 314, no. 5798, pp. 443–446, Oct. 2006. DOI: 10.1126/science.1132838.

[129] K. Zhao, Q. Zhang, M. Chini, Y. Wu, X. W. Wang, and Z. H. Chang, "Tailoring a 67 attosecond pulse through advantageous phase-mismatch", *Optics Letters*, vol. 37, no. 18, pp. 3891–3893, Sep. 2012.

[130] Y. Oishi, M. Kaku, A. Suda, F. Kannari, and K. Midorikawa, "Generation of extreme ultraviolet continuum radiation driven by a sub-10-fs two-color field.", *Optics Express*, vol. 14, no. 16, pp. 7230–7, Aug. 2006. DOI: 10.1364/OE.14.007230.

[131] Z. H. Chang, "Controlling attosecond pulse generation with a double optical gating", *Physical Review A*, vol. 76, no. 5, p. 051 403, Nov. 2007. DOI: 10.1103/PhysRevA.76.051403.

[132] F. Quere, H. Vincenti, A. Borot, S. Monchoce, T. J. Hammond, K. T. Kim, J. A. Wheeler, C. Zhang, T. Ruchon, T. Auguste, J. F. Hergott, D. M. Villeneuve, P. B. Corkum, and R. Lopez-Martens, "Applications of ultrafast wavefront rotation in highly nonlinear optics", *JOURNAL OF PHYSICS B-ATOMIC MOLECULAR AND OPTICAL PHYSICS*, vol. 47, no. 12, SI, 2014, ISSN: 0953-4075. DOI: {10.1088/0953-4075/47/12/124004}.

[133] H. Vincenti and F. Quere, "Attosecond lighthouses: how to use spatiotemporally coupled light fields to generate isolated attosecond pulses", *Physical Review Letters*, vol. 108, no. 11, p. 113 904, Mar. 2012. DOI: 10.1103/PhysRevLett.108.113904.

[134] K. T. Kim, C. Zhang, T. Ruchon, J.-F. Hergott, T. Auguste, D. M. Villeneuve, P. B. Corkum, and F. Quere, "Photonic streaking of attosecond pulse trains", *NATURE PHOTONICS*, vol. 7, no. 8, 651–656, 2013, ISSN: 1749-4885. DOI: {10.1038/NPHOTON.2013.170}.

[135] M. C. E. Galbraith, "Time-resolved spectroscopy with attosecond pulses and pulse trains: ultrafast relaxation in benzene cations", PhD thesis, Freie Universität Berlin, 2016.

[136] L. Poletto, G. Tondello, and P. Villoresi, "High-order laser harmonics detection in the EUV and soft X-ray spectral regions", *Review of Scientific Instruments*, vol. 72, no. 7, pp. 2868–2874, Jul. 2001. DOI: 10.1063/1.1378342.

[137] M. Swoboda, J. M. Dahlstrom, T. Ruchon, P. Johnsson, J. Mauritsson, A. L'Huillier, and K. J. Schafer, "Intensity dependence of laser-assisted attosecond photoionization spectra", *Laser Physics*, vol. 19, no. 8, pp. 1591–1599, Aug. 2009. DOI: 10.1134/S1054660X09150390.

[138] J. Samson and W. Stolte, "Precision measurements of the total photoionization cross-sections of He, Ne, Ar, Kr, and Xe", *Journal of Electron Spectroscopy and Related Phenomena*, vol. 123, no. 2-3, pp. 265–276, 2002, ISSN: 0368-2048. DOI: 10.1016/S0368-2048(02)00026-9. [Online]. Available: http://www.sciencedirect.com/science/article/pii/S0368204802000269.

[139] H. G. Muller, "Reconstruction of attosecond harmonic beating by interference of two-photon transitions", *Applied Physics B-lasers and Optics*, vol. 74, S17–S21, Jun. 2002. DOI: 10.1007/s00340-002-0894-8.

[140] K. T. Kim, D. H. Ko, J. Park, V. Tosa, and C. H. Nam, "Complete temporal reconstruction of attosecond high-harmonic pulse trains", *New Journal of Physics*, vol. 12, p. 083 019, Aug. 2010. DOI: 10.1088/1367-2630/12/8/083019.

[141] J. Itatani, F. Quéré, G. L. Yudin, M. Y. Ivanov, F. Krausz, and P. B. Corkum, "Attosecond streak camera.", eng, *Physical Review Letters*, vol. 88, no. 17, p. 173 903, Apr. 2002.

[142] Y. Mairesse and F. Quere, "Frequency-resolved optical gating for complete reconstruction of attosecond bursts", *Physical Review A*, vol. 71, no. 1, p. 011 401, Jan. 2005. DOI: 10.1103/PhysRevA.71.011401.

[143] D. J. Kane, "Recent progress toward real-time measurement of ultrashort laser pulses", *IEEE Journal of Quantum Electronics*, vol. 35, no. 4, pp. 421–431, Apr. 1999. DOI: 10.1109/3.753647.

[144] L. Gallmann, C. Cirelli, and U. Keller, "Attosecond science: recent highlights and future trends.", eng, *Annual Review of Physical Chemistry*, vol. 63, pp. 447–469, 2012. DOI: 10.1146/annurev-physchem-032511-143702. [Online]. Available: http://dx.doi.org/10.1146/annurev-physchem-032511-143702.

[145] Vrakking, Marc J. J., "Attosecond imaging", *PHYSICAL CHEMISTRY CHEMICAL PHYSICS*, vol. 16, 2775–2789, 2014.

[146] F. Frank, C. Arrell, T. Witting, W. A. Okell, J. McKenna, J. S. Robinson, C. A. Haworth, D. Austin, H. Teng, I. A. Walmsley, J. P. Marangos, and J. W. G. Tisch, "Invited review article: technology for attosecond science", *Review of Scientific Instruments*, vol. 83, no. 7, p. 071 101, Jul. 2012. DOI: 10.1063/1.4731658.

[147] D. Hecht, "Multifrequency acoustooptic diffraction", *Sonics and Ultrasonics, IEEE Transactions on*, vol. 24, no. 1, pp. 7–18, 1977, ISSN: 0018-9537. DOI: 10.1109/T-SU.1977.30905.

[148] S. Zeng, K. Bi, S. Xue, Y. Liu, X. Lv, and Q. Luo, "Acousto-optic modulator system for femtosecond laser pulses", *Review of Scientific Instruments*, vol. 78, no. 1, 015103, p. 015 103, 2007. DOI: 10.1063/1.2409868. [Online]. Available: http://link.aip.org/link/?RSI/78/015103/1.

[149] T. Oksenhendler, D. Kaplan, P. Tournois, G. Greetham, and F. Estable, "Intracavity acousto-optic programmable gain control for ultra-wide-band regenerative amplifiers", *Applied Physics B-lasers and Optics*, vol. 83, no. 4, pp. 491–494, 2006, ISSN: 0946-2171. [Online]. Available: http://dx.doi.org/10.1007/s00340-006-2231-0.

[150] P. Tournois, "Acousto-optic programmable dispersive filter for adaptive compensation of group delay time dispersion in laser systems", *Optics Communications*, vol. 140, no. 4-6, pp. 245–249, Aug. 1997, ISSN: 0030-4018. [Online]. Available: http://www.sciencedirect.com/science/article/pii/S0030401897001533.

[151] C. Iaconis and I. A. Walmsley, "Spectral phase interferometry for direct electric-field reconstruction of ultrashort optical pulses", *Optics Letters*, vol. 23, no. 10, pp. 792–794, May 1998. DOI: 10.1364/OL.23.000792.

[152] G. Gademann, "Expanding the attosecond toolbox", PhD thesis, Radboud Universiteit Nijmegen, 2011.

[153] G. Tondello, "Use of a toroidal mirror as a focusing element for a stigmatic grazing-incidence spectrometer", *Optica Acta*, vol. 26, no. 3, pp. 357–371, 1979.

[154] C. Bourassin-Bouchet, M. M. Mang, F. Delmotte, P. Chavel, and S. de Rossi, "How to focus an attosecond pulse", *Optics Express*, vol. 21, no. 2, pp. 2506–2520, Jan. 2013. DOI: 10.1364/OE.21.002506. [Online]. Available: http://www.opticsexpress.org/abstract.cfm?URI=oe-21-2-2506.

[155] D. H. Parker and A. T. J. B. Eppink, "Photoelectron and photofragment velocity map imaging of state-selected molecular oxygen dissociation/ionization dynamics", *Journal of Chemical Physics*, vol. 107, no. 7, pp. 2357–2362, Aug. 1997. DOI: 10.1063/1.474624.

[156] O. Ghafur, W. Siu, P. Johnsson, M. F. Kling, M. Drescher, and M. J. J. Vrakking, "A velocity map imaging detector with an integrated gas injection system", *Review of Scientific Instruments*, vol. 80, no. 3, pp. 033 110–6, Mar. 2009. [Online]. Available: http://dx.doi.org/10.1063/1.3085799.

[157] M. J. J. Vrakking, "An iterative procedure for the inversion of two-dimensional ion/photoelectron imaging experiments", *Review of Scientific Instruments*, vol. 72, no. 11, pp. 4084–4089, Nov. 2001. DOI: 10.1063/1.1406923.

[158] M. Araki and H. Taguchi, "Two-degree-of-freedom PID controllers", *International Journal of Control, Automation, and Systems*, vol. 1, no. 4, pp. 401–411, Dec. 2003. [Online]. Available: http://www.docstoc.com/docs/81695053/PID-Control.

[159] C. Neidel, J. Klei, C.-H. Yang, A. Rouzée, M. J. J. Vrakking, K. Klünder, M. Miranda, C. L. Arnold, T. Fordell, A. L'Huillier, M. Gisselbrecht, P. Johnsson, M. P. Dinh, E. Suraud, P.-G. Reinhard, V. Despré, M. A. L. Marques, and F. Lépine, "Probing time-dependent molecular dipoles on the attosecond time scale", *Phys. Rev. Lett.*, vol. 111, p. 033 001, 3 Jul. 2013. DOI: 10.1103/PhysRevLett.111.033001. [Online]. Available: http://link.aps.org/doi/10.1103/PhysRevLett.111.033001.

[160] F. Remacle, M. Nest, and R. D. Levine, "Laser steered ultrafast quantum dynamics of electrons in LiH.", eng, *Physical Review Letters*, vol. 99, no. 18, p. 183 902, Nov. 2007.

[161] B. Mignolet, A. Gijsbertsen, M. J. J. Vrakking, R. D. Levine, and F. Remacle, "Stereocontrol of attosecond time-scale electron dynamics in ABCU using ultrafast laser pulses: a computational study", *Physical Chemistry Chemical Physics*, vol. 13, no. 18, pp. 8331–8344, 2011. DOI: 10.1039/c1cp20094a.

[162] T. Burnus, M. A. L. Marques, and E. K. U. Gross, "Time-dependent electron localization function", *Physical Review A*, vol. 71, p. 010 501, 1 Jan. 2005. DOI:

10.1103/PhysRevA.71.010501. [Online]. Available: http://link.aps.org/doi/10.1103/PhysRevA.71.010501.

[163] J. Verschuur and H. L. V. D. Heuvell, "Dissociation and autoionization of the lowest doubly excited state in H_2", *Chemical Physics*, vol. 129, no. 1, pp. 1–10, 1989, ISSN: 0301-0104. DOI: 10.1016/0301-0104(89)80014-X. [Online]. Available: http://www.sciencedirect.com/science/article/pii/030101048980014X.

[164] G. U. Bublitz and S. G. Boxer, "Stark spectroscopy: applications in chemistry, biology, and materials science.", eng, *Annual Review of Physical Chemistry*, vol. 48, pp. 213–242, 1997. DOI: 10.1146/annurev.physchem.48.1.213. [Online]. Available: http://dx.doi.org/10.1146/annurev.physchem.48.1.213.

[165] W. Kohn, "Nobel lecture: electronic structure of matter-wave functions and density functionals", *Reviews of Modern Physics*, vol. 71, no. 5, pp. 1253–1266, Oct. 1999. DOI: 10.1103/RevModPhys.71.1253.

[166] M. A. Marques, N. T. Maitra, F. M. Nogueira, E. Gross, and A. Rubio, Eds., *Fundamentals of Time-Dependent Density Functional Theory*, ser. Lecture Notes in Physics. Springer Berlin Heidelberg, 2012, vol. 837, DOI: 10.1007/978-3-642-23518-4 Print ISBN: 978-3-642-23517-7 Online ISBN: 978-3-642-23518-4.

[167] A. Castro, H. Appel, M. Oliveira, C. A. Rozzi, X. Andrade, F. Lorenzen, M. A. L. Marques, E. K. U. Gross, and A. Rubio, "Octopus: a tool for the application of time-dependent density functional theory", *Physica Status Solidi B-basic Solid State Physics*, vol. 243, no. 11, pp. 2465–2488, Sep. 2006. DOI: 10.1002/pssb.200642067.

[168] F. Calvayrac, P. G. Reinhard, E. Suraud, and C. A. Ullrich, "Nonlinear electron dynamics in metal clusters", *Physics Reports-review Section of Physics Letters*, vol. 337, no. 6, pp. 493–578, Oct. 2000. DOI: 10.1016/S0370-1573(00)00043-0.

[169] V. Despré, In preparation.

[170] U. De Giovannini, G. Brunetto, A. Castro, J. Walkenhorst, and A. Rubio, "Inside cover: simulating pump-probe photoelectron and absorption spectroscopy on the attosecond timescale with time-dependent density functional theory", *ChemPhysChem*, vol. 14, no. 7, pp. 1298–1298, 2013, ISSN: 1439-7641. [Online]. Available: http://dx.doi.org/10.1002/cphc.201390032.

[171] W. Kohn and L. J. Sham, "Self-consistent equations including exchange and correlation effects", *Physical Review*, vol. 140, no. 4A, pp. 1133–&, 1965.

[172] P. Johnsson, J. Mauritsson, T. Remetter, A. L'Huillier, and K. J. Schafer, "Attosecond control of ionization by wave-packet interference", *Physical Review Letters*, vol. 99, no. 23, p. 233 001, Dec. 2007. DOI: 10.1103/PhysRevLett.99.233001.

[173] M. Schultze, E. M. Bothschafter, A. Sommer, S. Holzner, W. Schweinberger, M. Fiess, M. Hofstetter, R. Kienberger, V. Apalkov, V. S. Yakovlev, M. I. Stockman, and F. Krausz, "Controlling dielectrics with the electric field of light", *Nature*, vol. 493, no. 7430, pp. 75–78, Jan. 2013. DOI: 10.1038/nature11720.

[174] P. Baltzer, M. Larsson, L. Karlsson, B. Wannberg, and M. C. Gothe, "Inner-valence states of N_2^+ studied by UV photoelectron-spectroscopy and configuration-interaction calculations", *Physical Review A*, vol. 46, no. 9, pp. 5545–5553, Nov. 1992. DOI: 10.1103/PhysRevA.46.5545.

[175] K. Furuya, A. Matsuo, and T. Ogawa, "The production of CO^+ ($A^2\Pi$) from dissociative ionization of CO_2 : a fragment ion-photon coincidence spectroscopic investigation", *Journal of Physics B: Atomic, Molecular and Optical Physics*, vol. 35, no. 14, p. 3077, 2002. [Online]. Available: http://stacks.iop.org/0953-4075/35/i=14/a=305.

[176] K. Furuya, E. Koto, T. Ueda, K. Maruyama, and T. Ogawa, "Correlation between CH(A) and H^+ produced by dissociative ionization of ethylene", *Chemical Physics Letters*, vol. 288, no. 5-6, pp. 816–820, May 1998, ISSN: 0009-2614. [Online]. Available: http://www.sciencedirect.com/science/article/pii/S0009261498003674.

[177] D. M. P. Holland, D. A. Shaw, M. A. Hayes, L. G. Shpinkova, E. E. Rennie, L. Karlsson, P. Baltzer, and B. Wannberg, "A photoabsorption, photodissociation and photoelectron spectroscopy study of C_2H_4 and C_2D_4", *Chemical Physics*, vol. 219, no. 1, pp. 91–116, Jun. 1997. DOI: 10.1016/S0301-0104(97)00090-6.

[178] A. T. J. B. Eppink and D. H. Parker, "Velocity map imaging of ions and electrons using electrostatic lenses: application in photoelectron and photofragment ion imaging of molecular oxygen", *Review of Scientific Instruments*, vol. 68, no. 9, pp. 3477–3484, Sep. 1997. DOI: 10.1063/1.1148310.

[179] M. Lucchini, K. Kim, F. Calegari, F. Kelkensberg, W. Siu, G. Sansone, M. J. J. Vrakking, M. Hochlaf, and M. Nisoli, "Autoionization and ultrafast relaxation dynamics of highly excited states in N_2", *Physical Review A*, vol. 86, no. 4, p. 043 404, Oct. 2012. DOI: 10.1103/PhysRevA.86.043404.

[180] T. Aoto, K. Ito, Y. Hikosaka, A. Shibasaki, R. Hirayama, N. Yamamono, and E. Miyoshi, "Inner-valence states of N_2^+ and the dissociation dynamics studied by threshold photoelectron spectroscopy and configuration interaction calculation", *Journal of Chemical Physics*, vol. 124, no. 23, p. 234 306, Jun. 2006. DOI: 10.1063/1.2206586.

[181] C. Nicolas, C. Alcaraz, R. Thissen, M. Vervloet, and O. Dutuit, "Dissociative photoionization of N_2 in the 24-32 eV photon energy range", *Journal of Physics B: Atomic, Molecular and Optical Physics*, vol. 36, no. 11, pp. 2239–2251, Jun. 2003. DOI: 10.1088/0953-4075/36/11/309.

[182] J. H. D. Eland and E. J. Duerr, "Dissociation and electron-ion angular distributions in inner-valence photoionisation of CO and N_2", *Chemical Physics*, vol. 229, no. 1, pp. 13–19, Mar. 1998. DOI: 10.1016/S0301-0104(97)00332-7.

[183] P. Fournier, C. A. V. De Runstraat, T. R. Govers, J. Schopman, F. J. De Heer, and J. Los, "Collision-induced dissociation of 10 keV N_2^+ ions: evidence for predissociation of the $C^2\Sigma_u^+$ state", *Chemical Physics Letters*, vol. 9, no. 5, pp. 426–428, Jun. 1971. DOI: 10.1016/0009-2614(71)80259-2.

[184] C. A. van de Runstraat, F. J. D. Heer, and T. R. Govers, "Excitation and decay of $C^2\Sigma_u^+$ state of N_2^+ in case of electron-impact on N_2", *Chemical Physics*, vol. 3, no. 3, pp. 431–450, 1974. DOI: 10.1016/0301-0104(74)87010-2.

[185] L. Medišauskas, S. Patchkovskii, A. Harvey, D. S. Brambila, C. Neidel, J. Klei, A. Rouzée, M. J. J. Vrakking, and M. Y. Ivanov, "Initial electronic coherence in molecular dissociation induced by an attosecond pulse", *Phys. Rev. A*, vol. 92, p. 053 403, 5 Nov. 2015. DOI: 10.1103/PhysRevA.92.053403. [Online]. Available: http://link.aps.org/doi/10.1103/PhysRevA.92.053403.

[186] H.-J. Werner and E.-A. Reinsch, "The self-consistent electron pairs method for multiconfiguration reference state functions", *Journal of Chemical Physics*, vol. 76,

no. 6, pp. 3144–3156, Mar. 1982. [Online]. Available: http://dx.doi.org/10.1063/1.443357.

[187] T. H. Dunning Jr., "Gaussian basis sets for use in correlated molecular calculations. i. the atoms Boron through Neon and Hydrogen", *Journal of Chemical Physics*, vol. 90, no. 2, pp. 1007–1023, Jan. 1989. [Online]. Available: http://dx.doi.org/10.1063/1.456153.

[188] M. W. Schmidt, K. K. Baldridge, J. A. Boatz, S. T. Elbert, M. S. Gordon, J. H. Jensen, S. Koseki, N. Matsunaga, K. A. Nguyen, S. Su, T. L. Windus, M. Dupuis, and J. A. Montgomery, "General atomic and molecular electronic structure system", *Journal of Combinatorial Chemistry*, vol. 14, no. 11, pp. 1347–1363, 1993, ISSN: 1096-987X. [Online]. Available: http://dx.doi.org/10.1002/jcc.540141112.

[189] M. S. Gordon and M. W. Schmidt, "Advances in electronic structure theory: GAMESS a decade later", *Theory and Applications of Computational Chemistry: the First Forty Years*, pp. 1167–1189, 2005. DOI: 10.1016/B978-044451719-7/50084-6.

[190] H.-J. Werner, P. J. Knowles, G. Knizia, F. R. Manby, and M. Schütz, "Molpro: a general-purpose quantum chemistry program package", *Wiley Interdisciplinary Reviews: Computational Molecular Science*, vol. 2, no. 2, pp. 242–253, 2012, ISSN: 1759-0884. [Online]. Available: http://dx.doi.org/10.1002/wcms.82.

[191] H.-J. Werner, P. J. Knowles, G. Knizia, F. R. Manby, M. Schütz, P. Celani, T. Korona, R. Lindh, A. Mitrushenkov, G. Rauhut, K. R. Shamasundar, T. B. Adler, R. D. Amos, A. Bernhardsson, A. Berning, D. L. Cooper, M. J. O. Deegan, A. J. Dobbyn, F. Eckert, E. Goll, C. Hampel, A. Hesselmann, G. Hetzer, T. Hrenar, G. Jansen, C. Köppl, Y. Liu, A. W. Lloyd, R. A. Mata, A. J. May, S. J. McNicholas, W. Meyer, M. E. Mura, A. Nicklass, D. P. O'Neill, P. Palmieri, D. Peng, K. Pflüger, R. Pitzer, M. Reiher, T. Shiozaki, H. Stoll, A. J. Stone, R. Tarroni, T. Thorsteinsson, and M. Wang, *Molpro, version 2012.1, a package of ab initio programs*, http://www.molpro.net/, 2012.

[192] J. A. Fleck, J. R. Morris, and M. D. Feit, "Time-dependent propagation of high-energy laser-beams through atmosphere", *Applied Physics*, vol. 10, no. 2, pp. 129–160, 1976. DOI: 10.1007/BF00896333.

[193] R. Aebersold and M. Mann, "Mass spectrometry-based proteomics", *Nature*, vol. 422, no. 6928, pp. 198–207, Mar. 2003. DOI: 10.1038/nature01511.

[194] M. Sharon, "Structural MS pulls its weight", *Science*, vol. 340, no. 6136, pp. 1059–1060, 2013. DOI: 10.1126/science.1236303. eprint: http://www.sciencemag.org/content/340/6136/1059.full.pdf. [Online]. Available: http://www.sciencemag.org/content/340/6136/1059.short.

[195] G. L. Glish and R. W. Vachet, "The basics of mass spectrometry in the twenty-first century", *Nature Reviews Drug Discovery*, vol. 2, no. 2, pp. 140–150, Feb. 2003. DOI: 10.1038/nrd1011.

[196] M. Thevis, A. Thomas, and W. Schanzer, "Doping control analysis of selected peptide hormones using LC-MS(/MS)", *Forensic Science International*, vol. 213, no. 1-3, pp. 35–41, Dec. 2011. DOI: 10.1016/j.forsciint.2011.06.015.

[197] O. Barroso, D. J. Handelsman, C. Strasburger, and M. Thevis, "Analytical challenges in the detection of peptide hormones for anti-doping purposes", *Bioanalysis*, vol. 4, no. 13, pp. 1577–1590, Jul. 2012. DOI: 10.4155/BIO.12.128.

[198] B. Meyer, D. G. Papasotiriou, and M. Karas, "100% protein sequence coverage: a modern form of surrealism in proteomics", *Amino Acids*, vol. 41, no. 2, pp. 291–310, Jul. 2011. DOI: 10.1007/s00726-010-0680-6.

[199] W. D. Bowers, S. S. Delbert, R. L. Hunter, and R. T. McIver, "Fragmentation of oligopeptide ions using ultraviolet-laser radiation and Fourier-transform mass-spectrometry", *Journal of the American Chemical Society*, vol. 106, no. 23, pp. 7288–7289, 1984. DOI: 10.1021/ja00335a094.

[200] J. R. Eyler, "Infrared multiple photon dissociation spectroscopy of ions in Penning traps", *Mass Spectrometry Reviews*, vol. 28, no. 3, pp. 448–467, May 2009. DOI: 10.1002/mas.20217.

[201] J. Brodbelt, "Shedding light on the frontier of photodissociation", English, *Journal of the American Society for Mass Spectrometry*, vol. 22, no. 2, pp. 197–206, 2011, ISSN: 1044-0305. DOI: 10.1007/s13361-010-0023-6. [Online]. Available: http://dx.doi.org/10.1007/s13361-010-0023-6.

[202] T. Yatsuhashi and N. Nakashima, "Formation and fragmentation of quadruply charged molecular ions by intense femtosecond laser pulses", *Journal of Physical Chemistry A*, vol. 114, no. 28, pp. 7445–7452, Jul. 2010. DOI: 10.1021/jp103725s.

[203] H. Steen and M. Mann, "The ABCs (and XYZs) of peptide sequencing", *Nature Reviews Molecular Cell Biology*, vol. 5, no. 9, pp. 699–711, Sep. 2004. DOI: 10.1038/nrm1468.

[204] T. Laarmann, I. Shchatsinin, P. Singh, N. Zhavoronkov, M. Gerhards, C. P. Schulz, and I. V. Hertel, "Coherent control of bond breaking in amino acid complexes with tailored femtosecond pulses", *Journal of Chemical Physics*, vol. 127, no. 20, p. 201 101, Nov. 2007. DOI: 10.1063/1.2806029.

[205] T. Laarmann, I. Shchatsinin, P. Singh, N. Zhavoronkov, C. P. Schulz, and I. V. Hertel, "Femtosecond pulse shaping as analytic tool in mass spectrometry of complex polyatomic systems", *Journal of Physics B: Atomic, Molecular and Optical Physics*, vol. 41, no. 7, p. 074 005, Apr. 2008. DOI: 10.1088/0953-4075/41/7/074005.

[206] F. Xian, C. L. Hendrickson, and A. G. Marshall, "High resolution mass spectrometry", *Analytical Chemistry*, vol. 84, no. 2, pp. 708–719, Jan. 2012. DOI: 10.1021/ac203191t.

[207] A. G. Marshall and C. L. Hendrickson, "Fourier transform ion cyclotron resonance detection: principles and experimental configurations", *International Journal of Mass Spectrometry*, vol. 215, no. 1-3, pp. 59–75, Apr. 2002. DOI: 10.1016/S1387-3806(01)00588-7.

[208] E. Q. Lawrence and M. S. Livingston, "The production of high speed light ions without the use of high voltages", *Physical Review*, vol. 40, no. 1, pp. 19–35, Apr. 1932. DOI: 10.1103/PhysRev.40.19.

[209] J. A. HippleI, H. Sommer, and H. A. Thomas, "A precise method of determining the Faraday by magnetic resonance", *Physical Review*, vol. 76, no. 12, pp. 1877–1878, 1949. DOI: 10.1103/PhysRev.76.1877.2.

[210] R. T. McIver, "A pulsed grid modulation scheme for an ion cyclotron resonance spectrometer", *Review of Scientific Instruments*, vol. 41, no. 1, pp. 126–&, 1970. DOI: 10.1063/1.1684237.

[211] M. B. Comisaro and A. G. Marshall, "Fourier-transform ion-cyclotron resonance spectroscopy", *Chemical Physics Letters*, vol. 25, no. 2, pp. 282–283, 1974. DOI: 10.1016/0009-2614(74)89137-2.

[212] ——, "Frequency-sweep Fourier-transform ion-cyclotron resonance spectroscopy", *Chemical Physics Letters*, vol. 26, no. 4, pp. 489–490, 1974. DOI: 10.1016/0009-2614(74)80397-0.

[213] L. S. Brown and G. Gabrielse, "Geonium theory - physics of a single electron or ion in a Penning trap", *Reviews of Modern Physics*, vol. 58, no. 1, pp. 233–311, Jan. 1986. DOI: 10.1103/RevModPhys.58.233.

[214] K. Hakansson, H. J. Cooper, R. R. Hudgins, and C. L. Nilsson, "High resolution tandem mass spectrometry for structural biochemistry", *Current Organic Chemistry*, vol. 7, no. 15, pp. 1503–1525, Oct. 2003. DOI: 10.2174/1385272033486305.

[215] S. Guan and A. G. Marshall, "Ion traps for Fourier transform ion cyclotron resonance mass spectrometry: principles and design of geometric and electric configurations", *International Journal of Mass Spectrometry and Ion Processes*, vol. 146/147, pp. 261–296, Aug. 1995, ISSN: 0168-1176. [Online]. Available: http://www.sciencedirect.com/science/article/pii/016811769504190V.

[216] J. B. Jeffries, S. E. Barlow, and G. H. Dunn, "Theory of space-charge shift of ion-cyclotron resonance frequencies", *International Journal of Mass Spectrometry and Ion Processes*, vol. 54, no. 1-2, pp. 169–187, 1983. DOI: 10.1016/0168-1176(83)85016-2.

[217] S. E. Barlow and M. D. Tinkle, ""Linearizing" an ion cyclotron resonance cell", *Review of Scientific Instruments*, vol. 73, no. 12, pp. 4185–4200, Dec. 2002. DOI: 10.1063/1.1518787.

[218] E. N. Nikolaev, R. M. A. Heeren, A. M. Popov, A. V. Pozdneev, and K. S. Chingin, "Realistic modeling of ion cloud motion in a Fourier transform ion cyclotron resonance cell by use of a particle-in-cell approach", *Rapid Communications In Mass Spectrometry*, vol. 21, no. 22, pp. 3527–3546, 2007. DOI: 10.1002/rcm.3234.

[219] W. C. Wiley and I. H. McLaren, "Time-of-flight mass spectrometer with improved resolution", *Review of Scientific Instruments*, vol. 26, no. 12, pp. 1150–1157, 1955. DOI: 10.1063/1.1715212.

[220] T. Andersen, R. Jensen, M. K. Christensen, T. Pedersen, O. Hansen, and I. Chorkendorff, "High mass resolution time of flight mass spectrometer for measuring products in heterogeneous catalysis in highly sensitive microreactors", *Review of Scientific Instruments*, vol. 83, no. 7, p. 075 105, Jul. 2012. DOI: 10.1063/1.4732815.

[221] I. Wagner and H. Musso, "New naturally occurring amino acids", *Angewandte Chemie-international Edition*, vol. 22, no. 11, pp. 816–828, 1983, ISSN: 1521-3773. DOI: 10.1002/anie.198308161. [Online]. Available: http://dx.doi.org/10.1002/anie.198308161.

[222] G. S. Gorman, J. P. Speir, C. A. Turner, and I. J. Amster, "Proton affinities of the 20 common alpha-amino acids", *Journal of the American Chemical Society*, vol. 114, no. 10, pp. 3986–3988, May 1992, ISSN: 0002-7863. DOI: 10.1021/ja00036a062. [Online]. Available: http://dx.doi.org/10.1021/ja00036a062.

[223] S. Lee, S. J. Valentine, J. P. Reilly, and D. E. Clemmer, "Controlled formation of peptide bonds in the gas phase", *Journal of the American Chemical Society*, vol. 133, no. 40, pp. 15 834–15 837, Oct. 2011. DOI: 10.1021/ja205471n.

[224] E. Fischer and E. Fourneau, "A derivative from glykocolls", *Berichte Der Deutschen Chemischen Gesellschaft*, vol. 34, pp. 2868–2877, May 1901. DOI: 10.1002/cber.190103402249.

[225] P. Roepstorff and J. Fohlman, "Proposal for a common nomenclature for sequence ions in mass-spectra of peptides", *Biomedical Mass Spectrometry*, vol. 11, no. 11, pp. 601–601, 1984. DOI: 10.1002/bms.1200111109.

[226] K. Biemann, "Contributions of mass-spectrometry to peptide and protein-structure", *Biomedical and Environmental Mass Spectrometry*, vol. 16, no. 1-12, pp. 99–111, Oct. 1988. DOI: 10.1002/bms.1200160119.

[227] L. Katz, R. A. Pasternak, and R. B. Corey, "Configuration of the peptide link and of asparagine in Glycyl-L-Asparagine", *Nature*, vol. 170, no. 4338, pp. 1066–1066, Dec. 1952. [Online]. Available: http://dx.doi.org/10.1038/1701066a0.

[228] V. H. Wysocki, G. Tsaprailis, L. L. Smith, and L. A. Breci, "Mobile and localized protons: a framework for understanding peptide dissociation", *Journal of Mass Spectrometry*, vol. 35, no. 12, pp. 1399–1406, 2000, ISSN: 1096-9888. [Online]. Avail-

able: http://dx.doi.org/10.1002/1096-9888(200012)35:12%3C1399::AID-JMS86%3E3.0.CO;2-R.

[229] B. Paizs and S. Suhai, "Fragmentation pathways of protonated peptides", *Mass Spectrometry Reviews*, vol. 24, pp. 508–548, 2005.

[230] F. W. McLafferty, "Mass spectrometric analysis - molecular rearrangements", *Analytical Chemistry*, vol. 31, no. 1, pp. 82–87, 1959. DOI: 10.1021/ac60145a015.

[231] J. Laskin and J. H. Futrell, "Activation of large ions in FT-ICR mass spectrometry", *Mass Spectrometry Reviews*, vol. 24, no. 2, pp. 135–167, Mar. 2005. DOI: 10.1002/mas.20012.

[232] H. J. Cooper, K. Hakansson, and A. G. Marshall, "The role of electron capture dissociation in biomolecular analysis", *Mass Spectrometry Reviews*, vol. 24, no. 2, pp. 201–222, Mar. 2005. DOI: 10.1002/mas.20014.

[233] J. M. Wells and S. A. McLuckey, *Collision-induced dissociation (CID) of peptides and proteins*, 2005. DOI: 10.1016/S0076-6879(05)02005-7.

[234] R. C. Dunbar, "BIRD (blackbody infrared radiative dissociation): evolution, principles, and applications.", eng, *Mass Spectrometry Reviews*, vol. 23, no. 2, pp. 127–158, 2004. DOI: 10.1002/mas.10074. [Online]. Available: http://dx.doi.org/10.1002/mas.10074.

[235] M. W. Gardner, S. I. Smith, A. R. Ledvina, J. A. Madsen, J. J. Coon, J. C. Schwartz, G. C. Stafford, and J. S. Brodbelt, "Infrared multiphoton dissociation of peptide cations in a dual pressure linear ion trap mass spectrometer", *Analytical Chemistry*, vol. 81, no. 19, pp. 8109–8118, Oct. 2009. DOI: 10.1021/ac901313m.

[236] N. C. Polfer, "Infrared multiple photon dissociation spectroscopy of trapped ions", *Chemical Society Reviews*, vol. 40, no. 5, pp. 2211–2221, 2011. DOI: 10.1039/c0cs00171f.

[237] L. M. Mikesh, B. Ueberheide, A. Chi, J. J. Coon, J. E. P. Syka, J. Shabanowitz, and D. F. Hunt, "The utility of ETD mass spectrometry in proteomic analysis", *Biochimica Et Biophysica Acta-proteins and Proteomics*, vol. 1764, no. 12, pp. 1811–1822, Dec. 2006. DOI: 10.1016/j.bbapap.2006.10.003.

[238] T. Uzer and W. Miller, "Theories of intramolecular vibrational energy transfer", *Physics Reports-review Section of Physics Letters*, vol. 199, no. 2, pp. 73–146, 1991, ISSN: 0370-1573. DOI: http://dx.doi.org/10.1016/0370-1573(91)90140-H. [Online]. Available: http://www.sciencedirect.com/science/article/pii/037015739190140H.

[239] K. Fukui, Y. Takada, T. Sumiyoshi, T. Imai, and K. Takahashi, "Infrared multiphoton dissociation spectroscopic analysis of peptides and oligosaccharides by using Fourier transform ion cyclotron resonance mass spectrometry with a midinfrared free-electron laser", *The Journal of Physical Chemistry B*, vol. 110, no. 32, pp. 16 111–16 116, 2006. DOI: 10.1021/jp0607824. eprint: http://pubs.acs.org/doi/pdf/10.1021/jp0607824. [Online]. Available: http://pubs.acs.org/doi/abs/10.1021/jp0607824.

[240] R. A. Zubarev, N. L. Kelleher, and F. W. McLafferty, "Electron capture dissociation of multiply charged protein cations. a nonergodic process", *Journal of the American Chemical Society*, vol. 120, no. 13, pp. 3265–3266, Mar. 1998, ISSN: 0002-7863. DOI: 10.1021/ja973478k. [Online]. Available: http://dx.doi.org/10.1021/ja973478k.

[241] N. Leymarie, C. E. Costello, and P. B. O'Connor, "Electron capture dissociation initiates a free radical reaction cascade", *Journal of the American Chemical Society*, vol. 125, no. 29, pp. 8949–8958, 2003. DOI: 10.1021/ja028831n. eprint: http://pubs.acs.org/doi/pdf/10.1021/ja028831n. [Online]. Available: http://pubs.acs.org/doi/abs/10.1021/ja028831n.

[242] K. F. Medzihradszky. (), [Online]. Available: http://www.google.de/url?sa=t&rct=j&q=&esrc=s&frm=1&source=web&cd=8&ved=0CGwQFjAH&url=http://biotech.szbk.u-szeged.hu/docs/MFK_PF_ME_wFigs.doc&ei=BBuSUq3rBsKAtAbi44CYBQ&usg=AFQjCNHEiRbKoHVZDcasoSPLjOAy6nYFAw.

[243] K. Tanaka, "The origin of macromolecule ionization by laser irradiation (nobel lecture)", *Angewandte Chemie-international Edition*, vol. 42, no. 33, pp. 3860–3870, 2003, ISSN: 1521-3773. [Online]. Available: http://dx.doi.org/10.1002/anie.200300585.

[244] J. B. Fenn, M. Mann, C. K. Meng, S. F. Wong, and C. M. Whitehouse, "Electrospray ionization for mass-spectrometry of large biomolecules", *Science*, vol. 246, no. 4926, pp. 64–71, Oct. 1989. DOI: 10.1126/science.2675315.

[245] L. Pauling, "Interatomic distances in covalent molecules and resonance between two or more lewis electronic structures.", eng, *Proceedings of the National Academy of Sciences of the United States of America*, vol. 18, no. 4, pp. 293–297, Apr. 1932.

[246] A. R. Goldfarb and L. J. Saidel, "Ultraviolet absorption spectra of proteins", *Science*, vol. 114, no. 2954, pp. 156–157, 1951. DOI: 10.1126/science.114.2954.156.

[247] A. R. Goldfarb, L. J. Saidel, and E. Mosovich, "The ultraviolet absorption spectra of proteins", *Journal of Biological Chemistry*, vol. 193, no. 1, pp. 397–404, 1951.

[248] P. Seshan, "The absorption spectra of some aromatic compounds", English, *Proceedings of the Indian Academy of Sciences - Section A*, vol. 3, no. 2, pp. 148–171, 1936, ISSN: 0370-0089. DOI: 10.1007/BF03035826. [Online]. Available: http://dx.doi.org/10.1007/BF03035826.

[249] D. Wetlaufer, "Advances in protein chemistry", in, C. B. Anfinsen, Ed. Academic Press, 1963, vol. 17, ch. Ultraviolet Spectra of proteins and Amino Acids, pp. 304–412, ISBN 0080581900, 9780080581903.

[250] W. D. Bowers, S. S. Delbert, and R. T. McIver, "Consecutive laser-induced photodissociation as a probe of ion structure", *Analytical Chemistry*, vol. 58, no. 4, pp. 969–972, Apr. 1986. DOI: 10.1021/ac00295a066.

[251] W. Gabryelski and L. Li, "Photo-induced dissociation of electrospray generated ions in an ion trap/time-of-flight mass spectrometer", *Review of Scientific Instruments*, vol. 70, no. 11, pp. 4192–4199, Nov. 1999. DOI: 10.1063/1.1150051.

[252] V. Vorsa, T. Kono, K. F. Willey, and N. Winograd, "Femtosecond photoionization of ion beam desorbed aliphatic and aromatic amino acids: fragmentation via α-cleavage reactions", *Journal of Physical Chemistry B*, vol. 103, no. 37, pp. 7889–7895, Sep. 1999. DOI: 10.1021/jp991123c.

[253] B. A. Budnik, Y. O. Tsybin, P. Hakansson, and R. A. Zubarev, "Ionization energies of multiply protonated polypeptides obtained by tandem ionization in Fourier transform mass spectrometers", *Journal of Mass Spectrometry*, vol. 37, no. 11, pp. 1141–1144, Nov. 2002. DOI: 10.1002/jms.376.

[254] R. J. Levis and M. J. DeWitt, "Photoexcitation, ionization, and dissociation of molecules using intense near-infrared radiation of femtosecond duration", *Journal of Physical Chemistry A*, vol. 103, no. 33, pp. 6493–6507, Aug. 1999. DOI: 10.1021/jp984543v.

[255] M. J. DeWitt and R. J. Levis, "Observing the transition from a multiphoton-dominated to a field-mediated ionization process for polyatomic molecules in intense laser fields", *Physical Review Letters*, vol. 81, pp. 5101–5104, 23 Dec. 1998. DOI: 10.1103/PhysRevLett.81.5101. [Online]. Available: http://link.aps.org/doi/10.1103/PhysRevLett.81.5101.

[256] M. DeWitt and R. Levis, "Calculating the Keldysh adiabaticity parameter for atomic, diatomic, and polyatomic molecules", English, *Journal of Chemical Physics*, vol. 108, no. 18, 7739–7742, May 1998, ISSN: 0021-9606. DOI: {10.1063/1.476208}.

[257] M. Lezius, V. Blanchet, D. M. Rayner, D. M. Villeneuve, A. Stolow, and M. Y. Ivanov, "Nonadiabatic multielectron dynamics in strong field molecular ionization", *Physical Review Letters*, vol. 86, no. 1, pp. 51–54, Jan. 2001. DOI: 10.1103/PhysRevLett.86.51.

[258] M. Lezius, V. Blanchet, M. Y. Ivanov, and A. Stolow, "Polyatomic molecules in strong laser fields: nonadiabatic multielectron dynamics", *Journal of Chemical Physics*, vol. 117, no. 4, pp. 1575–1588, Jul. 2002. DOI: 10.1063/1.1487823.

[259] C. Zener, "Non-adiabatic crossing of energy levels", *Proceedings of the Royal Society of London Series A-containing Papers of A Mathematical and Physical Character*, vol. 137, no. 833, pp. 696–702, Sep. 1932. DOI: 10.1098/rspa.1932.0165.

[260] J. R. Rubbmark, M. M. Kash, M. G. Littman, and D. Kleppner, "Dynamical effects at avoided level-crossings - a study of the Landau-Zener effect using Rydberg atoms", *Physical Review A*, vol. 23, no. 6, pp. 3107–3117, 1981. DOI: 10.1103/PhysRevA.23.3107.

[261] A. Konar, Y. Shu, V. V. Lozovoy, J. E. Jackson, B. G. Levine, and M. Dantus, "Polyatomic molecules under intense femtosecond laser irradiation", *The Journal of Physical Chemistry A*, vol. 118, no. 49, pp. 11 433–11 450, 2014, PMID: 25314590. DOI: 10.1021/jp505498t. eprint: http://dx.doi.org/10.1021/jp505498t. [Online]. Available: http://dx.doi.org/10.1021/jp505498t.

[262] S. M. Hankin, D. M. Villeneuve, P. B. Corkum, and D. M. Rayner, "Intense-field laser ionization rates in atoms and molecules", *Phys. Rev. A*, vol. 64, p. 013 405, 1 Jun. 2001. DOI: 10.1103/PhysRevA.64.013405. [Online]. Available: http://link.aps.org/doi/10.1103/PhysRevA.64.013405.

[263] A. Gil, S. Simon, L. Rodríguez-Santiago, J. Bertrán, and M. Sodupe, "Influence of the side chain in the structure and fragmentation of amino acids radical cations", *Journal of Chemical Theory and Compution*, vol. 3, no. 6, pp. 2210–2220, Oct. 2007, ISSN: 1549-9618. DOI: 10.1021/ct700055p. [Online]. Available: http://dx.doi.org/10.1021/ct700055p.

[264] N. P. Lockyer and J. C. Vickerman, "Single photon and femtosecond multiphoton ionisation of the dipeptide valyl-valine", *International Journal of Mass Spectrometry*, vol. 197, pp. 197–209, Feb. 2000. DOI: 10.1016/S1387-3806(99)00249-3.

[265] ——, "Multiphoton ionization mass spectrometry of small biomolecules with nanosecond and femtosecond laser pulses", *International Journal of Mass Spectrometry*, vol. 176, no. 1-2, pp. 77–86, Jun. 1998. DOI: 10.1016/S1387-3806(98)14005-8.

[266] C. L. Kalcic, T. C. Gunaratne, A. D. Jonest, M. Dantus, and G. E. Reid, "Femtosecond laser-induced ionization/dissociation of protonated peptides", *Journal of the American Chemical Society*, vol. 131, no. 3, pp. 940–942, Jan. 2009. DOI: 10.1021/ja8089119.

[267] S. A. Smith, C. L. Kalcic, K. A. Safran, P. M. Stemmer, M. Dantus, and G. E. Reid, "Enhanced characterization of singly protonated phosphopeptide ions by femtosecond laser-induced ionization/dissociation tandem mass spectrometry (fs-LID-MS/MS)", *Journal of the American Society for Mass Spectrometry*, vol. 21, no. 12, pp. 2031–2040, Dec. 2010. DOI: 10.1016/j.jasms.2010.08.016.

[268] C. L. Kalcic, G. E. Reid, V. V. Lozovoy, and M. Dantus, "Mechanism elucidation for nonstochastic femtosecond laser-induced ionization/dissociation: from amino acids to peptides.", eng, *The Journal of Physical Chemistry A*, vol. 116, no. 11, pp. 2764–2774, Mar. 2012. DOI: 10.1021/jp208421d. [Online]. Available: http://dx.doi.org/10.1021/jp208421d.

[269] M. Duffy, O. Kelly, C. Calvert, R. King, L. Belshaw, T. Kelly, J. Costello, D. Timson, W. Bryan, T. Kierspel, I. Turcu, C. Cacho, E. Springate, I. Williams, and J. Greenwood, "Fragmentation of neutral amino acids and small peptides by intense, femtosecond laser pulses", English, *Journal of the American Society for Mass Spectrometry*, pp. 1–10, 2013, ISSN: 1044-0305. DOI: 10.1007/s13361-013-0653-6. [Online]. Available: http://dx.doi.org/10.1007/s13361-013-0653-6.

[270] G. Reitsma, O. Gonzalez-Magaña, O. Versolato, M. Door, R. Hoekstra, E. Suraud, B. Fischer, N. Camus, M. Kremer, R. Moshammer, and T. Schlathölter, "Femtosecond laser induced ionization and dissociation of gas-phase protonated leucine enkephalin", *International Journal of Mass Spectrometry*, vol. 365-366, pp. 365–371, 2014, Special issue: Tilmann Märk, ISSN: 1387-3806. DOI: http://dx.doi.org/10.1016/j.ijms.2014.01.004. [Online]. Available: http://www.sciencedirect.com/science/article/pii/S1387380614000086.

[271] R. Weinkauf, P. Aicher, G. Wesley, J. Grotemeyer, and E. W. Schlag, "Femtosecond versus nanosecond multiphoton ionization and dissociation of large molecules", *The Journal of Physical Chemistry*, vol. 98, no. 34, pp. 8381–8391, 1994. DOI: 10.1021/j100085a019. eprint: http://pubs.acs.org/doi/pdf/10.1021/j100085a019. [Online]. Available: http://pubs.acs.org/doi/abs/10.1021/j100085a019.

[272] G. Gregoire, H. Kang, C. Dedonder-Lardeux, C. Jouvet, C. Desfrancois, D. Onidas, V. Lepere, and J. A. Fayeton, "Statistical vs. non-statistical deactivation pathways in the UV photo-fragmentation of protonated tryptophan-leucine dipeptide", *Physical Chemistry Chemical Physics*, vol. 8, no. 1, pp. 122–128, 2006. DOI: 10.1039/b510406h.

[273] K. W. D. Ledingham and R. P. Singhal, "High intensity laser mass spectrometry - a review", *International Journal of Mass Spectrometry and Ion Processes*, vol. 163, no. 3, pp. 149–168, May 1997. DOI: 10.1016/S0168-1176(97)00015-3.

[274] A. Stalmashonak, N. Zhavoronkov, I. V. Hertel, S. Vetrov, and K. Schmid, "Spatial control of femtosecond laser system output with submicroradian accuracy", *Applied Optics*, vol. 45, no. 6, pp. 1271–1274, Feb. 2006. DOI: 10.1364/AO.45.001271.

[275] I. V. Hertel and C. P. Schulz, "Atome, Moleküle und optische Physik 2: Moleküle und Photonen - Spektroskopie und Streuphysik", in. Springer, 2010, ch. 13 Laser, Licht und Kohärenz.

[276] L. P. Maguire, S. Szilagyi, and R. E. Scholten, "High performance laser shutter using a hard disk drive voice-coil actuator", *Review of Scientific Instruments*, vol. 75, no. 9, pp. 3077–3079, Sep. 2004. DOI: 10.1063/1.1786331.

[277] A. G. Marshall, C. L. Hendrickson, and G. S. Jackson, "Fourier transform ion cyclotron resonance mass spectrometry: a primer", *Mass Spectrometry Reviews*, vol. 17, no. 1, pp. 1–35, Jan. 1998. DOI: 10.1002/(SICI)1098-2787(1998)17:1<1.

[278] M. E. Corrales, G. Gitzinger, J. González-Vázquez, V. Loriot, R. de Nalda, and L. Bañares, "Velocity map imaging and theoretical study of the coulomb explosion of ch3i under intense femtosecond ir pulses", *J. Phys. Chem. A*, vol. 116, no. 11, pp. 2669–2677, Nov. 2011, ISSN: 1089-5639. DOI: 10.1021/jp207367a. [Online]. Available: http://dx.doi.org/10.1021/jp207367a.

[279] P. A. Limbach, P. B. Grosshans, and A. G. Marshall, "Experimental-determination of the number of trapped ions, detection limit, and dynamic-range in Fourier-transform ion-cyclotron resonance mass-spectrometry", *Analytical Chemistry*, vol. 65, no. 2, pp. 135–140, Jan. 1993. DOI: 10.1021/ac00050a008.

[280] K. Brew, T. C. Vanaman, and R. L. Hill, "Role of α-lactalbumin and a protein in lactose synthetase - a unique mechanism for control of a biological reaction", *Proceedings of the National Academy of Sciences of the United States of America*, vol. 59, no. 2, pp. 491–&, 1968. DOI: 10.1073/pnas.59.2.491.

[281] E. A. Permyakov and L. J. Berliner, "α-Lactalbumin: structure and function", *Febs Letters*, vol. 473, no. 3, pp. 269–274, May 2000. DOI: 10.1016/S0014-5793(00)01546-5.

[282] D. M. Horn, Y. Ge, and F. W. McLafferty, "Activated ion electron capture dissociation for mass spectral sequencing of larger (42 kDa) proteins", *Analytical Chemistry*, vol. 72, no. 20, pp. 4778–4784, Oct. 2000. DOI: 10.1021/ac000494i.

[283] V. Zabrouskov, M. W. Senko, Y. Du, R. D. Leduc, and N. L. Kelleher, "New and automated msn approaches for top-down identification of modified proteins", *Journal of the American Society For Mass Spectrometry*, vol. 16, no. 12, pp. 2027–2038, Dec. 2005. DOI: 10.1016/j.jasms.2005.08.004.

[284] K. L. Durand, X. X. Ma, C. E. Plummer, and Y. Xia, "Tandem mass spectrometry (msn) of peptide disulfide regio-isomers via collision-induced dissociation: utility and limits in disulfide bond characterization", *International Journal of Mass Spectrometry*, vol. 343, pp. 50–57, Jun. 2013. DOI: 10.1016/j.ijms.2013.04.005.

[285] J. Seo and K. J. Lee, "Post-translational modifications and their biological functions: proteomic analysis and systematic approaches", *Journal of Biochemistry and Molecular Biology*, vol. 37, no. 1, pp. 35–44, Jan. 2004.

[286] B. Kuster and M. Mann, "Identifying proteins and post-translational modifications by mass spectrometry", *Current Opinion In Structural Biology*, vol. 8, no. 3, pp. 393–400, Jun. 1998. DOI: 10.1016/S0959-440X(98)80075-4.

[287] M. R. Larsen and P. Roepstorff, "Mass spectrometric identification of proteins and characterization of their post-translational modifications in proteome analysis", *Fresenius Journal of Analytical Chemistry*, vol. 366, no. 6-7, pp. 677–690, Mar. 2000. DOI: 10.1007/s002160051562.

[288] W. Cui, M. S. Thompson, and J. P. Reilly, "Pathways of peptide ion fragmentation induced by vacuum ultraviolet light", *Journal of the American Society for Mass Spectrometry*, vol. 16, no. 8, pp. 1384–1398, 2005, ISSN: 1044-0305. DOI: http://dx.doi.org/10.1016/j.jasms.2005.03.050. [Online]. Available: http://www.sciencedirect.com/science/article/pii/S1044030505002990.

[289] R. G. W. Norrish and F. W. Kirkbride, "204. primary photochemical processes. part i. the decomposition of formaldehyde", *J. Chem. Soc.*, pp. 1518–1530, 1932. DOI: 10.1039/JR9320001518. [Online]. Available: http://dx.doi.org/10.1039/JR9320001518.

[290] M. F. Kling, P. von den Hoff, I. Znakovskaya, and R. de Vivie-Riedle, "(sub-)femtosecond control of molecular reactions via tailoring the electric field of light", *Physical Chemistry Chemical Physics*, vol. 15, no. 24, pp. 9448–9467, 2013. DOI: 10.1039/c3cp50591j.

[291] H. Kang, C. Dedonder-Lardeux, C. Jouvet, G. Gregoire, C. Desfrancois, J. P. Schermann, M. Barat, and J. A. Fayeton, "Control of bond-cleaving reactions of free protonated tryptophan ion by femtosecond laser pulses", *Journal of Physical Chemistry A*, vol. 109, no. 11, pp. 2417–2420, Mar. 2005. DOI: 10.1021/jp0407167.

Appendix

Abstract

This thesis explores the field of ultrafast electron dynamics and the effects of electron-nuclear coupling in molecules. By extending the research to peptides and proteins the investigation of charge migration and charge transfer in larger molecular systems may be established as these phenomena play a crucial role in biological processes. The insights may lead to a higher degree of control over chemical reactions.

In the first part of the current work control over the electron distribution in neutral molecules on the attosecond timescale is achieved by employing an attosecond laser source in a pump-probe scheme (Chapter 3). Several small molecules (N_2, CO_2, C_2H_4) are illuminated with moderately strong near-infrared (NIR) laser radiation inducing a time-dependent dipole. The ultrafast charge displacement is subsequently probed by an attosecond pulse train (APT). The observed effect is interpreted as a varying XUV opacity induced by the molecular polarization.

Furthermore, the dissociative photo-ionization of N_2 molecules by an APT and under the influence of a NIR field is studied by recording the kinetic energy release (KER) spectrum of the N^+ fragments angle- and energy-resolved as a function of pump-probe delay (Chapter 4). Characteristic signal oscillations in conjunction with theory imply that the initial electronic phase acquired during sudden ionization can influence subsequent nuclear dynamics.

The last experiment conducted within the framework of this thesis combines an intense femtosecond laser source and a Fourier-transform mass spectrometer to enable accurate investigations of the interaction of short-pulse lasers with large biologically relevant molecular systems (Chapter 6). As a proof-of-principle investigation, the peptide sequencing capabilities of femtosecond laser-induced dissociation are studied in detail and the fragmentation pathways are characterized. In future experiments, this setup might be used for charge migration and pump-probe studies on various timescales and to establish site-specific fragmentation of biomolecules.

In conclusion, the work presented here explores attosecond pump-probe measurements on small multi-electron systems and how the investigations can be extended to the interaction of intense ultrashort laser pulses with biomolecules.

Kurzzusammenfassung

In der hier vorgestellten Arbeit werden Elektronendynamiken und die Wechselwirkung von Elektronen und Atomkernen in kleinen Molekülen mit Attosekundenzeitauflösung untersucht. Des weiteren soll ein Ansatz gefunden werden diese Forschung auf große Biomoleküle, wie z.B. Peptide oder Proteine, auszudehnen, da Ladungsmigration und -transport eine wichtige Rolle in biologischen Prozessen spielen. Verständnis und Kontrolle dieser Vorgänge könnten eine gezieltere Manipulation chemischer Prozesse ermöglichen.

Im ersten Teil der hier vorgestellten Arbeit wird gezeigt, dass die Ladungsverteilung in neutralen Molekülen unter Zuhilfenahme von Pumpe-Probe-Aufbauten mit Attosekundengenauigkeit manipuliert werden kann (Kapitel 3). Hierbei wurden kleine Moleküle (N_2, CO_2, C_2H_4) unter dem Einfluss eines Laserfeldes im Nahinfrarotbereich (NIR) mit Hilfe eines Attosekundenimpulszuges ionisiert. Die vom NIR-Feld hervorgerufene Änderung der Ladungsverteilung, welche in einem oszillierenden Dipol resultiert, kann experimentell als Modulation der Ionisationswahrscheinlichkeit beobachtet werden.

Desweiteren wird die Dissoziation von N_2 im NIR-Feld nach vorausgegangener Ionisation durch einen Attosekundenimpulszug untersucht (Kapitel 4). Die dabei entstehenden N^+ Fragmente werden energie- und winkelaufgelöst als Funktion der relativen attosekundengenauen Impulsverzögerung beobachtet. Hierbei auftretende charakteristische Oszillationen deuten darauf hin, dass die elektronische Phase, welche beim Ionisieren akkumuliert wird, die nachfolgenden Kernbewegungen beeinflussen kann.

Die Untersuchung der Wechselwirkung von ultrakurzen Lichtimpulsen mit biologisch relevanten Molekülen wird durch die Kombination einer Femtosekundenlaserquelle mit einem Fourier-Transformationsmassenspektrometer ermöglicht (Kapitel 6). Mit femtosekundenlaserinduzierter Dissoziation werden Fragmentationsmuster in der Peptidsequenzierung detailiert charakterisiert. Das Experiment kann als Ausgangspunkt für zeitaufgelöste Studien an komplexen Systemen dienen und dazu beitragen eine Methode zu entwickeln mit der gezielte Bindungsbrüche in Biomolekülen induziert werden können.

Zusammenfassend beschäftigt sich die hier vorgestellte Arbeit mit attosekunden Pumpe-Probe-Experimenten an kleinen Molekülen und der möglichen Ausdehnung der Experimente auf große Biomoleküle.

About the author

For reasons of data protection, the text about the author is not published in the electronic version.

Der Text über den Autor ist in der Online-Version aus Gründen des Datenschutzes nicht enthalten.

Curriculum vitae

For reasons of data protection, the curriculum vitae is not published in the electronic version.

Der Lebenslauf ist in der Online-Version aus Gründen des Datenschutzes nicht enthalten.

Author's contributions

Articles

[A1] J. Klei, L. Medišauskas, C. Neidel, C.-H. Yang, M. Galbraith, M. Ivanov, and M. J. J. M. Vrakking, "Signatures of the initial electronic phase observed in the photo-dissociation of molecular nitrogen", In preparation.

[A2] L. Medišauskas, S. Patchkovskii, A. Harvey, D. S. Brambila, C. Neidel, J. Klei, A. Rouzée, M. J. J. Vrakking, and M. Y. Ivanov, "Initial electronic coherence in molecular dissociation induced by an attosecond pulse", *Phys. Rev. A*, vol. 92, p. 053 403, 5 Nov. 2015. DOI: 10.1103/PhysRevA.92.053403. [Online]. Available: http://link.aps.org/doi/10.1103/PhysRevA.92.053403.

[A3] C. Neidel, A. Kühn, C. P. Schulz, F. Noack, T. Schultz, M. Linscheid, and I. V. Hertel, "Investigating biomolecules by femtosecond photolysis in an FT MS", In preparation.

[A4] C. Neidel, J. Klei, C.-H. Yang, A. Rouzée, M. J. J. Vrakking, K. Klünder, M. Miranda, C. L. Arnold, T. Fordell, A. L'Huillier, M. Gisselbrecht, P. Johnsson, M. P. Dinh, E. Suraud, P.-G. Reinhard, V. Despré, M. A. L. Marques, and F. Lépine, "Probing time-dependent molecular dipoles on the attosecond time scale", *Phys. Rev. Lett.*, vol. 111, p. 033 001, 3 Jul. 2013. DOI: 10.1103/PhysRevLett.111.033001. [Online]. Available: http://link.aps.org/doi/10.1103/PhysRevLett.111.033001.

Talks

[T1] J. Klei, C. Neidel, C.-H. Yang, L. Medišauskas, M. Ivanov, and M. J. J. Vrakking, *Signatures of attosecond dynamics in molecular dissociation*, DPG spring meeting, Devision: AMOP, Hannover, Germany, Talk, Mar. 2013. [Online]. Available: http://www.dpg-verhandlungen.de/year/2013/conference/hannover/part/mo/session/15/contribution/5?lang=en.

[T2] C. Neidel, A. Kühn, F. Noack, C. P. Schulz, I. V. Hertel, and L. Michael, *Femtolysis - investigation of biological relevant molecules by femtosecond lasers coupled to a FT ICR mass spectrometer*, DPG spring meeting, Division: AMOP, Dresden, Germany, Talk, Mar. 2011. [Online]. Available: `http://www.dpg-verhandlungen.de/year/2011/conference/dresden/part/mo/session/1/contribution/10`.

[T3] C. Neidel, J. Klei, C.-H. Yang, and M. J. J. Vrakking, *Attosecond dynamics of CO_2 and C_2H_4*, DPG spring meeting, Division: AMOP, Stuttgart, Germany, Talk, Mar. 2012. [Online]. Available: `http://www.dpg-verhandlungen.de/year/2012/conference/stuttgart/part/mo/session/6/contribution/10`.

Posters

[P1] J. Klei, C. Neidel, C.-H. Yang, L. Medišauskas, M. Galbraith, M. Ivanov, and M. J. J. Vrakking, *Attosecond molecular dynamics*, DPG spring meeting, Devision: AMOP, Hannover, Germany, Poster, Mar. 2013. [Online]. Available: `http://www.dpg-verhandlungen.de/year/2013/conference/hannover/part/mo/session/14/contribution/21`.

[P2] J. Klei, C. Neidel, C.-H. Yang, L. Medišauskas, A. Rouzée, M. Ivanov, and M. J. J. Vrakking, *Attosecond control of the dissociative ionization dynamics of N_2*, Attosecond Physics Conference (ATTO2013), Paris, France, Poster, Jul. 2013. [Online]. Available: `http://www.dpg-verhandlungen.de/year/2013/conference/hannover/part/mo/session/14/contribution/21`.

[P3] C. Neidel, A. Kühn, F. Noack, M. Linscheid, and I. V. Hertel, *Femtolysis of biomolecules*, IBBI conference - isolated biomolecules and biomolecular interactions, Berlin, Germany, Poster, Jun. 2010.

[P4] C.-H. Yang, C. Neidel, J. Klei, A. Gijsbertsen, M. J. J. Vrakking, and H. J. Wörner, *High harmonic spectroscopy of NO_2: electronic dynamics and molecular dissociation*, DPG spring meeting, Devision: AMOP, Stuttgart, Germany, Poster, Mar. 2012. [Online]. Available: `http://www.dpg-verhandlungen.de/year/2012/conference/stuttgart/part/mo/session/13/contribution/25?lang=en`.

Danksagung

Viele Menschen haben dazu beigetragen, dass die vorliegende Arbeit erstellt werden konnte. Ich werde hier einige nennen und bestimmt auch einige vergessen. Seht es mir nach, solltet ihr versehentlich nicht erwähnt werden.

Zu allererst möchte ich meinen beiden Professoren Ingolf-Volker Hertel und Marc Vrakking dafür danken, dass ich die Gelegenheit erhalten habe am MBI in Berlin und am AMOLF in Amsterdam die dieser Arbeit zugrunde liegenden Experimente durchführen zu dürfen. Marc, auch für das gewissenhafte Lesen und Korrigieren meiner Arbeit danke ich Dir sehr.

Ein besonderer Dank gilt Prof. Schultz. Thomas, vielen Dank für Deine Anstrengungen und die sehr gewissenhafte Betreuung vor allem des fs-LID Themas. Ich schätze das wirklich sehr, da zu dieser Zeit bereits die neue Aufgabe in Korea Deine volle Aufmerksamkeit forderte.

Auch die Kollegen der Chemie der HU Berlin haben Anteil an den hier vorgestellten Ergebnissen. Ich möchte mich herzlich bei Prof. Linscheid für seine Erlaubnis bedanken, dass FT MS nutzen gedurft zu haben. Und mein geschätzter Kollege Andreas Kühn hat geduldig nächtelang mit mir den Strahlengang justiert, Daten aufgenommen, Chemikalien aufbereitet und einen enormen Aufwand bei der Datenanalyse geleistet. Lieber Andreas, es war zwar eine anstrengende, aber auch eine tolle Zeit!

Auch die MBI Wissenschaftler Dr. Schulz, und Dr. Noack † haben mich bei diversen Aufgaben unterstützt und standen mir mit Rat und Tat zur Seite. Besonders möchte ich auch Prof. Ivanov erwähnen. Es war immer sehr erhellend und erheiternd mit ihm über die seltsamen Geheimnisse der Elektronen zu diskutieren.

Ebenso möchte ich unsere technischen Fachkräfte am MBI Helga, Andreas, Roman und die

gesamte Werkstatt-Mannschaft dankend erwähnen. Sie haben stets alle Fragen und Bitten nach Kräften bearbeitet. Auch die Administration des MBIs hat mir und den Kollegen den Rücken für unsere eigentlichen Arbeiten freigehalten.

Speziell die Attosekundenexperimente wurden durch meine Mitdoktoranden Jesse Klei, Lukas Medišauskas und Martin Galbraith zu einem großen Erfolg. Ich möchte auch Dr. Yang, Dr. Rouzée und Dr. Lépine für ihre Beiträge herzlich danken.

Auch den Kollegen anderer Gruppen Christian, Faruk, Fede und Sascha danke ich für die schöne Zeit, die wir gemeinsam verbracht haben. Erinnern möchte ich an unsere legendären Sommer-Grillabende weit ab in Adlershof. Leute, wir hatten wirklich viel Spaß.

Erwähnen möchte ich auch die Amsterdamer Kollegen Georg, Aneta, Julia, Freek, Kim und Wing-Kiu. Ihr habt den Aufenthalt in dieser wundervollen Stadt für mich unvergesslich gemacht und mir fiel der Abschied nicht leicht.

Schließlich möchte ich auch meiner gesamten Familie, vor allem Prof. Papa Andreas und Mama Ulla, danken. Sie waren diejenigen, die immer an mich geglaubt haben und unterstützt haben, wo sie nur konnten. Ganz besonders dankbar bin ich meiner zukünftigen Ehefrau Jule. Es ist wohl nicht in Worte zu fassen, was sie während der langen und anstrengenden Promotionszeit geduldig ertragen hat...